LASER DRIVEN PLASMA BASED ELECTRON ACCELERATION, APPLICABLE MECHANISMS AND ITS APPLICATIONS

By

DIPANJANA HAZRA

PHYS03201304009

Raja Ramanna Centre for Advanced Technology, Indore

A thesis submitted to the

Board of Studies in Physical Sciences

In partial fulfillment of requirements

for the Degree of

DOCTOR OF PHILOSOPHY

of

HOMI BHABHA NATIONAL INSTITUTE

August, 2019

Homi Bhabha National Institute

Recommendations of the Viva Voce Committee

As members of the Viva Voce Committee, we certify that we have read the dissertation prepared by **Dipanjana Hazra** entitled **"Laser driven plasma based electron acceleration, applicable mechanisms and its applications"** and recommend that it may be accepted as fulfilling the thesis requirement for the award of Degree of Doctor of Philosophy.

Chairman – Prof. S. Krishnagopal, BARC, Mumbai	
Guide / Convener – Prof. Anand Moorti, RRCAT, Indore	Anand Moorti 6/11/2020
Examiner - Prof. B. Ramakrishna, IIT-Hyderabad	R. Bhuvanesh
Member 1- Prof. Vinit Kumar, RRCAT, Indore	Vinit Kumar 6. 11. 20
Member 2- Prof. M. P. Singh, RRCAT, Indore	6.11.20
Member 3- Prof. Arup Bandyopadhyay, VECC, Kolkata	Arup Bandyopadhyay

Final approval and acceptance of this thesis is contingent upon the candidate's submission of the final copies of the thesis to HBNI.

I hereby certify that I have read this thesis prepared under my direction and recommend that it may be accepted as fulfilling the thesis requirement.

Anand Moorti

Date: 6-11-2020

Place: Indore

Guide

(Prof. Anand Moorti)

STATEMENT BY AUTHOR

This dissertation has been submitted in partial fulfillment of requirements for an advanced degree at Homi Bhabha National Institute (HBNI) and is deposited in the Library to be made available to borrowers under rules of the HBNI.

Brief quotations from this dissertation are allowable without special permission, provided that accurate acknowledgement of source is made. Requests for permission for extended quotation from or reproduction of this manuscript in whole or in part may be granted by the Competent Authority of HBNI when in his or her judgment the proposed use of the material is in the interests of scholarship. In all other instances, however, permission must be obtained from the author.

Dipanjana Hazra

DIPANJANA HAZRA

DECLARATION

I, hereby declare that the investigation presented in the thesis has been carried out by me. The work is original and has not been submitted earlier as a whole or in part for a degree / diploma at this or any other Institution / University.

Dipanjana Hazra

DIPANJANA HAZRA

List of Publications arising from the thesis

Journal

1. Betatron resonance electron acceleration and generation of quasi-monoenergetic electron beams using 200fs Ti:Sa laser pulses

   D. Hazra, A. Moorti, B. S. Rao, A. Upadhyay, J. A. Chakera, and P. A. Naik.

   Plasma Phys. Controlled Fusion **60,** 085015 (2018).

2. Electron radiography with different beam parameters using laser plasma accelerator.

   D. Hazra, S. Mishra, A. Moorti, and J. A. Chakera

   Physical Review Accelerators and Beams **22**, 074701 (2019).

3. Determination of hybrid and direct laser acceleration dominated regimes in a 55fs laser driven plasma accelerator with ionization induced injection

   D. Hazra, A. Moorti, A. Upadhyay, and J. A. Chakera

   Under review in *Phys. Review Accelerators and Beams*.

   arXiv:1902.01203v2 [physics.plasm-ph].

4. Direct laser acceleration of electrons in high-Z gas target and effect of threshold plasma density on electron beam generation

   D. Hazra, A. Moorti, S. Mishra, A. Upadhyay, and J. A. Chakera

   Plasma Physics and Controlled Fusion **61**, 125016 (2019).

5. An experimental study on high-energy electron acceleration in He gas-jet target and effect of laser pulse duration

   D. Hazra *et al*.

   Manuscript under preparation.

Chapters in books and lectures notes: NIL

Conferences:

1. Generation of quasi-monoenergetic electron beams through betatron resonance in self guided laser plasma channel.
   <u>**D. Hazra**</u>, A. Moorti, B. S. Rao, J. A. Chakera, P. A. Naik and P. D. Gupta.
   Indian Particle Accelerator Conference Proceedings (InPAC), Tata Institute of Fundamental Research, Colaba, Mumbai, India, December 21-25 **(2015).**
2. Generation of beyond 100 MeV electrons from laser wakefield acceleration through ionization induced injection.
   <u>**D. Hazra**</u>, B. S. Rao, A. Moorti, J. A. Chakera, P. A. Naik and P. D. Gupta
   30th National Symposium on Plasma Science and Technology, Saha Institute of Nuclear Physics, Kolkata, India, December 1-4 **(2015). (Received Best Poster Award)**
3. Quasi-monoenergetic electron beam generation by betatron resonance acceleration and SM-LWFA with ionization induced injection.
   <u>**D. Hazra**</u>, A. Moorti, B. S. Rao, J. A. Chakera, P. A. Naik, and P. D. Gupta.
   7th Asian Summer School and Symposium on Laser Plasma Acceleration and Radiation (ASSS-7), Shanghai Jiao Tong University, Shanghai, China, July 17-23 **(2016). (Received Best Poster Award)**
4. Direct laser Acceleration of Electrons in Nitrogen-Argon Mix Gas-Jet Targets.
   <u>**D. Hazra**</u>, A. Moorti , S. Mishra, J. A. Chakera and P. A. Naik.
   32nd National Symposium on Plasma Science and Technology, Institute of Plasma Research, Gandhinagar, Gujarat, November 7- 10 **(2017).**
5. Generation of quasi-monoenergetic electron beams through direct laser acceleration using ionization induced injection in high-Z mixed gas target.
   <u>**D. Hazra**</u>, S. Mishra, A. Moorti, R. A. Khan, and J. A. Chakera
   33rd National Symposium on Plasma Science and Technology, University of Delhi, Delhi, December 4-7 **(2018)**. **(Received best poster award)**
6. Study of radiography application of relativistic electron beams generated from laser plasma electron accelerator

D. Hazra, S. Mishra, A. Moorti and J. A. Chakera

33rd National Symposium on Plasma Science and Technology, University of Delhi, Delhi, December 4-7 **(2018).**

7. Laser driven plasma based electron acceleration, applicable mechanisms and its applications

   D. Hazra

   Indian Particle Accelerator Conference (InPAC), Inter University Accelerator Centre, New Delhi, India, November 18-21 **(2019)**. **(Received best thesis award)**

8. Laser driven plasma based electron acceleration, applicable mechanisms and its applications

   D. Hazra

   National Laser Symposium (NLS) -28, Vellore Institute of Technology, Chennai, January 8-11, 2020. **(Received best thesis award)**

Others: NIL

Dipanjana Hazra

DIPANJANA HAZRA

DEDICATIONS

The thesis is dedicated to my father

ACKNOWLEDGEMENTS

I shall begin with thanking laser, mechanical and other support team members: Riyaz Khan, Ankit Singla, S. Meena, D. Karmakar, S. Sebastin, R. P. Kushwaha, L. Kisku, K. C. Parmar, P. K. Tripathy, and R. K. Bhat, who are the people behind the scene, and I deeply recognize many enjoyable and fruitful time during experiments.

Sincere thanks to Prof. J. A. Chakera, Head, LPD for sharing his knowledge and experience in carrying out experimental investigations related to the thesis. I would also like to thank Prof. P. A. Naik, Former Director, RRCAT & Head, LPD, for his help and support. Heart felt thanks also to other members of LPD: Dr. Vipul Arora, Tirtha Mandal, Mukund Kumar, Dr. Himangshu Singhal, and Dr. Y.B. S. R. Prasad for their help and cooperation. I must thank Prof. V. K. Tripathi, Prof. M. P. Singh, and Prof. Arup Banerjee for help and discussions on theoretical understanding.

I thank to those who actively contributed to the research work presented in this thesis. I am thankful to Dr. B. S. Rao for his help in initial experiments, discussions and sharing his experience. I would specially like to thank Shikha Mishra for her sincere contributions in the experiments, data analysis and particularly running GEANT4 Monte Carlo simulations. I highly acknowledge Dr. Ajit Upadhyay for detailed EPOCH PIC simulations supporting various experiments. Thanks are also due to Dr. Mithun Karmakar, Dr. Bhabesh Patel, and Prof. S. Sengupta from IPR, Gandhinagar, for OSIRIS PIC simulation.

Now time to acknowledge my guide Prof. Anand Moorti, for whom I would not like to use the word “Thank”, but I would rather like to express my gratitude and sincere appreciation for guiding me in all the aspects of career goals in unimaginable way.

CONTENTS

LIST OF FIGURES

LIST OF TABLES

CHAPTER 9

Conclusion and future perspective

This chapter summarizes the present thesis work and discusses prospects of future investigations in light of it.

9.1. Conclusions:

Laser wakefield acceleration mechanism (LWFA) has been investigated in detail over years in various experimental conditions and has shown its potential for generation of high-quality GeV-class electron beams [1-5]. Developments during last two decades or so has led LPA to be recognized as a potential candidate for future generation compact table top accelerators suitable for various possible applications [6-9]. Today when LPA is considered as a source of high energy short wavelength radiation, the other dominant acceleration mechanism governing laser plasma interaction i.e. DLA is being considered again along with wakefield in a hybrid regime acceleration [10-15]. This regime of acceleration has two fold advantages: one is the enhancement of electron energy gain in LWFA as the electrons ~~now~~ gains additional energy from the DLA over wakefield [10-15], and the other very important advantage is the potential to generate high-energy betatron radiation compared to only wakefield mechanism as in this case oscillation amplitude of electrons could be comparatively larger [16-20]. Thus, DLA shows a promising path to enhance the betatron radiation generated from LWFAs. Realizing the importance of DLA, Shaw *et al*. [21] have proposed for optimization of the DLA in LWFA either by optimizing the laser pulse duration or by experimentally verifying the two laser pulse scheme of Zhang *et al*. [10,11].

The present thesis work focuses on the experimental investigation of LPA and identification of the role of direct laser acceleration (DLA) of electrons in a wide range of laser and plasma parameters. All the experiments were performed with the CPA based 150 TW, 25 fs, Ti:sapphire laser system of RRCAT, Indore, India. The laser and plasma parameters were varied such that it covers a long laser pulse duration regime of $L>>\lambda_p$ to shorter laser pulse duration regime of $L\geq\lambda_p$, and the laser pulse completely overlaps the injected electrons. Various gas-jet targets were used such He, N_2, Ar and mixed gas targets of He doped with few % of N_2 and N_2 doped with few tens of % of He with varying concentrations of dopant.

9.1.1: Identification of role of DLA in different experimental regime:

In $L>>\lambda_p$ regime, where laser plasma interaction of long laser pulse duration of 200 fs with underdense He plasma was studied, a pure DLA regime was identified as discussed in Chapter-4, as is also observed in earlier reports by Gahn *et al*. [22] and Mangles *et al*. [23].

On reducing the laser pulse duration to ~55-60 fs such that $L>\lambda_p$, contribution of DLA along with wakefield in the total energy of electrons was observed and thereby a hybrid regime of acceleration (DLA + wakefield) was identified in He gas-jet plasma with equal contribution from both wakefield and DLA. The identification of a hybrid regime of acceleration in $L>\lambda_p$ regime at the self-injection threshold density of He gas target has been discussed in Chapter-5 and was also verified later in another experiment using He gas-jet target and is discussed in Chapter-7.

The acceleration regime of short laser pulse duration of $L>\lambda_p$ was further explored in detail in similar conditions using ~55-60 fs duration laser pulses and mixed gas-jet targets of He + N_2 and high Z target of pure N_2. Due to the effect of ionization induced injection mechanism associated with mixed gas and high Z targets, the threshold density for generation of relativistic electron beams was reduced compared to the self-injection threshold density observed for He gas-jet target. However, the laser and plasma parameters still lies in the $L \geq \lambda_p$ regime and complete overlap of the laser pulse with the injected electrons takes place. On decrease of density, strength of wakefield was observed to reduce, and interestingly a pure DLA regime of acceleration was identified. To the best of our knowledge, such an observation of pure DLA mechanism with short laser pulse duration of few tens of fs regime using mixed and high Z gas targets has not been investigated earlier. The investigations have been discussed in Chapter-5 and Chapter-6.

Further, in the similar conditions, threshold density for generation of relativistic electron beams was varied in mixed gas-jet target by varying the doping concentration of He and N_2 in the gas mixture and its effect on acceleration mechanism was studied. With increase in density, role of wakefield was observed to increase and hybrid mechanism was identified as the dominant applicable acceleration mechanism. In this case, a regime of onset of wakefield was observed where strength of wakefield slowly increases and hence the contribution of energy gain from wakefield gradually increases. Thus the hybrid acceleration mechanism observed in case of mixed gas-jet target is associated with ionization injection mechanism and is different from that observed in case of He gas-jet target at the self-injection threshold density where equal contribution of wakefield and DLA was observed. The observations have been discussed in Chapter-5 and Chapter-6. Further, for comparison experiments were also performed with Ar gas-jet targets in the $L > \lambda_p$ regime using longer laser pulse duration of 120 fs. In this case also, a pure DLA regime was identified and the results are discussed in Chapter-6 and Chapter-8.

Hence, the present thesis focuses on the identification of DLA mechanism and the suitable laser and plasma conditions were identified in different gas-jet targets of He, N_2, Ar and mixed gas of He + N_2 either by varying the laser pulse duration or by varying the plasma density. The identification of the acceleration mechanism of DLA has been based on the theoretical analysis on DLA performed in the different laser and plasma conditions supported by various experimental observations and 2D PIC simulations performed using code EPOCH [24] and OSIRIS [25,26].

9.1.2: Generation of relativistic electron beams and its characteristics:

Stable and reproducible generation of electron beams were observed during the experiment for the wide range of laser and plasma parameters. However, the electron beam properties were observed to vary depending on the acceleration mechanism i.e. either a pure DLA or hybrid regime. Electron beam properties were also observed to be affected by the injection mechanism i.e. either self-injection in case of He gas-jet target or ionization induced injection mechanism in case of pure N_2, mixed (He + N_2) and Ar gas-jet target.

For 1.2 mm length of plasma, in pure He gas-jet target where a pure DLA regime of acceleration was identified with 200fs duration laser pulse, collimated electron beams with typical divergence of ~30-40 mrad were observed with mostly quasi-thermal electron spectra with maximum energy of ~30 MeV (Chapter-4). In few shots, quasi-monoenergetic electron beams with peak energy of ~17-22 MeV and energy spread of ~10-20% were also observed from the similar experimental conditions. With 55fs laser pulse and N_2 gas-jet target, collimated electron beams with divergence of ~15-30 mrad and quasi-thermal electron beams with maximum energy of ~ 60 MeV were observed in a pure DLA regime (Chapter-5). Electron beams with similar energy and with quasi-thermal spectra were also observed from mixed gas-jet target of He + N_2 in a pure DLA dominated regime (Chapter-5). However, enhancement of electron energy was observed up to ~90 MeV in mixed gas-jet target when electrons were accelerated from a hybrid regime of acceleration (Chapter-5). The electron beam spectra were quasi-thermal. With He gas-jet target, quasi-monoenergetic electron beams with peak energy of ~28 MeV and energy spread of ~64% were observed accelerated through hybrid mechanism (Chapter-5).

For 4 mm length of plasma, in mixed gas-jet target of N_2 + He, where a pure DLA regime was identified, collimated electron beams with divergence of ~7-8 mrad were observed. Electron beam spectra were quasi-monoenergetic with energy spread of ~21 % and peak energy of ~168 MeV (maximum energy ~206 MeV) were observed (Chapter-6). On increasing density, hybrid regime of acceleration was identified and enhancement of electron energy upto ~235 MeV was observed with quasi-thermal electron spectra (Chapter-6). Hybrid regime of acceleration was also identified in He gas-jet target where quasi-monoenergetic electron beam with peak energy of ~140 MeV and energy spread of ~18% were observed (Chapter-7). In few shots, the peak electron energy was observed to increase up to ~400-520 MeV with maximum energy in the range of ~620-750 MeV.

9.1.3: Radiography applications:

The present thesis also focuses on the study of radiography applications of various metallic and biological plant samples using the relativistic electron beams generated from LPA using He and Ar gas-jet targets (Chapter-8). The radiographs were generated with a minimum resolution of ~75 μm. Further, reconstruction of the radiographs of various samples was performed using GEANT4 simulations [27]. Penetration depth of electrons generated through LPA was studied through simulations and in this regard suitability of LPA in radiotherapy was also discussed.

9.2. Future outlook:

In the present thesis, experimental investigations in different parametric conditions were performed and role of DLA was identified. The complexity associated with this aspect of laser plasma accelerators suggests further investigations (experimental and simulations) which is not possible to address through a single thesis work. The thesis work thus brings out vast scope for possible future investigations, and several points could be considered as dedicated research problems for further investigations in this field.

Through experimental observations, various regimes of acceleration were identified viz. pure DLA, and hybrid (WF+DLA). DLA signatures were established through its manifestation in observed maximum electron energy, spectrum characteristics (quasi-monoenergetic, broad continuous spectrum and appearance of multiple groups of electrons), and also through electron beam profile (ellipticity and larger divergence) and transmitted laser spectrum wherever available and applicable. Dedicated experiments towards establishing the signature of DLA could be useful in establishing and improving the understanding, e.g. appearance of fork structures in energy spectrum when dispersed perpendicular to the laser polarization as observed by Shaw *et al.*, [12], and also other parameters as stated above. Simultaneous use of many diagnostics such as recording of laser forward spectrum, laser channeling and propagation inside plasma through Thomason scattering, Shadowgraphy, interferrogram would lead to more detailed information about the interaction of the high intense laser pulse with plasma. Although positive chirp was found favorable for present experimental conditions, further detailed study in this direction on effect of laser chirp on DLA would be of interest. Effect of other laser parameters e.g. focal spot size, pulse front tilt etc. could also be considered. Finally, as high-power laser systems are mostly operated in single shot mode, and therefore in general there has been limitation on statistics of data on LPA, investigations with detailed statistics could be targeted.

Another signature of DLA mechanism would be manifested from the simultaneous recording of betatron radiation experimentally which would be another aspect of our future investigation. Optimum regimes could be identified for generation of betatron radiation from the accelerating electrons particularly in the laser created channel in high Z gas-targets. Studies devoted to fundamental understandings e.g. injection mechanism of electrons in DLA, particularly injection through surface wave generation so that better control of the accelerator can be achieved, would also be necessary and interesting.

2D PIC simulation studies were performed primarily to support the experimental observations and distinguish the underlying acceleration mechanism for which bubble formation, channel creation, separate contributions in energy gain has been studied. However, more detailed investigation could be useful such as retrieving electron beam profile, charge, betatron radiation etc. would strengthen the claim. A much more rigorous study of 2D PIC simulations on DLA and hybrid acceleration mechanism is required particularly tracking of individual electrons and understanding the electron energy gain separately from wakefield and DLA.

Further, a more detailed theoretical model on the understanding of electron dynamics in the laser channel accelerated by DLA would be of much interest. It is understood that the applicability of theoretical estimation of the maximum energy gain in the hybrid regime is not straight forward. Study of dynamics of the electron in the presence of laser and wakefield and the trapping conditions of electrons in such complex field structure would be of interest. Subsequently, detailed theoretical analysis of the hybrid regime of acceleration of electrons needs to be performed and this leaves a huge scope for future investigation from the theoretical point of view. Another important study in this direction could be study of effect of chirp on generation relativistic electron beams through DLA.

Further experimental investigation on the radiography application using electrons generated from LPA should be performed for special target samples and optimization of parameters is required for achieving higher resolution. Also, study with biological samples should also be performed and experimental estimation of dose deposition on adipose tissue could also be carried out.

References

[1] Physics of laser driven plasma based electron accelerators, E. Esarey, C. B. Schroeder, and W. P. Leemans, *Rev. Mod. Phys.*, **81**, 1229 (2009).

[2] Laser plasma accelerators, V. Malka, *Phys. Plasmas,* **19**, 055501 (2012).

[3] Developments in laser-driven plasma accelerators, S. M. Hooker, *Nature Photonics*, **7**, 775 (2013).

[4] Laser-driven plasma accelerators operating in the self-guided, blowout regime, C. Joshi, *IEEE Transactions on Plasma Science*, **45**, 3134 (2017).

[5] Plasma-based accelerators: then and now, C. Joshi, *Plasma Phys. Controlled Fusion*, (2019), doi.org/10.1088/1361-6587/ab396a.

[6] Applications of laser wakefield accelerator-based light sources, F. Albert and A. G. R. Thomas, *Plasma Phys. Control. Fusion*, **58**, 103001 (2016).

[7] Principles and applications of compact laser–plasma accelerators, V. Malka, J. Faure, Y. A. Gauduel, E. Lefebvre, A. Rousse *et al*., *Nature Physics*,**4**, 447 (2008).

[8] Applications of laser driven particle acceleration, P. R. Bolton, K. Parodi and J. Schreiber, *CRC Press*, Taylor & Francis Group (2018).

[9] Laser-Driven Particle Acceleration Towards Radiobiology and Medicine, Antonio Giulietti, *Springer International Publishing, Switzerland*, (2016).

[10] Synergistic Laser-Wakefield and Direct-Laser Acceleration in the Plasma-Bubble Regime, Xi Zhang, V. N. Khudik, and S. Gennady, *Phys. Rev. Lett.*,**114**, 184801 (2015).

[11] Laser wakefield and direct acceleration with ionization injection, Xi Zhang, V. N Khudik, A. Pukhov and G. Shvets, *Plasma Phys. Control. Fusion*, **58**, 034011(2016).

[12] Role of Direct Laser Acceleration of Electrons in a Laser Wakefield Accelerator with Ionization Injection, J. L. Shaw, N. Lemos, L. D. Amorim, N. Vafaei-Najafabadi, K. A. Marsh *et al*., *Phys. Rev. Lett.*,**118**, 064801 (2017).

[13] Experimental signatures of direct-laser-acceleration-assisted laser wakefield acceleration, J. L. Shaw, N. Lemos, K. A. Marsh, D. H. Froula and C. Joshi, *Plasma Physics and Controlled Fusion*, **60**, 044012 (2018).

[14] Role of direct laser acceleration in energy gained by electrons in a laser wakefield accelerator with ionization injection, J. L. Shaw, F. S. Tsung, N. Vafaei-Najafabadi, K. A. Marsh, N. Lemos *et al*., Plasma Phys. Control. Fusion, **56**, 084006 (2014).

[15] Estimation of direct laser acceleration in laser wakefield accelerators using particle-in-cell simulations, J. L. Shaw, N. Lemos, K. A. Marsh, F. S. Tsung, W. B. Mori *et al*., *Plasma Physics and Controlled Fusion*,**58**, 034008 (2016).

[16] Bright betatron X-ray radiation from a laser-driven-clustering gas target, L. M. Chen, W. C. Yan, D. Z. Li, Z. D. Hu, L. Zhang *et al.*, *Scientific Reports*, **3**, 1912 (2013).

[17] Observation of Synchrotron Radiation from Electrons Accelerated in a Petawatt-Laser-Generated Plasma Cavity, S. Kneip, S. R. Nagel, C. Bellei, N. Bourgeois, A. E. Dangor *et al., Phys. Rev. Lett.*,**100**, 105006 (2008).

[18] Gamma-rays from harmonically resonant betatron oscillations in a plasma wake, S. Cipiccia, M. R Islam, B. Ersfeld, R. P. Shanks, E. Brunetti, *et al.*, *Nat. Phys.* **7**, 867 (2011).

[19] Femtosecond x rays from laser-plasma accelerators, S. Corde, K. Ta Phuoc, G. Lambert, R. Fitour, V. Malka *et al.*, *Rev. Mod. Phys.*, **85** 1 (2013).

[20] Characteristics of betatron radiation from direct-laser-accelerated electrons, T. W. Huang, A. P. L. Robinson, C. T. Zhou, B. Qiao, B. Liu *et al.*, *Phys. Rev. E.*, **93** 063203 (2016).

[21] Direct laser acceleration in laser wakefield accelerators, PhD Thesis, J. L. Shaw, University of California (2016).

[22] Multi-MeV Electron Beam Generation by Direct Laser Acceleration in High-Density Plasma Channels, C. Gahn, G. D. Tsakiris, A. Pukhov, J. Meyer-ter-Vehn, G. Pretzler *et al.*, *Phys. Rev. Lett.*, **83**, 4772 (1999).

[23] Electron Acceleration in Cavitated Channels Formed by a Petawatt Laser in Low-Density Plasma, S. P. D. Mangles, B. R. Walton, M. Tzoufras, Z. Najmudin, R. J. Clarke *et al.*, *Phys. Rev. Lett.*, **94**, 245001 (2005).

[24] Contemporary particle-in-cell approach to laser-plasma modelling, T. D. Arber, K. Bennett, C. S. Brady, A. Lawrence-Douglas, M. G. Ramsay *et al.*, *Plasma Physics and Controlled Fusion*, **57,** 1 (2015).

[25] Lecture Notes in Computer Science: Computation Science–ICCS 2002, R. A. Fonseca *et al.*, *edited by* P. M. A. Sloot *et al.*, Berlin: Springer **2331**, 342 (2002).

[26] Particle-in-Cell Modeling of Plasma-Based Accelerators in Two and Three Dimensions, R. G. Hemker, PhD Dissertation UCLA (1999) [arXiv:1503.00276].

[27] GEANT 4-a simulation toolkit, S. Agostinelli, J. Allison, K. Amako, J. Apostolakis, H. Araujo *et al*., *Nucl. Instrum.vMethods Phys. Res. A*, **506**, 250 (2003).

SUMMARY

The thesis work presents investigations on laser driven electron acceleration in underdense gas-jet plasma with emphasis on identification of different applicable acceleration mechanism and also demonstrates electron radiography application. Experiments were performed using Chirped Pulse Amplification based 25 fs, 150 TW Ti:sapphire laser system at RRCAT, Indore, India. Direct laser acceleration (DLA) and hybrid regime of acceleration (DLA + wakefield) of electrons in different gas-jet targets of He, N_2, Ar and mixed gas targets of He + N_2 were identified. A pure DLA regime was identified as the applicable acceleration mechanism with long laser pulse duration of 200 fs in He gas-jet target. Interestingly, a pure DLA regime of acceleration was also identified with short laser pulse duration of 55-60 fs in high-Z N_2 and mixed gas targets. Electron beams with few tens of MeV energy with quasi-thermal distribution, and also quasi-monoenergetic (energy spread ~21%) electron beams with peak energy of ~168 MeV were observed. Hybrid regime of acceleration in He has demonstrated acceleration of electrons to few hundreds of MeV and maximum up to ~750 MeV. Further, radiography application of relativistic electron beams was explored (minimum resolution of ~75 μm was achieved), along with suitability for radiotherapy application. 2D PIC simulations were performed using code EPOCH, and also OSIRIS, for supporting electron acceleration results, and GEANT-4 for radiography and radiotherapy. Many interesting results have been brought out through these investigations which to the best of our knowledge are not reported earlier. The studies would be of significance for developing stable laser plasma accelerator through understanding of acceleration mechanisms involved and high flux short wavelength betatron radiation source based on that.

CHAPTER 1

Introduction

1.1. Particle acceleration and advanced accelerator concepts: An overview

Today we all understand that ‘Atom’ (basic constituent of matter) consists of three types of particles viz. nucleons [protons (positive charge) and neutrons (neutral) found in nucleus] and electrons (negative charge) revolving around it, and numbers of which are different in every element [1]. An atom as a whole is electrically neutral, however, on removing one or more electrons from the atom, it becomes positively charged and is called ‘ion’, e.g. removing one electron from hydrogen atom gives H^+ ion i.e. proton. There are many particles in the nature, which are also available as free stable particles like electrons, protons and ions, such as cosmic rays consist of very high-energy particles (GeV-TeV). They are also generated in some natural processes like radioactive decays of some of the heavy nucleus where ‘alpha (helium nucleus)’ ‘beta (electrons)’ and ‘gamma (photons) are generated. Photon is the particle associated with light or electromagnetic radiation.

The importance of high energy charged particles was realized way back in 1911, the above described structure of atom was understood through an experiment performed by Ernest Rutherford (a British Physicist) by bombarding gold foil by alpha particles (of energies ~5.5 MeV, generated from Americium: Am^{241}, a radioactive substance) and hence discovered the existence of nucleus [2,3]. This was the first experimental study showing the importance of charged particles of high-energies in understanding the nature. Subsequent to his discovery, in his presidential address to the Royal Society, in 1927 [4], Rutherford urged, ‘‘I have long hoped for a source of positive particles more energetic than those emitted from natural radioactive substances’’, which was motivated by the desire to study even smaller dimensions. This necessitated finding out the ways to accelerate charged particles in the laboratory and accelerators were built.

Most of the knowledge of the subatomic world has been achieved using particle accelerators. Initially, accelerators were developed particularly for the nuclear and particle physics research with the demand for higher and higher particle energies. Presently, worldwide a number of particle accelerators are operational which are also used for other numerous applications covering wide range of field such as understanding the structure and dynamics of materials and their properties (physics, chemistry, biology), application in medicine such as treatment of tumors and cancers, production of medical isotopes, sterilization, ion implantation etc, industrial applications such as cross-linking and polymerization of tyres, rubbers, plastics, semiconductor manufacturing, food irradiation, welding, cutting etc and applications in security such as scanning of materials, radiography etc [5,6]. Beams of accelerated particles can be further used to produce beams of secondary particles: Photons (x-rays, gamma-rays, visible light) are generated from beams of electrons (light sources) [7, 8] and neutrons are generated from beams of protons (spallation neutron sources) [9, 10].

Among many particle accelerators, electron accelerators have received much importance because of being elementary particle and its lighter mass compared to other heavy particles and hence cheaper compared to other heavier particles. Currently two main applications have been identified that motivated the majority of developments in the science and technology of electron accelerators: the first one concerns medical uses [11, 12], and the second one deals with the production of x-rays for further utilization in research in several fields, the so called synchrotron light sources [7, 8]. Also, electron accelerators play an important role in many other industrial applications and are becoming more and more present in scientific, medical and industrial field. The increasing demand in improving electron beam properties necessitated greater control and efficiency of electron accelerators, leading to incredible advances in the accelerator technologies.

In this regard, accelerator technologies have evolved tremendously over years starting from the DC acceleration technique, and currently majority of accelerators rely on the electromagnetic fields to accelerate charge particles, namely the radio-frequency (rf) technology [13-16]. RF acceleration technique although evolved to be a robust technique [16] yet suffers from the drawback of limited acceleration gradients. The maximum achievable gradient reported is ~100 MV/m [17]. However, this is still in a prototype stage, majority of conventional linear accelerators mostly operate at gradients of ~20-30 MV/m leading to large accelerator size, for example, the longest rf linear particle accelerator is the Stanford Linear Accelerator at Stanford Linear Accelerator Centre (SLAC), California, USA which accelerates electrons and positrons upto 50 GeV in 3.2 km length operating with an accelerating gradient of ~20 MV/m [18]. As an alternative, use of superconducting rf cavities have also been adopted. A proposed superconducting rf based linear accelerator is the 500 GeV electron positron collider: the International Linear Collider (ILC) with an overall length of 31 km (accelerating gradient of 31.5 MV/m) which is about 10 times larger than SLAC [19] and would be the largest linear accelerator. The large accelerator size and the associated huge infrastructure costs has made the scientific community to think for alternative options to increase the acceleration gradients and consequently several advanced accelerator concepts have emerged [20,21].

In this regard, lasers were proposed to be a suitable candidate and advanced acceleration techniques on use of huge electric field associated with intense laser pulses were suggested and explored [20-24]. Simultaneously, plasma was also proposed for use as an accelerating structure, as it can sustain fields beyond material breakdown limits. Subsequently, various plasma based advanced acceleration schemes, have been proposed [20, 21, 24-28], which rely on the generation of plasma waves or wakes through the space charge forces. In 1979, Tajima and Dawson proposed a scheme of driving these wakes using high intense laser pulses and a laser plasma interaction based advanced acceleration scheme evolved termed as **L**aser **P**lasma **A**ccelerator (LPA) [29].It was found to be promising as the wakes could generate high acceleration gradients of >100 GV/m [20, 21, 24-28]. Wakes could also beexcited by charged (electron/positron/proton) particle beams and is called **P**lasma **W**akefield **A**cceleration (PWFA) [30].

Plasma acceleration have been extensively investigated over years as research in plasma is scientifically very rich as it involves understanding of highly non-linear physics and leads to rigorous scientific research beyond just use of accelerators. Various schemes have been adopted for improvement of the accelerator performance in terms of efficiency and beam parameters and much more detailed investigations is required to bring these accelerators to practical applications. In this thesis, we present a detailed experimental investigation of LPA.

1.2. Brief history of technological developments of electron accelerators:

Acceleration techniques of electron accelerators have shown immense progress over years [13-16]. It began with the simplest DC acceleration technique where electrons generally produced from thermionic cathodes were accelerated in constant electric field between two electrodes generated by high voltage generators such as the Van de Graff generators, which could produce voltage upto 1.5 MV [31]. With the motivation to increase the particle energy, instead of DC voltages, use of alternating time varying fields was proposed [32] and linear accelerators (rf linac) consisting of alternating drift tubes of increasing lengths connected to the same terminal of a rf generator were built [33]. Length of RF linacs may vary from few meters to kilometres depending on the application, the largest electron linac being the 50 GeV Stanford Linear Accelerator (SLAC) of 3.7 km long [18]. Further, betatron was developed where acceleration of electrons relied on the induced electric field resulting from time varying magnetic field [34]. However, this scheme suffers from the drawback of available maximum magnetic field. Betatrons in the range of 7-20 MeV are now manufactured, especially for use for medical purposes. Later on microtrons were developed relying on rf electron acceleration with a constant magnetic field and increasing electron orbit radius [35]. Mostly, microtrons are used as injectors to storage rings.

The most important technological development of electron accelerators was the synchrotrons, where, the electrons rotate in fixed radius orbits, gain energy in rf cavities and the strength of magnetic field increases in synchronous with the increasing kinetic energy of electrons [36]. Electrons revolving in circular orbits loses energy and emit synchrotron radiation in a narrow cone tangent to the circular path of the magnets, which lies within the UV and X-ray range of the electromagnetic spectrum [7, 8]. Loss of synchrotron radiation meant reduction in electron energy and it became a problem for particle physicists, but soon became a very important tool for material studies. As the synchrotron radiation user community grew, there was an increasing pressure for storage rings designed and dedicated to the production of synchrotron radiation. Facilities like the European Synchrotron Radiation Facility (ESRF, in Grenoble, France, with 6 GeV electrons), Advanced Photon Source (APS, in Argonne, USA, with 7 GeV electrons), and Japan Synchrotron Radiation Research Institute (JASRI, with Spring-8 a 8 GeV storage ring, in Hyogo, Japan) are examples of high brightness sources.

1.3 Laser based advanced acceleration techniques:

Charged particle net energy gain and hence acceleration in an electromagnetic field requires violating the Lawson-Woodward theorem which states that highly relativistic electrons interacting with an electromagnetic field in vacuum cannot gain any net energy [37]. Several ways to violate the Lawson-Woodward theorem have been explored-

1. By limiting the interaction region.
2. By focusing the laser to a finite spot size and considering the ponderomotive force.
3. By applying magnetic field in the interaction region.
4. By changing the medium of interaction by introducing gas or plasma into the region.

Electron acceleration and net energy gain can be achieved through interaction with laser in vacuum by limiting the laser electron interaction to approximately in a region of the Rayleigh length by tightly focusing high intense lasers to finite size spot or by introducing optics close to the focus [38]. In this case, the electric field of high intense focussed laser fields in vacuum were used to accelerate electrons within the focal region and was demonstrated experimentally [39].Finite energy gain in vacuum is also possible through the ponderomotive acceleration where energy gain results from the non-linear force of the high intense laser [40]. Acceleration by this technique can generate electron upto a few MeV with laser energy spread and high scattering.

Energy gain can also result from the introduction of a periodic magnetic wiggler field, as in case of Inverse Free Electron Laser (IFEL) [22]. Relativistic electrons are co-propagated with the laser field in presence of a magnetic field, that allows the electrons to oscillate in the same plane as that of laser and at resonance exchange of energy between the laser (wave) and the electrons (particles) takes place. The acceleration of electrons through IFEL was first demonstrated in 1992 [41] and two notable experiments were reported on the IFEL scheme: one at Brookhaven National Laboratory (BNL), USA, known as Staged Electron Laser Acceleration (STELLA) [42, 43] and the other at UCLA's Neptune laboratory, USA [44]. In the UCLA experiment, 14.5 MeV electron beam was accelerated upto 30 MeV with an acceleration gradient of 70 MV/m. Recently, micro bunching of electron in a cascaded acceleration scheme was demonstrated where a 54 MeV electron beam was accelerated to 82 MeV with an rms energy spread of ~1% [45].

Finite energy gain can be achieved by introducing a background of gas into the interaction region, such that the phase velocity of the laser is reduced to match with that of the electrons as in the case of Inverse Cherenkov Acceleration (ICA) [23]. Electron beam is intersected with laser beam at certain angle. When the angle matches with Cherenkov angle, phase matching between the electron and the laser pulse takes place and results in acceleration of the electron beam. Using this scheme, Kimura *et al*., demonstrated experimentally a 3.7 MeV modulation on a 40 MeV electron beam using a 580 MW CO_2 laser [46].

1.4. Plasma based advanced acceleration techniques:

Introduction of plasma medium also provides a possible means to support electron acceleration and hence gives rise to several plasma based electron accelerators, like the PWFA [30] and LPA [29] and since plasma is already a broken state of matter, no further electrical breakdown is possible and hence accelerating electric field of >100 GV/m can be produced in plasma by driving giant plasma waves (wakefields) using charged particle beams or intense laser pulses [20, 21, 24-28].

In case of PWFA, the wake-field is driven by an intense, high-energy, charged particle beam of either electron or positron when it passes through the plasma [30]. In case of electron beam driven wakefield, the space charge force of the electron bunch blows out the plasma electrons. If the driver bunch density is much higher than the plasma density then all the electrons will be blown out. In such time scales, the ions do not respond and a cavity void of electrons is created. When a second bunch of electrons is trapped inside such cavity is accelerated by the longitudinal field of the cavity. In the first experimental demonstration of generation of wakefield by a relativistic electron beam, a field gradient of 2 MeV/m was reported [47]. Subsequently, experiments performed using this technique have demonstrated an energy gain of more than 2.7 GeV [48], energy doubling of 42 GeV electrons [49], and the first acceleration of positrons in a plasma [50]. However, the accelerated electron beams showed continuous energy spectrum. Further PWFA experiments were performed at Facilities for Accelerator Science and Experimental Test (FACET) at SLAC, USA aiming towards achieving higher acceleration gradient and lower energy spread and reduced transverse emittance [51]. Apart from FACET, a new beamline at CERN [52], at DESY in Germany, a new beamline called FLASHForward (Future oriented wakefield accelerator research and development at FLASH) [53] and another beamline called FACET-II at SLAC demonstrating high quality electron beams through wakefield induced ionization induced injection [54] has been constructed to further explore this scheme.

1.5. Laser Plasma Accelerator (LPA):

In case of LPA, the wakefield is driven by intense short laser pulses. LPA has attracted lot of attention in the scientific community because of being cheap and compact and also for applications covering wide range of fields due to the unique characteristics of particle beams produced and hence has proved to be one of the potential future generation accelerators.

In LPA, a short (few tens to few hundreds of fs duration), intense ($\sim 10^{18}$-10^{19} W/cm^2) laser pulse interacts with plasma (density $\sim 10^{17\text{-}20}$cm^{-3}) produced using gases (e.g. He, N_2 or mixed) of lengths few mm to few cms. Mostly, Ti:sapphire laser system (λ=800nm), based on chirped pulse amplification (CPA) technique [55] is used. In CPA technique, an ultra-short (10-20fs) laser pulse is at first stretched in time, then amplified, and subsequently compressed close to its original pulse duration, providing short pulse of extreme peak powers from few Terawatt (TW) to Petawatt (PW) level. Most widely investigated scheme in LPA is wakefield acceleration i.e.

Laser **W**akefield **A**cceleration (LWFA) [29]. In LWFA, intense ultra-short laser pulse is used to excite accelerating electric field (known as wakefield) in the wake of the laser pulse through driving large amplitude electron plasma wave. Efficient excitation of wakefield requires $L \sim \lambda_p$, where $L=c\tau$ is the laser pulse length, τ is the FWHM laser pulse duration and λ_p is the plasma wavelength which is inversely proportional to the square root of the plasma density. For example for electron densities of $\sim 10^{19}$ cm^{-3}, this matching requires a laser pulse lengths of ~30 fs.

In the following sub-sections, the different schemes of electron acceleration under LPA and their respective current experimental status is discussed in detail.

1.5.1: Beat Wave Laser Wakefield Acceleration (BW-LWFA):

Initially during the proposition of LWFA in 1979, the available laser pulse lengths were much longer such that the resonance condition of $L \sim \lambda_p$ condition was impossible to satisfy. In such scenario, plasma beat-wave LWFA or BW-LWFA was suggested [29, 56]. In this case, two long laser pulses (~ 100 ps) of frequencies ω_1 and ω_2 are collinearly propagated through the plasma. These two laser pulses will beat at a frequency $\Delta\omega=\omega_1-\omega_2$. To resonantly excite the plasma wave, it must satisfy the matching conditions such that the beat frequency is almost equal to the plasma frequency ω_p, i.e.$\Delta\omega \cong \omega_p$. Effectively a series of laser pulses are formed each of duration $\Delta\tau=2\pi/\Delta\omega=2\pi/\omega_p$. These short train of pulses move with the group velocity of the laser pulse. Now, plasma wave is generated by the ponderomotive force associated with the intensity gradient of these short laser pulses. Since a number of these short pulses resonantly excite the plasma wave moving with the group velocity of the laser, high amplitude plasma wave can be generated with phase velocity equal to the group velocity of the laser, and electrons can be accelerated to very high energies. Generally, BW-LWFA is operated at moderate intensities of around10^{14}-10^{16}W/cm^2.

However, electron acceleration by this method is limited by the detuning of the resonant process. After travelling certain distance with the beat wave, the plasma wave amplitude becomes so high such that its oscillation frequency ω_p decreases. Whereas, the beat wave frequency remains fixed. So, after certain beat periods, the resonant condition breaks and the plasma wave goes out of phase with the laser beat wave. In order to avoid this limitation, the beat wave frequency is made slightly lower than the plasma frequency, i.e. $\Delta\omega<\omega_p$ [57]. In addition to the resonant detuning and a very challenging scheme due to its requirements of a two-frequency laser system, and precise matching to the plasma frequency, BW-LWFA process is subjected to various laser plasma instabilities as it is operated in the long pulse regime.

The first experimental observation of accelerated electron beams using this scheme showed generation of electrons upto 10 MeV using CO_2 laser having two of ~10.6 and 9.57 pm respectively [58]. Subsequently, experiments were also performed by the UCLA group where electron energy gain of externally injected electrons to ~28 MeV using the PBWA technique was demonstrated [59] and several more experimental demonstrations were reported using this technique [60,61]. The maximum energy of electrons obtained through PBWA is ~38 MeV in a laser beat wave induced plasma channel [62].

1.5.2. Self-Modulated Laser Wakefield Acceleration (SM-LWFA):

Later with the development of laser technology, and availability of comparatively short laser pulses, PBWA scheme was replaced by the SM-LWFA scheme where single intense laser pulse was used to excite wakefields directly. During this time the available shortest laser pulse durations were of the order of ps or hundreds of fs such that the pulse length was still longer compared to the plasma wavelength i.e. $L>>\lambda_p$. However, with the availability of shorter laser pulses of several tens of fs, $L>\lambda_p$ regime could also be realized experimentally. Long laser pulses, after self-focusing inside plasma are modulated on the order of plasma wavelength, which subsequently drives strong wakefield. SM-LWFA generally operates at high plasma densities of the order of $\sim 10^{19}cm^{-3}$ or higher.

Subsequently, several groups have reported acceleration of electrons through SM-LWFA in the $L>>\lambda_p$ regime using laser pulses of several hundreds of fs and peak powers of few TW interacting with underdense plasma targets of densities of the order of $\sim 10^{19}cm^{-3}$ and gain in maximum electron energy up to few tens of MeV were observed [63-68]. However, electron beams with broad continuous spectrum were generated. There were experiments performed in the $L>\lambda_p$ regime also using several tens of fs duration laser pulses and densities of the order of $\sim 10^{19}cm^{-3}$ [70-80]. In all these experiments electron beams with higher energy of several tens of MeV with quasi-monoenergetic spectra have been observed. Acceleration of electrons in the SM-LWFA regime has been explored extensively. It was demonstrated that in case of wakefield acceleration, electron energy decreases with increase in the plasma density [81]. Further, various experiments have been performed on increasing the self-modulation instability of the laser pulse to generate large amplitude wakefields such as by using asymmetric or chirped laser pulses [82,83] or by increasing the growth rate of Raman Forward Scattering (FRS) instability [84] where generation of electron beams with improved beam parameters have been observed.

1.5.3. Blowout or bubble acceleration:

In 2004, interestingly, three groups simultaneously reported generation of quasi-monoenergetic electron beams with energy spread (<10%) and low divergence (<10 mrad) and comparatively higher electron energies in the range of 100-200 MeV [85-87]. This marked a break-through in the evolution of LPA and on its potentials. The generation of quasi-monoenergetic feature in the electron spectra was explained by the mechanism of bubble formation: a scheme of LWFA known as 'bubble' or 'blow-out' [88, 89] applicable for the condition of $L<\lambda_p$ regime, for comparatively shorter laser pulse duration of few tens of fs and at lower plasma densities of $\sim 10^{17-18}$ cm^{-3}. In order to operate the LPA in a blow-out regime, it requires to fulfil certain matching conditions between the laser intensity (a_0), laser focal spot (ω_0) and the plasma density (n_e) such that,

$$k_p \omega_0 = k_p R = 2\sqrt{a_0}\ , \tag{1.1}$$

where $k_p = 2\pi / \lambda_p$ and $\lambda_p(\mu m) = 3.33\times10^{10} / \sqrt{n_e(cm^{-3})}$ is the plasma wavelength [89] and R is the bubble radius.

Several experimental investigations performed in the bubble regime demonstrated generation of good quality quasi-monoenergetic electron beams with energy in the range of several hundreds of MeV to sub-GeV [90-95]. Later, several experiments have reported generation of multi-GeV electron beams with few percent energy spread [96-102]. Recently, with the availability of PW laser facilities, generation of ~8 GeV electron beams with few per cent energy spread have been demonstrated through wakefield mechanism [103].

Observation of quasi-monoenergetic electron beams in the experiments performed in the SM-LWFA regime i.e. $L>\lambda_p$ [70-80] was also explained by the bubble regime of acceleration. Although initially laser and plasma parameters were not matched, however, the non-linear self-evolution of laser pulse in plasma would lead to achieve bubble regime conditions leading to quasi-monoenergetic features in the electron spectra.

Mostly, LWFA experiments (described above) were performed in low Z He gas-jet targets. In low Z gas targets plasma formation takes place at the foot of the laser pulse and main laser pulse interact with the fully ionized plasma therefore ionization effects on laser propagation could be avoided. Relativistic self-focusing and channelling of laser pulse for long plasma lengths exceeding several times beyond the Rayleigh length has been observed in several experiments using He gas-jet targets [91, 104-112].Pure high Z gases are not preferred for laser plasma acceleration experiments primarily due to inherent drawback of ionization induced defocusing of the laser pulse [113-115]. Still, electron acceleration in high Z gases e.g. N_2 and Ar etc. have been explored for comparison purpose and particularly N_2 as being readily available and cheap [116-126]. In case of N_2 targets, experiments have been performed both in the SM-LWFA [116-121] and bubble regime [122-126] and generation of QM electron beams with peak energy in the range of few hundred MeV has also been demonstrated [121-124]. LWFA experiments have also been carried out in mixed gas-jet target of where few percent (0.1-10%) of high Z gas (such as N_2, CO_2, O_2 etc.) is doped in low Z gas (such as H_2, He) [127-138]. Experiments were mostly operated in the bubble regime of acceleration and generation of few hundred MeV to GeV electron beams has been reported.

This bubble regime of acceleration has therefore proved to be a promising technique in generating very high energy good quality electron beams through LPA. Thereafter, concept of staged plasma acceleration was proposed where electrons accelerated from one stage is injected into the other for further acceleration [139] and were demonstrated experimentally [132,133, 140, 141].

1.5.4: Direct Laser Acceleration (DLA) in plasma:

Another applicable acceleration mechanisms in laser created channels in the long laser pulse regime i.e. in $L>>\lambda_p$ (using hundreds of fs laser pulse duration) or even in $L>\lambda_p$ (using tens of fs laser pulse duration) regime is the direct laser acceleration (DLA) of electrons.

One way to observe DLA in plasma is by the ponderomotive acceleration [142]. At very high intensities, the v×B force of the laser field becomes strong enough to eject electrons radially as well as in the longitudinal directions to the laser propagation axis. Typically, the energy gained by this process is due to the quivering of the electrons in the laser ponderomotive potential. So, typically with $a_0=1$, the electron energy results to be 200-300keV and θ~64°, suggesting generation of very low diffused energy electron beams. Electron acceleration through this scheme was experimentally demonstrated by G. Malka *et al*. where energy gain of ~2.7 MeV was achieved [40].

The second very dominant DLA mechanism in this regime is the betatron resonance accelerationwas first investigated through 2D PIC simulation by Pukhov *et al.* [143]. In this scheme, the electrons oscillate at betatron frequency in the self-generated static fields of the ion channel created by high intensity laser pulse in underdense plasma. The static electric field is generated by the depletion of electrons from the laser channel axis by the radial ponderomotive force of the laser and the static magnetic field is generated from the stream of accelerated electrons. When this betatron frequency becomes equal to the doppler shifted laser frequency, resonant transfer of energy from the laser field to the electrons occurs. This transverse energy gain of electrons is converted into longitudinal direction by the v×B force and as a result effective energy gain of the accelerated electron beams in the longitudinal direction occurs. The electron energies in this case are far in excess of the ponderomotive potential energy as discussed above and the acceleration is directly a consequence of energy exchange with the laser, and not by the wake field as is in the case of LWFA. In contrast to wakefield, in case of DLA, the electrons perform larger transverse oscillations in the laser field and hence become a better candidate for generation of high energy betatron radiation compared to the wakefield [144-149].

There are very few reports on the experimental study of DLA, particularly using long laser pulse duration of hundreds of fs in He gas-jet target [150-152]. The first experimental demonstration was by Gahn *et al*. [150]. They showed acceleration of electrons of maximum energy of ~12 MeV with quasi-thermal distribution on interaction of long laser pulses of duration of 200 fs. Experiments on DLA have shown generation of electron beam with continuous [152], or quasi-thermal [150, 151] energy spectrum.

Applicability of DLA mechanism has also been reported in other gas-jet targets such as clustering Ar gas-jet where mostly broad continuous spectrum has been observed [144, 153, 154].

Since in the regime of L>λ_p and L>>λ_p, both SM-LWFA and DLA are plausible acceleration mechanisms, a competition between the two in terms of dominance of one mechanism over the other is obvious. For the regime L>>λ_p, several simulation results have shown that the wakefields are effective only at the foot of the laser pulse, signifying dominant electron acceleration mechanism of DLA [143,149,155,156]. It was found that the contribution of DLA vs wakefield mechanism was also dependent on the value of P/P_c where P is the initial laser power and P_c is the critical power for self-focusing, and for large values of $P/P_c>6$, DLA could take over wakefield [143]. This is because a high value of P/P_c would lead to strong relativistic self-focusing of the laser pulse and front of the pulse creates almost complete blowout of the electrons from the laser axis, and form a near hollow waveguide. The trailing part of the laser pulse propagates though this waveguide and therefore does not drive strong plasma wave i.e. wakefield [156].

However, in the regime of L>λ_p using comparatively shorter laser pulse duration of tens of fs, earlier in some of the reports on SM-LWFA also applicability of DLA mechanism has been discussed using He [157,81] and N_2 [158] gas target and electron energies of few tens of MeV with exponential spectrum have been observed. Recently, dominance of both wakefield and DLA together with equal contributions from each have been identified and a regime of hybrid acceleration (DLA + wakefield) was proposed in mixed gas target of He+N_2 [159, 160]. In this experiment, electrons with continuous spectrum with maximum energy of ~120 MeV have been observed. Accelerated electrons were dispersed in the perpendicular plane of the magnetic spectrograph and fork-like structures appeared in the electron spectrum, which suggested the contribution of DLA. Renewed interest in the hybrid regime of acceleration was due to the fact that DLA can double the energy of the accelerating electrons in a LWFA which was observed through detailed PIC simulations performed [161-163]. Also, it was shown that DLA electrons can even have lower energy spread compared to the wakefield electrons [162, 163].

1.6. Applications of laser plasma accelerators:

LPAs are now matured enough to generate good quality stable electron beams with energies in the range of few tens of MeV to few hundreds of MeV. Hence, applications of these electron beams for various potential applications are also being explored [164-167].

1.6.1: Radiation generation:

LPAs can now produce electrons of energies comparable to those in 3rd generation synchrotron facilities, and the use of wakefield accelerators for photon light source applications is a near-term potential prospect [164-166]. Radiation generated from electrons generated from LPAs could cover a wide range from tera-hertz to gamma rays of the electromagnetic spectrum generated through various mechanisms.

Betatron radiation is emitted when electron perform betatron oscillation either in the plasma bubble or the plasma channel in case of bubble or DLA mechanism of acceleration respectively. Several reports on experimental observation of betatron radiation in the blowout regime have been performed [168-178]. Highest betatron brightness to date from the blowout regime (peaking at ~20 keV) have been reported from 2 GeV electron beams accelerated at the Texas Petawatt Laser [174]. Some work has been done in the DLA regime with picosecond long laser pulses [145], where x-rays up to 50 keV have been reported. It has been shown that betatron radiation is enhanced in the presence of laser field due to the increased oscillation amplitude of electrons in the laser field [146-148, 179]. Betatron spectra peaked at 150 keV produced by 700 MeV electron beams have been reported in a slightly different regime at the Astra-Gemini laser facility [146]. Several studies have also been reported on using betatron radiation as a tool for characterizing electron beam properties such as electron beam source size [169, 172, 180, 181], initial angular momentum [182, 183], anisotropy in electron oscillations [173, 184] and self-injection into the plasma bubble or channel [147].

Another approach of generation of radiation from LPAs is by the inverse Compton scattering process [185]. In this case, generally two laser beams are used. One laser accelerates the electrons to relativistic energies whereas the other laser propagating in the opposite direction to the accelerated electron beams gets scattered. In the rest frame of the electrons, since the electrons and the laser field is moving towards each other (counter propagating), due to Doppler effect, the frequency of the laser field is up shifted. Another up shift of the radiated frequency occurs due to the Doppler effect when the scattered radiation is observed in the laboratory frame, thereby providing two fold increase in the scattered radiation. Various theoretical study has been reported on the mechanism [186, 187] and the first study using 3D PIC simulations on LPA Compton radiation source, predicted that with accelerating electrons of energy up to 300 MeV and nC charge generated from LPA, photon energies of 1 MeV with 10^7 photons per pulse of x-ray flux could be generated [188]. However, recent simulation studies have even predicted generation of 10 MeV photon energy with 10^{11} photons from interaction with 200 MeV, 100 pC electron beam [189].The first experimental demonstration was performed with a 10 TW laser producing Maxwellian electron distributions with scattered photons having energies up to 2 keV [190]. Consequently, several experiments were performed showing generation of hard x-rays [191, 192] and even gamma-rays [193-196] through this mechanism. The first experimental showing generation of hard x-rays of energy up to 300 keV (peak ~50 keV) was demonstrated using single laser pulse reflection from a plasma mirror [191]. A recent study has demonstrated the tunability of photon energy in the range of 75-200 keV with a quasi-monoenergetic (50%) spectrum [192]. Also, experimental demonstration have shown generation of even higher energy gamma-ray photons between 1-4 MeV from 300 MeV electrons generated from LPA using two independent laser pulses[193], which have the advantage of optimising x-ray output and scalability of higher γ-ray flux with increasing scattering pulse energy. The highest photon energy obtained from a LWFA Compton source is 18 MeV (approximately 10^7 photons with energies exceeding 6 MeV per shot) from Astra-Gemini laser facility [194].

Short wavelength radiation can also be generated by the mechanism of XFEL [198]. LPA is capable of generating high energy electron beams to be injected to x-ray free electron lasers (XFEL) and are being considered as a candidate for compact XFEL source. There are reports showing undulator radiation produced, with 55-75 MeV, 1% energy spread electron beams in the visible wavelengths [199], with 200

MeV electron beams in the soft x-ray range (few nm) [200] and with 120-130 MeV electron beams in the vacuum ultra-violet (VUV) spectral range [201].

Radiation emission by bremsstrahlung process takes place when energetic electrons are propagated through dense target and collisions with ions and other particles takes place. LWFA electrons have been also employed to produce gamma-rays by passing it through high-Z material converters. This technique has distinct advantages over direct laser irradiation of solid targets as in the LWFA-driven case, the source is much more collimated (5°) [202 - 204]. Gamma-rays with energies in the range of 8-17 MeV with ~10^8 photons were generated by 10-45 MeV LWFA electron beams incident on a 2 mm tantalum slab and the yield was found to be exceeding two orders of magnitude compared to direct radiation on solid targets [205, 206]. Production of tunable gamma-ray sources based on bremsstrahlung from LWFA electron beams have also been reported [207].

In LPA, coherent transition radiation (CTR) is generated by the electron beam induced currents at the boundary of the plasma/vacuum interface (typically in the THz regime) [206]. Several experiments have been performed showing generation of CTR from LWFA, and detection of CTR have been mostly used as a diagnostic of electron bunch duration and its longitudinal profile for LWFA electrons [207-213].

1.6.2. Radiography and Radiotherapy:

Another potential application of LPA which has been sparsely explored is electron beam radiography [214-218] and radiotherapy [219]. Electron beam has been found to be a potential alternative for radiography compared to other particles such as photons, neutrons and other charges particles such as protons [214]. In this regard, LPA have unique advantages over conventional accelerators based on RF technology, apart being cheap, compact table top source. Laser driven electron sources can generate electron bunches of very short duration of the order of fs [220]. As a result, it can deliver dose at high rate [221, 222]. It also allows for time-resolved studies. Experimental investigation of electron beams generated from LPA has been sparsely investigated [223-228].

For radiotherapy applications, mostly linacs were used for the purpose of treatment of superficial tumors [229], whereas to attend the deep seated tumors very high energy electron beams (VHEE) of ~ 150 - 250 MeV will be required [230-233]. In this regard, LPA has also been proposed to be considered as it can routinely generate electron energies of ~150-250 MeV and also have the advantage of ease and control of high dose delivery [221, 222, 234, 235]. Considering the important applications of electron beams in radiography and radiotherapy, further investigations using advanced accelerators like LPA is desirable, more so when there are very few reports in this direction.

1.7. Advantages and limitations:

LPA have been pursued rigorously by several groups worldwide and have now emerged to be one of the potential candidates among the advanced accelerator family. It has several advantages over conventional accelerators [24-28].

1. It can support acceleration gradient of upto ~100GV/m (three orders of magnitude higher than conventional RF accelerators), and hence can accelerate trapped plasma electrons to very high energies in small distances (few mms to few cms) [24-28]. Hence, LPA is seen as a promising technique to develop compact tabletop and cheap electron accelerators.

2. It can generate very high energy quasi-monoenergetic electron beams ~GeV with energy spread of few percent, and bunch duration of the order of fs [220].

3. LPA represent a tunable source, capable of addressing a broad range of applications [164-167].

However, LPA also suffers from various limitations also.

1. LPA has demonstrated generation of electron beams with total charge of the order of nC which is comparable to conventional accelerators. However, the average beam current is lower due to limitation of lower repetition rate of operation of LPA.

2. Since LPA is dominantly governed by the laser pulse propagation inside plasma, it suffers from some inherent limitations such as laser diffraction, pump depletion and various laser plasma instabilities.

3. It is associated with highly non-linear processes and hence electron beam stability required for potential applications still now remains a challenge.

In the above sections, we have discussed about the various advantages of LPAs over RF linear electron accelerators and its potential applications in the industrial, research and medical fields that could be realized from the relativistic electron beams with unique beam characteristics. However, LPA is still in the research and development phase and has several issues still associated with it viz. controlling the non-linear intense laser plasma interaction and hence generation of high-quality stable electron beams. Various non-linear phenomena associated with the high intense laser plasma interaction in LPA viz. relativistic self-focusing and channeling of laser pulse in underdense plasma, different electron injection mechanisms and dynamics of trapping of electrons in different complex field structures formed etc., is of paramount importance in order to control the accelerator performance and generate stable electron beams. Particularly understanding the dominant acceleration mechanisms applicable in different laser and plasma parameters is also of much significance along with exploring the applicability of LPA for various potential applications. In Table-1.1 below a summary of the understanding of different acceleration and injection mechanism in different laser and plasma parameters is provided.

Table-1.1: Summary of the experimental studies performed in LPA showing dominant acceleration and injection mechanism in different laser and plasma conditions.

Gas-jet target	**Reported experimental investigations**			**Injection mechanism**
	Regime	**wakefield**	**DLA/ hybrid**	
Low Z gases (He, H_2)	$L>>\lambda_p$	Mostly SM-LWFA	Two reports on pure DLA	Self-injection of electrons through wave-breaking process
	$L>\lambda_p$	Mostly SM-LWFA	Two reports suggested role of DLA	
	$L<\lambda_p$	bubble	------	
High Z gas (N_2)	$L>>\lambda_p$	Mostly SM-LWFA	One report on cascade of wakefield + DLA	Ionization induced injection
	$L>\lambda_p$	Mostly SM-LWFA	------	
	$L<\lambda_p$	bubble	------	
High Z gas (Ar)	$L>>\lambda_p$	-----	Mostly DLA	Ionization induced injection
	$L>\lambda_p$	-----	Mostly DLA	

Mixed gas target (He+ few % N_2, O_2, CO_2)	$L>>\lambda_p$	------	-------	Ionization induced injection
	$L>\lambda_p$	Mostly wakefield	One report on hybrid	
	$L<\lambda_p$	Mostly wakefield	-----	

1.8. Scope of the present thesis:

In the present research work, we focus on the generation of relativistic electron beams using Ti:sapphire laser pulses (λ=800 nm) of varying durations in the range of ~55 - 200 fs to cover $L\sim\lambda_p$ to $L>>\lambda_p$ regimes. Different gas-jet plasma targets e.g. He, mixed gas-jet targets of He+N_2, N_2 and Ar were used with plasma density in the range of ~10^{18}-10^{20} cm^{-3} to explore conditions suitable for applicability of different acceleration mechanisms such as wakefield, direct laser acceleration (DLA) and hybrid (i.e. DLA + wakefield) regime of acceleration. Generation of stable and reproducible electron beams was observed with maximum energies in the range of ~30-700 MeV in various experimental conditions explored. Particularly, quasi-monoenergetic electron spectra with peak energies in the range of ~30-500 MeV and energy spread in the range of ~10-20% were observed. Finally, we also focus on the radiography applications of these relativistic electron beams generated from the laser plasma interactions and radiographs of various metallic and biological samples using relativistic electron beams generated from LPA were recorded.

The chapter wise summary of the research work carried out is as follows:

Chapter 2 focuses on the theoretical aspects of different mechanisms of acceleration applicable in LPA. Laser wakefield acceleration (LWFA) mechanism and various schemes of electron injection viz. self-injection and ionization induced injection mechanisms etc. which are relevant to the present research work are discussed. This follows by direct laser acceleration (DLA) mechanism, where theoretical estimation of maximum energy gain and trapping conditions of electrons interacting with the laser field are described. Further, analytical expressions to estimate the dephasing length of electrons and rate of dephasing have been derived. Lastly, a short discussion on the generation of surface wave as a pre-acceleration and injection mechanism to DLA is also included.

In **Chapter 3**, details of the experimental set up used for various investigations are provided. First, details of a 150TW, Chirped Pulse Amplification (CPA) based Ti:sapphire laser system is provided and measurement techniques of various laser parameters such as laser pulse energy, laser pulse duration, focal spot and pre-pulse contrast is discussed. Description of the super-sonic gas-jet system used during the experiment and details of the gas-line system designed for precise control of mixing gases is provided. Details of various diagnostics used to record electron beam profile and its energy spectrum, and study laser propagation in underdense gas-jet plasma e.g. optical diagnostics such as 90° Thomson side scattering imaging, shadowgraphy, forward laser spectrum set up are also provided. Details of various detectors used in the experiment viz. phosphor screens, image plates and CCD cameras are also given.

In **Chapter 4,** experimental investigation on LPA using longer laser pulse duration of 200 fs corresponding to $L>>\lambda_p$ using He gas-jet plasma is described where a pure DLA regime was identified. The above observations were also supported by theoretical analysis on DLA and 2D PIC simulations using code EPOCH. Further, generation of quasi-monoenergetic electron beams was also observed although with a low probability of occurrence, even with such long laser pulses and where the dominant acceleration mechanism was found to be DLA, and a plausible explanation for such an observation was provided through the estimation of dephasing length of electrons for DLA theoretically.

In **Chapter 5,** experimental investigation on LPA using shorter laser pulse duration of 55 fs corresponding to $L>\lambda_p$ using three different gas-jet targets of He, N_2 and mixed gas targets (He + N_2) is described. In this case, two different acceleration regimes was identified: a pure DLA regime in N_2 and mixed gas target at a lower plasma density of $\sim 2\times10^{19}$ cm^{-3} and a hybrid regime acceleration in mixed and He gas target toward comparatively higher plasma side. The results were supported by 2D PIC simulation using code EPOCH and also showed an interesting aspect of surface wave generation on the boundary of laser plasma channel which could be suggested as a pre-acceleration mechanism for DLA. Effect of acceleration mechanism on electron beam parameters was also observed and discussed.

In **Chapter 6,** experimental investigation on LPA using shorter laser pulse duration of 60-70fs corresponding to $L\sim\lambda_p$ using N_2 and mixed gas targets (N_2 + He) is described. At first, experiments were performed with N_2 gas target and gradually doping concentration of He was increased in N_2. With increasing doping concentration of He in N_2, threshold density for generation of relativistic electron beams was found to increase which in turn affects the electron beam properties. At an optimum composition of N_2+50 % He, at a threshold density of $\sim 2\times10^{18}$ cm^{-3}, electron beam parameters were also found to be optimized. DLA was identified as the dominant acceleration mechanism and with increase in density; role of wakefield was also observed leading to a hybrid regime of acceleration. Results were supported by

2D PIC simulations performed using code EPOCH. Optimization of electron beam parameters in a DLA dominated regime was explained through the variation of rate of change of dephasing of electrons in the laser field with plasma density.

In **Chapter 7** experimental investigation on LPA using shorter laser pulse duration of 60-100fs corresponding to $L>\lambda_p$ using He gas-jet target is described. For lower laser pulse duration of ~60 fs, quasi-monoenergetic electron beams with average peak energy of ~180 MeV were observed and electron acceleration was primarily attributed to the wakefield mechanism. However, for longer laser pulse duration of ~100 fs, electron energy was found to increase with maximum energy reaching upto ~620-750 MeV. In this case, role of DLA could be identified leading to a hybrid regime of acceleration. The results are supported by 2D PIC simulations performed using code OSIRIS.

In **Chapter 8,** an investigation on radiography application of relativistic electron beams generated during the experimental investigation described in Chapter 6 and 7 above using Ar and He gas-jet targets respectively is described. Radiography of various metallic samples was performed and a minimum resolution of ~ 75 µm was achieved. Effect of different electron beam parameters on the quality of radiograph has also been discussed. Further, GEANT4 Monte Carlo simulations were performed to reconstruct the radiographic images and were found to be consistent with the experimental results and further, suitability of these electron beams in radiotherapy applications has also been discussed.

Lastly, in **Chapter 9**, summary and conclusion of the present research work is presented. It also includes a brief discussion on the future prospects of both experimental and theoretical study on LPA towards generation of high-energy stable electron beams, role of different acceleration mechanisms and potential applications.

References

[1] Atomic physics, Max Born, *Dover Publication*, Inc., New York, (1969).

[2] The scattering of α and β particles by matter and the structure of the atom, E. Rutherford, *Philosophical Magazine*, **21**, 669 (1911).

[3] Radiations from radioactive substances, E. Rutherford, J. Chadwick and C. D. Ellis, *Cambridge University Press,* (2010).

[4] Address of the President, Sir Ernest Rutherford, O. M., at the Anniversary Meeting, November 30, 1927, E. Rutherford, *117 Proc. R. Soc. Lond. A,* 300 (1927).

[5] Application of accelerators in Research and industry", J.L. Guggan& I. L. Morgan, *AIP Proceedings,* 16th International Conference, Denton, Texas, **576** (2000).

[6] Particle Accelerators and their uses, Waldemar Scharf, *Harwood Academic Publishers,* (1986).

[7] The Physics of Synchrotron Radiation, A. Hofmann, *Cambridge University Press*, (2004).

[8] Accelerator X-ray sources, R. Talman, *WILEY-VCH Verlag GmbH & Co. KGaA, Weinheim*, (2006).

[9] Handbook of Spallation Research, D. Filges and F. Goldenbaum, *WILEY-VCH Verlag GmbH & Co. KGaA, Weinheim,* (2009).

[10] Physics and technology of Spallation Neutron Sources, G.S. Bauer, *Nuclear Instruments and Methods in Physics Research A*,**463**, 505 (2001).

[11] Biomedical particle accelerators, Waldemar Scharf, *AIP Press*, New York, (1994).

[12] Medical electron accelerators, C. J. Karzmark, C. S. Nunan and E. Tanabe, *McGraw-Hill*, Inc. (1993).

[13] The Physics of Particle Accelerators- An Introduction, Klaus Wille, *Oxford University Press*, (2000).

[14] Particle accelerator physics, H. Weidemann, *Springer International Publishing*, (2015).

[15] Electron accelerators: History, applications and perspectives, M. N. Martins and T.F. Silva, *Radiation Physics and Chemistry*, **95**, 78 (2014).

[16] New techniques for future accelerators-RF and microwave systems, M. Puglisi, S. Stipcich and G. Torelli, *Plenum Press*, New York, (1989).

[17] A Multi-TeV Linear Collider based on CLIC Technology: CLIC Conceptual Design Report. Tech. rep, M. Aicheler et al., Geneva, CERN (2012).

[18] The High-Gradient S-Band Linac for Intitial Acceleration of the SLC Intense Positron Bunch, J. E. Clendenin, S D. Ecklund and H. A. Hoag, SLAC-PUB. 5049 (1989).

[19] ILC Technical Design Report Volume 1: Executive Summary. Tech. rep, Y. Behnke, J Brau, B. Foster, J. Fuster, M. Harrison *et al*., pp-1, (2013). arXiv: 1306.6327. url: http://arxiv.org/pdf/1306.6327v1.

[20] Laser driven electron acceleration in vacuum, gases, and plasmas, P. Sprangle, E. Esarey, and J. Krall, *Physics of Plasmas*, **3**, 2183(1996).

[21] The Los Alamos laser acceleration of particles workshop and beginning of the advanced accelerator concepts field, C. Joshi, *AIP Conference Proceedings*, **1507**, 61 (2012).

[22] Interaction of relativistic particles and free electromagnetic waves in the presence of a static helical magnet, R. Palmer, *J. Appl. Phys.*,**43**, 3014 (1972).

[23] Observation of inverse Cerenkov interaction between free electrons and laser light", J. A. Edighoffer, W. D. Kirnura, R. H, Pantell, M. A. Piestrup, and D. Y. Wang, *Phys. Rev. A*, **23**, 1848 (1981).

[24] Physics of laser driven plasma based electron accelerators, E. Esarey, C. B. Schroeder, and W. P. Leemans, Rev. Mod. Phys., **81**, 1229 (2009).

[25] Laser plasma accelerators, V. Malka, *Phys. Plasmas*, **19**, 055501 (2012).

[26] Developments in laser-driven plasma accelerators, S. M. Hooker, *Nature Photonics*,**7**, 775 (2013).

[27] Laser-driven plasma accelerators operating in the self-guided, blowout regime", C. Joshi, *IEEE Transactions on Plasma Science*, **45**, 3134 (2017).

[28] Plasma-based accelerators: then and now, C. Joshi, *Plasma Phys. Controlled Fusion*, (2019), doi.org/10.1088/1361-6587/ab396a.

[29] Laser electron accelerator, T. Tajima and J. M. Dawson, *Phys. Rev. Lett.*, **43**, 268 (1979).

[30] Acceleration of electrons by the interaction of a bunched electron beam with a plasma, P. Chen, J. M. Dawson, R. W. Huff, and T. Katsouleas, *Phys. Rev. Lett.*, **54**, 693 (1985).

[31] A 15000000 volt electrostatic generator, R. J. van de Graaff, *Phys. Rev.*, **38**, 1919 (1931).

[32] G. Ising, Arkivför Matematik, Astronomioch Fysik, **18**, 1 (1924).

[33] A linear electron accelerator, E. L. Ginzton, W. W. Hansen and W. R. Kennedy, *Rev. Sci. Instrum.*, **19**, 89 (1948).

[34] Some memories and dreams from the childhood of particle accelerators, R. Wideröe, *Europhysics News*, **15**, 9 (1984).

[35] The development of the microtron, S. Rosander, *Nucl. Instrum.& Methods*, **177**, 411 (1980).

[36] The synchrotron-A proposed high energy particle accelerator, E.M. McMillan, *Phys. Rev*., Letter to the editor, **68**,143 (1945).

[37] Lasers and accelerators, J. D. Lawson, *IEEE Transactions on Nuclear Science*, **26**, 4217 (1979).

[38] Laser acceleration of electrons in vacuum, E. Esarey, P. Sprangle, and J. Krall, *Phys. Rev.*,**52**, 5443 (1995).

[39] Visible laser acceleration of relativistic electrons in a semi-infinite vacuum, T. Plettner, R. L. Byer, E. Colby, B. Cowan, C. M. S. Sears *et al*., *Phys. Rev. Lett.*, **95**, 134801 (2005).

[40] Experimental observation of electron accelerated in vacuum to relativistic energy by a high intensity laser, G. Malka, E. Lefebvre, and J. L. Miquel, *Phys. Rev. Lett.,* **78**, 3314 (1997).

[41] Experimental test of the inverse free electron laser accelerator principal, I. Wernick and T. C. Marshal, *Phys. Rev. A*, **46**, 3566 (1992).

[42] First staging of two laser accelerators, W. D. Kimura, A. van Steenbergen, M. Babzien, I. Ben-Zvi, L. P. Campbell *et al*., *Phys. Rev. Lett.*,**86**, 4041 (2001).

[43] Demonstration of High-Trapping Efficiency and Narrow Energy Spread in a Laser-Driven Accelerator, W. D. Kimura, M. Babzien, I. Ben-Zvi, L. P. Campbell, D. B. Cline *et al.*, *Phys. Rev. Lett.*, **92**, 054801 (2004).

[44] High Energy Gain of Trapped Electrons in a Tapered, Diffraction-Dominated Inverse-Free-Electron Laser, P. Musumeci, S.Ya. Tochitsky, S. Boucher, C. E. Clayton, A. Doyuran *et al.*, *Phys. Rev. Lett.*,**94**, 154801 (2005).

[45] Demonstration of Cascaded Modulator-Chicane Microbunching of a Relativistic Electron Beam, N. Sudar, P. Musumeci, I. Gadjev, Y. Sakai, S. Fabbri *et al*., *Phys. Rev. Lett.*,**120**, 114802 (2018).

[46] Laser Acceleration of Relativistic Electrons Using the Inverse Cherenkov Effect, W. D. Kimura, G. H. Kim, R. D. Romea, and L. C. Steinhauer, I. V. Pogorelsky *et al*., *Phys. Rev. Lett.*, **74**, 546 (1995).

[47] Experimental Observation of Plasma Wake-Field Acceleration, J. B. Rosenzweig, D. B. Cline, B. Cole, H. Figueroa, W. Gai, R. Konecny *et al*., *Phys. Rev. Lett.*, **61**, 98 (1988).

[48] Multi-GeV Energy Gain in a Plasma-Wakefield Accelerator", M. J. Hogan, C. D. Barnes, C. E. Clayton, F. J. Decker, S. Deng *et al*., *Phys. Rev. Lett.*, **95**, 054802 (2005).

[49] Energy doubling of 42 GeV electrons in a metre-scale plasma wakefield accelerator, I. Blumenfeld, C. E. Clayton, F. Decker, M. J. Hogan, C. Huang *et al*., *Nature*, **445**, 741 (2007).

[50] Plasma-Wakefield Acceleration of an Intense Positron Beam, B. E. Blue, C. E. Clayton, C. L. O'Connell, F.-J. Decker, M. J. Hogan et al., *Phys. Rev. Lett.*, **90**, 214801 (2003).

[51] Plasma wakefield acceleration experiments at FACET, M. J. Hogan, T. O. Raubenheimer, A. Seryi, P. Muggli, T. Katsouleaset al., *New Journal of Physics*, **21**, 055030 (2010).

[52] Proton-driven plasma-wakefield acceleration, A. Caldwell, K. Lotov, A.Pukhov and F. Simon, *Nat. Phys.*,**5**, 363 (2009).

[53] The FLASHForward facility at DESY, A. Aschikhin, C. Behrens, S. Bohlen, J. Dale, N. Delbos *et al*., *Nucl. Instrum. Methods A*, **806**, 175 (2016).

[54] High-Quality Electron Beams from Beam-Driven Plasma Accelerators by Wakefield-Induced Ionization Injection, A. Martinez de la Ossa, J. Grebenyuk, T. Mehrling, L. Schaper, and J. Osterhoff, *Phys. Rev. Lett.*, **111**, 245003 (2013).

[55] Compression of amplified chirped optical pulses, D. Strickland and G. Mourou, *Opt. Commun.*, **55**, 447 (1985).

[56] Ultrahigh gradient particle acceleration by intense laser-driven plasma density waves, C. Joshi, W. B. Mori, T. Katsouleas, J. M. Dawson, J. M. Kindel *et al*., *Nature* (London), **311**, 525 (1984).

[57] Dynamics of space-charge waves in the laser beat wave accelerator, C. Tang, P. Sprangle, and R. N. Sudan, *Phys. Fluids*, **28**, 1974 (1985).

[58] Beat-Wave Excitation of Plasma Wave and Observation of Accelerated Electrons, Y. Kitagawa, T. Matsumoto, T. Minamihata, K. Sawai, K. Matsuo *et al*., *Phys. Rev. Lett.*, **68**, 48 (1992).

[59] Ultrahigh-Gradient Acceleration of Injected Electrons by Laser-Excited Relativistic Electron Plasma Waves, C. E. Clayton, K. A. Marsh, A. Dyson, M. Everett, A. Lal, *Phys. Rev. Lett.*, **70**, 38 (1993).

[60] Electron Acceleration in Nd-Laser Plasma Beat-Wave Experiments, F. Amiranoff, D. Bernard, B. Cros, F. Jacquet, G. Matthieussent, *et al*., *Phys. Rev. Lett.*, **74**, 5220 (1995).

[61] Nonresonant beat-wave excitation of relativistic plasma waves with constant phase velocity for charged-particle acceleration, C. V. Filip,, R. Narang, S. Tochitsky, C. E. Clayton, P. Musumec *et al*., *Phys. Rev. E*, **69**, 026404 (2004).

[62] Enhanced Acceleration of Injected Electrons in a Laser-Beat-Wave-Induced Plasma Channel, S.Ya. Tochitsky, R. Narang, C.V. Filip, P. Musumeci, *Phys. Rev. Lett.*, **92**, 095004 (2004).

[63] Electron acceleration from the breaking of relativistic plasma waves, A. Modena, Z. Najmudin, A. E. Dangor, C. E. Clayton, K. A. Marsh *et al.*, *Nature* (London) **377**, 606 (1995).

[64] Nonlinear Optics in Relativistic Plasmas and Laser Wake Field Acceleration of Electrons, D. Umstadter,S.-Y. Chen, A. Maksimchuk, G. Mourou, R. Wagner *et al.,Science*, **273**, 472 (1996).

[65] Electron Acceleration by a Laser Wakefield in a Relativistically Self-Guided Channel, R. Wagner, S.-Y. Chen, A. Maksimchuk, and D. Umstadter, *Phys. Rev. Lett.*, **78,** 3125 (1997).

[66] Observation of Electron Energies Beyond the Linear Dephasing Limit from a Laser-Excited Relativistic Plasma Wave, D. Gordon, K. C. Tzeng, C. E. Clayton, A. E. Dangor, V. Malka *et al*., *Phys. Rev. Lett*., **80,** 2133 (1998).

[67] Electron Trapping in Self-Modulated Laser Wakefields by Raman Backscatter, C. I. Moore, A. Ting, K. Krushelnick, E. Esarey, R. F. Hubbard *et al.*, *Phys. Rev. Lett.*,**79**, 3910 (1997).

[68] Quasi-monoenergetic electron beam generation by using a pinhole like collimator in a self-modulated laser wakefield acceleration, N. Hafz, M. S. Hur, G. H. Kim, C. Kim, I. S. Ko *et al.*, *Phys. Rev. E*, **73**, 016405 (2006).

[69] Generation of Quasi-monoenergetic Electron Bunches with 80-fs Laser Pulses, B. Hidding, K.-U. Amthor, B. Liesfeld, H. Schwoerer, S. Karsch *et al., Phys. Rev. Lett.*, **96**, 105004 (2006).

[70] Demonstration of quasi-monoenergetic electron-beam generation in laser-driven plasma acceleration, E. Miura, K. Koyama, S. Kato, N. Saito, M. Adachi *et al.,Appl. Phys. Lett.*,**86**, 251501 (2005).

[71] Quasi-monoenergetic electron beam generation during laser pulse interaction with very low density plasmas, A. Yamazaki, H. Kotaki, I. Daito, M. Kando, S. V. Bulanov *et al., Phys. Plasmas*,**12**, 093101 (2005).

[72] Observation of strong correlation between quasimonoenergetic electron beam generation by laser wakefield and laser guiding inside a preplasma cavity, T. Hosokai, K. Kinoshita, T. Ohkubo, A. Maekawa, M. Uesaka *et al., Phys. Rev. E*, **73**, 036407 (2006).

[73] Tomography of Injection and Acceleration of Monoenergetic Electrons in a Laser-Wakefield Accelerator, C.-T. Hsieh, C.-M.Huang, C.-L.Chang, Y.-C. Ho, Y.-S. Chen *et al., Phys. Rev. Lett.*,**96**, 095001 (2006).

[74] Energy scaling of monoenergetic electron beams generated by the laser-driven plasma based accelerator, S. Masuda, E. Miura, K. Koyama, S. Kato, M. Adachi *et al*., *Phys. Plasmas*, **14**, 023103 (2007).

[75] Transverse dynamics and energy tuning of fast electrons generated in sub-relativistic intensity laser pulse interaction with plasmas, M. Mori, M. Kando,

I. Daito, H. Kotaki, Y. Hayashi, A. Yamazaki *et al*., *Phys. Lett. A*, **356**, 146 (2006).

[76] Laser-Wakefield Acceleration of Monoenergetic Electron Beams in the First Plasma-Wave Period, S. P. D. Mangles, A. G. R. Thomas, M. C. Kaluza, O. Lundh, F. Lindau *et al*., *Phys. Rev. Lett.*, **96**, 215001 (2006).

[77] Production of a monoenergetic electron bunch in a self-injected laser-wakefield accelerator, C.-L. Chang, C.-T.Hsieh, Y.-C. Ho, Y.-S. Chen, J.-Y.Lin *et al*., *Phys. Rev. E.*,**75**, 036402 (2007).

[78] Generation of a highly collimated, mono-energetic electron beam from laser-driven plasma-based acceleration, B. S. Rao, A. Moorti, P.A. Naik and P. D. Gupta, *New Journal of Physics*, **12**, 045011 (2010).

[79] Generation of quasi-monoenergetic electron beams with small normalized divergences angle from a 2 TW laser facility, D. Z. Li, W. C. Yan, L. M. Chen, K. Huang, Y. Ma *et al*., *Opt. Express*,**22**, 12836 (2014).

[80] Generation of quasi-monoenergetic electron beams with small normalized divergences angle from a 2 TW laser facility, B. S. Rao, A. Moorti, R. Rathore, J. A. Chakera, P. A. Naik *et al*., *Phys. Rev*. ST Accel. Beams, **17**, 011301 (2014).

[81] Characterization of electron beams produced by ultrashort (30 fs) laser pulses, V. Malka, J. Faure, J. R. Marquès, F. Amiranoff *et al*., *Phys. Plasmas*, **8**, 2605 (2001).

[82] Electron-Yield Enhancement in a Laser-Wakefield Accelerator Driven by Asymmetric Laser Pulses, W. P. Leemans, P. Catravas, E. Esarey, C.G. R. Geddes, C. Toth *et al*., *Phys. Rev. Lett.*,**89**, 174802 (2002).

[83] Effect of chirp on self-modulation and laser wakefield electron acceleration in the regime of quasimonoenergetic electron beam generation, B. S. Rao, A. Moorti, P. A. Naik, and P. D. Gupta, *Phys. Rev. Special Topic-Accl. And Beams*, **16**, 091301 (2013).

[84] Optically Controlled Seeding of Raman Forward Scattering and Injection of Electrons in a Self-Modulated Laser-Wakefield Accelerator, W.-T. Chen, T.-Y.Chien, C.-H.Lee, J.-Y.Lin, J. Wang, and S.-Y. Chen, *Phys. Rev. Lett.*, **92**, 075003 (2004).

[85] Monoenergetic beams of relativistic electrons from intense laser–plasma interactions, S. P. D. Mangles, C. D. Murphy, Z. Najmudin, A. G. R. Thomas, J. L. Collier *et al.*, *Nature*, **431**, 535 (2004).

[86] High-quality electron beams from a laser wakefield accelerator using plasma-channel guiding, C. G. R. Geddes, Cs. Toth, J van Tilborg, E. Esarey, C. B. Schroeder *et al.*, *Nature*, **431**, 538 (2004).

[87] A laser–plasma accelerator producing monoenergeticelectron beams, J. Faure, Y. Glinec, A. Pukhov, S. Kiselev, S. Gordienko *et al.*, Nature **431**, 541 (2004).

[88] Phenomenological theory of laser-plasma interaction in “bubble” regime, A. Pukhov and J. Meyer-ter-Vehn, *Appl. Phys. B*: Lasers Opt.**74**, 355 (2002).

[89] Generating multi-GeV electron bunches using single stage laser wakefield acceleration in a 3D nonlinear regime, W. Lu, M. Tzoufras, C. Joshi, F. S. Tsung, W. B. Mori *et al.*, *Phys. Rev.* ST Accel. Beams,**10**, 061301 (2007).

[90] Measurements of the critical power for self-injection of electrons in a laser wakefield accelerator, D. H. Froula, C. E. Clayton, T. Döppner, K. A. Marsh, C. P. J. Barty, *et al.*, *Phys. Rev. Lett.* **103**, 215006 (2009).

[91] Near-GeV acceleration of electrons by a nonlinear plasma wave driven by a self-guided laser pulse, S. Kneip, S. R. Nagel, S. F. Martins, S. P. D. Mangles, C. Bellei *et al.*, *Phys. Rev. Lett.*,**103**, 035002 (2009).

[92] Generation of tunable, 100–800 MeV quasi-monoenergetic electron beams from a laser-wakefield accelerator in the blowout regime, S. Banerjee, N. D. Powers, V. Ramanathan, I. Ghebregziabher, K. J. Brown *et al.*, *Phys. Plasmas*,**19**, 056703 (2012).

[93] Self-guided laser wakefield acceleration beyond 1 GeV using ionization-induced injection, C. E. Clayton, J. E. Ralph, F. Albert, R. A. Fonseca, S. H. Glenzer *et al.*, *Phys. Rev. Lett.*,**105**, 105003 (2010).

[94] Study of near-GeV acceleration of electrons in a non-linear plasma wave driven by a self-guided laser pulse, S. Kneip, S R Nagel, C Bellei, O Cheklov, R J Clarke *et al.*, *Plasma Phys. Control. Fusion*, **53,** 014008 (2011).

[95] Laser wakefield acceleration at reduced density in the self-guided regime, J. E. Ralph, C. E. Clayton, F. Albert, B. B. Pollock, S. F. Martins *et al*, *Phys. Plasmas*, **17**, 056709 (2010).

[96] Multi-GeV electron beams from capillary-discharge-guided subpetawatt laser pulses in the self-trapping regime, W. P. Leemans, A. J. Gonsalves, H.-S. Mao, K. Nakamura, C. Benedetti *et al.*, *Phys. Rev. Lett.*,**113**, 245002 (2014).

[97] Quasi-monoenergetic laser-plasma acceleration of electrons to 2 GeV, X. Wang, R. Zgadzaj, N. Fazel, Z. Li, S. A. Yi *et al.*, *Nat. Commun.*, **4**, 1988 (2013).

[98] Enhancement of electron energy to the multi-GeV regime by a dual-stage laser-wakefield accelerator pumped by petawatt laser pulses, H. T. Kim, K. H. Pae, H. J. Cha, I. J. Kim, T. J. Yu *et al., Phys. Rev. Lett.*,**111**, 165002 (2013).

[99] GeV electron beams from a centimetre-scale accelerator W. P. Leemans, B. Nagler, A. J. Gonsalves, Cs. Tóth, K. Nakamura, *et al.*, Nat. Phys. 2, 696 (2006) .

[100] Generation and pointing stabilization of multi-GeV electron beams from laser plasma accelerator driven in a pre-formed plasma waveguide, A. J. Gonsalves, K. Nakamura, J. Daniels, H.-S. Mao, C. Benedetti *et al*., *Phys. Plasmas*, **22**, 056703 (2015).

[101] Laser wakefield acceleration of electron beams beyond 1 GeV from an ablative capillary discharge waveguide, H. Lu, M. Liu, W. Wang, C. Wang, J. Liu *et al., Appl. Phys. Lett.*, **99**, 091502 (2011).

[102] Stable generation of GeV-class electron beams from self-guided laser–plasma channels, N. Hafz, T. M. Jeong, I. W. Choi, S. Ku Lee, K. H. Pae *et al., Nature Photonics*, **2**, 571 (2008).

[103] Petawatt Laser Guiding and Electron Beam Acceleration to 8 GeV in a Laser-Heated Capillary Discharge Waveguide, A. J. Gonsalves, K. Nakamura, J. Daniels, C. Benedetti, C. Pieronek *et al., Phys. Rev. Lett.*, **122**, 084801 (2019).

[104] Observation of relativistic and charge-displacement self-channelling of intense subpicosecond ultraviolet (248 nm) radiation in plasmas, A. B. Borisov, A. V.

Borovskiy, V. V. Korobkin, A. M. Prokhorov, O. B. Shiryaev *et al*., *Phys. Rev. Lett*., **68**, 2309 (1992).

[105] Experimental Demonstration of Relativistic Self-Channeling of a Multiterawatt Laser Pulse in an Underdense Plasma, P. Monot, T. Auguste, P. Gibbon, F. Jakober, G. Mainfray *et al*., *Phys. Rev. Lett*., **74**, 2953 (1995).

[106] Electron Acceleration by a Laser Wakefield in a Relativistically Self-Guided Channel, R. Wagner, S.-Y. Chen, A. Maksimchuk, and D. Umstadter, *Phys. Rev. Lett*., **78**, 3125 (1997).

[107] Plasma Wave Generation in a Self-Focused Channel of a Relativistically Intense Laser Pulse, C. E. Clayton, K.-C. Tzeng, D. Gordon, P. Muggli, W. B. Mori, *Phys. Rev. Lett*., **81**, 100 (1998).

[108] Electron Acceleration and the Propagation of Ultrashort High-Intensity Laser Pulses in Plasmas, X. Wang, M. Krishnan, N. Saleh, H. Wang, and D. Umstadter, *Phys. Rev. Lett*., **84**, 5324 (2000).

[109] Influence of laser pulse duration on relativistic channels, C. Delfin, V. Lokhnygin, J. Mauritsson, A. Sjögren, and C.-G. Wahlström, *Phys. Plasmas,* **9**, 937 (2002).

[110] Polyethylene Glycol Reduces Early and Long-Term Cold Ischemia-Reperfusion and Renal Medulla Injury, J. Faure, T. Hauet, Z. Han, J. M. Goujon, I. Petit *et al.*, *Phys. Plasmas,* **9**, 756 (2002).

[111] Effect of Laser-Focusing Conditions on Propagation and Monoenergetic Electron Production in Laser-Wakefield Accelerators, A. G. R. Thomas, Z. Najmudin, S. P. D. Mangles, C. D. Murphy, A. E. Dangor *et al., Phys. Rev. Lett*., **98**, 095004 (2007)

[112] Self-Guiding of Ultrashort, Relativistically Intense Laser Pulses through Underdense Plasmas in the Blowout Regime, J. E. Ralph, K. A. Marsh, A. E. Pak, W. Lu, C. E. Clayton *et al.*, *Phys. Rev. Lett*., **102**, 175003 (2009).

[113] Focusing limits of a terawatt laser in an underdense plasma, P. Monot, T. Auguste, L. A. Lomprè, G. Mainfray and C. Manus, *J. Opt. Soc. Am. B*,**9**, 1579 (1992).

[114] Ionization-induced defocusing of intense laser pulses in high-pressure gases, S.C. Rae, *Opt. Communications*, **97,** 25 (1993).

[115] Onset of relativistic self-focusing in high density gas jet targets, R. Fedosejevs, X. F. Wang, and G. D. Tsakiris, *Phys. Rev. E*, **56**, 4615 (1997).

[116] Monoenergetic electron beam generation from a laser-plasma accelerator, K. Koyama, M. Adachi, E. Miura, S. Kato, S. Masuda *et al*., *Laser and Particle Beams***, 24,** 95 (2006).

[117] Quasi-monoenergetic electron beams generated from 7 TW laser pulses in N_2 and He gas targets, Z. L. Chen, C. Unick, N. Vafaei-Najafabadi, Y. Y. Tsui, R. Fedosejeves *et al*., *Laser and Particle Beams*, **26**,147 (2008).

[118] Manipulation and electron-oscillation-measurement of laser accelerated electron beams, H. Kotaki, Y. Hayashi, K. Kawase, M. Mori, M. Kando *et al*., *Plasma Phys. Controlled Fusion,* **53** 014009 (2011).

[119] Physics of fully-loaded laser-plasma accelerators, E. Guillaume, A. Döpp, C. Thaury, A. Lifschitz, J-P. Goddet *et al*., *Phys. Rev. ST Accel. Beams*, **18**, 061301 (2015).

[120] Quasi-monoenergetic electron beams from a few-terawatt laser driven plasma acceleration using a nitrogen gas jet, B. S. Rao, A. Moorti, J. A. Chakera, P. A. Naik, and P. D. Gupta, *Plasma Phys. Control. Fusion*, **59**, 065006 (2017).

[121] Characteristics of electron beam in laser wakefield accelerator using pure nitrogen gas, J. Kim, Y. H. Hwangbo, and K. N. Kim, *Plasma Phys. Control. Fusion*, **60**, 034008 (2018).

[122] Quasimonoenergetic electron beams from laser wakefield acceleration in pure nitrogen, M. Z. A. Mo, A. Ali, S. Fourmaux, P. Lassonde, J. C. Kieffer, and R. Fedosejevs, *Appl. Phys. Lett.*, **100**, 074101 (2012).

[123] Simultaneous generation of quasi-monoenergetic electron and betatron X-rays from nitrogen gas via ionization injection, K. Huang, D. Z. Li, W. C. Yan, M. H. Li, M. Z. Tao *et al.*, *Appl. Phys. Lett.*, **105**, 204101 (2014).

[124] Quasimonoenergetic collimated electron beams from a laser wakefield acceleration in low density pure nitrogen, M. Tao , N. A. M. Hafz, S. Li, M. Mirzaie, A. M. M. Elsied *et al.*, *Phys. Plasmas*, **21**, 073102 (2014).

[125] Comparison of self-injection thresholds in He and N_2 and role of self-focusing in LWFA, D. Palla, F. Baffigi, F. Brandi, L. Fulgentini, P. Koester *et al.*, *Nucl. Instrum.Methods Phys. Res.A*, **829**, 408 (2016).

[126] Small energy spread electron beams from laser wakefield acceleration by self-evolved ionization injection, J. Wang, J. Feng, C. Zhu, Y. Li, Y. He *et al.*, *Plasma Phys. Control. Fusion*, **60**, 034004 (2018).

[127] Ionization Induced Trapping in a Laser Wakefield Accelerator, C. McGuffey, A. G. R. Thomas, W. Schumaker, T. Matsuoka, V. Chvykov *et al.*, *Phys. Rev. Lett.*, **104**, 025004 (2010).

[128] Dynamics of ionization-induced electron injection in the high density regime of laser wakefield acceleration, F. G. Desforges, B. S. Paradkar, M. Hansson, J. Ju1, L. Senje *et al.*, *Phys. Plasmas*, **21**, 120703 (2014).

[129] Generation of 500 MeV–1 GeV energy electrons from laser wakefield acceleration via ionization induced injection using CO_2 mixed in He, M. Z. Mo, A. Ali, S. Fourmaux, P. Lassonde, J. C. Kieffer *et al.*, *Appl. Phys. Lett.*,**102**, 134102 (2013).

[130] Self-Guided Laser Wakefield Acceleration beyond 1 GeV Using Ionization-Induced Injection, C. E. Clayton, J. E. Ralph, F. Albert, R. A. Fonseca, S. H. Glenzer *et al*., *Phys. Rev. Lett.*,**105**, 105003 (2010).

[131] Injection and Trapping of Tunnel-Ionized Electrons into Laser-Produced Wakes, A. Pak, K. A. Marsh, S. F. Martins, W. Lu, W. B. Mori *et al*., *Phys. Rev. Lett.*,**104**, 025003 (2010).

[132] All-Optical Cascaded Laser Wakefield Accelerator Using Ionization-Induced Injection, J. S. Liu, C. Q. Xia, W. T. Wang, H. Y. Lu, Ch. Wang *et al*., *Phys. Rev. Lett.*,**107**, 035001 (2011).

[133] Demonstration of a Narrow Energy Spread, ∼0.5GeV Electron Beam from a Two-Stage Laser Wakefield Accelerator, B. B. Pollock, C. E. Clayton, J. E. Ralph, F. Albert, A. Davidson *et al*., *Phys. Rev. Lett.*,**107**, 045001 (2011).

[134] Shock assisted ionization injection in laser-plasma accelerators, C. Thaury, E. Guillaume, A. Lifschitz, K. Ta Phuoc, M. Hansson *et al.*, *Scientific Reports*, **5**, 16310 (2015).

[135] Localization of ionization-induced trapping in a laser wakefield accelerator using a density down-ramp, M. Hansson, T. L. Audet, H. Ekerfelt, B. Aurand,

I. Gallardo González *et al*., *Plasma Phys. Controlled Fusion*,**58**, 055009 (2016).

[136] Demonstration of self-truncated ionization injection for GeV electron beams, M. Mirzaie, S. Li, M. Zeng, N. A. M. Hafz, M. Chen *et al*., *Scientific Reports*, **5**, 14659 (2015).

[137] Demonstration of a beam loaded nanocoulomb-class laser wakefield accelerator, J. P. Couperus, R. Pausch, A. Köhler, O. Zarini, J. M. Krämer *et al*., *Nature Communications*, **8**, 487 (2017).

[138] Improved performance of laser wakefield acceleration by tailored self-truncated ionization injection, A. Irman, J. P. Couperus, J. P. Debus, A. Köhler, A. Krämer, J. M. Pausch *et al.*, *Plasma Phys. Controlled Fusion*,**60**, 044015 (2018).

[139] Staged concept of laser-plasma acceleration toward multi-GeV electron beams, V. Malka, A. Lifschitz, J. Faure, and Y. Glinec, *Phys. Rev. ST Accel. Beams*,**9**, 091301 (2006).

[140] Tunable monoenergetic electron beams from independently controllable laser-wakefield acceleration and injection, G. Golovin, S. Chen, N. Powers, C. Liu, S. Banerjee *et al*., *Phys. Rev. ST Accel. Beams,***18**, 011301 (2015).

[141] Multistage coupling of independent laser-plasma accelerators, S. Steinke, J. van Tilborg, C. Benedetti, C. G. R. Geddes, C. B. Schroeder *et al*., *Nature*, **530**, 190 (2016).

[142] Electron cavitation and acceleration in the wake of an ultraintense, self-focused laser pulse, Patrick Mora and Thomas M. Antonsen, Jr., *Phys. Rev. E*., **53,** 2068(1996).

[143] Particle acceleration in relativistic laser channels, A. Pukhov, Z.-M.Sheng, and J. Meyer-ter-Vehn, *Phys. Plasmas*, **6**, 2847 (1999).

[144] Bright betatron X-ray radiation from a laser-driven-clustering gas target, L. M. Chen, W. C. Yan, D. Z. Li, Z. D. Hu, L. Zhang *et al.*, *Scientific Reports*, **3**, 1912 (2013).

[145] Observation of Synchrotron Radiation from Electrons Accelerated in a Petawatt-Laser-Generated Plasma Cavity, S. Kneip, S. R. Nagel, C. Bellei, N. Bourgeois, A. E. Dangor *et al.*, *Phys. Rev. Lett.*,**100**, 105006 (2008).

[146] Observation of Synchrotron Radiation from Electrons Accelerated in a Petawatt-Laser-Generated Plasma Cavity, S. Kneip, S. R. Nagel, C. Bellei, N. Bourgeois, A. E. Dangor *et al.*, *Nat. Phys.*,**7**, 867 (2011).

[147] Gamma-rays from harmonically resonant betatron oscillations in a plasma wake, S. Cipiccia, M. R Islam, B. Ersfeld, R. P. Shanks, E. Brunetti, *et al.*, *Nat. Phys.***7**, 867 (2011).

[148] Femtosecond x rays from laser-plasma accelerators, S. Corde, K. Ta Phuoc, G. Lambert, R. Fitour, V. Malka *et al.*, *Rev. Mod. Phys.*, **85** 1 (2013).

[149] Characteristics of betatron radiation from direct-laser-accelerated electrons, T. W. Huang, A. P. L. Robinson, C. T. Zhou, B. Qiao, B. Liu *et al.*, *Phys. Rev. E.*, **93** 063203 (2016).

[150] Multi-MeV Electron Beam Generation by Direct Laser Acceleration in High-Density Plasma Channels, C. Gahn, G. D. Tsakiris, A. Pukhov, J. Meyer-ter-Vehn, G. Pretzler *et al.*, *Phys. Rev. Lett.*, **83**, 4772 (1999).

[151] Generation of MeV electrons and positrons with femtosecond pulses from a table-top laser system, C. Gahn, G. D. Tsakiris, G. Pretzler, K. J. Witte, P. Thirolf *et al.*,*Phys. Plasmas*, **9**, 987 (2002).

[152] Electron Acceleration in Cavitated Channels Formed by a Petawatt Laser in Low-Density Plasma, S. P. D. Mangles, B. R. Walton, M. Tzoufras, Z. Najmudin, R. J. Clarke *et al.*, *Phys. Rev. Lett.*,**94**, 245001 (2005).

[153] Electron radiography using a table-top laser-cluster plasma accelerator, Bussolino G, C Faenov, A Giulietti, A Giulietti, D Koester *et al.*, *J. Phys. D: Appl. Phys.*, **46**, 245501 (2013).

[154] Ultrarelativistic electron generation during the intense, ultrashort laser pulse interaction with clusters, Y. Fukuda, Y.Akahane, M. Aoyama, Y. Hayasi, T. Homma *et al.*, *Physics Letters A*, **363,** 130 (2007).

[155] Relativistic laser-plasma interaction by multi-dimensional particle-in-cell simulations, A. Pukhov and J. Meyer-ter-Vehn, *Phys. Plasmas*, **5**, 1880 (1998).

[156] Self-modulated laser wakefield accelerators as x-ray sources, N. Lemos, J. Martins, L. Tsung, F. S. Shaw, J. L. Marsh *et al.*, *Plasma Phys. Control. Fusion*, **58**, 034018 (2016).

[157] Generation and analysis of quasimonoenergetic electron beams by laser-plasma interaction in transitional region from the self-modulated laser wakefield to bubble acceleration regime, S. Masuda and E. Miura , *Phys. Plasmas*, **16**, 093105(2009).

[158] Cascade Acceleration of Electrons by Laser Wakefield and Direct Laser Field, M. Adachi, E. Miura, S. Kato, K. Koyama, S. Masuda *et al.*, *Japanese Journal of Applied Physics*, **45**, 4214 (2006).

[159] Role of Direct Laser Acceleration of Electrons in a Laser Wakefield Accelerator with Ionization Injection, J. L. Shaw, N. Lemos, L. D. Amorim, N. Vafaei-Najafabadi, K. A. Marsh *et al*., *Phys. Rev. Lett.*,**118**, 064801 (2017).

[160] Experimental signatures of direct-laser-acceleration-assisted laser wakefield acceleration, J. L. Shaw, N. Lemos, K. A. Marsh, D. H. Froula and C. Joshi, *Plasma Physics and Controlled Fusion*, **60**, 044012 (2018).

[161] Estimation of direct laser acceleration in laser wakefield accelerators using particle-in-cell simulations, J. L. Shaw, N. Lemos, K. A. Marsh, F. S. Tsung, W. B. Mori *et al*., *Plasma Physics and Controlled Fusion*,**58**, 034008 (2016).

[162] Synergistic Laser-Wakefield and Direct-Laser Acceleration in the Plasma-Bubble Regime, Xi Zhang, V. N. Khudik, and S. Gennady, *Phys. Rev. Lett*., **114**, 184801 (2015).

[163] Laser wakefield and direct acceleration with ionization injection, Xi Zhang, V. N Khudik, A. Pukhov and G. Shvets, *Plasma Phys. Control. Fusion*, **58**, 034011(2016).

[164] Applications of laser wakefield accelerator-based light sources, F. Albert and A. G. R. Thomas, *Plasma Phys. Control. Fusion*, **58**, 103001 (2016).

[165] Principles and applications of compact laser–plasma accelerators, V. Malka, J. Faure, Y. A. Gauduel, E. Lefebvre, A. Rousse *et al*., *Nature Physics*,**4**, 447 (2008).

[166] Applications of laser driven particle acceleration, P. R. Bolton, K. Parodi and J. Schreiber, *CRC Press*, Taylor & Francis Group (2018).

[167] Laser-Driven Particle Acceleration Towards Radiobiology and Medicine, Antonio Giulietti, *Springer International Publishing, Switzerland*, (2016).

[168] Production of a kev x-ray beam from synchrotron radiation in relativistic laser-plasma interaction, A. Rousse, K. Ta Phuoc, R. Shah, A. Pukhov, E. Lefebvre *et al*., *Phys. Rev. Lett.*,**93**, 135005 (2004).

[169] Low-emittance electron bunches from a laser-plasma accelerator measured using single-shot x-ray spectroscopy, G. R. Plateau, C. G. R. Geddes, D. B. Thorn, M. Chen, C. Benedetti *et al*., *Phys. Rev. Lett*.,**109**, 064802 (2012).

[170] Bright spatially coherent synchrotron x-rays from a table-top source, S. Kneip, C. McGuffey, J. L. Martins, C Bellei, V. Chvykov *et al*., *Nat. Phys.*,**6**, 980 (2010).

[171] Demonstration of the synchrotron type spectrum of laser-produced betatron radiation, S Fourmaux, S Corde, K Ta Phuoc, P M Leguay, S Payeur *et al.*,*New J. Phys.*,**13**, 033017 (2011).

[172] Optical control of hard x-ray polarization by electron injection in a laser wakefield accelerator, M. Schnell, A. Sävert, I. Uschmann, M. Reuter, M. Nicolai *et al*., *Nat. Commun*., **4**, 2421 (2013).

[173] Angular dependence of betatron x-ray spectra from a laser wakefield accelerator, F. Albert, B. B. Pollock, J. L. Shaw, K. A. Marsh, J. E. Ralph *et al*., *Phys. Rev. Lett.*,**111**, 235004 (2013).

[174] Quasi-monoenergetic laser-plasma acceleration of electrons to 2 GeV, X. Wang, R. Zgadzaj, N. Fazel, Z. Li, S. A. Yi, *et al*., *Nat. Commun.*,**4** ,1988 (2013).

[175] Laser-wakefield accelerators as hard x-ray sources for 3d medical imaging of human bone, J. M. Cole, J.C. Wood, N. C. Lopes, K. Poder, R. L. Aber *et al*., *Sci. Rep.*, **5**, 13244 EP (2015).

[176] Observation of Betatron X-Ray Radiation in a Self-Modulated Laser Wakefield Accelerator Driven with Picosecond Laser Pulses, F. Abert, N. Lemos, J. L. Shaw, B. B. Pollock, C. Goyon *et al*, *Phys. Rev. Lett.*,**118**, 134801 (2017)

[177] On the properties of synchrotron-like X-ray emission from laser wakefield accelerated electron beams, Mc. Guffey, W. Schumaker, T. Matsuoka, V. Chvykov, F. Dollar *et al.*, *Phys. Plasmas*, **25**, 043104 (2018).

[178] High-resolution µCT of a mouse embryo using a compact laser-driven X-ray betatron source J. M. Cole , D. R. Symes, N. C. Lopes, J. C. Wood , K. Poder *et al*., *PNAS*, **115**, 6335 (2018).

[179] Betatron x-ray generation from electrons accelerated in a plasma cavity in the presence of laser fields, A. G. R. Thomas and K. Krushelnick, *Phys. Plasmas,* **16**, 103103 (2009).

[180] Deducing the electron-beam diameter in a laser-plasma accelerator using x-ray betatron radiation", Michael Schnell, Alexander Sävert, Björn Landgraf, Maria Reuter, Maria Nicolai *et al*., *Phys. Rev. Lett.* **108**, 075001(2012).

[181] Spectroscopy of betatron radiation emitted from laser-produced wakefield accelerated electron, M. Schnell, A. Sävert, B. Landgraf, M. Reuter, M. Nicolai *et al*., *Rev. Sci. Instrum.*, **81**, 10E325 (2010).

[182] Imaging electron trajectories in a laser-wakefield cavity using betatron x-ray radiation, K. Ta Phuoc, S. Corde , R. Shah , F. Albert, R. Fitour *et al*., *Phys. Rev. Lett.*,**97**, 225002 (2006).

[183] Angular-momentum evolution in laser-plasma accelerators, C. Thaury , E. Guillaume, S. Corde, R. Lehe, M. Le Bouteiller *et al.*, *Phys. Rev. Lett.*,**111**, 135002 (2013).

[184] Measuring the angular dependence of betatron x-ray spectra in a laser-wakefield accelerator Plasma, F. Albert, B. B. Pollock, J. L. Shaw, K. A. Marsh, J. E. Ralph *et al.*, *Phys. Control. Fusion*, **56**, 084016 (2014).

[185] The Spectrum of Scattered X-Rays, A. H. Compton, *Phys. Rev*. **22**, 409 (1923).

[186] Nonlinear Thomson scattering of intense laser pulses from beams and plasmas, E. Esarey, S. K. Ride, and P. Sprangle, *Phys. Rev. E* **48**, 3003 (1993).

[187] Nonlinear Thomson scattering: a tutorial, Y. Y. Lau, F. He, D. P. Umstadter and R. Kowalczyk , *Phys. Plasmas***10** 2155 (2003)

[188] Compton scattering x-ray sources driven by laser wakefield acceleration, Hartemann F V, Gibson D J, Brown W J, Rousse A, Ta Phuoc K, *et al*., *Phys. Rev. Sp. Accel. Beams***10,** 011301 (2007).

[189] Spectral bandwidth reduction of thomson scattered light by pulse chirping, I. Ghebregziabher, B. A. Shadwick and D. Umstadter, *Phys. Rev. Sp. Accel. Beams*, **16,** 030705 (2013).

[190] Thomson-backscattered x rays from laser-accelerated electrons, H. Schwoerer, B. Liesfeld, H-P. Schlenvoigt, K-U. Amthor and R. Sauerbrey, *Phys. Rev. Lett.*, **96**, 014802 (2006).

[191] All optical compton gamma-ray source , K. Ta Phuoc, S. Corde, C. Thaury, V. Malka, A. Tafzi *et al*., *Nat. Photon*.,**6**, 308 (2012).

[192] Compact tunable compton x-ray source from laser-plasma accelerator and plasma mirror, H-E. Tsai, X. Wang, J. M. Shaw, Z. Li, A. V. Arefiev, X. Zhang *et al*., *Phys. Plasmas*, **22**, 023106 (2015).

[193] MeV-energy x rays from inverse compton scattering with laser-wakefield accelerated electrons, S. Chen, N. D. Powers, I. Ghebregziabher, C. M. Maharjan, C. Liu *et al*., *Phys. Rev. Lett.*,**110**, 155003 (2013).

[194] Ultrahigh brilliance multi-mev γ-ray beams from nonlinear relativistic Thomson scattering, G. Sarri, D. J. Corvan, W. Schumaker, J. M. Cole, A. Di Piazza *et al*., *Phys. Rev. Lett.*,**113**, 224801 (2014)

[195] Quasi-monoenergetic and tunable X-rays from a laser-driven Compton light source, N. D. Powers, I. Ghebregziabher, G. Golovin, C. Liu, S. Chen *et al*., *Nat. Photon*.,**8**, 28 (2014).

[196] Generation of 9 MeV γ-rays by all-laser-driven compton scattering with second-harmonic laser light, C. Liu, G. Golovin, S. Chen, J. Zhang, B. Zhao *et al*., *Opt. Lett.*, **39**, 4132 (2014).

[197] Tunable all-optical quasimonochromaticthomson x-ray source in the nonlinear regime, K. Khrennikov, J. Wenz, A. Buck, J. Xu, M. Heigoldt *et al.*, *Phys. Rev. Lett.*, **114**, 195003 (2015).

[198] Review of x-ray free-electron laser theory, Z. Huang and K-J. Kim, *Phys. Rev. Sp. Accel. Beams,***10,** 034801 (2007).

[199] A compact synchrotron radiation source driven by a laser-plasma wakefield accelerator, H.P. Schlenvoigt, K. Haupt, A. Debus, F. Budde, O. Jäckel *et al.*, *Nat. Phys.,***4**, 130 (2008).

[200] Laser-driven soft-x-ray undulator source, M. Fuchs, R. Weingartner, A. Popp, Z. Major, S. Becker *et al*., *Nat. Phys.*,**5**, 826 (2009).

[201] An ultrashort pulse ultra-violet radiation undulator source driven by a laser plasma wakefield accelerator, M. P. Anania, E. Brunetti, S. M. Wiggins, D. W. Grant, G. H. Welsh *et al.*, Appl. Phys. Lett. 104, 264102 (2014).

[202] Characterization of a gamma-ray source based on a laser-plasma accelerator with applications to radiography, R. D. Edwards, M. A. Sinclair, T. J. Goldsack, K. Krushelnick, F. N. Beg *et al.*, *Appl. Phys. Lett*.,**80**, 2129 (2002).

[203] High-Resolution γ-Ray Radiography Produced by a Laser-Plasma Driven Electron Source, Y. Glinec, J. Faure, L. Le Dain, S. Darbon, T. Hosokai *et al*., *Phys. Rev. Lett.*, **94**, 025003 (2005).

[204] Towards high-energy, high-resolution computed tomography via a laser driven micro-spot gamma-ray source, Y. C. Wu, B. Zhu, G. Li, X. H. Zhang, M. H. Yu *et al*., *Scientific Reports*, **8**, 15888 (2018).

[205] Intense gamma ray source in the giant-dipole-resonance range driven by 10 TW laser pulses, A. Giulietti, N. Bourgeois, T. Ceccotti, X. Davoine, S. Dobosz *et al.*, *Phys. Rev. Lett.*,**101**, 105002 (2008).

[206] Evaluation of yields of γ-rays produced by electrons from gas jets irradiated by low-energy laser pulses: towards virtual radioisotopes, Y. Oishi, T. Nayuki, A. Zhidkov, T. Fujii and K. Nemoto, *Japan. J. Appl. Phys*., **50**, 042702 (2011).

[207] A tuneable ultra-compact high-power, ultra-short pulsed, bright gamma-ray source based on bremsstrahlung radiation from laser-plasma accelerated electrons, S. Cipiccia, S. M. Wiggins, R. P. Shanks, M. R. Islam, G. Vieux *et al*., *J. Appl. Phys*.,**111**, 063302 (2012).

[208] Theory of coherent transition radiation generated at a plasma-vacuum interface, C. B. Schroeder, E. Esarey, J.van Tilborg and W. P. Leemans, *Phys. Rev. E*, **69**, 016501 (2004).

[209] Observation of terahertz emission from a laser-plasma accelerated electron bunch crossing a plasma-vacuum boundary, W. P. Leemans, C. G. R. Geddes, J. Faure, Cs. Tóth, J. van Tilborg, *Phys. Rev. Lett.*, **91**, 074802 (2003).

[210] Longitudinal electron bunch profile reconstruction by performing phase retrieval on coherent transition radiation spectra, S. I. Bajlekov, M. Heigoldt, A. Popp, J. Wenz, K. Khrennikov *et al*., *Phys. Rev. Sp. Accel. Beams*, **16**, 040701 (2013).

[211] Electron bunch length measurements from laser-accelerated electrons using single-shot thz time-domain interferometry, A. D. Debus *et al*., *Phys. Rev. Lett.*,**104**, 084802 (2010).

[212] Temporal characterization of femtosecond laser-plasma-accelerated electron bunches using terahertz radiation, J. van Tilborg, C. B. Schroeder, C. V. Filip, Cs. Tóth, C. G. R. Geddes *et al*., *Phys. Rev. Lett.*,**96**, 014801 (2006).

[213] Terahertz radiation as a bunch diagnostic for laser-wakefield accelerated electron bunches, J.van Tilborg, C. B. Schroeder, C. V. Filip, Cs. Tóth, C. G. R. Geddes *et al.*, *Phys. Plasmas*,**13**, 056704 (2006).

[214] Single-shot measurement of the spectral envelope of broad-bandwidth terahertz pulses from femtosecond electron bunches, J.van Tilborg, Cs. Tóth, N. H. Matlis, G. R. Plateau and W. P. Leemans, *Opt. Lett.*,**33**, 1186 (2008).

[215] Single-shot spatiotemporal measurements of high-field terahertz pulses, J. van Tilborg, C. B. Schroeder, Cs Tóth, C. G. R. Geddes, E. Esarey *et al*., *Opt. Lett*.,**32**, 313 (2007).

[216] Charged particle radiography, C. L. Morris, N. S. P. King, K. Kwiatkowski, F. G. Mariam, F. E. Merrill *et al*, *Rep. Prog. Phys*. **76**, 046301 (2013).

[217] Charged particle radiography, F. E. Merrill, C. L. Morris, K. Folkman, F Harmon, A Hunt *et. al*., *IEEE Particle Accelerator Conf. (PAC)*, 1–4, 1704–6,4387, (2005).

[218] Electron radiography, F. E. Merrill, F. Harmon, A. Hunt, F. Mariam, K. Morley, *et al,Nuclear Instrum. Methods Phys. Res. B*, **261**, 382 (2007).

[219] The Physics of Radiation Therapy, F. M. Khan, Williams &Wilkins, (1994).

[220] Few femtosecond, few kiloampere electron bunch produced by a laser–plasma accelerator, O. Lundh, J. Lim, C. Rechatin, L. Ammoura, A. Ben-Ismaï *et al*., *Nature Physics*, **7**,219 (2011).

[221] Ultra-short electron beams based spatio-temporal radiation biology and radiotherapy, V. Malka, J. Faure and Y. A. Gauduel, *Mutation Research*,**704**, 142 (2010).

[222] Radiotherapy with laser-plasma accelerators: Monte Carlo simulation of dose deposited by an experimental quasimonoenergetic electron beam, Y. Glinec, J. Faure, V. Malka, T. Fuchs, H. Szymanowski *et al*., *Med. Phys.*, **33** (1), 155 (2006).

[223] Table-top laser-plasma acceleration as an electron radiography source, S. P. D. Mangles, B. R. Walton, Z. Najmudin, A. E. Dangor, K. Krushelnick *et al*., *Laser and Particle beams*, **24**, 185, (2006).

[224] Electron radiography using hot electron jets from sub-millijoule femtosecond laser pulses, C. G. Serbanescu, and R. Fedosejevs, *Appl. Phys B*, **83**, 521 (2006).

[225] Submillimeter-resolution radiography of shielded structures with laser-accelerated electron beams, V. Ramanathan, S. Banerjee, N. Powers, N. Cunningham, A. Nathan. C. Smith *et al.*, *Physical Review Special Topics - Accelerators and Beams*, **13**, 104701 (2010).

[226] Electron radiography using a table-top laser-cluster plasma accelerator, Bussolino G, C Faenov, A Giulietti, A Giulietti, D Koester *et al.*, *J. Phys. D: Appl. Phys.*, **46**, 245501 (2013).

[227] High-charge divergent electron beam generation from high-intensity laser interaction with a gas-cluster target, P. Koester, G. C. Bussolino, G. Cristoforetti, A. Faenov, A. Giulietti *et al.*, *Laser and Particle Beams*, **33**, 331 (2015).

[228] Ultrafast electron radiography of magnetic fields in high-intensity laser-solid interactions, W. Schumaker, N. Nakanii, A. Maksimchuk, C. McGuffey, K. A. Tanaka *et al.*, *Phys. Rev. Lett.*, **110**, 015003 (2013).

[229] Review of electron beam therapy physics, K. Hogstrom and P. R. Almond, *Phys. Med. Biol.*, **51**, R455 (2006).

[230] 150-250 MeV electron beams in radiation therapy, C. DesRosiers, V. Moskvin, A. F. Bielajew and L. Papiez, *Phys. Med. Biol.*, **45**, 1781 (2000).

[231] Treatment planning for radiotherapy with very high-energy electron beams and comparison of VHEE and VMAT plans, M. B.-Carter, B. Qu, B. Palma, B. Hårdemark, E. Hynning *et al.*, *Medical Physics*,**42**, 2615 (2015).

[232] Very high-energy electron (VHEE) beams in radiation therapy; Treatment plan comparison between VHEE, VMAT, and PPBS, E. Schüler, K. Eriksson, E. Hynning, S. L. Hancock, S. M. Hiniker, *Med. Phys.*, **44**, 2544 (2017).

[233] Treatment planning for radiotherapy with very high-energy electron beams and comparison of VHEE and VMAT plans, M. B. Carter, B. Qu, B. Palma, B Hardemark, E. Hynning *et al.*, *Medical Physics*, **42**, 2615 (2015).

[234] Laser-Driven Particle Acceleration Towards Radiobiology and Medicine, Antonio Giulietti, *Springer International Publishing, Switzerland*, (2016).

[235] Principles and applications of compact laser–plasma accelerators, V. Malka, J. Faure, Y. A. Gauduel, E. Lefebvre, A. Rousse *et al*., *Nature Physics*,**4**, 447 (2008).

CHAPTER 2

Fundamental aspects of laser plasma acceleration

In this chapter, we discuss in detail about the theoretical background of the different acceleration mechanisms governing laser plasma acceleration and the injection mechanisms of electrons associated with the different acceleration mechanisms. First, we discuss laser interaction and propagation in underdense gas-jet plasma target.

2.1 Laser interaction and propagation in gas-jet targets:

When a high intense laser pulse is focused on a gas-jet target plasma is rapidly created at the foot of the laser pulse. The peak intensities of ~10^{18}-10^{20} W/cm^2 achievable with the present laser 100 TW or PW laser systems is much higher compared to the ionization threshold of mostly used low Z gases e.g. hydrogen and helium and also of comparatively high-Z gases e.g. N_2, O_2 and Ar etc. The physical processes through which the initial ionization takes place, strongly depends upon the intensity and the temporal profile of the laser beam. The electric field (E in V/cm) associated with laser intensity (I in W/cm^2) is given by:

$$E(V/cm) = 27.5\sqrt{I_L(W/cm^2)} \tag{2.1}$$

Electric field associated with the hydrogen atom is ~$5.1\text{x}10^9$ V/cm, and as per above expression intensity required to ionize the hydrogen atom is ~3.5×10^{16} W/cm^2.However, depending on the incident laser intensity, plasma formation in gas can take place through a number of ionization processes. Multi-photon ionization [1, 2] and above threshold ionization (ATI) process [3] are effective at lower laser intensities of ~10^{13}W/cm^2 where the atomic potential remains unperturbed. But when the incident laser intensity is much higher as that is achieved currently, the associated laser electric field perturb the atomic potential and suppress the barrier. As a result, electrons are released more spontaneously and the effective threshold intensity for ionization reduces as is given by:

$$I(laser) = 4\times10^{9}(E_{ion}/eV)^{4}Z^{-2}W/cm^{2} \qquad (2.2)$$

where Z denotes the charge of the gas. So, for hydrogen, the effective ionization threshold intensity reduces to ~10^{14} W/cm^2 which is two orders lower than the actual threshold intensity. This is called the over the barrier ionization (OBI) or tunneling ionization [4, 5]. This process is very important in formation of plasma by interaction of short laser pulse. Refractive index (μ) of the plasma is written as:

$$\eta = (1-\frac{\omega_p^2}{\omega^2})^{1/2} = (1-\frac{n_e}{n_c})^{1/2} \qquad (2.3)$$

where, $\omega_p^2 = {4\pi e^2 n_e}/{m} = 5.64\times10^{4}\times\sqrt{n_e}$ is called the plasma frequency, ω is the laser frequency, n_e is the plasma density and n_c is the critical density.

From the above relation, we see that for the laser frequency less than plasma frequency, the refractive index becomes imaginary. But light propagation is only possible for real values of refractive index for which it is necessary that $\omega > \omega_p$. This condition states that the laser propagation in plasma is only limited up to $\omega = \omega_p$. So the corresponding density at which $\omega = \omega_p$ is called critical density and is given by,

$$n_c = 1.1\times(\frac{\lambda_L}{\mu m})^{-2}cm^{-3} \qquad (2.4)$$

For a Ti:sapphire laser operating at wavelength (λ) of 800 nm, n_c is calculated to be $\sim 1.7\times10^{21}$ cm^{-3}. Plasma medium with density lower or higher than the critical density for a given laser wavelength is called underdense and overdense plasma respectively. In case of plasma produced on solid targets using intense lasers all absorption processes occur in the under dense plasma region up to the critical density layer as it defines the maximum plasma density up to which laser light can propagate. In case of gas-jet plasma targets with density in the underdense region laser can propagate through the plasma medium. However, focused laser pulse propagation distance is limited to Rayleigh length given by, $Z_R=\pi r_0^2/\lambda$, (where r_0 is the initial laser spot radius at $1/e^2$ value of peak intensity and λ is the laser wavelength) due to its natural diffraction. This relation is valid for ideal Gaussian beam, but in practical cases, the presence of higher order modes in the laser beam limits the beam from being perfect Gaussian. How much a real beam is deviated from the ideal Gaussian beam is described by M^2 parameter, which is defined as $W\theta = M^2 2\pi/\lambda$, where W and θ are the laser focal spot size and angular spread of the real beam [6]. The M^2 parameter is a positive number ranging from unity to greater than unity: larger the value of M^2, larger is the deviation of real laser pulse from Gaussian. Considering M^2 parameter, Rayleigh length of a real beam is redefined as $Z_R'=\pi W^2/M^2\lambda$. Hence for larger values of M^2 Rayleigh length decreases and effectively the laser pulse is diffracted much earlier. For focal spot size of few microns to few tens of microns, the Rayleigh length ranges from sub mm to few mm.

In addition, inside plasma, propagation distance is further limited due to ionization induced defocusing effects [7-10]. The degree of ionization of an atom by an intense laser field depends on the atomic number (Z) of the atom and on the laser pulse intensity. Considering a Gaussian laser pulse profile both in the transverse and longitudinal direction, propagating inside a high Z gas target, the outer shell electrons having lower binding energies are ionized at the foot or the wings whereas, the inner shell electrons with comparatively higher binding energies are ionized at the peak of the laser pulse. Thus, corresponding to laser intensity profile, a radial density profile is formed with a density maximum at the peak of the pulse (i.e. on axis), subsequently reducing the on-axis refractive index of the plasma. This leads to increase in the on-axis phase velocity, compared to the wings, and hence acts like a diverging lens effect and results into laser pulse defocusing. Ionization induced defocusing effects can be minimized for low Z gas targets such as H_2 and He due to complete ionization occurring at the foot or wings of the laser pulse and no further ionization at the pulse peak. However, without any guiding the laser propagation shall still be limited by Rayleigh length and is generally not sufficient to achieve high-energy acceleration of electrons.

Guiding and propagation of intense laser pulses in underdense plasma beyond Rayleigh lengths can be achieved by modification of the refractive index of the plasma such that the refractive index is maximum on the laser propagation axis compared to the wings i.e. $d\eta/dr < 0$. Various non-linear processes such as relativistic self-focusing [11, 12], and ponderomotive channeling [13, 14] takes place inside plasma and hence helps self-guiding of the laser pulse over several Rayleigh lengths. At very high laser intensities, the electrons quiver relativistically in the laser field [11, 12]. The relativistic mass ($m'=\gamma m$, where γ is the relativistic factor) effectively modifies the local plasma frequency ($\omega_p'=\omega_p/\sqrt{\gamma}$) and hence increases the refractive index along the laser axis, leading to relativistic self-focusing and guiding of the laser pulse. Whereas, in case of ponderomotive channeling, the electrons are expelled radially outward from the laser propagation axis by the ponderomotive force of the laser pulse leading to increase in the refractive index along the laser axis [13, 14]. It has been shown that when laser power exceeds critical power for relativistic self-focusing, P_c (GW) = 17.4 (n_c/n_e), diffraction can be overcome, and relativistic self-guiding of the pulse occurs [11, 12]. Consideration of ponderomotive self-channeling along with relativistic self-focusing enhances this effect by slightly reducing the critical power for guiding to P_c (GW) $\geq$ 16.2 (n_c/n_e) [13, 14].

Relativistic self-guiding of the laser pulse depends on laser and plasma parameters viz. laser pulse length (L) ($L=c\tau_L$, τ_L is laser pulse duration at FWHM: full width at half maximum), plasma wavelength (λ_p), initial laser spot radius (r_0), peak amplitude of the normalized laser intensity (a_0), input laser power (P) and plasma electron density (n_e). Self-focusing and guiding of intense long as well as short laser pulses in plasma have been observed experimentally [15-20]. Based on initial laser and plasma parameters, bubble (complete cavitation) / wakefield or a long channel is created and both the conditions are suitable for electron acceleration as discussed in the next sections.

2.2. Laser Wakefield Acceleration (LWFA):

As has been discussed in the previous chapter, laser wakefield acceleration of electrons is operated both in the long and short laser pulse regime i.e. $L>\lambda_p$ / $L>>\lambda_p$ and $L\leq\lambda_p$ respectively, where $L=c\tau$ is the laser pulse length, τ is the FWHM laser pulse duration and $\lambda_p=3.33\times10^{10}/\sqrt{n_e}$, is the plasma wavelength, n_e is the electron plasma density. SM-LWFA is generally observed in the long laser pulse regime of $L>\lambda_p/L>>\lambda_p$. In this case, long laser pulses are at first modulated of the order of λ_p

which subsequently drives large wakefields. Whereas, bubble regime of acceleration is observed in the short laser pulse regime of $L<\lambda_p$. In the following sub-sections we discuss in detail, the theoretical understanding of generation of linear and non-linear wakefields, acceleration mechanisms in case of SM-LWFA followed by bubble regime of acceleration. Lastly, we will discuss about the various electron injection schemes associated with LWFA.

2.2.1. Theoretical understanding of generation of linear and non-linear wakefield:

Generation of wakefield involves complex physical processes of charge separation induced by laser ponderomotive force and restoration force due to electrostatic force, thereby setting up a plasma oscillation behind the laser pulse called the wake which is longitudinal in nature. Generation of wakefield driven by high intense laser pulse has been studied analytically by solving the Maxwell's and Lorentz equation of motion of electrons inside plasma.

The Lorentz equation is given by:

$$\frac{\partial \boldsymbol{p}}{\partial t} + (\boldsymbol{v}.\nabla)\boldsymbol{p} = -e(\boldsymbol{E} + \frac{1}{c}\boldsymbol{v}\times\boldsymbol{B}) \tag{2.5}$$

The Maxwell's equations are given by:

$$\nabla.\boldsymbol{E} = 4\pi e(n_0 - n_e) \tag{2.6 a}$$

$$\nabla\times\boldsymbol{E} = -\frac{1}{c}\frac{\partial \boldsymbol{B}}{\partial t} \tag{2.6 b}$$

$$\nabla\times\boldsymbol{B} = -\frac{4\pi}{c} e n_e \boldsymbol{v} + \frac{1}{c}\frac{\partial \boldsymbol{E}}{\partial t} \tag{2.6 c}$$

$$\nabla.\boldsymbol{B} = 0 \tag{2.6 d}$$

Here, **p** = γm**v** is the total momentum of the electron with mass m, **v** is the total velocity of the electron and $\gamma = (1+E/E_0)$ is the energy gain of the electron, where E is the energy gain in units of MeV and E_0 (=0.5 MeV) is the rest mass energy of the electron. Here $n=n_e-n_0$ gives the perturbed electron density in plasma and n_0 is the background electrons.

Linear plasma wave: Solving the above equations assuming a coordinate system in which laser pulse is polarized along y-direction and propagating along x-direction such that $\vec{E} = (0, E_y, 0)$ and $\vec{B} = (0, 0, B_x)$, longitudinal wakefield are generated in the z-direction (E_z). In the small pump strengths limit $v_y << 1$, i.e. at normalized laser intensity of $a_0 \leq 1$ (where, a_0 is the peak value of laser envelop, $a = {}^{v_y}\!/_{c}$), describes a linear regime. The wakefield generation is in the linear limit is thus given by [21, 22]:

$$(\frac{\partial^2}{\partial \xi^2} + \omega_p^2) n_e = \frac{n_0}{2} \frac{\partial^2 a^2}{\partial \xi^2} \tag{2.7}$$

The above equation shows a simple harmonic equation of the density perturbation driven by the intensity gradient force of the laser i.e. the ponderomotive force. The solution of Eq. (2.7) is a sinusoidal wave with oscillation frequency ω_p which is governed by the plasma electron density and the linear plasma wavelength λ_p.

Using the Poisson's equation given by:

$$\frac{\partial E_z}{\partial \xi} = -4\pi e n_e$$

The electric field associated with the wake field can be derived to

$$(\frac{\partial^2}{\partial \xi^2} + k_p^2) E_z = k_p^2 \frac{\partial \varphi_L}{\partial \xi} \tag{2.8}$$

Where, the driving term a^2 is equated to the laser ponderomotive potential φ_L through $\varphi_L = -\frac{1}{2} < a^2 >$ and $k_p = \frac{2\pi c}{\lambda_p}$. For a sinusoidal laser pulse,

$$E_z = \frac{2\pi^2 \varphi_L}{(4\pi^2 - k_p^2 \xi_L^2)} [\cos k_p(\xi - \xi_L) - \cos k_p \xi] \tag{2.9}$$

So the field is maximum when $k_p\xi_L = 2\pi$ i.e. $\xi_L = \lambda_p$. This is a very important condition to generate the wake field which shows that for resonantly exciting the plasma to generate very high wake, the laser pulse length must match with the plasma wavelength.

The maximum electric field associated with plasma wave depends on the density of the plasma and is given by [23]:

$$E_0 = \frac{mc\omega_p}{e} \cong 96\sqrt{n_e(cm^{-3})} \tag{2.10}$$

This is also called the cold non-relativistic wave breaking field. For a density of $\sim 10^{18}$ cm^{-3}, $E_0 \sim 96$ GV/m.

Electron energy gain through wakefield is limited by two important factors i.e. either dephasing of electrons [24] or pump depletion [25]. When the accelerating electrons gain sufficient energy (longitudinal velocity ~c) such that they begin to outrun the accelerating phase of the wakefield (phase velocity <c), these electrons enters the decelerating phase and begin to loose energy. These electrons are said to be dephased and the length over which the electrons remain in the accelerating phase of the wake is known as the dephasing length (L_d) [24]. Electron energy gain limitation by pump depletion occurs when the laser pulse losses its energy by continuously blowing out electrons from the axis. Consequently, after propagating a certain length called the pump depletion length (L_{pd}) [25] the laser pulse would not be left with

enough energy to excite further wakefield, thereby acceleration of electron is terminated. Depending on the laser and plasma conditions, either of the two limiting factors decides the overall electron energy gain.

In the linear regime (a_0^2<<1), the dephasing limited electron energy gain is given by [24]:

$$\gamma = 2\times\frac{\omega^2}{\omega_p^2} = 2\times\frac{n_c}{n_e} \tag{2.11}$$

Eq. (2.11) shows that, the electron energy gain in the linear wakefield regime is governed by the electron plasma density, i.e. lower the plasma density higher is the energy gain.

Non-linear plasma wave: For high pump strengths, i.e. for intensities beyond 10^{18} W/cm^2 and when p_y/mc>>1, the system becomes fully non-linear. Analytical solutions of the non-linear wakefield has been studied in 1D, 2D and 3D cases [26-32]. Assuming that the plasma and the laser intensity profile are both function of ξ, the non-linear wakefield equation is given by [29, 30, 32]:

$$\frac{\partial^2\varphi}{\partial\xi^2} = k_p^2\gamma_p^2\left\{\beta_p\left[1-\frac{(1+a^2)}{\gamma_p^2(1+\varphi)^2}\right]^{-1/2}-1\right\} \tag{2.12}$$

This is a non-linear ordinary differential equation for the wake potential φ. Here, $\beta_p=v_p/c$ and $\gamma_p=(1-v_p^2/c^2)^{-1/2}$ where v_p is the phase velocity of wake. Solution of Eq. (2.12) shows that unlike the linear wakefield case, the wave is no longer simple sinusoidal, rather it is a saw tooth profile. The wavelength of the non-linear plasma wave increases due to the increase in amplitude of oscillation and is given by [27-29]:

$$\lambda_{Np} = \lambda_p \times \frac{2}{\pi}\left\{\frac{E_{\max}}{E_0}+\frac{E_0}{E_{\max}}\right\}\left(\frac{E_{\max}}{E_0} >> 1\right) \tag{2.13}$$

Here, E_{max} is the peak electric field of the plasma wave.

The maximum energy gain of electrons in a 3D non-linear plasma wave is given by [25]:

$$\gamma = \frac{2}{3} \times \frac{n_c}{n_e} \times a_0 \tag{2.14}$$

Eq. (2.14) shows that unlike in the linear wakefield case, the maximum energy gain of electrons now also depend on the laser intensity.

2.2.2. Self-Modulated Laser Wakefield Acceleration (SM-LWFA):

The self-modulated acceleration technique uses a single long laser pulse to excite plasma waves which is broken into a number of pulses when propagated through high density plasma ($\geq 10^{19}$ cm^{-3}). As the pulse propagates it faces a density variation within the pulse length. The regions with higher plasma density have a lower refractive index and hence the phase velocity of the pulse in that region increases, compared to regions with lower plasma density. This variation in the phase velocity within the single laser pulse leads to the breaking up of the pulse. Within one plasma wavelength, the variation of density occurs once and hence laser pulse lengths greater than the plasma wavelength is necessary for modulation to take place. This breaking of the long laser pulse into smaller pulses by its own, without any external stimulation is called the self-modulation. Since in this technique long pulses are used, the power (P) of the laser pulse must be greater than the critical power (P_c) required for self-focusing of the laser [11]. Hence the necessary condition for the SM-LWFA is that, $L>\lambda_p$ and $P \geq P_c$. Associated with the formation of number of small laser pulses is the generation of large amplitude plasma wave upto the wave-breaking limit [Eq. (2.10)] can be achieved.

Initially, theoretical study on self-modulation of the laser pulse by the plasma wave was first reported by Esaray *et al*. [33] and later observed through simulations [34-37]. It has also been shown that, self-modulation of the laser pulse can also be triggered by the Forward Raman scattering (FRS) instability [38, 39]. Since, in this case, the self-modulation process requires a high value of P/P_c, relativistic self-focusing of the laser pulse up to several Rayleigh lengths can be achieved. However, since the process involves high laser intensities and plasma densities, it becomes highly unstable and uncontrolled, resulting in poor beam qualities.

2.2.3. Bubble or blow-out acceleration:

The blow out regime is operated in the short laser pulse regime of $L \leq \lambda_p$ using comparatively shorter laser pulse duration of few tens of fs [32, 40]. It has been discussed in the previous section that, wakefields driven in the linear regime are sinusoidal in nature with wavelength λ_p and in the non-linear regime the wakefield is saw-tooth wave with increase in λ_p [26-28]. Since the laser intensity is maximum on axis compared to off-axis, the non-linear plasma wavelength along axis is greater than that off-axis. This result in curvature of the wake phase fronts [36], and the completely blown out electrons from the laser axis [40-42], form a bubble behind the laser pulse following the curved wave front. This cavitated almost spherical region devoid of electrons is called bubble. The maximum radius of the bubble (R_b) can be scaled with the laser focus spot size ω_0 i.e. $R_b \sim \omega_0$ [43].

The exact shape of the bubble depends on the growth of the electron bunch with time inside the cavity. Hence initially the shape is governed by the transverse ponderomotive force of the laser pulse only. The transverse radius of the bubble reaches maximum at the mid plane of the bubble. At this position the Lorentz force on the electrons due to the ions at the channel axis is balanced by the ponderomotive force. The radial force due to the ions can be calculated by applying Gauss's law. Assuming the bubble to be exactly spherical and of uniform charge, the maximum radial field comes out to be,

$$E_r \sim \frac{k_p}{2} E_0 R_b \tag{2.15}$$

The ponderomotive force in this relativistic region scales as

$$F_p \sim k_p \frac{\nabla a_0^2}{\gamma} \tag{2.16}$$

Equating Eq. (2.15) and (2.16),

$$k_p R_b \approx \sqrt{a_0}$$

Since, $R_b \sim \omega_0$, So, $k_p \omega_0 = k_p R_b \approx \sqrt{a_0}$

From simulation of Lu *et al*. [32] this relation exactly comes out to be

$$k_p \omega_0 = k_p R_b = 2\sqrt{a_0} \tag{2.17}$$

The minimum intensity for the bubble to be formed is governed by the threshold power required for self-focusing of the laser pulse. From simulations of Lu *et al*. [32] it is seen that the acceleration in the bubble regime holds best between the limit,

$$2 \le a_0 \le 4$$

To be in the spherical blow-out regime, the laser pulse in addition would also require a threshold power given by [42, 44]:

$$P \approx \left(\frac{a_0^3}{8}\right) \times P_c \tag{2.18}$$

The bubble consists of both the accelerating longitudinal field (E_z) and the transverse focusing field (E_r) given by [42, 45],

$$E_r \approx \frac{k_p}{2} E_0 r \tag{2.19}$$

$$E_z \approx \frac{k_p}{2} E_0 \xi \tag{2.20}$$

where ξ is the distance of the wake behind the laser pulse.

The advantage of the bubble acceleration regime is that, the focusing force in the radial direction linearly varies with the radial distance r. This helps to minimize the transverse emittance of the beam. The emittance of electron beams is given by $\varepsilon = \sqrt{\langle y^2 \rangle \langle y'^2 \rangle - \langle yy' \rangle^2}$ where y and y' is the spatial and angular co-ordinates respectively [25]. Additionally, since all the electrons are blown out from the laser propagation axis, the laser pulse will remain focused for a longer distance leading to longer acceleration lengths. Thus, blow out regime has the high potential of producing high-energy good quality electron beams.

Bubble regime of acceleration can also be achieved in the long laser pulse ($L>\lambda_p$) regime of SM-LWFA, where it was suggested that long laser pulses after entering into plasma after undergoing relativistic self-focusing and can achieve bubble matching conditions. Plasma blowout in a SM-LWFA regime has been studied analytically [13, 36, 41, 46], where they showed complete cavitation of electrons in the region of the laser pulse with formation of highly non-linear wake, generated through pulse self-steepening, pulse compression and pulse self-focusing.

2.2.4. Electron injection mechanisms in LWFA:

One of the crucial aspects for a stable laser plasma accelerator, is the electron injection mechanism as it strongly impacts ~~on~~ the final electron beam parameters. In LWFA, a short laser pulse interacts with underdense plasma and subsequently excites highly non-linear wakefield or bubble and electrons injected in such an accelerating structure gain very high energies. For typical plasma densities of ~10^{18}-10^{19} cm^{-3}, the accelerating structure or the plasma wavelength is in the range of 10-30 µm, and it is essential that electrons are injected into such micron size structures moreso, in proper accelerating phase of the wakefield. These stringent requirements make the external injection of electrons quite challenging to achieve experimentally specially in highly non-linear phenomena involved laser plasma interactions.

For resonant excitation of plasma wave by laser, the phase velocity of the wakefield should match with the group velocity of the laser (v_g) such that,

$$v_p \sim \frac{c}{\sqrt{1-\frac{\omega_p^2}{\omega^2}}} \sim v_g \sim \frac{\omega}{\omega_p} \sim c \tag{2.21}$$

The key parameter in determining injection of electrons into the plasma wake potential is the interplay between the phase velocity of the wake (v_p) and the particle velocity (v). For injection of electrons to take place electrons should gain enough longitudinal momentum to catch up with the wake, which suggests that the electron longitudinal velocity (u_z) should be almost equal to the phase velocity of the wake i.e. $v_p \sim u_z$ [31, 47]. Based on this requirement several methods for injecting electron into the exciting plasma wakefield have been proposed which can be summarized into three following general principals.

1. Provide an initial longitudinal momentum to the background electrons such that they catch up with the wake phase velocity.
2. Create electrons at the right phase of the wakefield even if their initial longitudinal momentum is zero i.e. born at rest.
3. Slow down the wakefield phase velocity by some means locally can facilitate electron trapping.

Based on this, various injection schemes of electrons have been adopted which are as follows [48-50]:

1. Self-injection (SI) of electrons through wave breaking
2. Optical Injection
   i) Ponderomotive injection
   ii) Colliding pulse injection
3. Ionization induced injection
4. Density transition injection

Among the various injection mechanisms, optical injection techniques are used to obtain an electron bunch with a small energy spread. Optical injection is carried out in two different ways. First, is the ponderomotive injection, which was first proposed in 1996 [51]. In this scheme two laser beams are used-one is the pump beam and other is the injector beam. The pump beam excites a wake field behind it, and the injector beam focused perpendicular to the pump beam interacts with the wake generated with the pump beam at some distance behind it. Recently, electron injection by this technique has been demonstrated experimentally [52]. Second, is the colliding pulse injection [53, 54] using three laser beams. One is the pump pulse and the other two are the injector pulse, which are made beat at an axial region behind the pump pulse. This helps in tuning the injection point and electrons can be injected at proper phase of the wake. Colliding pulse injection using two laser pulses has also been proposed [55, 56] and was experimentally demonstrated also [57].

Self-trapping of electrons in the plasma waves can also be achieved using downward density transitions with scale length long compared to the plasma wavelength. In such a density profile, the phase velocity of the electron plasma wave decreases, which in turn helps in injection. The density transition can be experimentally achieved by passing a laser beam orthogonal to the main laser beam and thus creating a parabolic density profile in the path of the main laser pulse [58], by inserting a thin wire through the gas target, and by directly focusing the laser beam on the downstream edge of the thin gas jet target [59].

In the following paragraph, we discuss in detail the wave-breaking process and the ionization induced injection scheme which are relevant to the present thesis work.

Self-injection (SI) of electrons/ wave breaking:

It is the most widely investigated injection mechanisms [49, 60, 61]. It relies on the principal of self-trapping of background electrons, i.e. by driving electrons comparable to the phase velocity of the wake. In a plasma, most of the background electrons oscillate with the fluid velocity (assuming a Maxwellian distribution), which are far behind v_p and are not trapped in the wave. However, by exciting the plasma waves to very high amplitudes up to the wave breaking limit, electrons can be trapped.

Assuming a 1D model, electron plasma waves are oscillations of the electrons in plasma with a characteristic plasma oscillation frequency ω_p about the immobile ions due to the space charge force generated between the electrons and the ions. The maximum electric field that the wave can sustain is called the cold wave breaking field (E_0) given by Eq. (2.10). Linear plasma wave executes simple sinusoidal oscillation with frequency ω_p and the phase velocity $v_p \cong c$. The electric field oscillation maintains a constant phase relation with the density oscillation (being out of phase by $\pi/2$) and thus grows indefinitely. On the other hand, in case of highly non-linear plasma waves the oscillation exhibits a sawtooth profile with steepening of the plasma wave, leading to longer oscillation amplitudes such that the frequency of oscillation of these non-linear plasma wave decreases from ω_p and the phase velocity is also reduced to $v_p<c$. So, for trapping, non-linear wakefields are more favorable compared to the wakefields in the linear regime. Hence, wave breaking process requires very high laser intensities and plasma densities to reach to the wave breaking limit in the non-linear regime. Simulations performed in 2D and 3D in the highly non-linear regime, have showed generation of plasma waves in excess of E_0 and the threshold required for wave breaking process is a_0~4 in 1D for typical plasma densities of ~10^{19} cm^{-3} [62].

Solving Lorentz and Maxwell equations for underdense plasma given by Eq. (2.5 & 2.6), the density perturbation equation is given by:

$$n = \frac{\beta_p n_0}{\beta_p - u_z} \tag{2.22}$$

It can be seen that, for excitation of highly non-linear plasma wave, at $u_z \sim \beta_p$, i.e. when electron longitudinal velocity equals the phase velocity of the wave, n becomes highly peaked and density spikes are formed. Hence, in such case, the amplitude of the wave may become so high that the maximum amplitude exceeds the cold wave breaking value E_0. The plasma wave then cannot sustain such a high density and loses its coherency. The wave is then said to break. These electrons are then trapped in the potential trough of the plasma wave and are accelerated.

In the relativistic limit, the maximum field amplitude of the plasma wave breaking is given by [25, 31],

$$E_{WB} = \frac{mc\omega_p}{e}\sqrt{2}(\gamma_p - 1)^{1/2} \tag{2.23}$$

However, in ideal 3D case, the bubble is formed and complete electron expulsion about the laser axis leads to highly non-linear wakefield. The blown out electrons after traversing a curved path return to the axis behind the laser at the rear end of the bucket. So, within a small region the density increases and since $E \propto \sqrt{n_e}$, the longitudinal electric field forms a local spike at that point. The electron becomes trapped only if it receives enough energy from the spike to reach the phase velocity of the wake. The spike at the rear end accelerates these electrons to high velocities such that they are further accelerated by the longitudinal field. Simulation studies have also showed self-injection of electrons from the rear of the bubble [44, 45].

However, for efficient acceleration, the electrons have also to be injected in the proper phase of the wake such that they get trapped in the wakefield. Analytical study of trapping of electrons in the wake potential has been studied by tracking the electron trajectories in the field through the Hamiltonian treatment [31]. The Hamiltonian of an electron is given by:

$$H(\gamma,\psi) = \gamma(1-\beta\beta_p) - \varphi(\psi) \tag{2.24}$$

where, $\beta = u_z/c$ and ψ is the phase of the electron with the wakefield. The separatrix is the boundary in phase space (γ,ψ) separating the closed orbit (trapped orbit) from the open orbits (untrapped electrons). The separatrix is defined by a threshold $\gamma_s(\psi)$, characterized by the condition that, H (γ_s,ψ) = H (γ_p,ψ_{min}), which defines the separatrix orbit as [63],

$$H_s = \frac{\gamma(\psi_{\min})}{\gamma_p} - \varphi_{\min} \tag{2.25}$$

The width of the separatrix along the ψ-axis is 2 (ψ_{max}-ψ_{min}) = $k_p\lambda_p$ and height of the separatrix along the γ-axis gives γ_{max}-γ_{min}, suggesting the maximum electron energy gain. Only the trapped electrons inside the closed orbits of the separatrix can gain maximum electron energy.

However, the drawback of the process is that, it is highly non-linear and unstable and the parameters are not under control. Hence, electron beam generation also becomes unstable. As the laser propagates, continuous trapping of the background electrons takes place. Therefore, spread in the electron bunches takes place and the beam loses its monochromaticity. To gain very high energy (~GeV), the accelerator needs to operate at very lower densities (~10^{18} cm^{-3}), where for self-trapping of electrons requires very high laser peak powers (~few tens of TW) [64].

Ionization induced injection:

A promising alternative approach to injection at low densities, which is actively perused recently, is ionization-induced injection [63, 65]. Fig. 2.1 shows the schematic of the ionization induced injection mechanism.

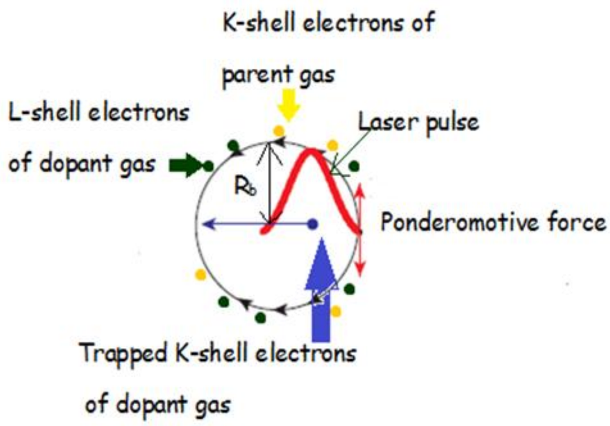

Fig. 2.1: A pictorial representation of ionization induced injection mechanism.

In this mechanism, a trace amount of high Z gases (dopant) such as N_2, O_2, CO_2 etc. are added with the parent low Z gases such as He. The choice of the dopant gas depends on the intensity of the laser. The dopant gas should be such that, the ionization energy of the K-shell electrons of the dopant gas must be high such that they are ionized only at the peak of the laser field. These dopant K-shell electrons, which are born at the centre of the bubble at rest, initially do not have sufficient momentum to be accelerated with the wave. So, they begin to slip backwards. Before leaving the rear end of the bucket, if these electrons gain sufficient momentum then they will be accelerated with the phase velocity of the wave. Several experimental studies have been performed relying on this mechanism and have shown generation of stable electron beams [64-69]. These reports have also shown that, compared to the wave breaking thresholds, ionization induced injection mechanism operates at lower threshold plasma densities ($\sim 10^{18}$ cm^{-3}) and laser intensities ($a_0 \sim 1.6$). This helps in generating more stable electron beams compared to the wave-breaking process. Moreover, ionization induced injection mechanism has also shown to generate comparatively higher electron beam charge. However, this mechanism also suffers from the drawback of broad energy spread of electrons due to continuous injection of electrons.

Theoretically, ionization induced injection mechanism have been studied where dynamics of electron ionization and trapping conditions of the inner K-shell electrons have been derived [63]. Since, the inner K-shell electrons are ionized at a later instant, inside the laser pulse, unlike the wave breaking process, in this case, contribution of the transverse momentum comes into play and the total energy γ can be now written as

$$\gamma = \sqrt{\gamma_{\perp}^2 + u_z^2} \tag{2.26}$$

where, $\gamma_{\perp} = \sqrt{1+u_{\perp}^2}$, where $u_{\perp}$ is the normalized transverse momentum of the electron.

Accordingly, the separatrix orbit is defined by [63]:

$$H_s = \frac{\gamma_{\perp}(\psi_{\min})}{\gamma_p} - \varphi_{\min} \tag{2.27}$$

However, in this case, since the electrons are ionized within the wake potential, the phase of injection of the electron (i.e. ψ_i) is important and since they are born at rest, $u_{\perp}(\psi_i)=0$. This finally modifies the Hamiltonian for the electron to be trapped as:

$$H_i = 1 - \varphi(i) \tag{2.28}$$

where φ_i is the wake potential at the ionization position *i*. The ionization mechanism also affects the formation of the wake potential and the modified wake potential which is a function of the potential at the position *i* is given by:

$$\frac{1}{k_p^2}\frac{\partial^2\varphi}{\partial\xi^2} = \frac{\alpha}{2}\left[\frac{1+a^2}{(1+\varphi)^2} - 1\right] + H(\psi-\psi_i)\frac{(1-\alpha)}{2}\left[\frac{1+a^2}{(1-\varphi(i)+\varphi)^2} - 1\right] \tag{2.29}$$

where, α is the fraction of the ionized electron and $H(\psi-\psi_i)$ is a heaviside function.

2.3. Direct laser acceleration (DLA):

DLA takes place in the long laser pulse duration case when $L \gg \lambda_p$ or even in $L > \lambda_p$ whenever there is substantial overlap of the laser pulse with the injected electrons take place. In such case, the electrons interact with the laser pulse and gain energy directly from the laser pulse itself. Hence, in this case, the theoretical study of acceleration of electrons consists of the interaction of a single electron with the laser field in a plasma channel where, in addition to the transverse laser electric field, electron also interacts with the static fields of the plasma channel.

2.3.1. Plasma channel creation by laser:

There are very few analytical reports on DLA [70-73]. However, a detailed study of the interaction of an electron with the laser and static electric and magnetic field of the plasma channel has been reported by Tsakiris *et al*. [70].

When a long laser pulse ($L>\lambda_p/L\gg\lambda_p$) propagates through an underdense plasma, a plasma electron depletion or a plasma channel is formed by the radial ponderomotive force of the laser. The plasma channel comprises of the self-generated static electric and magnetic filed in addition to the transverse laser electric field, which makes the electrons perform betatron oscillations in the channel. The transverse static fields help to confine the radial bounce motion of the electrons developed due to the interacting with the transverse electric field of the laser.

Considering Gaussian laser electric and magnetic field with polarization along x-direction and propagating along z-direction given by,

$$\boldsymbol{E}_L = A_0 e^{r^2 / 2r_0^2} (\cos\psi \hat{x} - \frac{x}{kr_0^2} \sin\psi \hat{z}) \tag{2.30}$$

$$\boldsymbol{B}_L = A_0 \eta e^{r^2/2r_0^2} (\cos\psi \hat{y} - \frac{y}{kr_0^2} \sin\psi \hat{z}) \tag{2.31}$$

where, $\psi = kz - \omega t$, $k = (\omega / c)\eta$, A_0 denotes the peak laser electric field such that $a_0 = \frac{eA_0}{m\omega c}$, $\eta = \left\{ 1 - \frac{\omega_p^2}{\omega^2}(1 + \frac{a_0^2}{2})^{1/2} \right\}^{1/2}$ is the ratio of group velocity of the laser in plasma to that in vacuum. As the long laser pulse propagated through the plasma, it expels electrons by the ponderomotive force and develops an ion channel. As a result, a radial quasi-static transverse electric field evolves in the channel. In the quasi-static state, the static electric and magnetic field is given by [70]:

$$\boldsymbol{E}_s = \nabla \phi_p = \frac{E_{os}}{(1 + \frac{a_0^2}{2})^{1/2}} \frac{x}{r_0} \hat{x} \tag{2.32}$$

Where, $E_{os} = \frac{mc^2}{2er_0} \times a_0^2$

Here ϕ_p is the ponderomotive potential, r_0 is the vacuum spot size of the focused laser.

$$\boldsymbol{B}_s = -B_{0\phi} \frac{x}{r_o} \hat{y} \tag{2.33}$$

gives the azimuthal magnetic field generated by the current due to energetic electrons and $B_{0\phi} = 5.44 \pi n_h e r_0$ where n_h is the average density of the energetic electrons. This shows that for motion of electron along either $+\hat{x}$ or $-\hat{x}$ direction, the electrons experience a $v \times B$ force in the + z-direction.

The motion of electron in presence of only the azimuthal magnetic field is periodic motion in $\hat{x}$ with no energy gain of the electron i.e. the electron energy remains constant to the initial energy. However, in presence of both the static electric and magnetic field, the electrons gains energy and also gain periodic oscillation in the laser channel.

The energy and parallel momentum equations in the presence of static electric and magnetic field is given by,

$$mc^2\frac{d\gamma}{dt} = -e\boldsymbol{E}_s.\boldsymbol{v} = -\frac{E_{0s}}{(1+\frac{a_0^2}{2})^{1/2}}\frac{x}{r_0}\frac{dx}{dt} \tag{2.34}$$

$$\frac{dp_z}{dt} = \frac{eB_{0\phi}}{2r_0c}\frac{dx^2}{dt} \tag{2.35}$$

which gives the x-motion of electron as

$$\frac{d^2x}{dt^2} + \omega_b^2 x = \frac{eE_{os}}{mr_0}\frac{v_x^2}{c^2}x \tag{2.36}$$

where, $\omega_b = \frac{\omega_{bo}}{\sqrt{\gamma}}$, $\omega_{bo} = \left[\frac{e}{mr_0}\{\frac{E_{os}}{(1+\frac{a_0^2}{2})^{1/2}} + \frac{v_z}{c}B_{o\phi}\}\right]$.

Hence, in the presence of both static electric and magnetic field, the electron in the plasma channel perform an anharmonic periodic motion in $\hat{x}$ direction with a bounce frequency of ω_b. The bounce frequency of the electron is solely dependent on the static field strengths of the plasma channel formed under different laser and plasma conditions and also on the electron energy gain.

Simulation studies have shown that, in case of a steady state channel, the channel forms a coaxial structure with flow of energetic electrons along the channel axis in the forward direction along the laser propagation and a flow of the return current at the outer periphery of the channel [73]. In such laser created channels, where high current flows near the channel axis, pinching of the laser channel at the later stage of propagation was observed [74, 75]. This could be attributed to the observed electron acceleration in the channel and its subsequent pinching due to self-generated quasi-static magnetic field which in turn affects the laser propagation. Such an effect was reported experimentally during propagation of a 1 ps laser pulse (intensity ~5 - 9×10^{18} W/cm^2) in near critical density plasma (produced from a foil target) with a density gradient in the laser propagation direction [74]. Mangles *et al.* [76] have also observed this effect through simulation for plasma density of ~10^{19} cm^{-3} (n_e=0.01 n_c) but at much higher laser intensity of >10^{20} W/cm^2.

2.3.2. Theoretical energy estimation and electron trapping in DLA:

Now, in presence of both the laser electric field and the channel static field, the electron gains energy both from the static electric field and the transverse laser field. To estimate the electron energy gain in such as a condition, we consider plane uniform laser propagating along z-direction, having electric field $\mathbf{E_L}$ with polarization along x-direction and magnetic field $\mathbf{B_L}$ with polarization along y-direction given by [66]:

$$\boldsymbol{E}_L = A_0 \cos(\omega t - kz)\hat{x} \tag{2.37}$$

$$\boldsymbol{B}_L = \eta A_0 \cos(\omega t - kz)\hat{y} \tag{2.38}$$

So, the energy gain equation is given by,

$$mc^2 \frac{d\gamma}{dt} = -e\boldsymbol{E}.\boldsymbol{v} = -\frac{e}{2r_0} \frac{E_{os}}{(1+\frac{a_0^2}{2})^{1/2}} \frac{dx^2}{dt} - eA_0 v_x \cos(\omega t - kz) \tag{2.39}$$

Since, in the presence of the laser, the electrons will perform betatron oscillations in the transverse direction, the x-motion of the electron is defined as,

$$x \sim \frac{v_{xA}}{\omega_b}\sin(\int \omega_b dt)$$

$$v_x \sim v_{xA}\cos(\int \omega_b dt)$$

where, ω_b is the betatron oscillation frequency. Hence, Eq. (39) can be written as,

$$\frac{d\gamma}{dz} = -\frac{eA_0 v_{xA}}{2mc^2 v_z}\cos\phi \tag{2.40}$$

$$\frac{d\phi}{dz} = \frac{\omega - \omega_b - kv_z}{v_z} \tag{2.41}$$

where, $\phi = \omega t - \int \omega_b dt - kz + \phi_0$ is the phase of the electron with the laser field and ϕ_0 is the initial phase of the electron. Eq. (2.40) and (2.41) can be written as:

$$\frac{d\gamma}{dz} = -\frac{eA_0 v_{xA}\cos\phi}{2mc^2(\omega - \frac{\omega_{b0}}{\sqrt{\gamma}} - kv_z)} \tag{2.42}$$

Integrating Eq. (2.42),

$$F(\gamma) = -P\sin\phi + c_1 \tag{2.43}$$

where, $$F(\gamma) = \gamma - \eta\sqrt{(1-\alpha_0)\gamma^2 - 1} + \eta\cos^{-1}\frac{1}{\gamma\sqrt{(1-\alpha_0)}} - 2\sqrt{\gamma}\,\frac{\omega_{b0}}{\omega} \tag{2.44}$$

$P = \frac{\alpha_0 v_{xA}}{2c}$, $\alpha_0 = \frac{v_{xA}^2}{2c^2}$ and $c_1 = F(\gamma_0) + P\sin\phi_0$ is the integration constant and γ_0 is the initial value of γ. The expression F (γ) in Eq. (2.44) is a function of γ and η. In Fig. 2.2 we plot F(γ) vs γ for different values of η i.e. for different densities for a fixed a_0=1, α_0=0.3 and ω_{b0}/ω=0.2.

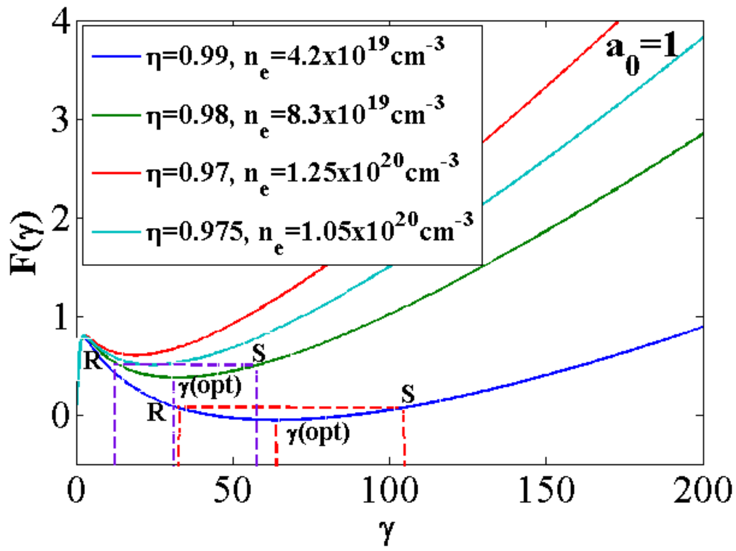

Fig. 2.2: Plot of F (γ) vs γ for different values of η.

The F(γ) vs γ curve at first decreases, attains a minimum value at F = F_{min} at γ = γ_{opt} and then increases which shows that for a single value of F (γ), there will be two values of γ. The separatrix is defined by:

$$F(\gamma) - F_{\min} = P(1 - \sin\phi) \tag{2.45}$$

Fig. 2.3 shows the separatrix plot i.e. γ vs ϕ plot for η=0.99 and a_0=1.

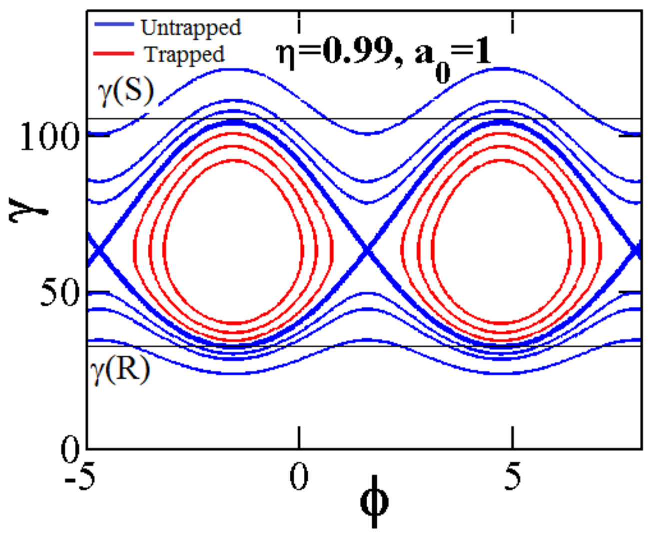

Fig. 2.3: Separatrix (γ vs ϕ) plot

The largest value of the right hand side of Eq. (2.45) is equal to 2P. Therefore, to estimate the maximum energy gain of electrons, a horizontal line is drawn in Fig. 2.2 at a height of 2P from F_{min}, which cuts the $F(\gamma)$ curve at two points, R and S, which corresponds to the bottom and top of the separatrix (Fig. 2.3) respectively. The value at $\gamma = \gamma(S)$ corresponding to the top of the separatrix gives the maximum energy gain of electrons in the laser field. From Fig. 2.2, it is seen that, maximum electron energy increases with increasing η, and it also widens the gap between $\gamma(R)$ and $\gamma(S)$, so that ~~a~~ electrons in the wider range of γ values can be trapped. However, the gap between $\gamma(R)$ and $\gamma(S)$ depends also on 2P i.e., a function of a_0. For a fixed η, the gap increases with increasing a_0 as can be seen from the Fig. 2.4.

The trapping of electrons in the laser field and the subsequent energy gain depends entirely on the phase space evolution of the electrons with respect to the laser field. The cross points of the separatrix occur at $\gamma = \gamma_{opt}$. Fig. 2.3 shows that electrons in the range between $\gamma = \gamma$ (R) and $\gamma = \gamma$ (S) are trapped, however, $\gamma = \gamma_{opt}$ electrons are also trapped and interacts with the laser field for the maximum time period. The probability of trapping or interaction with the laser pulse for $\gamma = \gamma_{opt}$ electrons is maximum which gradually decreases and becomes minimum for $\gamma = \gamma$ (R) and $\gamma = \gamma$ (S) electrons. Electrons with $\gamma > \gamma$ (S) and $\gamma < \gamma$ (R) are too fast and too slow respectively to catch up with the laser pulse and are not trapped and just oscillate in the laser field. Hence, for electrons to be trapped and gain energy from the laser field, a threshold energy or pre-acceleration of the electron is required equal to $\gamma = \gamma$ (R). However, in some particular cases as shown in Fig. 2.5 (b), the experimental conditions are such that, the separatrix on the lower energy side is not complete and γ (R) cannot be defined, consequently, pre-acceleration of electrons for such cases would be appropriate to define at higher energy towards $\gamma = \gamma_{opt}$ instead of $\gamma = \gamma$ (R).

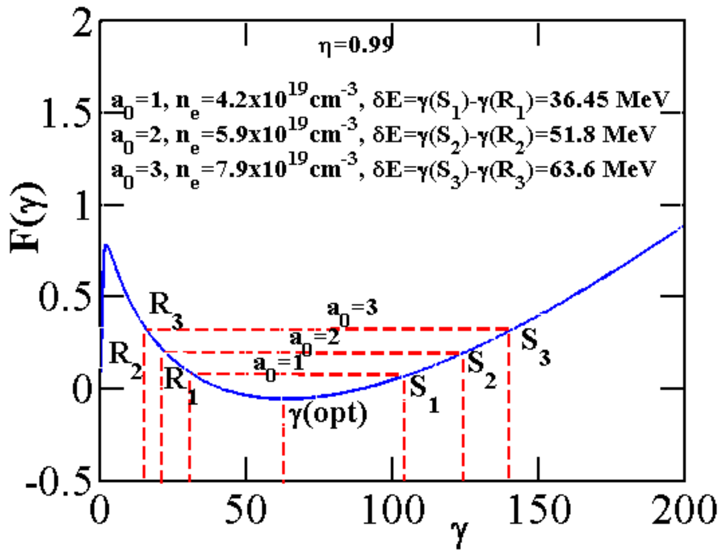

Fig. 2.4: Plot of F (γ) vs γ for fixed values of η but varying a_0 and density.

In Fig. 2.4, we plot F(γ) vs γ for different values of a_0 keeping η constant to study the effect of a_0 on the energy gain, which shows that electron energy gain increases with laser intensity.

Another important parameter affecting the electron interaction with the laser pulse is the laser wavelength (λ) / frequency (ω). In Eq. 2.44, i.e., the F (γ) curve, the dependency of laser frequency on the electron energy gain comes from the ratio of ω_{b0}/ω, given by $\omega_{b0}/\omega{\sim}\gamma^{1/2}(1\text{-}kc/\omega\sqrt{(1\text{-}1/\gamma^2\text{-}v_x^2/c^2)})$ [70]. When the bounce frequency matches with the Doppler shifted laser frequency, the amplitude of oscillation of electrons would grow on successive bounce and hence the electron energy also. For lower energy electrons (γ~1), $\omega_{b0}/\omega{\sim}\gamma$, and for higher energy electrons (γ>>1), $\omega_{b0}/\omega{\sim}\gamma^{1/2}(1\text{-}\eta)$. Hence, resonance is a dynamical phenomena varying with the electron energy. In this regard, using chirped laser pulses would be helpful in maintaining a better quasi-resonance with the drive laser pulse for energy gain through DLA. For the experimental investigations presented in this thesis, positive chirp was found to be favourable for generation of relativistic electron beams.

The above theoretical estimation of the trapping of electrons in the laser field and maximum energy gain has been applied to understand the interaction and acceleration of electrons for the conditions of two experimental reports on DLA by Gahn *et al*. [77] and Mangles *et al.* [76]. Gahn *et al*. [77] observed maximum electron energy of ~12 MeV with quasi-thermal spectra from the interaction of long laser pulse duration of ~200 fs with under dense plasma density of $\sim 2.3\times10^{20}cm^{-3}$, with normalized laser intensity of $a_0=1.42$. Fig. 2.5 (a & b) shows the F (γ) vs γ curve and the separatrix plot for this condition.

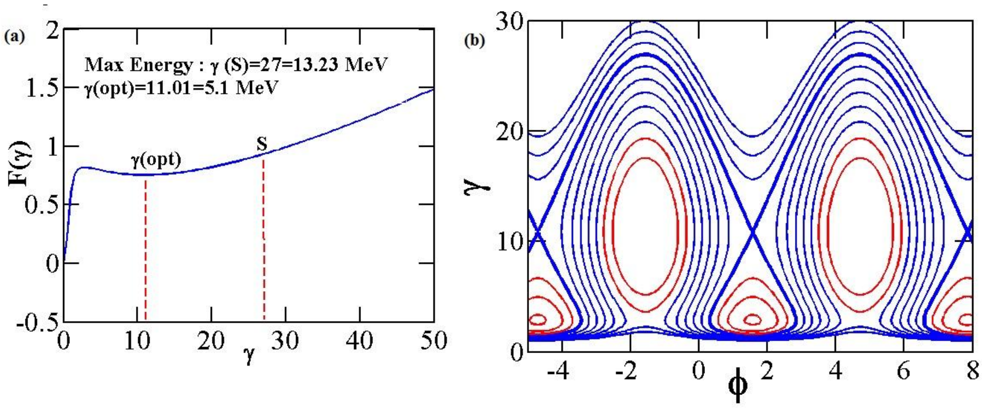

Fig. 2.5: (a) F (γ) vs γ and (b) separatrix plot, for experimental parameters of Gahn et al. [77]

The maximum electron energy estimated from Fig. 2.5 (a), in this case γ(S) ~13 MeV, which very well matches with the experimental observed value of ~12 MeV. However, the curve does not cut the F (γ) curve at the lower energy side i.e., at R, which suggests that although the electrons gain maximum energy, they are not trapped in the lower energy side. This is also obvious from Fig. 2.5 (b), where it is observed that the separatrix is not complete at the bottom suggesting that the electrons cannot catch up with the laser field at the lower energy side and moves out of phase with the laser field. Hence, in this case, experimental conditions are not so favourable for electrons to be completely trapped in the laser field. However, electrons interacts with the laser field in a narrow region in phase, thereby generates small bumps and hence quasi-thermal spectra.

In case of Mangles *et al*. [76], maximum electron energy of ~300 MeV was observed with exponential/ quasi-thermal spectra on interaction of long laser pulse of duration of ~650 fs, a_0~15 interacting with under dense plasma of density of ~7.7×10^{18} cm^{-3}. Fig. 2.6 (a & b) shows the energy gain curve and the separatrix for the above conditions.

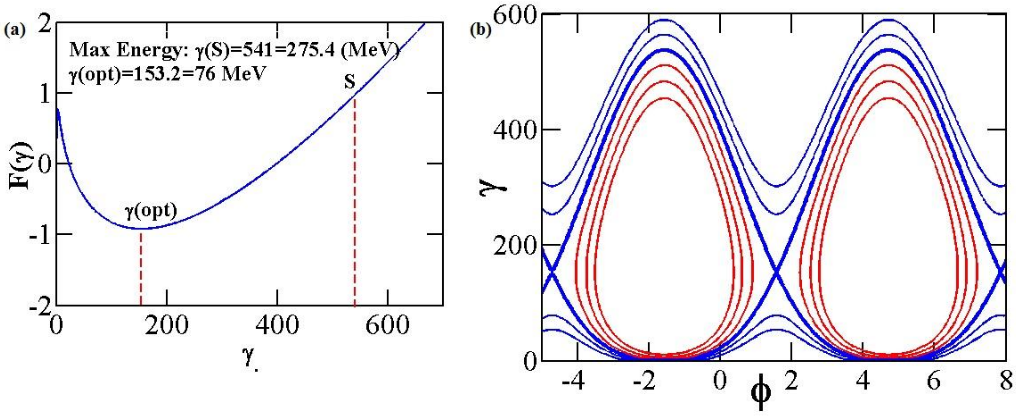

Fig. 2.6: (a) F (γ) vs γ and (b) separatrix plot; For experimental parameters of Mangles et al. [76]

In this case also, the maximum energy gain of electrons estimated (~275 MeV) matches very well with the experimental observed value, however, the conditions are also not so favourable for electrons to be trapped completely in the laser field, they move out of phase from the laser field at the lower energy side. However, compared to the case of Gahn *et al*. [77], the electrons in this case, traverse almost the whole of the phase space and remains trapped in the laser field for a longer time. γ_{opt} in this case is estimated ~76 MeV and it may be pointed out here that the observed spectrum shows a quasi-thermal feature with a prominent bump at ~76 MeV (c/f Fig.1 in Ref. 76).

The above theoretical analysis and its agreement with the reported experimental results validates the theory very well in estimation of maximum electron energy gain in case of DLA and in understanding the trapping dynamics of electrons in the laser field. The two very important parameter governing the interaction is the plasma density and the laser intensity i.e. in turn η. The analysis also shows the importance of the threshold electron energy of γ_{opt} for resonance with the laser field and also remain trapped in phase. This shows that an optimization of the experimental parameter is possible where the electrons will remain trapped in the laser field for the complete phase space cycle to generate good quality electron beams.

Another important parameter apart from η, which plays crucial role gaining transverse energy is the vacuum laser spot radius at focus (r_0). For a Gaussian laser beam, the transverse energy gain of electron is derived as [70]:

$$\gamma_T = \frac{1}{1-\eta^2}\left[-Q\eta + (1+Q^2-\eta^2)^{1/2}\right] \tag{2.46}$$

where,

$$Q = \eta\left[(1+\frac{a_0^2}{2}e^{-x_T^2/r_0^2})^{1/2} - (1+\frac{a_0^2}{2})^{1/2} + \frac{\omega_c \pi r_0}{\omega\eta\lambda}(e^{-x_T^2/r_0^2}-1) - \frac{1}{\eta}\sqrt{\gamma_0^2-1} + \gamma_0\right] \tag{2.47}$$

In Fig. 2.7, we plot the transverse energy gain (γ_T) vs the normalized turning point radius (x_T/r_0), for different values of η, r_0 and a_0.

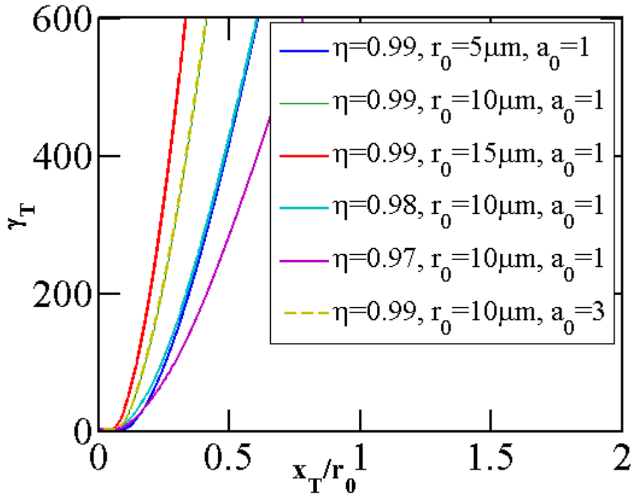

Fig. 2.7: Plot of γ_T vs x_T/r_0

The plot shows that, for fixed η (=0.99) and a_0 (=1), increase spot radius of the laser leads to sharp gain in electron energy from lower x_T values i.e. closer to the channel axis (blue, red and green curve). Although, for fixed η (=0.99) and fixed r_0 (=10 μm), increase in a_0 does not have any significant effect on the transverse energy gain (green curve and yellow dashed curve), but the overall longitudinal energy gain is very much affected by the variation of a_0 as is shown in Fig. 2.4.

Theoretical studies have also been reported on DLA studying the various other aspects that affects the electron interaction with the laser pulse. It was found that the presence of transverse static field in the laser channel helps in significant energy enhancement by reducing the dephasing of electrons with the laser field [78] and thereby longer interaction of electrons with the laser field takes place. Static electric field in the channel can also have a longitudinal component, which also similarly helps in reducing dephasing of electrons with the laser field and hence lead to electron energy enhancement [71]. All the above studies were performed considering linear polarization of the laser pulse along one particular direction, however when the laser polarization is arbitrary then non-linear modulations of the betatron frequency occurs and it has been shown that parametric amplification of the oscillations of electrons can lead to significant energy enhancement of electron compared to the vacuum [79].

From the theoretical discussion above it is clear that, as in the case of wakefield acceleration, in case of DLA mechanism also, the process of electrons remaining in phase with the laser field or dephasing is a very important factor for efficient acceleration of electron in DLA and in turn generating good quality electron beams.

2.3.3. Estimation of dephasing length and rate of dephasing of electrons in DLA:

Dephasing of electron in laser field relevant to DLA regime has not been studied in detail neither theoretically nor experimentally. Theoretical study of dephasing of electrons in laser field and the factors governing it are very crucial. This would lead to control electron interaction with the laser field and in turn control the electron beam properties. So, in this section an expression for estimating the dephasing length of electrons in laser field, which is the length at which electron gains maximum energy is derived. Subsequently rate of dephasing of electron in the laser field is estimated theoretically and its variation with the plasma density is studied.

To proceed, the propagation distance is replaced by the normalized distance given by:

$$\xi = \frac{z\omega}{c}$$

Substituting this in Eq. (2.40) and (2.41), the variation of electron energy gain γ and phase ϕ with the propagation distance ξ is given by:

$$\frac{d\gamma}{d\xi}=-\frac{a_0\sqrt{\alpha_0}}{(1-\alpha_0-\frac{1}{\gamma^2})^{1/2}}\cos\phi \qquad (2.48)$$

$$\frac{d\phi}{d\xi}=\frac{1-\frac{\omega_{b0}}{\omega\sqrt{\gamma}}}{(1-\alpha_0-\frac{1}{\gamma^2})^{1/2}}-\eta \qquad (2.49)$$

Eq. (2.48) and (2.49) represent a set of coupled differential equations. Applying the boundary conditions such that at $\xi=0$, $\gamma_0=1.6$ and $\phi=\pi/2+\Delta$ where $\Delta=0.2$, the coupled differential equation is solved numerically and plot of γ vs z is shown in Fig. 2.8 for $\eta=0.99$ and $a_0=1$.

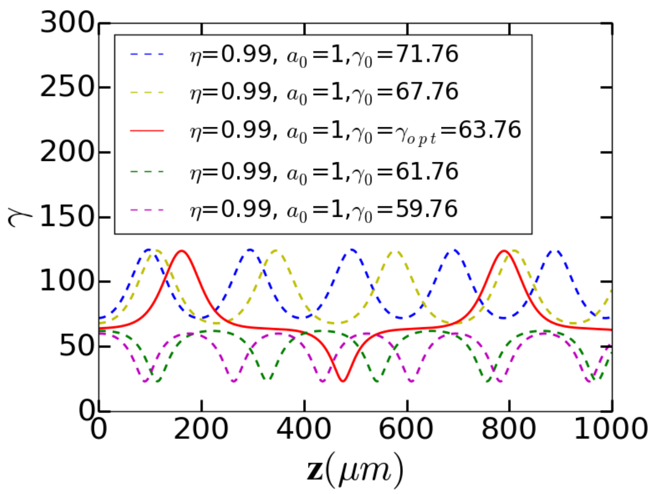

Fig. 2.8: Estimation of dephasing length: Plot of γ vs z

It is clear from the above solution that, electron with $\gamma = \gamma_{opt}$ (red curve), are only trapped, and exchange energy with the laser pulse, whereas electrons with $\gamma > \gamma_{opt}$ (blue and yellow dashed curve) and $\gamma < \gamma_{opt}$ (green and purple dashed curve), the electrons are untrapped and just oscillate with the laser field. Although electrons with $\gamma>\gamma_{opt}$ gain almost similar energy as $\gamma=\gamma_{opt}$ electrons, but these are untrapped electrons therefore not constitute the group of DLA accelerated electrons which in practical conditions keep gaining energy in successive oscillations. In the figure, the trapped electrons complete about one phase space rotation within ~500 μm of propagation. However, the dephasing length corresponds to the length from where the energy gain curve begins to decrease for the case of γ_{opt} electrons. For the present case, it is estimated to be ~175 μm. Beyond this length, the electron looses energy and is said to dephase. However, they do not outrun the laser field, instead they remain trapped in the laser field as they gain and loose energy while oscillating with the positive and negative cycles of the laser electric field.

Next, rate of dephasing (R) is defined as the rate of change of phase ϕ of the electron with time. It has been shown that slower the rate of dephasing of electron with the laser field, longer will be the interaction time and hence maximum energy gain of the electrons will take place [71, 72]. Hence, expression for R can be derived as:

$$R = -\frac{1}{\omega}\frac{d\phi}{d\tau} = -\frac{1}{\omega}\frac{d\phi}{dt}\frac{dt}{d\tau} = -\frac{\gamma}{\omega}\frac{d\phi}{dt} = -\frac{\gamma c}{\omega}\frac{d\phi}{dz} = -\gamma\frac{d\phi}{d\xi}$$

From Eq. (2.49), substituting the value of $\frac{d\phi}{d\xi}$, we obtain,

$$R = -\gamma[\frac{1-\omega_{b0}/\omega\sqrt{\gamma}}{(1-\alpha_0-1/\gamma^2)^{1/2}} - \eta] \qquad (2.50)$$

where, τ is the proper time defined as $d\tau/dt = 1/\gamma$.

The first term of Eq. (2.50) is a γ-dependent term, whereas the second term is a density dependent term for a fixed a_0. So, rate of dephasing of electrons in the laser field is the interplay between the energy gain γ and density. This quantifies rate of dephasing and shows the variation of R as a function of density.

2.3.4. Electron injection and pre-acceleration mechanism in DLA:

Another important aspect in case of DLA is the electron injection mechanism, which has been sparsely addressed. The acceleration process of the electrons in laser created channel is affected by the different initial conditions of the injected electrons [80]. An initial discussion has been made by Arefiev *et al*. [73], where they have also pointed out the need for detailed theoretical modelling for electron injection in case of DLA. In all the above theoretical analysis, electron interaction with the laser pulse was studied considering the electron was initially present in the channel. However, it has been shown that, in steady state plasma channel, apart from the transverse static electric field, presence of longitudinal static electric field have also been observed which persists mostly at the channel entrance [71]. This field arises because of the boundary effect of the coaxial structure of channel with positively charged core and negatively charged shell and does not provide significant acceleration of electron in terms of direct energy gain such as is the case of wakefield acceleration. The longitudinal electric field of the channel helps in continuous injection of electrons at the channel opening [73].

Another probable mechanism of electron injection in DLA has been studied and discussed through the generation of surface wave [81-84]. The cavitated channels created by the steep gradient of the long laser pulse with $P>P_c$, gives rise to the excitation of surface waves at the channel boundaries. Naseri *et al*. [81-84] have shown that, in case of channels formed by laser pulses, the electrons are trapped by the surface waves at the channel boundaries and pre-accelerate them to relativistic energies. Formation of surface waves at the channel boundaries is associated with formation of complicated current loop structures [84, 85]. As the laser pulse interacts with the electrons in the current loops, particularly at the regions where the laser electric field is aligned with the direction of current loop, interacts with the electrons and the radius of gyration of the current loop increases. This leads the current to get pushed more into the channel towards the channel axis where the laser field intensity is high. By this, electrons can be injected into the channel from the channel boundaries and accelerated through DLA [85].

Recently, a detailed theoretical study has been performed on the injection dynamics of the electrons in a laser created channel and has been verified by 3D PIC simulations [86]. As laser pulse enters underdense plasma, it pushes the electrons in the forward direction, leaving the ions back and this excites a longitudinal charge separation. The electric field associated with the charge separation plays a crucial role in the injection of electrons in the channel and modifies the local electric field such that it can guide the electrons present at the channel edges to the channel centre where it can accelerate efficiently through DLA. It was further shown that, the self-generated magnetic field suppresses the injection of electrons into the channel.

DLA has also been considered recently in high Z or mixed gas targets along with ionization induced mechanism [87]. In this case, electrons are ionized within the laser pulse and are trapped within the laser channel itself. This mechanism does not require any additional injection process to trap and accelerate electrons in the laser field.

Once the electrons are injected into the laser channel, for efficient acceleration through DLA, one of the pre-requisite is the pre-acceleration of the electrons to relativistic energies ($\gamma = \gamma_{opt}$) as has been discussed in the previous section. The pre-acceleration of electrons to gain energy up to $\gamma = \gamma_{opt}$ can be achieved in the following ways:

1. Electrons in laser created channel can be trapped and pre-accelerated by wakefield formed in the channel only at the foot of the long laser pulse when it enters the plasma [76, 77, 88, 89], and electrons are accelerated through DLA by the rear of the pulse [89].

2. The surface waves traps electrons at the boundaries and pre-accelerates them to relativistic energies to make them interact with the laser pulse [81-85, 90, 91]. Electrons trapped in the surface wave would gain energy given by

$$\gamma_{SW}^2 = \gamma_L^2 + p_M^2 \tag{2.51}$$

where $\gamma_L^2 = 1+(E_y^{SW})^2/2$ and p_M denotes the maximum normalized electron momentum in the surface wave that corresponds to potential well $\Delta\Phi = \Phi_{max}-\Phi_{min} \sim 2E_x^{SW}/k_{SW}$, where $k_{SW} = 2\pi/\lambda_{SW}$. Here, E_y^{SW} and E_x^{SW} are the transverse and the longitudinal field associated with the surface waves at the channel boundaries and λ_{SW} is the wavelength of oscillations of the surface wave.

3. Another way of gaining pre-acceleration energy is through the mechanism of ionization induced injection by using mixed gas targets [63, 92, 89]. In case of ionization induced injection, the electrons ionized at the peak of the laser pulse gain residual transverse momentum equal to

$$\gamma_\perp = \sqrt{1+u_\perp^2} = \sqrt{1+a_\perp^2(\psi_i)} \tag{2.52}$$

It has been shown through simulations, the gain of electron energy in the transverse direction further helps to be accelerated to the required threshold and get trapped.

References

[1] Multi-photon ionization of atoms, G. Mainfray and G. Manus, *Reports on Progress in Phys*. **54**, 1333 (1991).

[2] Multiphoton ionization of hydrogen and rare gases", P. Agostini, G. Barjot, J. F. Bonnal, G. Mainfray, and C. Manus, *IEEE J. Quant. Elec*, **QE-4**, 667 (1968).

[3] Free-free transitions following 6-photon ionization of xenon atoms", P. Agostini, F. Fabre, G. Mainfray, G. Petite and N. K. Rahman, *Phys. Rev. Lett.*, **42**, 1127, (1979).

[4] Tunnel ionization of complex atoms and of atomic ions in an alternating electromagnetic field, M. V. Ammosov, N. B. Delone, and V. P. Krainov, *Soviet Physics, J. Experimental and Theoretical Phys.* **64**, 1191, (1986).

[5] Multiphoton processes in atoms, N. B. Delone and V. P. Krainov, *Springer Verlag*, *Heidelberg*, 2nd edition, (1994).

[6] Laser Fundamentals, William T. Silfast, Cambridge University Press, (2004)

[7] Defocusing effects of a picosecond tera watt laser pulse in an underdense plasma, T. Auguste, P. Monot, L.-A.Lompré, G. Mainfray, and C. Manus, *Optics Commun*. **89**, 145, (1992).

[8] Focusing limits of a terawatt laser in an underdense plasma, P Monot, T Auguste, L A Lomprè, G Mainfray and C Manus *J. Opt. Soc. Am. B*, **9**, 1579, (1992).

[9] Ionization -induced defocusing of intense laser pulses in high pressure gases, S. C. Rae, *Opt. Communications,* **97,** 25, (1993).

[10] Onset of relativistic self-focusing in high density gas jet targets, R Fedosejeves, X F Wang, and G D Tsakiris *Phys. Rev. E,* **56,** 4615, (1997).

[11] Self-modulation and self-focusing of electromagnetic waves in plasmas, C. E. Max, J. Arons, and A. B. Langdon, *Phys. Rev. Lett.* **33**, 209, (1974).

[12] Relativistic self-focusing of short-pulse radiation beams in plasmas, Sprangle, C.-M. Tang, and E. Esarey, *IEEE Trans. Plasma Sci*. **15**, 145, (1987).

[13] Self-focusing of short intense pulses in plasmas, G.-Z. Sun, E. Ott, Y. C. Lee, and P. Guzdar, *Phys. Fluids* **30**, 526, (1987).

[14] Relativistic focusing and ponderomotive channeling of intense laser beams, B. Hafizi, A. Ting, P. Sprangle, and R. F. Hubbard, *Phys. Rev. E*. **62**, 4120, (2000).

[15] Electron acceleration by a laser wakefield in a relativistically self-guided channel, R. Wagner, S.-Y. Chen, A. Maksimchuk, and D. Umstadter, *Phys. Rev. Lett*. **78**, 3125, (1997).

[16] Plasma wave generation in a self-focused channel of a relativistically intense laser pulse, C. E. Clayton, K. Tzeng, D. Gordon, P. Muggli, W. B. Mori *et al*., *Phys. Rev. Lett*. **81**, 100 (1998).

[17] Effects of pulse duration on self-focusing of ultra-short lasers in underdense plasmas," J. Faure, V. Malka, J.-R.Marqués, P.-G.David, F. Amiranoff *et al*., *Phys. Plasmas* **9**, 756 (2002).

[18] The physics of the nonlinear optics of plasmas at relativistic intensities for short-pulse lasers, W. B. Mori, *IEEE J. Quantum Electron*. **33**, 1942 (1997).

[19] Self-focusing and guiding of short laser pulses in ionizing gases and plasmas, E. Esarey, P. Sprangle, J. Krall, and A. Ting, *IEEE J. Quantum Electron*. **33**, 1879 (1997).

[20] Optics in the relativistic regime, G. A. Mourou, T.Tajima, and S.V. Bulanov, *Rev. Mod. Phys*., **78**, 309, (2006).

[21] Excitation of plasma waves by an electromagnetic wave packet, L. M. Gorbunov, V. I. Kirsanov, *Sov. Phys. JETP*, **66**, 290, (1987).

[22] Laser wakefield acceleration and relativistic optical guiding, P. Sprangle, E. Esarey, A. Ting, and G. Joyce, *Appl. Phys. Lett.* **53**, 2146 (1988).

[23] Nonlinear electron oscillation in a cold plasma, J. M. Dawson, *Phys. Rev.* **113**, 383 (1959).

[24] Laser electron accelerator, T. Tajima and J. M. Dawson, *Phys. Rev. Lett*., **43**, 268 (1979).

[25] Generating multi-GeV electron bunches using single stage laser wakefield acceleration, W. Lu, M. Tzoufras, C. Joshi, F. S. Tsung, W. B. Mori *et al*., *Phys. Rev. ST Accel. Beams* **10,** 061301 (2007).

[26] Theory of wave motion of an electron plasma, Akhiezer, A. I., and R. V. Polovin, Zh. Eksp. Teor.Fiz.30, 1956 (1956).

[27] Nonlinear interaction of intense laser pulses in plasmas, P. Sprangle, , E. Esarey, and A. Ting, *Phys. Rev. A* **41**, 4463 (1990a); Nonlinear theory of intense laser-plasma interactions, P. Sprangle, , E. Esarey, and A. Ting, *Phys. Rev. Lett*. **64**, 2011 (1990b).

[28] Excitation of ultrarelativistic plasma waves by pulse of electromagnetic radiation, S. V. Bulanov, V. I. Kirsanov, and A. S. Sakharov, *JETP Lett*. **50**, 198 (1989).

[29] Relativistic wake-field generation by an intense laser pulse in a plasma, V. I. Berezhiani, and I. G. Murusidze, *Phys. Lett. A* **148**, 338 (1990).

[30] Nonlinear analysis of relativistic harmonic generation by intense lasers in plasmas, E. Esarey, A. Ting, P. Sprangle, D. Umstadter, and X. Liu, *IEEE Trans. Plasma Sci*. **21**, 95 (1993).

[31] Two-dimesional regimes of self-focusing wake field generation and induced focusing of a short intense laser pulse in an underdense laser plasma, S. V Bulanov, F. Pegoraro, and A. M. Pukhov, *Phys. Rev. Lett.* **74**, 710 (1995).

[32] Trapping and acceleration in nonlinear plasma waves, E. Esarey, and M. Pilloff, *Phys. Plasmas* **2**, 1432 (1995).

[33] Comment on Cascade focusing in the beat-wave accelerator, Esarey, E., and A. Ting, *Phys. Rev. Lett*. **65**, 1961 (1990).

[34] Study of laser wakefield acceleration by using particle-in-cell simulation, N. E. Andreev, L. M. Gorbunov, V. I. Kirsanov, A. A. Pogosova, and R. R. Ramazashvili, *Pis'maZh. Eksp. Teor.Fiz*. **55**, 551 (1992).

[35] Self-focusing and Raman scattering of laser pulses in tenuous plasmas, T. M. Antonsen Jr., and P. Mora, *Phys. Rev. Lett.* **69**, 2204 (1992).

[36] Propagation and guiding of intense laser pulses in plasmas, P. Sprangle, E. Esarey, J. Krall, and G. Joyce, *Phys. Rev. Lett*. **69,** 2200 (1992).

[37] Enhanced acceleration in a self-modulated-laser wake-field accelerator, J. Krall, A. Ting, E. Esarey, and P. Sprangle, *Phys. Rev. E* **48**, 2157 (1993).

[38] Raman forward scattering of short-pulse high -intensity lasers, W. B. Mori, C. D. Decker, D. E. Hinkel, and T. Katsouleas, *Phys. Rev. Lett.* **72**, 1482 (1994).

[39] Overview of plasma-based accelerator concepts, E. Esarey, , P. Sprangle, J. Krall, and A. Ting, *IEEE Trans. Plasma Sci*. **24,** 252 (1996).

[40] Laser wakefield acceleration: tje highly non-linear broken-wave regime, A. Pukhov and J. Meyer-ter-Vehn, *Appl. Phys. B: Lasers Opt.***74,** 355 (2002).

[41] Electron cavitation and acceleration in the wake of an ultraintense,self-focused laser pulse, P. Mora, and T. M. Antonsen Jr., *Phys. Rev. E* **53**, R2068 (1996).

[42] A nonlinear theory for multidimensional; relativistic plasma wave wakefields, W. Lu, C. Huang, M. Zhou, M. Tzoufras, F. S. Tsung, W. B. Mori, and T. Katsouleas, *Phys. Plasmas* **13**, 056709 (2006).

[43] Scalings for ultrarelativistic laser plasmas and quasimonoenergetic electrons, S. Gordienko, and A. Pukhov, *Phys. Plasmas* **12,** 043109 (2005).

[44] Nonlinear theory for relativistic plasma wakefields in the blowout regime, W. Lu, C. Huang, M. Zhou, W. B. Mori, and T. Katsouleas, *Phys. Rev. Lett.* **96**, 165002 (2006).

[45] Phenomenological theory of laser-plasma interaction in “bubble” regime, I. Kostyukov, A. Pukhov, and S. Kiselev, *Phys. Plasmas* **11**, 5256 (2004).

[46] Self-focusing of an optical beam in a plasma, T.Kurki-Suonio, P. J. Morrison, and T. Tajima, *Phys. Rev. A* **40**, 3230 (1989).

[47] Trapping dark current and wave breaking in nonlinear plasma waves, C. B. Schroeder, E. Esarey, B. A. Shadwick, and W. P. Leemans, *Phys. Plasmas* **13**, 033103 (2006).

[48] Physics of laser driven plasma based electron accelerators, E. Esarey, C. B. Schroeder, and W. P. Leemans, *Rev. Mod. Phys.*, **81**, 1229 (2009).

[49] Laser plasma accelerators, V. Malka, *Phys. Plasmas*, **19**, 055501 (2012).

[50] Plasma Injection Schemes for Laser–Plasma Accelerators, J. Faure, *CERN Yellow Reports*, **1**, 143 (2016). doi:http://dx.doi.org/10.5170/CERN-2016-001.14

[51] Laser injection of ultrashort electron pulses into wakefield plasma waves, D. Umstadter, J. K. Kim, and E. Dodd, *Phys. Rev. Lett.***76**, 2073 (1996).

[52] Electron trapping from interactions between laser-driven relativistic plasma waves, G. Golovin , W. Yan, Ji Luo, C. Fruhling, D. Haden *et al.*, *Phys. Rev. Lett*. **121**, 104801 (2018).

[53] Electron injection into plasma wakefields by colliding laser pulses, E. Esarey, R. F. Hubbard, W. P. Leemans, A. Ting and P. Sprangle, *Phys. Rev. Lett*. **79**, 2682 (1997).

[54] Laser-driven plasma-based accelerators: Wakefield excitation, channel guiding ,and laser triggered particle injection, W. P. Leemans, P. Volfbeyn, K. Z. Guo, S. Chattopadhyay, C. B. Schroeder *et al.*, *Phys. Plasmas* **5**, 1615 (1998).

[55] Beat wave injection of electrons into plasma waves using two interfering laser pulses, G. Fubiani, E. Esarey, C. B. Schroeder and W. P. Leemans, *Phys. Rev. E,* **70**, 016402 (2004).

[56] Head-on injection of a high quality electron beam by the interaction of two laser pulses, H. Kotaki, S. Masuda, M. Kando, J. K. Koga, and K. Nakajima, *Phys. Plasmas* **11**, 3296 (2004).

[57] Controlled injection and acceleration of electrons in plasma wakefields by colliding laser pulses, J. Faure, C. Rechatin, A. Norlin, A. Lifschitz, Y. Glinec, and V. Malka, *Nature London* **444**, 737 (2006).

[58] Electron trapping and acceleration across a parabolic plasma density profile, J. U. Kim, N. Hafz, and H. Suk, *Phys. Rev. E* **69**, 026409 (2004).

[59] Plasma-density-gradient injection of low-absolute momentum-spread electron bunches, C. G. R. Geddes, K. Nakamura, G. R. Plateau, C. Toth, E. Cormier-Michel, *et al.*, *Phys. Rev. Lett*. **100**, 215004 (2008).

[60] Particle injection into the wave acceleration phase due to nonlinear wake wave breaking, S. Bulanov, N. Naumova, F. Pegoraro, and J. Sakai, *Phys. Rev. E* **58,** R5257 (1998).

[61] Transverse wake wave breaking, S.V. Bulanov, F. Pegoraro, A. M. Pukhov, and A. S. Sakharov, *Phys. Rev. Lett.* **78,** 4205 (1997).

[62] Near-GeV energy laser-wakefield accleration of self-injected electrons in a centimeter-scale plasma channel, F. S. Tsung, R. Narang, W. B. Mori , C. Joshi , R. A. Fonseca *et al*., *Phys. Rev. Lett*. **93** 185002 (2004).

[63] Theory of ionization-induced trapping in laser-plasma accelerators, M. Chen , E. Esarey , C. B. Schoeder , C. G. R. Geddes and W. P. Leemans, *Phys. Plasmas* **19** 033101 (2012).

[64] Measurements of the critical power for self-injection of electrons in a laser wakefield accelerator, D. H. Froula, C. E. Clayton, T. Döppner, K. A. Marsh, C. P. J. Barty, *et al.*, *Phys. Rev. Lett.* **103**, 215006 (2009).

[65] Injection and trapping of tunnel-ionized electrons into laser-produced wakes, A. Pak, K. A. Marsh, S. F. Martins, W. Lu, W. B. Mori *et al.*, *Phys. Rev. Lett*. **104,** 025003 (2010).

[66] Ionization induced trapping in a laser wakefield accelerator, C. McGuffey , A. G. R. Thomas , W. Schumaker , T. Matsuoka *et al*., *Phys. Rev. Lett.* **104,** 025004 (2010).

[67] Dynamics of ionization-induced eletron injection in the high density regime of laser wakefield acceleration, F. G. Desforges, B. S. Paradkar, M. Hansson, J. Ju, L. Senje *et al. Phys. Plasmas* **21,** 120703 (2014).

[68] Generation of 500 MeV–1 GeV energy electrons from laser wakefield acceleration via ionization induced injection using CO_2 mixed He, M. Z. Mo, A. Ali, S. Fourmaux, P. Lassonde, J. C. Kieffer and R. Fedosejeves *Appl. Phys. Lett*. **102,** 134102 (2013).

[69] Self-guided laser wakefield acceleration beyond 1 GeV using ionization-induced injection, C. E. Clayton, J. E. Ralph, F. Albert, R. A. Fonseca, S. H. Glenzer *et al. Phys. Rev. Lett.*, **105,** 105003 (2010).

[70] Laser induced electron acceleration in the presence of static electric and magnetic fields in a plasma, G. D. Tsakiris , C. Gahn, and V. K. Tripathi, *Phys. Plasmas* **7** 3017 (2000).

[71] Generating "superponderomotive" electrons due to a non-wake-field interaction between a laser pulse and a longitudinal electric field, A. P. L. Robinson, A. V. Arefiev and D. Neely, *Phys. Rev. Lett.*, **111,** 065002 (2013).

[72] Beyond the ponderomotive limit: Direct laser acceleration of relativistic electrons in sub-critical plasmas, A. V. Arefiev, V. N. Khudik, A. P. L. Robinson, G. Shvets, L. Willingale *et al.*, *Phys. Plasmas* **23,** 056704 (2016).

[73] Novel aspects of direct laser acceleration of relativistic electrons, A. V. Arefiev, A. P. L. Robinson and V. N. Khudik, *J. Plasma Physics*, **81,** 475810404 (2015).

[74] Relativistic magnetic self-channeling of light in near-critical plasma: three-dimensional particle-in-cell simulation, A. Pukhov and J. Meyer-ter-Vehn, *Phys. Rev. Lett.***76**, 3975 (1996).

[75] Relativistic channeling of a picosecond laser pulse in a near-critical preformed plasma, M. Borghesi, A. J. MacKinnon, L. Barringer, R. Gaillard, L. A. Gizzi *et al., Phys. Rev. Lett.* **78**, 879 (1997).

[76] Electron acceleration in cavitated channels formed by a petawatt laser in low-density plasma, S. P. D. Mangles, B. R. Walton, M. Tzoufras, Z. Najmudin, R. J. Clarke, *et al., Phys. Rev. Lett.* **94**, 245001 (2005).

[77] Multi-MeV electron beam generation by direct laser acceleration in high-density plasma channels, C. Gahn, G. D. Tsakiris, A. Pukhov, J. Meyer-ter-Vehn, G. Pretzler, et al., *Phys. Rev. Lett.* **83**, 4772 (1999).

[78] Enhancement of laser-driven electron acceleration in an ion channel, A. V. Arefiev, V.N. Khudik, and M. Schollmeier, *Phys. Plasmas,* **21**, 033104 (2014).

[79] Parametric Amplification of Laser-Driven Electron Acceleration in Underdense Plasma, A. V. Arefiev, B. N. Breizman, M. Schollmeier, and V. N. Khudik, *Phys. Rev. Lett.*, **108**, 145004 (2012).

[80] Nonlinear parametric resonance of relativistic electrons with a linearly polarized laser pulse in a plasma channel, T. W. Huang, C. T. Zhou, A. P. L. Robinson, B. Qiao, A. V. Arefiev, *et al.*, *Phys. Plasmas*, **24**, 043105 (2017).

[81] Self-channelling of relativistic laser pulses in large-scale underdense plasmas, N. Naseri, S. G. Bochkarev, and W. Rozmus, *Phys. Plasmas*, **17**, 033107 (2010).

[82] Channeling of Relativistic Laser Pulses, Surface Waves, and Electron Acceleration, N. Naseri, D. Pesme, W. Rozmus and K. Popov, *Phys. Rev. Lett.*, **108,** 105001 (2012).

[83] Electron acceleration in cavitated laser produced ion channels, N. Naseri, D. Pesme, and W. Rozmus, *Phys. Plasmas,* **20**, 103121 (2013).

[84] High-Power, Kilojoule Class Laser Channeling in Millimeter-Scale Underdense Plasma, L. Willingale, P. M. Nilson, A. G. R. Thomas, J. Cobble, R. S. Craxton *et al., Phys. Rev. Lett.* **106**, 105002 (2011).

[85] Surface waves and electron acceleration from high-power, kilojoule-class laser interactions with underdense plasma, L.Willingale, A. G. R. Thomas, P.M. Nilson, H. Chen, J. Cobble *et al., New J. Phys*., **15**, 025023 (2013).

[86] Injection dynamics of direct-laser accelerated electrons in a relativistically transparent plasma, K. Jiang, C. T. Zhou, T. W. Huang, C. N. Wu, L. B. Ju, *et al., Phys. Rev. E,* **98**, 033206 (2018).

[87] Role of direct laser acceleration of electrons in a laser wakefield accelerator with ionization injection, J. L. Shaw, N. Lemos, L. D. Amorim, N. Vafaei-Najafabadi , K. A. Marsh, F. S. Tsung, W. B. Mori and C. Joshi, *Phys. Rev. Lett.*, **118,** 064801 (2017).

[88] Particle acceleration in relativistic laser channels, A. Pukhov, Z.-M. Sheng, and J. Meyer-ter-Vehn, *Phys. Plasmas* **6**, 2847 (1999).

[89] Self-modulated laser wakefield accelerators as x-ray sources, N. Lemos, J. L. Martins, F. S. Tsung, J. L. Shaw, K. A. Marsh, F. Albert, B. B. Pollock and C. Joshi, *Plasma Phys. Control. Fusion* **58,** 034018 (2016).

[90] Characteristics of betatron radiation from direct-laser-accelerated electrons, T. W. Huang, A. P. L. Robinson, C. T. Zhou, B. Qiao, B. Liu *et al.*, *Phys. Rev. E*, **93**, 063203 (2016).

[91] Generating overcritical dense relativistic electron beams via self-matching resonance acceleration, B. Liu, H. Y. Wang, J. Liu, L. B. Fu, Y. J. Xu *et al.*, *Phys. Rev. Lett.*, **110**, 045002 (2013).

[92] Synergistic laser-wakefield and direct-laser acceleration in the plasma-bubble regime, X. Zhang, V. N. Khudik, and G. Shvets, *Phys. Rev. Lett.* **114**, 184801 (2015).

[93] Laser wakefield and direct acceleration with ionization injection, X. Zhang, V. N Khudik, A. Pukhov and G. Shvets, *Plasma Phys. Control. Fusion*, **58**, 034011 (2016).

CHAPTER 3

Experimental Equipments and Diagnostics

In this chapter, we will first discuss about the various experimental equipments used during the experiment: laser system, gas-jet targets followed by various diagnostics to detect the electron beams and optical diagnostics to study the laser plasma interaction. All experimental investigations presented in this thesis were performed using 150TW, 25fs, Ti:sapphire laser system at Raja Ramanna Centre for Advanced Technology (RRCAT), Indore, India.

3.1. Ti:sapphire laser system:

It is a Chirped Pulse Amplification (CPA) [1] based 150 TW, 25 fs Ti:sapphire laser system supplied by M/s Amplitude Technologies, France. The system provides laser pulses at a central wavelength of ~800nm. The maximum laser pulse energy is ~3.5J and the minimum laser pulse duration of ~25fs could be achieved. Thus the system provides a maximum peak power of ~140 TW. The system can operate in a single shot mode or in a multiple burst mode with a repetition rate of 5 Hz at full power. However, all experiments were performed in a single shot mode due to limitations of compressor grating distortion, gas load on vacuum system due to firing of the gas-jet and also data acquisition. It consists of a Ti:sapphire oscillator, booster amplifier, a pulse stretcher, a regenerative amplifier, three successive multi-pass amplifiers and a vacuum compressor.

The overall laser system can be divided into three parts, the front end, the high energy multi-pass amplifiers and the vacuum compressor. The overall set up of the laser system is shown in Fig. 3.1. The front end consists of the oscillator, booster, pulse stretcher, regenerative amplifier and the pre-amplifier. The oscillator (‘Synergy’ of M/s Femtolasers) generates a short pulse through 'Kerr lens mode locking' [2] with single pulse energy of ~6 nJ (~500 mW average power with a repetition rate of 76 MHz). The pulse from the oscillator is sent to the booster (pumped by Nd:YAG laser @532 nm: CRF-Ultra) which amplifies the pulse energy up to the µJ level. The pulse is then cleaned by a saturable absorber that removes residual ASE background of the oscillator pulses. Following the booster, the pulse enters stretcher which includes the öffner stretcher [3] and the Dazzler [4]. The Dazzler is used as a phase modulator that compensates for dispersion and phase distortions introduced throughout the laser system. The pulse then enters the regenerative amplifier unit which is pumped by Nd: YAG laser @ 532 nm (CFR Ultra). The pulse energy in this stage is increased to few mJ levels where a gain of order of 10^3 is obtained. For achieving ultra-short pulse duration (below 25 fs) an optional Acousto-Optic Programmable Gain Control Filter (AOPGCF) or "Mazzler" by M/s Fastlite, USA [4] is added into the regenerative amplifier cavity. The purpose of this device is to enlarge spectrum. The larger is the output spectrum, the shorter the compressed pulse duration can be achieved after amplification.The pulse then enters the pre-amplifier stage which is a multi-pass amplifier pumped by Nd: YAG laser @ 532 nm (CFR 200). The laser energy at the end of the front end is 30 mJ with laser pulse duration of 800 ps.

The high energy multi-pass amplifier stage consists of the amplifier-2 and amplifier-3 stages. The amplifier-2 is pumped by Nd: YAG laser @ 532 nm (pro-pulse laser) with 1.6 J. The laser energy after this stage is ~400 mJ. Following this, the pulse enters the final amplifier stage (amplifier 3) which is pumped by four Nd: YAG laser @ 532 nm (Titan lasers) where the laser pulse makes four passes through the Ti:sapphire crystal. The laser pulse energy after the final amplification stage is ~5.5 J with laser pulse duration of 800 ps. Due to the high average power of the pump beams the third amplifier is cryogenically cooled. The amplified beam is extracted out of the amplifier and sent to the laser pulse compressor through the polarizer and half-wave plate based attenuator (for energy variation) and beam expanders.

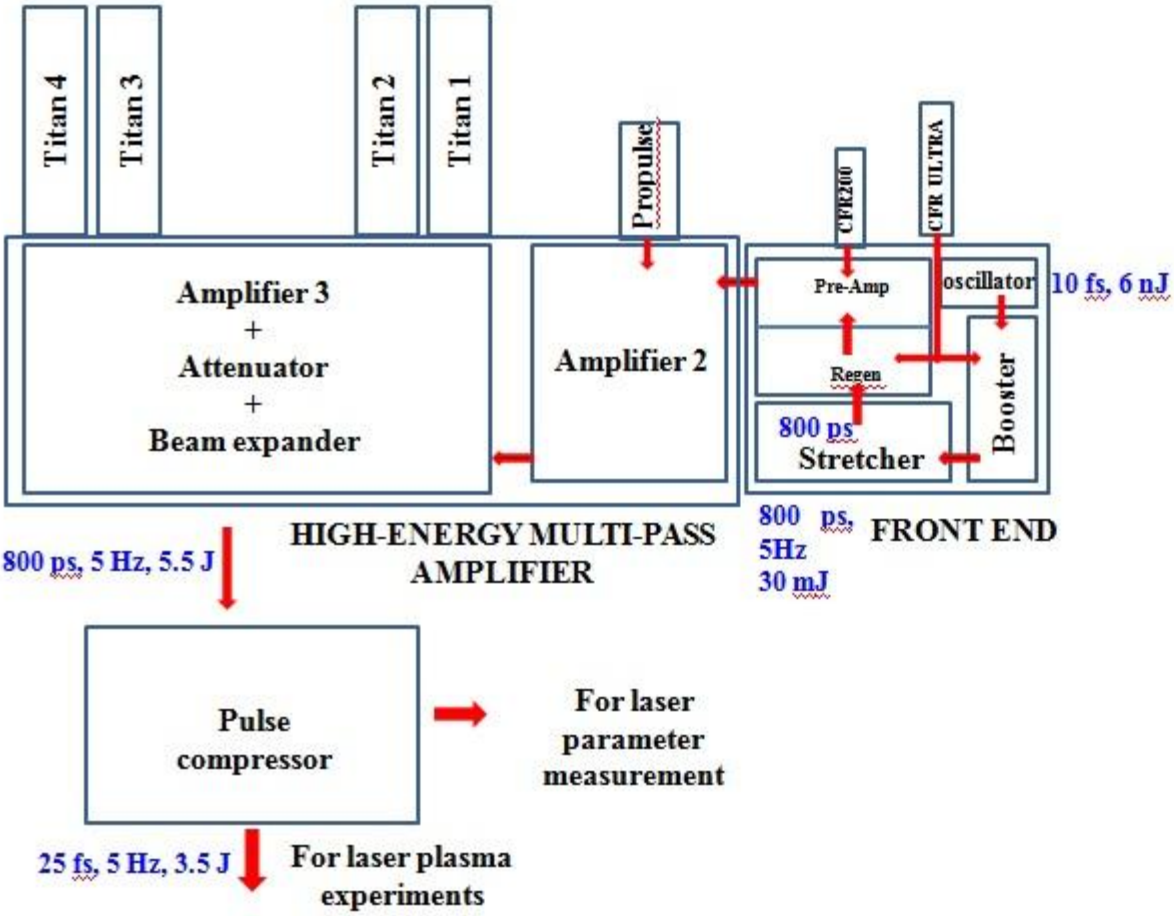

Fig. 3.1: Scheme of the 150 TW, 25 fs Ti:sapphire laser system

The third unit is the pulse compressor chamber where the stretched laser pulse is compressed back to the short pulse duration. It consists of a geometry with 4 gratings having a grove density of 1480 lines/mm and retro mirrors. At optimum conditions, minimum pulse duration of ~25fs is achieved, and by adjusting the grating separation laser pulse duration could be increased as per requirement. However, as the grating separation is increased it introduces negative chirp to the pulse and when decreased it introduces positive chirp.

A photograph of the Ti:sapphire laser system with different components is shown Fig. 3.2 (a & b) and the parameters of the laser are summarized in Table 3.1.

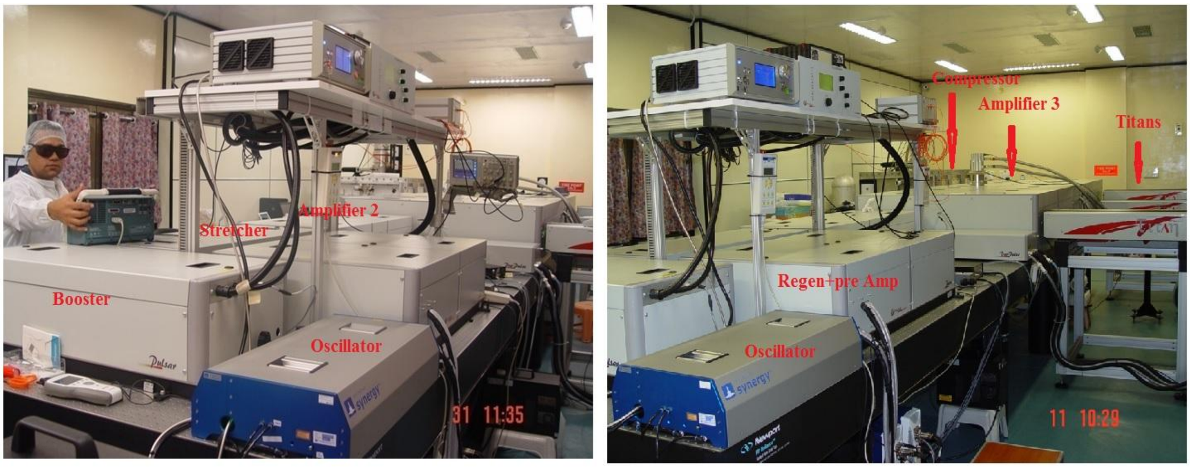

Fig. 3.2: Pictures of 150 TW, 25 fs Ti:sapphire laser system at RRCAT, Indore. (a) Shows oscillator, booster, stretcher and amplifier-2 and (b) shows regenerative amplifier, pre-amplifier, amplifier-3 pumped by Titans and the compressor chamber.

Table 3.1: 150 TW, 25 fs, Ti:sapphire laser parameters

150 TW Ti:sapphire laser pulse parameters	
Maximum laser energy (Compressed pulse)	~3.75 J
Shortest pulse duration	~25 fs
Peak Power	~150 TW
Central wavelength	~800 nm
Bandwidth	~70 nm
ASE	~10^{-9} at 1 ns
Pre-pulse contrast ratio	~10-^{7} at 11 ns

3.2. Measurement of laser parameters:

Since the laser plasma interaction process largely depends on the laser parameters, hence its measurement and characterization are very crucial. In the following we describe various laser parameters measurements relevant to the presented experimental investigations.

3.2.1 Laser Beam profile:

CPA based high power laser systems are prone to various distortions in the laser beam spatial profile as it passes through various optics in different stages of its propagation. Hence, the laser beam profile deviates from the ideal Gaussian or flat top profile. Laser beam profile at various stages of the system is recorded using CCD camera and also through burn pattern on photographic paper which was generally used after final amplifier at full energy. A typical laser beam profile recorded on CCD camera after pre-amplifier is shown in Fig. 3.3.

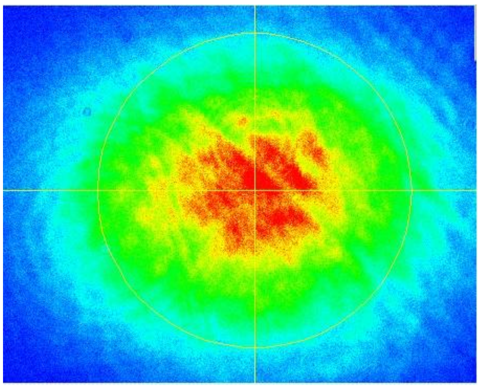

Fig. 3.3: Typical laser beam profile after amplifier-2

3.2.2. Laser energy:

Laser energy after the final amplifier was measured regularly using an energy meter (pyroelectric sensor-Gentec Model: Maestro-224443). During the experiments, typically maximum laser energy used after final amplifier was approximately 4.8 J.

With 70% of the laser energy transmitted through the compressor unit the maximum laser energy used at the target was approximately 3.36 J.

3.2.3. Laser pulse duration:

Laser pulse duration is an important parameter in high intensity laser plasma interactions. The laser pulse duration in high power laser systems is governed by the spectral width, the larger the bandwidth the shorter will be the laser pulse duration. In CPA based laser systems where the pulse is stretched in time, and after several stages of amplification it passes through various optical devices accumulatinghigher order non-linearities corresponding to positive chirp. Hence, the phase content of the pulse is modified which affects the laser pulse duration. Finally, in the compressor chamber, where the laser pulse is compressed again to the shortest pulse duration, the phase non-linearities is exactly compensated by the gratings of the compressor chamber by introducing equal negative chirp to the laser pulse. Also, during the experiment, the laser pulse duration variation studies were performed where longer laser pulse duration were used. This was achieved by varying the grating separation ofthecompressor, such that the phase non-linearities are not exactly compensated. So, calibration between the grating separation and the laser pulse duration is an important parameter.

The pulse duration was measured using a femtosecond single shot second order auto correlator [5]. The auto-correlation set up was installed in a single compact unit and named Bonzai [6] and was provided by the supplier with the laser system. The laser light from the compressor chamber window was put into the Bonzai for the laser pulse duration measurement and by changing the grating separation, the auto-correlation signal is measured. To measure the dispersion introduced by the compressor chamber window, separate measurement were performed including the glass window and also without the glass window. It was found that, with glass window in path, an additional 200 μm of grating separation was required to compensate for the phase non-linearities. A typical signal recorded by the auto-correlator is shown in Fig. 3.4 showing recording of the shortest laser pulse duration of ~24 fs which corresponds to the optimum compressor gratings separation.

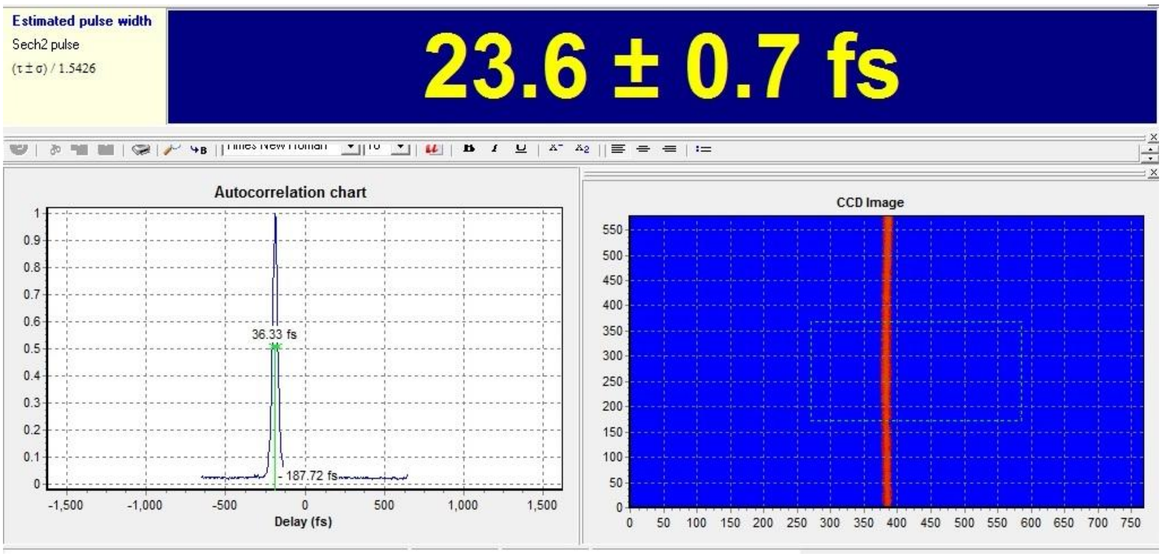

Fig. 3.4: Second order auto-correlator trace for pulse duration measurement.

Further, measurements were performed by varying the grating separation both in the positive and the negative directions from the compressor zero position to obtains variation in laser pulse duration. In Fig. 3.5, we show a calibration of the laser pulse duration with the grating separation. The offset of ~200 μm is due to the presence of compressor chamber glass window in the beam path during laser pulse duration measurement.

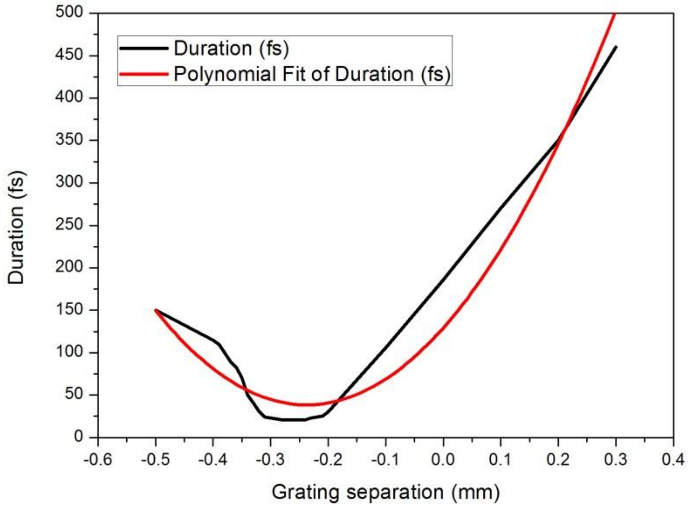

Fig. 3.5: Variation of laser pulse duration with grating separation

3.2.4. Measurement of laser pre-pulse contrast:

In high power laser systems, prior to the main laser pulse, some additional pre-pulse arises which are generated from the leakage of the polarizer of the regenerative amplifier or from the improper seeding of the pulse into the regenerative amplifier. There are two main pre-pulses that occur at the ns time scale prior to the main laser pulse: one is the Amplified Spontaneous Emission (ASE) which comes at 1 ns before the main laser pulse and the other is the pre-pulse contrast ratio which comes at 11 ns before the main laser pulse. The temporal purity of the laser pulse is defined by the intensity ratio of the ASE and the pre-pulse with respect to the main laser pulse. The measurement of these two parameters prior to experiments is very essential as it may lead to formation of pre-plasma and affect the overall laser plasma interaction. The ns pre-pulses were measured using a fast photodiode with 0.8 ns rise time on a 500 MHz digital oscilloscope (Tektronix TDS 3054B). The intensity ratio of the pre-pulse at 11 ns was found to be 10^{-7} and the ASE contrast ratio at 1 ns was 10^{-9}. This shows that in our case, the pre-pulse and ASE contrast peak intensities are much below the main laser intensity and hence will not affect the laser plasma interaction. Further, a third order auto-correlator 'Sequoia" developed by M/s Amplitude Technologies, France [7] was also used to measure the laser pulse contrast close to the peak of the main laser pulse. A typical Sequoia trace is shown in Fig. 3.6.

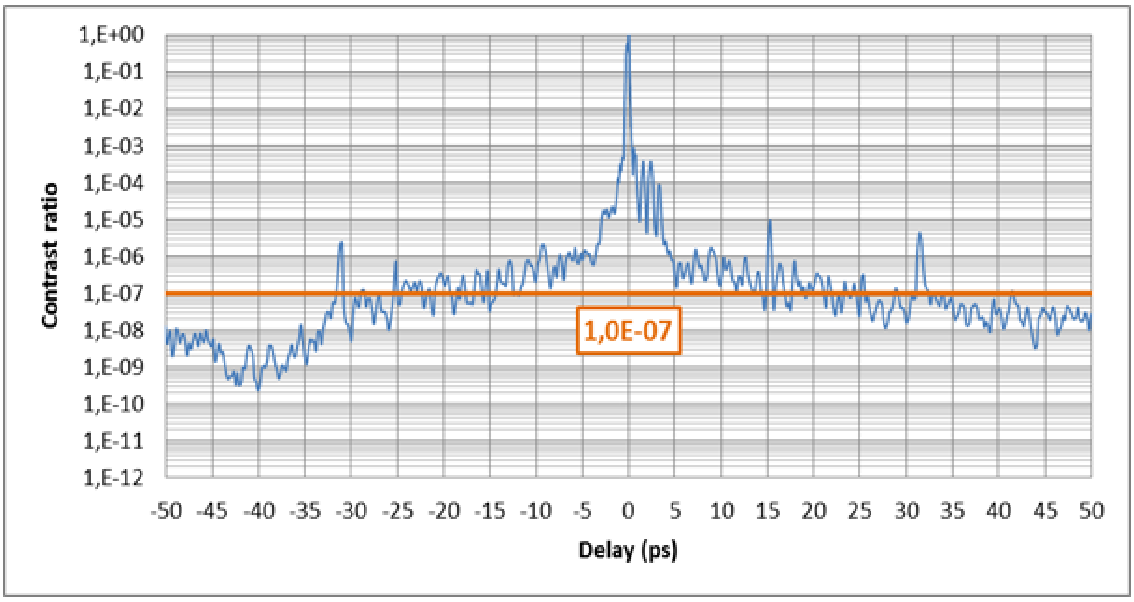

Fig. 3.6: Third order auto-correlator trace of measurement of contrast ratio close to peak of main laser pulse.

3.2.5. Measurement of laser focal spot:

The laser pulse was focused using the off-axis parabolic mirror (OAP). Two types of OAPs were used of same focal length (f) of 50cm: one with dielectric coated and the other with gold coated. The laser beam size on the OAP was ~100 mm, providing an imaging optics of f/5. The imaging system consists of a microscope objective lens of magnification 10X or 40X and the magnified focal spot was recorded on a 14 bit Pixelfly CCD camera mounted on a XYZ translational stage such that the focal spot size can be scanned in the direction of laser beam propagation and also for its alignment on the CCD centre. In order to protect the CCD camera from damage from the high intensity of the focused laser pulse, suitable neutral density (ND) filters were used to attenuate the light intensity. Fig. 3.7 shows the schematic of the setup for the laser focal spot measurement.

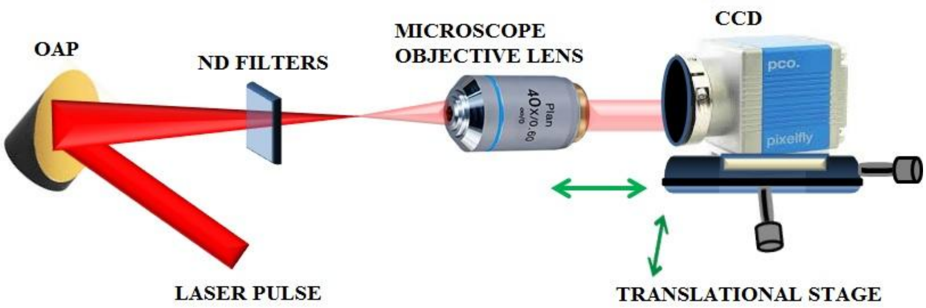

Fig. 3.7: Set up for laser focal spot measurement

Fig. 3.8 shows typical laser focal spot recorded with 10X magnification and the corresponding lineouts of the focal spot in the horizontal and vertical directions respectively. The focal spot in Fig. 3.8 (a), obtained with gold-coated OAP, was estimated to be ~25×12 μm along the horizontal and vertical directions respectively ($1/e^2$radius i.e. ω_0 equals to ~21.2 ×10.16 μm^2) and that in Fig. 3.8 (d), obtained with dielectric-coated OAP is ~7.7×11μm ($1/e^2$radius i.e. ω_0 equals to 6.5×9.3μm^2).

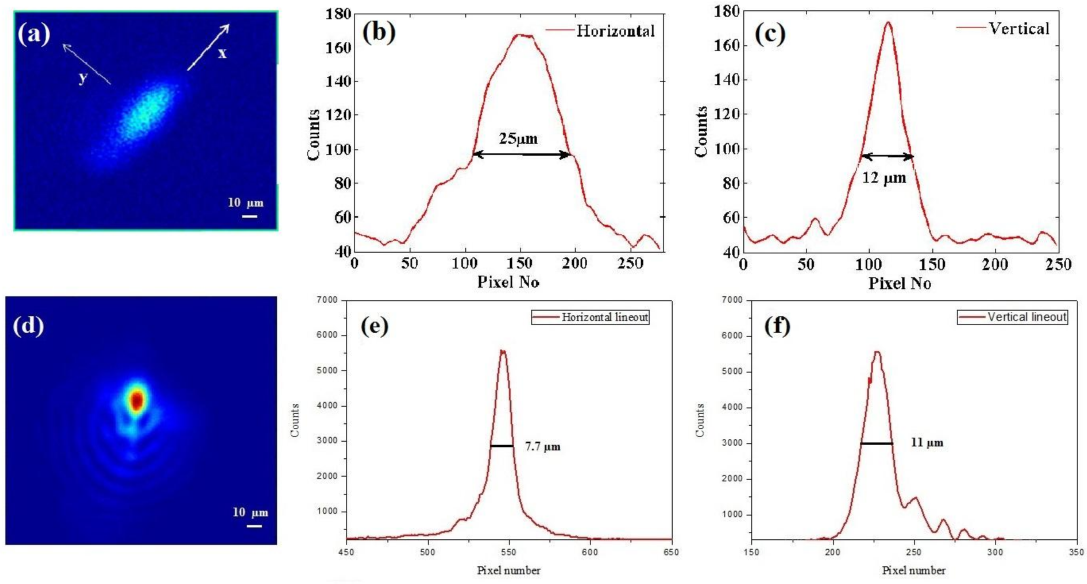

Fig. 3.8: Typical laser focal spot recorded during the experiment (a) 25µm×12µm, (b & c) is the corresponding horizontal and vertical lineout, (d) 7.7µm×11µm, (e & f) is the corresponding horizontal and vertical lineout.

Along with the laser focal spot, the energy content inside the focal spot of $1/e^2$ (ω_0) radius was also estimated from the ratio of the integrated pixel counts under the focal spot of diameter $2\omega_0$ and the overall image area. It was estimated that ~50% and ~40% of total energy is contained in the $1/e^2$ focal spot for the particular spot shown in Fig. 3.8 (a) and (d) respectively. Improvement in the focal spot in the second case (Fig. 3.8-d) could be attributed to use of better quality dielectric coated OAP and also better laser alignment and optimization of grating alignment in the compressor.

3.3. Gas-jet system and characterization:

The plasma target used in laser driven electron acceleration experiments were created using different gas medium of He and various high Z gases such as N_2, Ar and mixed gas targets of He + varying percent of N_2, and N_2 + varying percent of He. The whole gas jet system comprises of the supersonic gas jet nozzle for shock free high pressure gas flow and the gas line system using electronic regulators for precisely control of the backing pressure.

The gas jet system used for the experiments is a shockwave free supersonic gas jet system (M/s Smartshell Co. Ltd., Japan) comprises of three major components viz. asupersonic slit nozzle, high-speed solenoid valve, and fast pulsed valve driver. The systemuses a Laval type slit nozzle. Two different gas-jet nozzle were used during the experiments: one with dimensions of 10mm×1.2mm and second with dimensions of 4 mm×1.2 mm to produce highly localized high density gas jet with uniform gas density. Laser was propagated along the 1.2 mm and 4 mm length of the nozzle respectively. Fig. 3.9 (a) shows a view of the nozzle and Fig. 3.9 (b) shows the gas-jet mounted in the experimental chamber along withsolenoid valve and the gas-line connected to it. The gas jet operation can be precisely synchronized with laser pulses or signals from other devices. Such synchronization was obtained through a delay generator (M/s Stanford Research Systems, Model: DG535). The delay generator can generate number of independent delay pulses using the laser trigger pulse which arrives before the main laser pulse for triggering different diagnostics units. The response time of the solenoid valve for full opening is ~4.5 ms and hence, the trigger timing was set such that the gas-jet is opened ~5 ms before the main laser pulse. The gas jet was operated in single shot mode synchronised with the laser pulse.

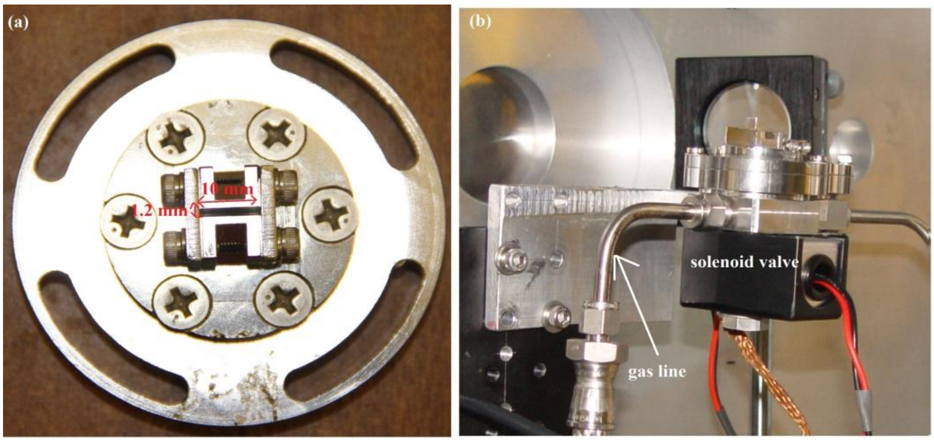

Fig. 3.9: Pictures of gas-jet target system (a) Rectangular gas jet nozzle, (b) Mounted gas-jet with solenoid valve and gas-line connection

For precise adjustment of the backing gas pressure, a high pressure gas line was set up from 150TW laser control room to the radiation shielded experiment room. The gas line includedgas cylinder, needle valves, exhausts valves, 2 electronic gas regulators, 2 reservoir gas cylinders of volume 1litre each and 1 reservoir gas cylinder of volume 250 ml, 3 digital pressure sensors with electronic displays. Digital pressure sensors were used tomonitor the backing gas pressure of the line after the main cylinder, after the two 1litre cylinders and third one just before the entry of the experimental chamber. Scheme of the gas line set up is shown in Fig 3.10. The main gas cylinders are fitted with manual regulators. Manual gas regulators were used to control gas pressure which, has two analog displays of which one shows cylinder pressure and another one shows gas release pressure. Electronic regulators have a large range (0.1 bar to 70 bar) to control gas pressure with a resolution of 0.1 bar. These regulators were operated by DC power supplies. Two electronic regulators were used in the line: the first one to precisely fill in the two large 1 litre cylinders from the main gas cylinder and the second one to precisely fill in the small 250 ml cylinder before the experimental chamber from the 1litre cylinders. By this process, mixing of two gases were done very accurately in the initial two 1 liter cylinders and the mixed gas was finally send to the final small 250 ml cylinder from where the backing gas pressure into the experimental chambers were precisely controlled through electronic regulator. The backing pressure of the gas jet was varied to change the density of the gas jet.

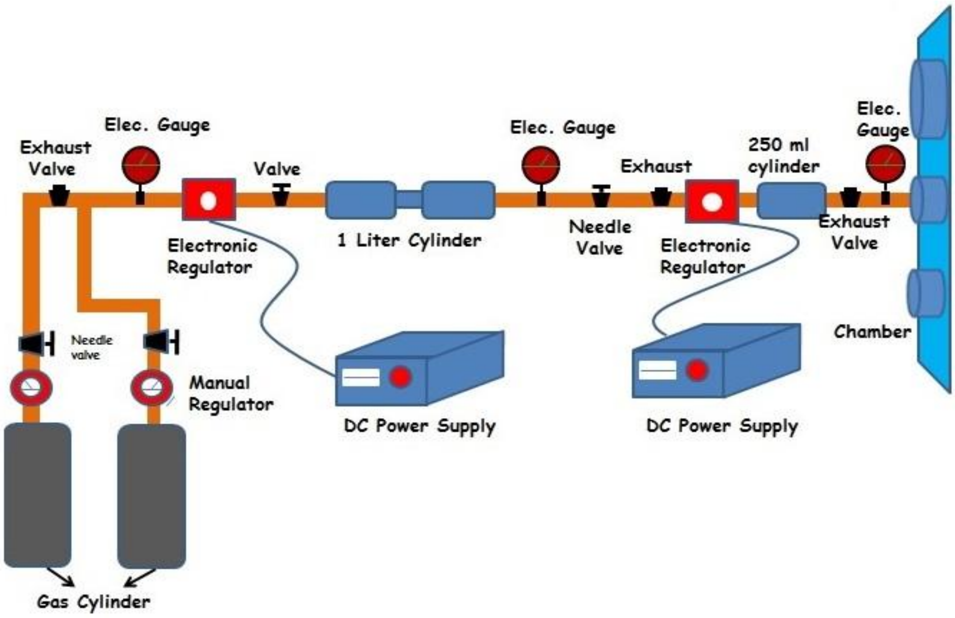

Fig. 3.10: Scheme of the gas-line set up

The gas jet was well characterized using interferometry [9]. The density data was further confirmed from the forward Raman scattering measurements [10]. The plasma density profile shows sharp boundary between vacuum and gas-jet forming a ramp structure at the rising and falling edge and a plateau structure in the middle. Also, characterization of the rectangular nozzle was also performed using offline Mach Zehnder interferometry. The schematic of the set up used is shown in Fig.3.11.

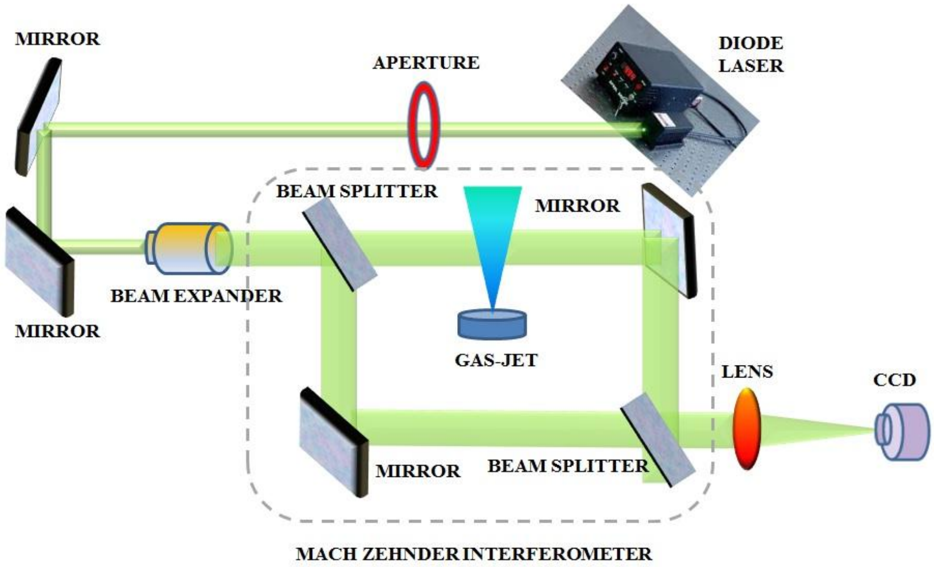

Fig. 3.11: Schematic of the interferometry set up used for gas-jet characterization

The experiment was performed using diode laser (M/s: Laserglow Technologies, wavelength, 532 nm, Max. power output: <5mW). Fringes were generated due to the interference from the two arms of the Mach Zehnder separated by 50%-50% beam splitter and when one of the arm was passed through the gas-jet, fringe shift was observed due to the path difference of the laser in traversing the gas medium. For recording the fringe shift, the gas-jet plane was imaged onto a CCD camera with a magnification of ~1X. Two different gas-jets of dimension 10 mm × 1.2 mm and 4 mm ×1.2 mm was characterized for different gas targets of He, N_2 and Ar over a range of backing pressures varying from 0.5 bar to 55 bar. Separate fringe shift data was recorded for laser pulse propagation along 1.2 mm and 4 mm length of the nozzle. The phase shift generated due to the path difference of the laser beam was retrieved by Fourier transform of the fringe shift, and finally the density values were estimated through tomography, as the nozzles used were rectangular in shape withasymmetric geometry. The data analysis was performed using the software

"IDEA" [11]. Fig. 3.12 (a & b) shows typical fringe shift of the laser recorded while traversing along 4 mm length of the nozzle for two different gas pressures of 10 bar and 20 bar in case of N_2 gas target and Fig. 3.12 (c & d) shows the corresponding phase space diagram.

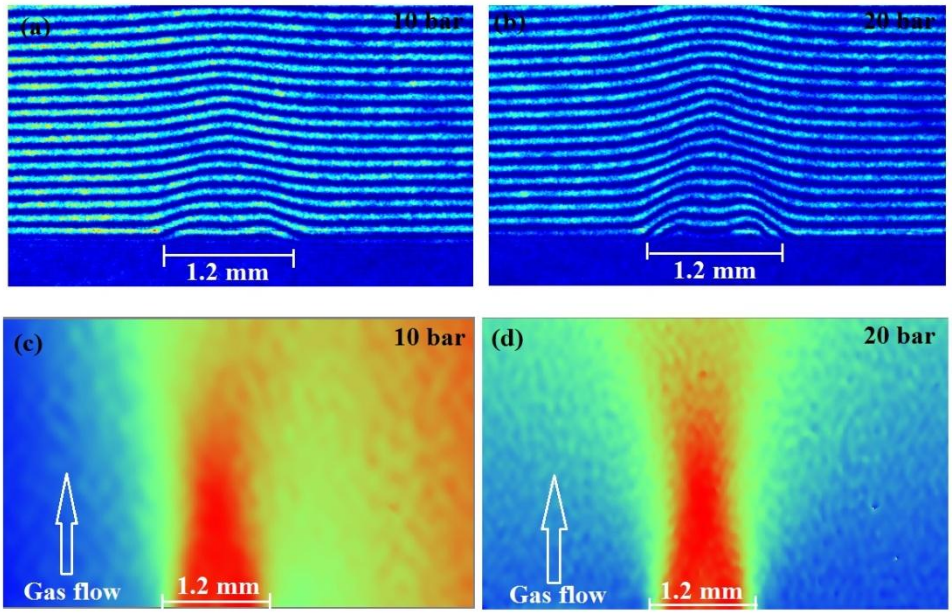

Fig. 3.12: Interferrograms recorded for N_2 gas-jet target: Fringe shift at (a) 10 bar pressure, (b) 20 bar pressure, and corresponding phase space diagram for (c) 10 bar and (d) 20 bar respectively.

The calibration of gas density vs the backing pressure for N_2 gas target is shown in Fig. 3.13 and the result was compared with the calibration provided by the manufacturer and was found to be consistent. Plasma electron density was estimated in a given experimental conditions by multiplying the neutral gas density by expected charge state of the gas medium used. In LPA, in general threshold density is defined as the plasma electron density at which generation of relativistic electrons is first observed for given conditions. In the present studies also, electron beam generation was studied with varying gas-pressure (plasma density), and threshold density is considered at the point where the probability of generation of electron beams in each shot was significant and was found to be closer/slightly higher than the density at which generation was first observed.

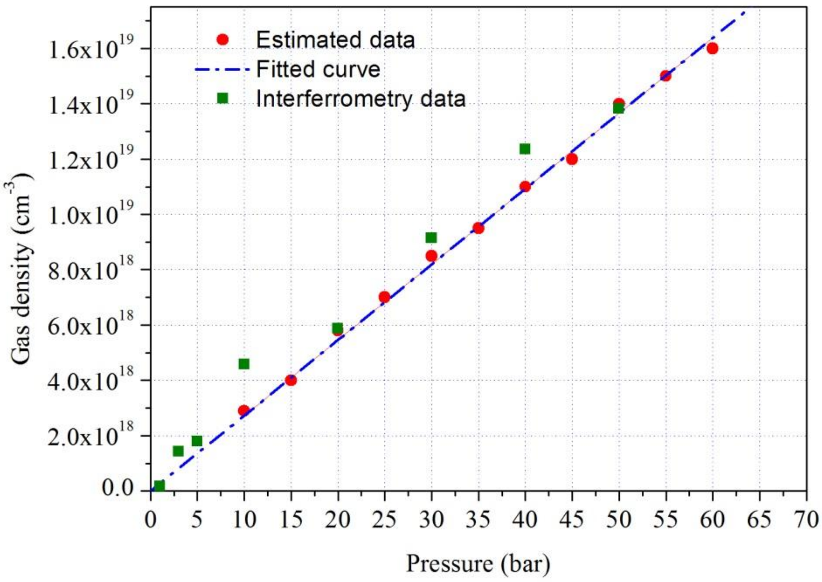

Fig. 3.13: Calibration of gas density vs backing pressure for N_2 gas-jet target. Red dots show the estimated data obtained from manufacture, blue dashed line shows the fitted linear curve and the green square shows the data obtained from interferometry measurements.

3.4. Electron beam diagnostics:

A schematic of the typical laser wakefield experimental set up is shown in Fig. 3.14. High intense ultra-short Ti:sapphire laser is generally focussed at the gas jet. Interaction of laser pulses with underdense gas jet plasma generates relativistic electrons in the forward propagation direction of the laser pulse propagation. Detection and characterization of different properties of these electron beams such as electron beam energy, electron beam charge, transverse profile etc. are required.

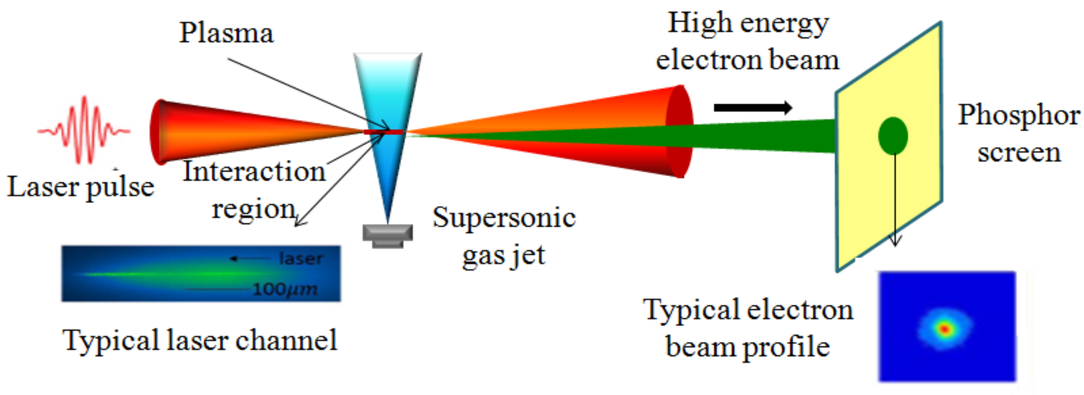

Fig. 3.14: A typical scheme of LPA experiment.

3.4.1. Scintillation screens:

Generally, scintillation screens are used to detect the electron beam profile of the accelerated electrons as these provide for a non-destructive method for recording electron beam profile. Two types of scintillation screens are mostly used. They are the imaging plates (IPs) [12] and the phosphor screens [13]. The typical layer structure of IP and phosphors is shown in Table-3.2 below.

Table-3.2: Layer structure of IP and phosphor screen

Structure of IP	**Structure of phosphor screen**
Protective layer	Supporting layer
Phosphor layer	Phosphor layer (Gd_2O_2S:Tb)
Supporting layer	Plastic layer
Magnetic layer	

Imaging plates (IPs) are made of scintillating material namely barium fluoro-bromide (BaFBr) doped with Eu^{+2}. When relativistic electron beams is incident on IP, it excites the electrons of the scintillating material to a higher energy states. Generally, the scintillating materials are chosen such that the decay time of de-excitation of electrons is long and thus the IP is able to hold the information for a longer time. To extract the information, the IP is illuminated by an external laser source such the electrons are de-excited and emit florescence. This is known as photo-stimulated luminescence (PSL) effect. The IPs are scanned by commercially available IP readers CR 35 Bio of M/s Durr Medical, Australia [14], which is used for data extraction from IPs. The main disadvantage of IP is its single shot usage due to large decay time. Resolution achieved using IP is of the range of tens of microns. The response curve for IP shows constant sensitivity to the incident electron energy beyond 1 MeV [15], suggesting that the emission intensity is proportional to electron flux and independent of their energy.

Nowadays, another type of scintillating screen is generally used called phosphor screens to detect electron beam profiles. Various types of phosphor materials are used, and among them the most effective is the P43 (Gadolinium Oxysulfide with impurity of Terbium, Gd_2O_2S: Tb) which is in the powder form. The phosphor laser remains embedded within a supporting layer and a plastic layer. The phosphor material emits green light with wavelength around 550 nm, with a decay time of 2ms. The plastic layer faces the incident electron beams as the emitted visible light would get absorbed in the plastic layer. Depending on the different thickness of the phosphor material and the phosphor density, there are different types of phosphor screen available commercially. Table-3.3 below shows the details of the different types of phosphor screen. The sensitivity of all the phosphor screens shows saturation for incident electron energies beyond 1 MeV [16].

Table-3.3: Different type of phosphor screens, their corresponding thickness and density

Phosphor Screen Type	Thickness (μm)	Density (gm/cm^3)
Lanex Regular	380	4.25
Lanex Fine	377	3.80
DRZ-High	504	4.67

3.4.2. Magnetic spectrograph:

Magnetic spectrographs are used in LPA experiments for recording of electron beam spectra (electron beam energy) by dispersing the electrons by a suitable magnet. This is a standard method for measuring energy of any charged particle which makes use of the magnetic field to deflect the charged particles. When electron enters in the uniform magnetic field its path is deflected due to effect of the Lorenz force which is given by:

$$F= -e\ (v \times B)$$

Here e is the charge of the electron, v is the velocity of the electron and B is the magnetic field. The spectrograph allows to measure the momentum (velocity) of the electron beam by measuring angle of deflection in the magnetic field. This requires the beam position both at entrance and at exit of the magnet and so the angle introduced by the magnetic field can be estimated.

During the experiment, two types of magnetic spectrographs were used. One is by using a circular magnet with peak magnetic field of ~0.45 T, diameter of 5 cm and pole gap of 9 mm (Fig. 3.15-a). The magnetic material consists of NdFeB.

This magnetic spectrograph was used for detection of low energy electron in the range of 10-60 MeV with resolution of ~34% at 30 MeV and ~67% at 60 MeV (for 10 mrad beam). In order to define the entry angle of the electrons into the magnet a small aperture of 10 mm diameter was placed in front of the magnet, which makes an acceptance of angle of ~36 mrad at the entrance of the magnet as shown in Fig. 3.15 (b). In Fig. 3.15 (c) the magnetic field profile for the circular dipole magnet is shown. Since the magnet dimension was small it was placed inside the plasma vacuum chamber during the experiment. A metallic flag was placed at the centre of the magnet, to mark the undeflected position of the electron beams on the phosphor.

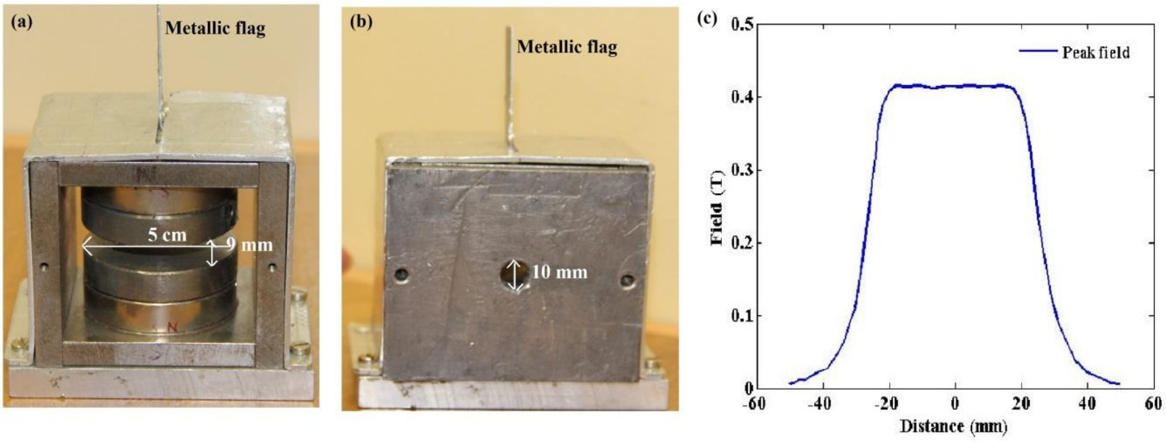

Fig. 3.15: (a) A picture of circular dipole magnet (front surface) (b) Circular aperture before magnet, (c) Field profile with peak magnetic field of 0.45 T.

For higher energy electrons, another magnetic spectrograph was used. It consists of a C-shaped rectangular magnet with peak magnetic field strength of ~0.9 T (dimensions 10×10×20 cm: pole gap 15 mm) covering a broad energy rangeof ~15 MeV to 1 GeV, with a resolution of ~8% at 100 MeV and 25% at 300 MeV (for 10 mrad divergence beam) (Fig. 3.16-a). Fig. 3.16 (b) shows the rectangular magnet and its field profile with peak magnetic field of ~0.9T

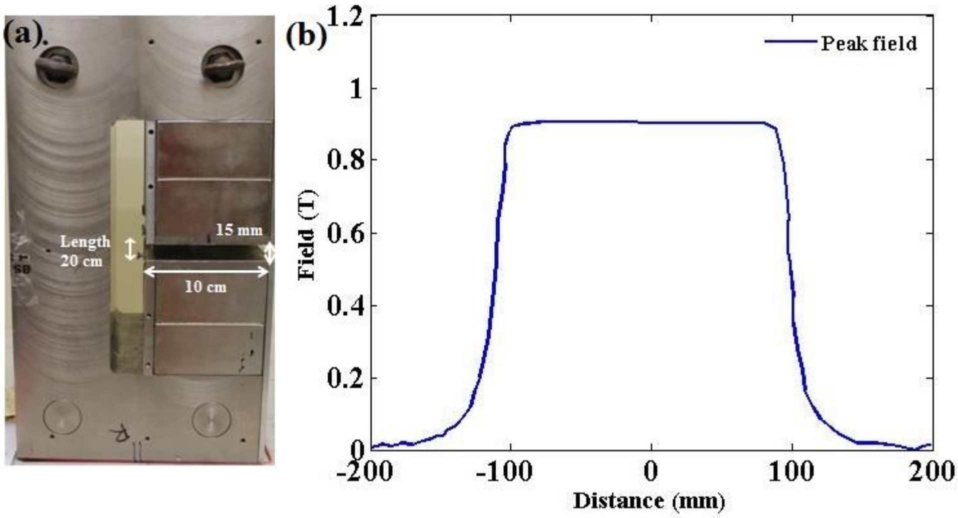

Fig. 3.16: (a) A picture of rectangular permanent dipole magnet (b) Field profile along 20cm length with peak magnetic field of 0.9 T.

The magnet dimension was comparatively larger than the circular magnet and was also comparatively much bulky. So, the whole magnetic spectrograph was placed outside of the plasma vacuum chamber during the experiment and electron beams were taken out of the chamber through a 54 μm thick Ti foil. In this case, no aperture was used before the magnet to define its entry angle. However, to mark the undeflected path, electron beam position was recorded by placing two phosphor screens along the electron beam path at two different distances from the gas-jet target without magnet in path. The correlation between the position of the electrons on the first and second phosphor gives the information of direction of electron beam pointing and hence mark as the zero position of the magnet from where deflection of electrons was estimated. Fig. 3.17 shows the set up for detection of the undeflected path of the magnet and the correlation of the electron beam position at the two phosphors.

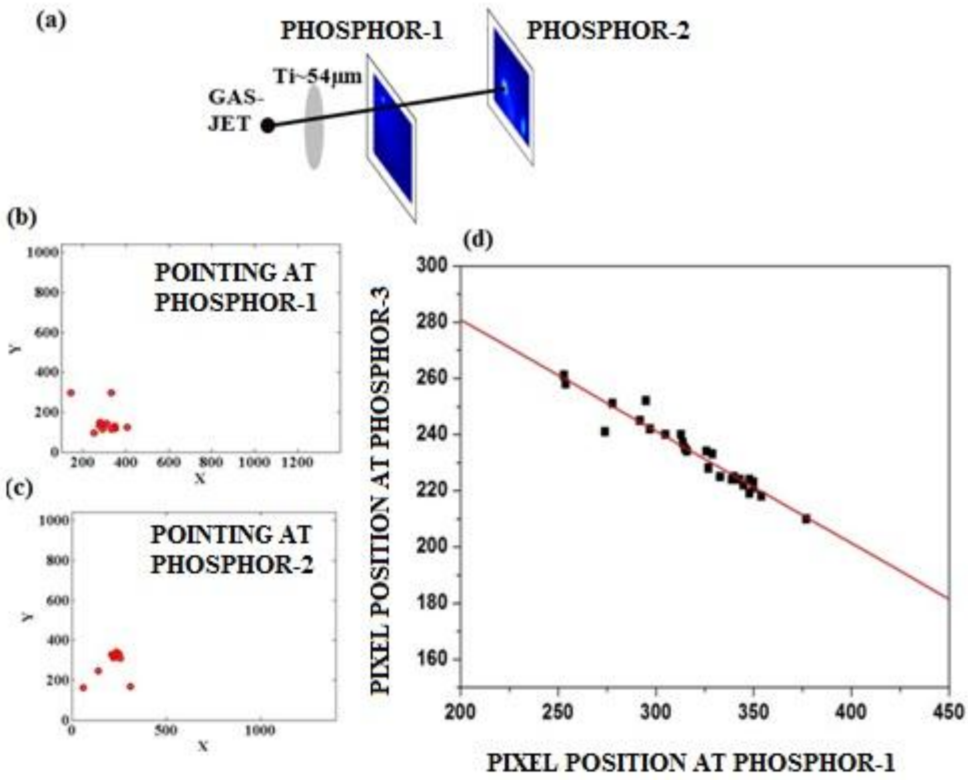

Fig. 3.17: (a) Schematic of estimation for undeflected electron position on phosphor-2, (b) Electron beam pointing at phosphor-1, (c) Electron beam pointing at phosphor-2, (d) Correlation between electron beam positions on phosphor-1 and phosphor-2.

For correlation of the electron energy with the deflection distance of electrons from the undeflected position, the equation of motion of the electron beam trajectory in a magnetic field was derived separately for the circular and the rectangular magnet. In case of the circular magnet, the schematic of the electron beam trajectory is shown in Fig. 3.18 (a). The electron enters the magnetic field of radius 'r' at the point A along x-direction andexits the magnet at the point C. Due to the magnetic field, the trajectory of the electron is deflected by an angle θ and the arc AC shows the trajectory of the deflected electron beam. The arc makes a radius ‘ρ’ with center of a larger circle from P. The electron strikes the phosphor at a distance 'y' from the undeflected position. The phosphor is placed at a distance of ‘x’ from the exit of the magnet such that the distance between the magnet entrance and the phosphor screen is ‘x+2r’. From the geometry, the deflection is given by,

$$tan\theta = \frac{y}{x} \rightarrow y = x\,tan\theta$$

$$tan\theta = \frac{2r\rho}{\rho^2 - r^2} \tag{3.1}$$

Experimentally, we can measure 'r','x' and 'y' and calculate ρ. The radius ρ is related to the energy of electron by,

$$p = Be\rho E = \left[(pc)^2 + (m_0c^2)^2\right]^{1/2} \tag{3.2}$$

Resolution of a magnetic system is mainly limited by the divergence of the electron beam and is given by,

$$R_{es} = \frac{\delta y}{dx/dE} \tag{3.3}$$

Where, δy is the beam size along the dispersive plane and dx/dE is the slope of the dispersion curve.

Eq. (3.1) shows the dispersion relation for the circular dipole magnet and Fig. 3.18 (b) shows the dispersion curve for a typical case of magnet to phosphor distance of 5 cm. The resolution of the magnetic spectrograph for the range of electron energy for a typical electron beam divergence of 10 mrad is shown in the inset of Fig. 3.18 (b).

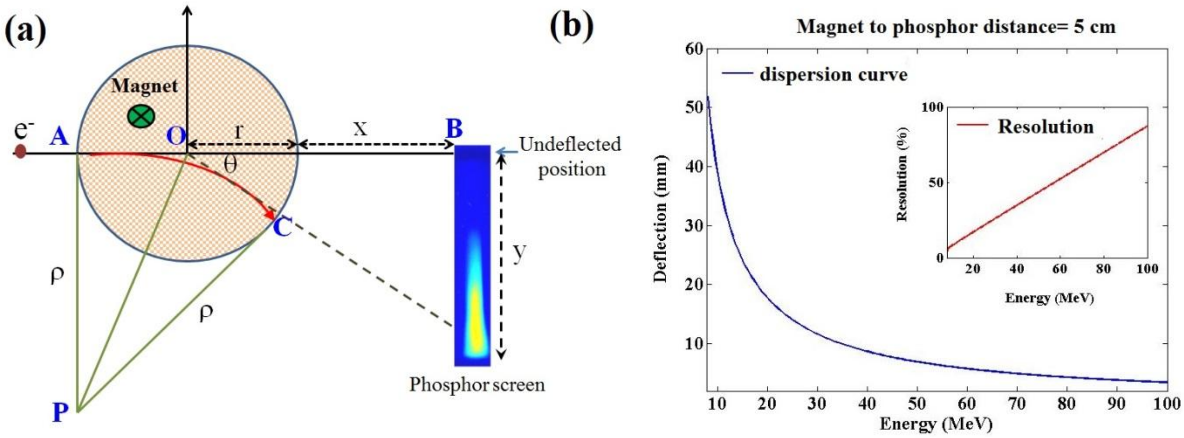

Fig. 3.18: (a) Electron trajectory in circular dipole magnet, (b) Dispersion curve of electron for magnet to phosphor distance of 5 cm (inset: resolution of measurement at various energies)

In case of the C-shaped rectangular magnet, the trajectory for electrons was derived for two different configurations: the front configuration in which the electrons are deflected along the dispersive plane in the forward direction of laser propagation and the side configuration in which the electrons are deflected in the perpendicular direction to the laser propagation. In case of the front configuration, the electrons traverse the whole length of the magnet. The schematic of the electron trajectory is shown in Fig. 3.19 (a). Electron enters the magnet from the position A, and traverse the whole length of the magnet (L_m), and exits out of the magnet at the point C. The phosphor is placed at a distance of D_p from the exit of the magnet. The undefected position of the electron on the phosphor is B. Due to the magnetic field, the electron trajectory is deflected by angle θ and the electron trajectory represents an arc AC of a circle of radius R with centre at O. The deflection 'y' on the phosphor is given by

$$y = (Lm + Dp) \times \tan\theta \tag{3.4}$$

Where $tan\theta = \frac{\sqrt{R^2 - (R - y_m)^2}}{R - y_m}$

y_m is the distance between the point of entry of the electron in the magnet and the edge along the magnet width, and for electron with energy E, moving in magnetic field B, R is given by;

$$R(m) = \frac{E(MeV)}{0.3\times10^8 \times B(T)} \tag{3.5}$$

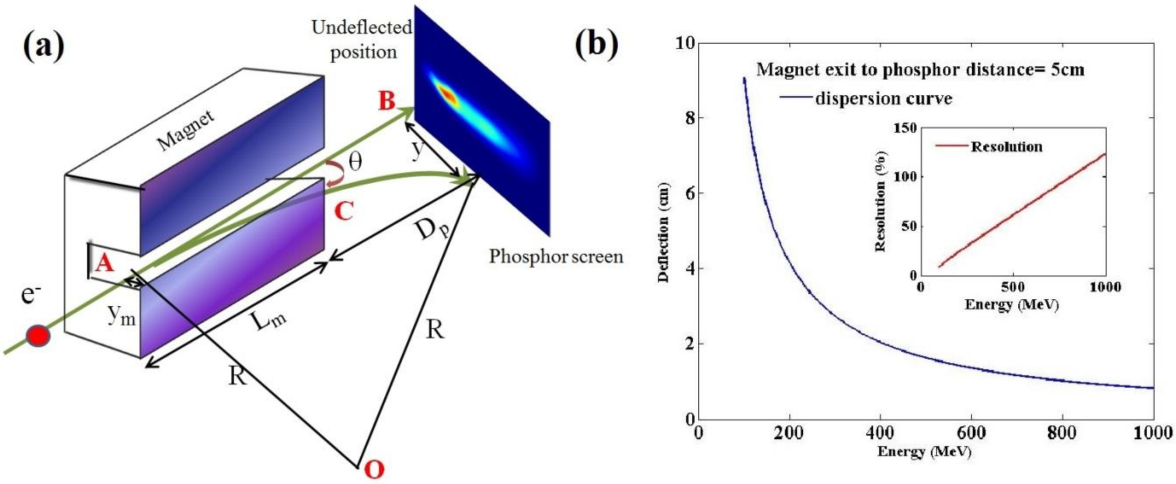

Fig. 3.19: (a) Electron trajectory in C-shaped rectangular dipole magnet along the front configuration, (b) Dispersion curve of electron for magnet to phosphor distance of 5 cm (inset: resolution of measurement at various energies)

Eq. (3.4) gives the dispersion relation of the electron moving along the front configuration and the dispersion curve for a typical value of magnet exit to phosphor distance (D_p) of 5 cm is shown in Fig. 3.19 (b). The corresponding resolution of the magnetic spectrograph is shown in the inset of Fig. 3.19 (b). In this configuration, high energy electrons beyond 80 MeV were dispersed and detected on the phosphor screen and the electron energy decreases with increase in deflection distance.

However, electrons with low energy are deflected before covering the whole length of the magnet and are dispersed along the side direction perpendicular to the laser propagation direction. For the side configuration, the undeflected position of the electron on phosphor (B) is considered the edge of the magnet and electrons deflected less than 90° are deflected less and electrons with deflection greater than 90° are deflected more. The schematic of the electron trajectory is shown in Fig. 3.20 (a).

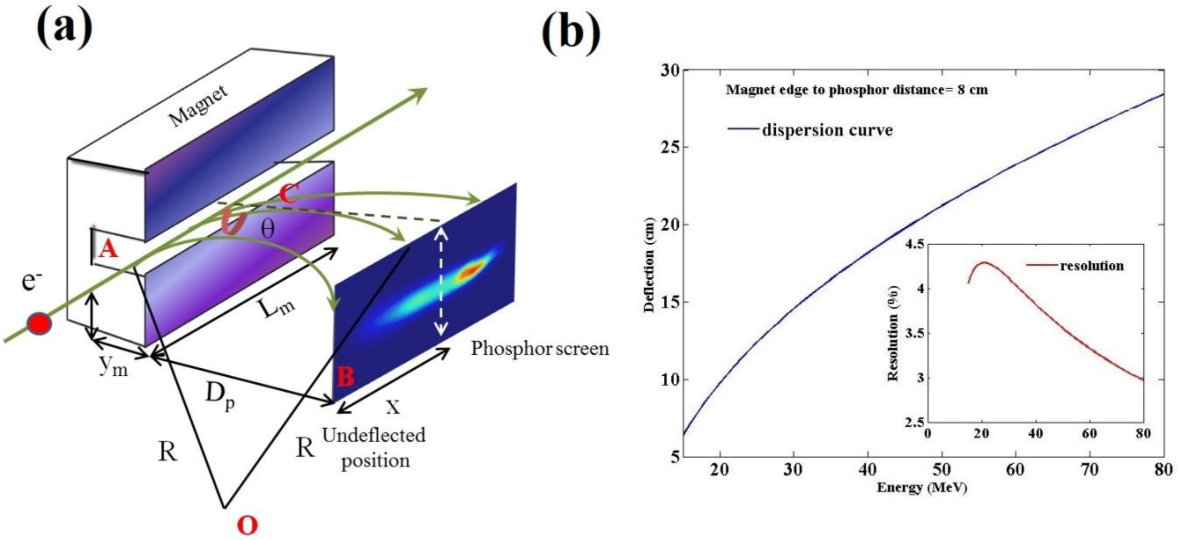

Fig. 3.20: (a) Electron trajectory in C-shaped rectangular dipole magnet along the side configuration, (b) Dispersion curve of electron for magnet to phosphor distance of 8 cm (inset: resolution of measurement at various energies)

The deflection ‘x’ on the phosphor is given by

$$x = D_p \times tan\,\theta \tag{3.6}$$

The dispersion curve for the side configuration is shown in Fig. 3.20 (b) for a typical magnet edge to phosphor distance (D_p) of 8 cm. In this case, the electron energy increases with the increase in deflection of the electron beam from the undeflected position. Resolution of the spectrograph is shown in the inset of Fig. 3.20 (b).

In order to cover the broad range of energy spectrum, detector screens are kept placed both in the side direction which covers energy range from ~15-80 MeV and in the front of the magnet which covers a energy range of ~80 MeV to 1GeV. Fig. 3.21 (a) shows the overall scheme broadband magnetic spectrograph and Fig. 3.21 (b) shows a corresponding picture of the experimental set up. This provided the simultaneous recording of the electron beam profile at the first phosphor (phosphor-1) and the electron beam spectra at the second phosphor (phosphor-2).

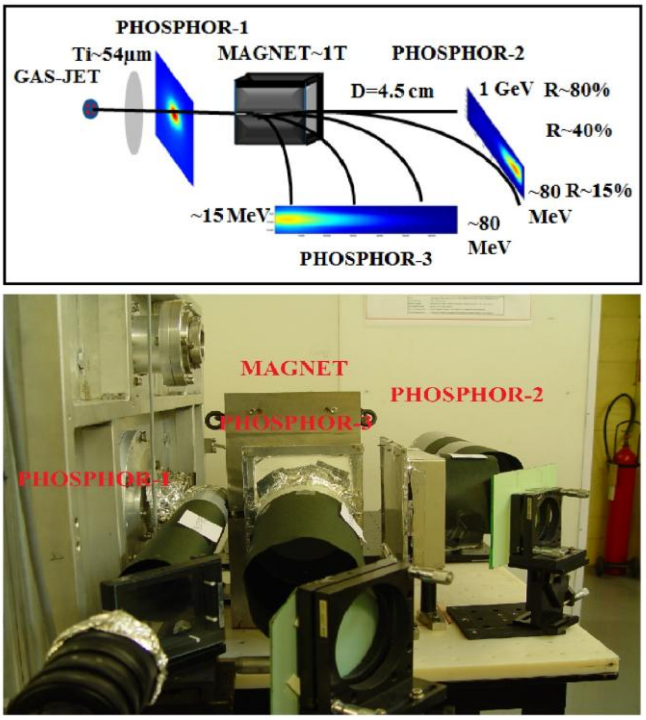

Fig. 3.21: (a) Overall scheme of broad band magnetic spectrograph and (b) A picture of the experimental set up of electron spectrograph used outside vacuum chamber.

GEANT4 [17] simulations were performed to estimate the divergence introduced by various phosphor screen for a range of incident electron energy [18, 19]. For simulation a monoenergetic parallel collimated electron beam i.e. zero initial divergence, and 10^6 number of particles was considered [19]. For electron energy in the range of 1-700 MeV, the divergence introduced by various phosphor screens were found to be in good agreement with the earlier report [20]. The results showed that, compared to other, the divergence introduced by DRZ-high was higher. Therefore, during the experiments, Lanex regular screen (phosphor-1) was kept before the magnet for the detection of electron beam profile. Also, estimation of increase in the electron beam divergence and energy depositions in the various components of the electron beam path such as Ti foil, 36 μm Al foil, phosphor-1 was made through GEANT4 simulation for a 150 MeV electron beam and shown in Table-3.4. This shows that electron undergo negligible modification in divergence due to Ti foil, however, since Lanex (Phosphor-1) consists of a dense material the electron beam divergence is increased by ~10 mrad. But the energy loss of the electron beam is negligible while passing through the various components. Simulations were also performed considering electron beam of 5 mrad divergence, and a quasi-monoenergetic spectrum with peak energy of 150 MeV and standard deviation energy of ~30 MeV, and observed divergences of electron beam profiles at positions of Lanex (phosphor-1) and DRZ (phosphor-2) were found to be similar to that recorded experimentally [19,20]. This study has been made prior to the experiment; hence, during investigation spectrum was not checked with and without this screen as this screen was required to simultaneously record electron beam profile, which was also used to find out undeflected beam position on the DRZ screen.

Table-3.4: Estimation of divergence and energy loss by different components in electron beam path using GEANT4 simulations. Incident electron beam energy:150 MeV

Components in beam path	Introduced Divergence (mrad)	Energy (keV) Loss
Ti foil	~2	Few hundreds of keV
36 μm Al foil	~1	
Lanex	~10	

3.4.3. Measurement of electron beam charge:

In laser plasma accelerator, electron beam charge can be generally measured by two ways. One of the ways, is by using Integrating Current Transformer (ICT) and the other way is by calibration of the phosphor screen used for detection of electron beam profile. The schematic of use of ICT and the electron beam diagnostic set up using phosphor screens in the experiments carried out is shown in Fig. 3.22 (1).

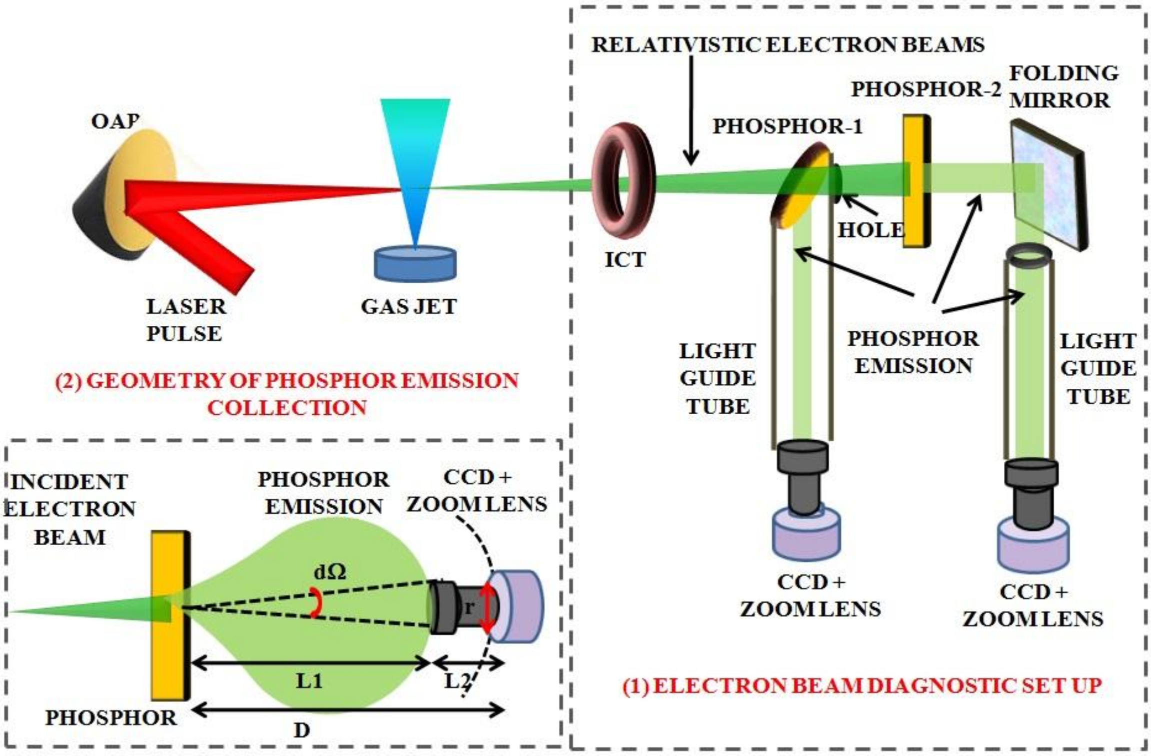

Fig.3.22: (1) Electron beam diagnostics set up and (2) geometry of phosphor emission collection

The ICT used in the present experiment was from M/s: Bergoz Model: ICT-082-070-5: l. It consists of a primary capacitive circuit coupled to a secondary circuit. When an electron beam passes through the ICT, the charge gets stored in the capacitor of the ICT. Through electromagnetic induction, the charge is dissipated in the secondary coil. The voltage associated with the current in the secondary was measured with a 500 MHz oscilloscope using 50 ohm termination resistance to match the impedance of the BNC cable with the input impedance of the oscilloscope so that maximum energy can be transferred. The area under the output pulse gives the total charge of the electron bunch using sensitivity calibration of ICT provided by the manufacturer. During the experiment, the ICT was placed after the gas-jet nozzle (Fig. 3.22-1). As a result, the output signal of the ICT corresponds to the all the electrons contained within the accelerated beam. It has been suggested that the ICT over estimates the electron beam charge [21]. Also, there are serious problem of EMI noise pick. Fig. 3.23 shows a typical signal recorded with ICT in interaction with He gas-jet target (experiment described in Chapter-8), showing a maximum voltage of 140 mV which corresponds to a beam charge of 560 pC.

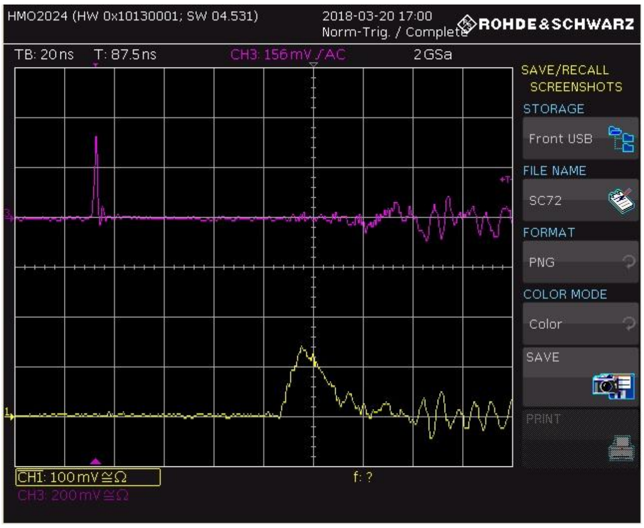

Fig.3.23: A typical ICT signal recorded.

Another method of estimation of charge of electron beam is by the calibration of phosphor screen used for detection of electron beam profile. When relativistic electrons are incident on the phosphor screen, the phosphor emits light which is collected and imaged onto the CCD camera by an appropriate zoom lens. The path of the collection of phosphor emission is light guided using a plastic tube to avoid light loss and collection of other stray lights of the chamber hall into the CCD. To avoid the CCD in coming in direct path of the relativistic electrons, light from the phosphor-2 is bent by a folding mirror. In the case of simultaneous measurement of electron beam profile, another phosphor-1 was placed in the electron beam path making an angle

45°, such that emission from phosphor is collected at 90° to the beam propagation direction. A hole is made in the light guide tube to pass the electrons in the forward direction and incident on the phosphor-2. The schematic of the set up is shown in Fig. 3.22 (1).

The incident photon on the CCD camera, ejects electrons from the CCD pixels which gets reflected into the CCD counts which we measure experimentally. Hence, estimation of charge of the electron beams includes the following steps:

1. Calibration of number of photons emitted from phosphor per incident electron. This varies with different phosphors and the calibration for different phosphors has been reported in the literature in units of photons per unit solid angle and per unit pC [16,22,23]. For e.g. the calibration for Lanex regular is 3.1×10^{9} ph/str/pC [22] and 7.82×10^{9} ph/str/pC for DRZ high [16].

2. The photon emission takes place following Lambertian law [24], of which only the photons emitted in a cone with solid angle dΩ subtended by the point of emission on the phosphor and the zoom lens aperture is collected by the CCD. The schematic of the geometry for collection of the phosphor emission is shown in Fig. 3.22 (2). The solid angle subtended is given by:

$$d\Omega = \frac{\pi r^2}{D^2} \tag{3.7}$$

where, r is the effective aperture radius of the CCD and the zoom lens system and D is the distance of the CCD from the phosphor. The effective radius r depends on the focal length of the zoom lens (f) and the effective f# given by,

$$r = \frac{f}{(1+\frac{L_2}{L_1})\times f\#} \tag{3.8}$$

where, f# of the particular zoom lens is 1.8 and L1 is the distance of zoom lens from phosphor and L2 is the distance of CCD from lens i.e. the focal length of lens. For the present experiment, in the configuration of simultaneous measurement of electron beam profile and its spectra, where two screens phosphor-1 and phosphor-2 were used, the zoom lens with focal length of 8 cm and 5 cm were kept at a distance of 58 cm and 102 cm respectively from the phosphor screen. Accordingly, the solid angle estimated was 0.0023 str and 0.0004 str for phosphor-1 and phosphor-2 respectively.

The above formulation is made considering the electron beam is incident at the centre of the phosphor screen and the complete emission subtending the solid angle is collected by the CCD. However, another geometrical factor comes into play when the electron beam is incident away from the centre of the phosphor and in that case, emission of a part of the solid angle is collected by the CCD. In the experiments, the electrons were found to be incident away from the centre of the phosphor and the geometrical factor was estimated for the different configuration of phosphor-1 and phosphor-2. Its effect was considered in estimation of charge. The offset of position of electrons from the phosphor centre was estimated by taking the average beam pointing on the phosphor of a number of shots and correspondingly the solid angle subtended by the CCD was calculated.

3. As the photons are incident on the CCD, it liberates electrons. The quantum efficiency (QE) of the CCD provides the calibration for the number of electrons liberated per incident photon. For 14 bit pixelfly CCD camera used in the experiments, the quantum efficiency is 62% @ peak 546 nm.

Phosphor emission consists of wavelengths other than 546 nm also. So the spectral corrections corresponding to the ratio of peak at 546 nm to that at different wavelengths was also considered in estimating the conversion efficiency of the CCD from photon to electrons. For the 14 bit pixelfly camera, the ratio was estimated to be 0.59.

4. Conversion efficiency of the electrons ejected into the CCD counts. This calibration is given by A/D conversion factor. For the 14 bit pixelfly camera, the A/D conversion efficiency factor is $1e^{-}$/count, which suggests that the count observed on CCD corresponds to an equal number of electrons.

However, during the experiments to avoid saturation of CCD signal, suitable neutral density filters were used in front of the zoom lens. This in turn reduced the incoming photon flux and the CCD counts by the corresponding fraction. Hence, a correction factor from the filter transmission was also taken into account while considering the CCD counts. Another factor which affects the CCD counts is the lens transmission factor which was also considered while estimating charge.

Hence, including all the factors discussed above, the final charge of the electron beams were estimated by the following relation

$$\text{Charge} = \frac{(\text{CCDcounts} \times \text{A/Dconversion factor} \times \text{spectral correstions})}{\begin{array}{c}(\text{QE} \times \text{lens transmission} \times \text{filter transmission} \times \\ \text{solid angle} \times \text{geometric factor} \times \text{phosphor calibration})\end{array}} \tag{3.9}$$

Following the above relation, charge was estimated from electron beam profiles recorded on phosphor-1. The charge estimated from ICT was found to 10-15% higher than that estimated from phosphor screen.

3.4.4. Estimation of electron beam spectrum and its characterization:

To understand the spectral characteristics of the electron beams, the absolute electron spectrum is deduced from the raw images obtained from dispersed electron beams by the magnetic spectrograph. The absolute spectrum is obtained by plotting the number of electrons within a energy interval between E and E + dE vs E. The area under the curve represents the total number of electrons within the whole energy range. The number of electrons per energy interval s given by [25]:

$$\frac{dN(E)}{dE} = \frac{counts(E)}{\delta s} \times \frac{ds}{dE} \tag{3.10}$$

where, counts (E) is the number of counts of the CCD at energy E integrated along the non-dispersive plane, δs is the CCD pixel size projected along the phosphor screen and ds/dE is the magnetic dispersion. A typical absolute spectra derived from the raw dispersed electron beam is shown in Fig. 3.25

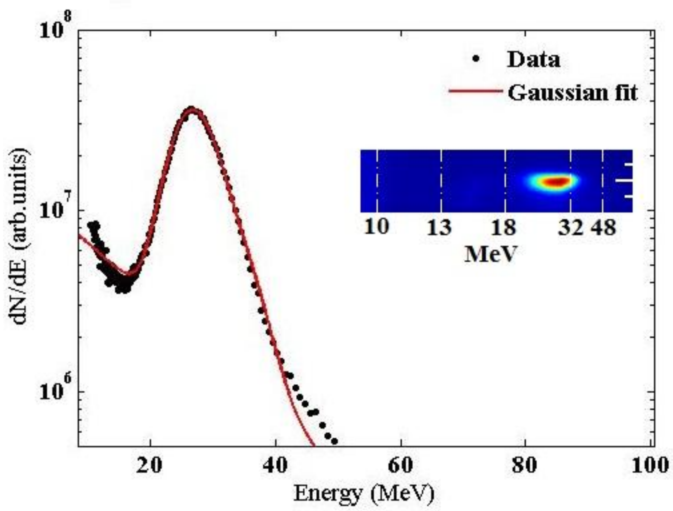

Fig. 3.24: Typical absolute spectra of dispersed electron beam recorded showing quasi-monoenergetic feature. Inset shows the corresponding raw image of the dispersed electron beam. The spectrum is fitted with higher order Gaussian function (red curve).

The absolute spectrum shows quasi-monoenergetic feature. For analysis of the spectrum, it is fitted with higher order Gaussian function. The peak value of the Gaussian denotes the peak energy value of the electron beam and the FWHM width of the Gaussian denotes the energy spread at the peak value. For the typical spectrum shown in Fig. 3.24 the peak energy is ~26 MeV and the energy spread is ~34% at the peak value.

3.5. Optical diagnostics:

Different optical diagnostics were set up to study the laser interaction with plasma such as the laser forward spectrum, 90° Thomson side scattering and the shadowgraphy. A schematic of the different optical diagnostics is shown in Fig. 3.25.

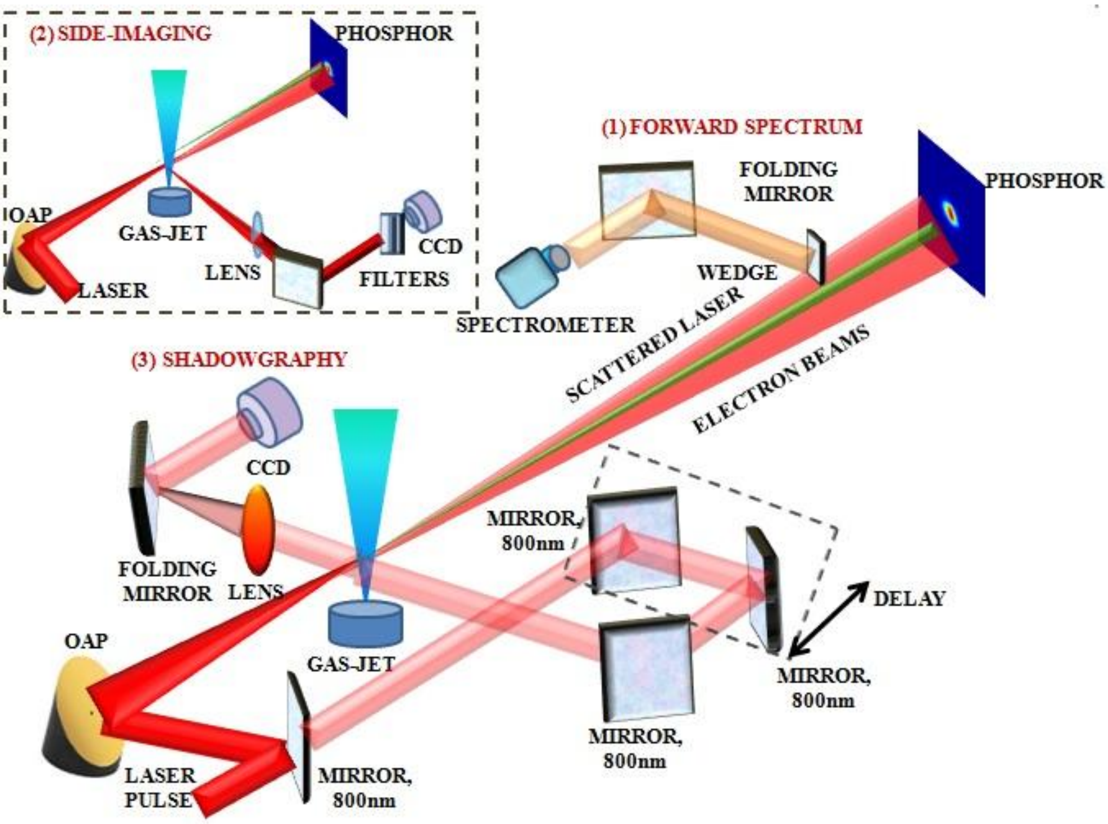

Fig. 3.25: Schematic of experimental set up for different optical diagnostics: (1) Laser forward spectrum, (2) Thomson side scattering and (3) Shadowgraphy

3.5.1. Forward laser spectrum:

The modified transmitted laser spectrum after interaction with plasma could be used to infer information on laser plasma interaction processes. The plasma waves scatter the incident laser light at frequencies, which satisfies their energy and momentum conservation laws such that:

$$\omega_s = \omega_0 \pm \omega_p \tag{3.11}$$

where, ω_s is the scattered frequency, ω_0 is the central laser frequency. The laser light can be back scattered ($\omega_s = \omega_0 + \omega_p$) or can be scattered in the forward along the laser propagation direction ($\omega_s = \omega_0 - \omega_p$). These incident and the scattered waves beat with the frequency $\Delta\omega = \omega_0 - \omega_s = \omega_p$. The axial ponderomotive force of this beat wave excites large amplitude plasma wave at resonance. As it grows, it scatters more incident light, thereby increasing the intensity of the scattered light. Thus both the plasma wave and the scattered wave grow in amplitude at the cost of the incident wave. Thus the forward scattered laser light is associated with the formation of wakefield inside plasma and the shift equals to ω_p that is dependent on the plasma density [26, 27]. This is more prominent in case of $L > \lambda_p$.

On the other hand, blue shift of the laser is associated with the ionization induced shifts of the gas by the laser itself [28, 29]. During the propagation of intense laser pulses inside plasma, instantaneous ionization of the gas atoms leads to increase in the plasma density along the laser axis which decreases the refractive index of the plasma. For further propagation of the laser pulse into plasma, the laser energy depletes very rapidly and the transmitted laser spectrum contains blue-shifted components. Generally, in case of low Z gas targets such as He, where the gas is ionized early at the foot of the laser pulse and the main laser interacts with fully ionized plasma driving strong wakefield, redshift of the transmitted laser light is observed. On the other hand, when high Z gases such as N_2, Ar etc. are used as gas-jet targets for the experiments, ionization induced defocusing of the laser pulse takes place and the laser is said to blue-shifted.

In the present experiment, this diagnostic was set up to get information about the interaction mechanism of the laser plasma interaction. A part of the transmitted laser light after interaction with the plasma was collected along the laser propagation direction by a glass wedge of 2° angle and imaged onto a spectrometer with the help of an optical fibre. The spectrometer used was a high resolution spectrometer, Model: AVASPEC 3648. The wavelength range of the spectrometer was between 200-1100 nm with a wavelength resolution in the range of 0.025-20 nm. A schematic of the set up is shown in Fig. 3.25 (1). The spectrometer was synchronized with the main laser through a trigger and the exposure time was set up to ~2 ms. The signal recorded was further processed through the AVANTES software.

3.5.2. 90° Thomson scattering:

When an electron is subjected to an electromagnetic field, it oscillates with the same frequency in the direction of polarization of the field. When the intensity of the electromagnetic wave becomes very high, the interaction of the electron with the field becomes highly non-linear and motion of the electron becomes relativistic. Therefore, these electrons serve as a non-linear medium for interaction and hence the radiation emitted from the oscillating electrons leadto higher harmonics of the incident electromagnetic wave. The $v \times B$ term of the force gives rise to the non-linearity and generates a longitudinal component. So, a highly relativistic electron is subjected to a transverse force due to the transverse electric component of the field and a longitudinal force which arises due to the non-linearity. Therefore, the combined effect of both the longitudinal and the transverse drifts give rise to helical orbits. This motion of the electrons in the helical orbits is called the figure of eight motion [30, 31] as shown in Fig. 3.26.

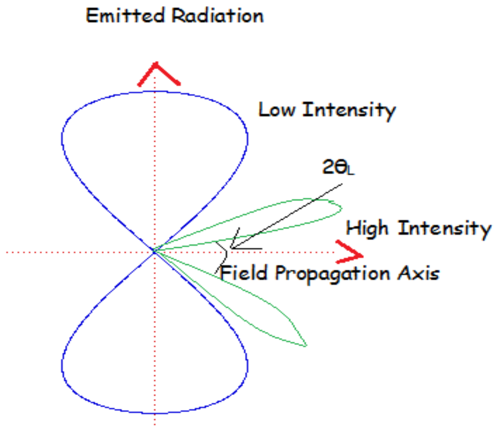

Fig. 3.26: Figure of eight motion

When the intensity of the field is very high, then the longitudinal drift velocity of the electron increases. This results in the radiation loop to be bend in the forward direction. The angle the cone makes with the propagation axis is given by,

$$\theta_L = \frac{\sqrt{8}}{a_0} \tag{3.12}$$

The spectrum of the emitted radiation is then a superposition of all the harmonics given by,

$$\omega_L = \frac{m\omega_0}{1 + \frac{a_0^2}{2} sin^2 \frac{\theta_L}{2}} \tag{3.13}$$

where, m is the harmonic number, ω_0 is the incident radiation frequency, a_0 is the incident field strength.The power radiated from the first harmonic is similar to the radiation emitted from classical Thomson scattering cross-section and is given by:

$$P_1 \simeq W_0 \frac{8\pi}{3} a_0^2 \tag{3.14}$$

where, W_0 is the scattered power per electron for a given laser frequency ω_0. Hence, the total power of the first harmonic of the scattered radiation depends on the laser intensity a_0 and the also on the number of electrons emitting the radiation. Hence, when a high intense laser propagates through plasma the electrons oscillate non-linearly in the laser field and leads to high harmonic content in the re-emitted radiation. These radiation when collected through a lens and imaged on to a CCD camera gives the information of the intensity of radiation and the density at a particular position which in turn gives the information of self-focusing and channelling of the laser pulse in plasma. The schematic of the side scattering set up is shown in Fig. 3.25 (2). There are several reports on study of relativistic self-focusing of the laser pulse inside plasma through the Thomson scattering signal [32-34]. A typical laser created channel in under dense plasma observed through 90° Thomson scattering of the laser pulse recorded during one of our experiments is shown in Fig. 3.27 below.

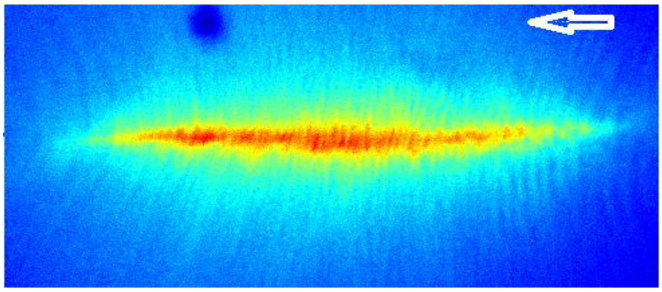

Fig. 3.27: Typical side scattering image of laser created channels recorded in He gas-jet target

3.5.3. Shadowgraphy:

Another diagnostic, which is commonly used to study the laser propagation inside plasma, is the shadowgraphy. In this case, a probe beam is sent at 90° to the propagation direction of the main laser pulse. The probe beam size is kept such that it covers the whole nozzle length. When the probe beam is synchronized with the main laser pulse, shadowgram of the laser interaction with the plasma can be recorded by imaging the transmitted probe beam on to a CCD camera. In experiments performed in this thesis, we have used the leakage of the main laser pulse (0.1%) through a folding mirrorbefore sending it to the OAP. The leakage of the main beam is then made to pass through a delay system consisting of three mirrors (coating of 800 nm), set on a translational motor stage. The synchronization between the probe beam and the main laser pulse is set such that the distance covered by the main laser pulse from the folding mirror to the entrance of the gas-jet nozzle is equal to the length covered by the probe beam from the folding mirror to the gas-jet nozzle. Accordingly, the delay is set between the main laser pulse and the probe beam such that we can probe the laser interaction from a time before the interaction of the main laser pulse with plasma. This helps in studying the presence of any pre-pulse in the main laser pulse and formation of any pre-plasma. The transmitted light from the plasma is then collected through a lens and imaged on to a 14 bit CCD camera. The schematic of the set up is shown in Fig. 3.25 (3). During the experiments the delay was set to few ps such that it can probe the whole length of propagation of the main laser pulse through the plasma.

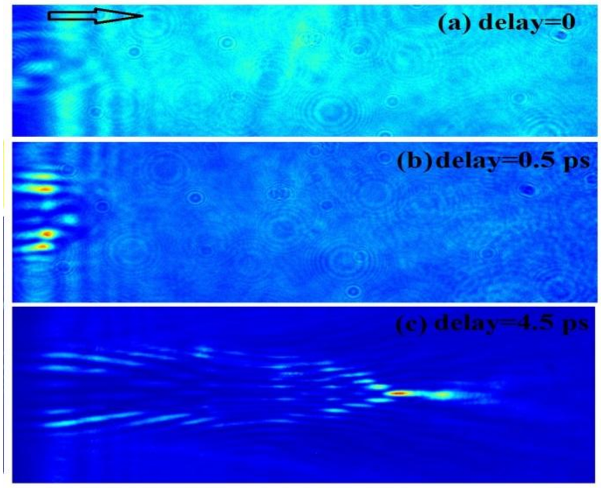

Fig. 3.28: Typical shadowgram of laser created channels recorded in N_2 gas-jet target for (a) delay=0, (b) delay= 0.5 ps and (c) delay= 4.5 ps. The arrow on top of first frame shows the direction of laser propagation.

Fig. 3.28 (a-c) shows the typical shadowgram of laser created channel in N_2 gas-jet target for three different delays timings. The laser pulse propagates from left to right as shown by the arrow sign. Fig. 3.28 (a) shows the conditions at delay=0 i.e. when the laser pulse just enters the plasma. Fig. 3.28 (b) shows the condition at a delay=0.5 ps, when the laser pulse has propagated some distance into the plasma. There is no signature of pre-plasma formation. At a much later delay of 4.5 ps, the laser pulse has completed the whole length of propagation into the plasma and Fig. 3.28 (c) shows the shadowgram of the complete laser created channel into the plasma showing multiple filamentation of the laser channel. Hence in contrast to the Thomson scattering images, where we get a time integrated information of the laser propagation inside plasma, in this case we can probe the propagation of the laser pulse inside plasma with time.

References

[1] Compression of amplified chirped optical pulses, D. Strickland and G. Mourou, *Opt. Commun.*, **55**, 447 (1985).

[2] 60-fsec pulse generation from a self-modelocked Ti:sapphire lasers, D. E. Spence, P. N. Kean, and W. Sibbett, *Opt. Lett.* **60**, 42 (1990).

[3] Aberration-free stretcher design for ultra-short pulse amplification, G. Cheriaux, P. Rousseau, F. Salin, and J. P. Chambaret, *Opt. Lett.*, **21**, 414 (1996).

[4] Amplitude and phase control of ultrashort pulses by use of an acousto-optic programmable dispersive filter: pulse compression and shaping, F. Verluise, V. Laude, Z. Cheng, Ch. Spielmann and P. Tournois, *Optics Letts.*, **28**, 575 (2000).

[5] Single-shot characterization of ultrashort light pulses, A. Brun. P. Georges, G. Le Saux, and F. Satin, *J. Phys. D: Appl. Phys*. **24**, 1225 (1991).

[6] Bonzai, Femtosecond single shot auto correlator, User's manual, Version 1.0, Amplitude Technologies

[7] A single-shot third-order autocorrelator for pulse contrast and pulse shape measurements, J. Collier, C. Hernandez-Gomez, R. Allott, C. Danson, and A. Hall, *Laser and Particle Beams*, **19**, 231 (2001).

[8] Laser Fundamentals, William T. Silfast, Cambride University Press, (2004).

[9] Supersonic gas jet target for generation of relativistic electrons with 12TW-50fs laser pulse, T. Hosokai, K. Kinoshita, T. Watanabe, K. Yoshii, T. Ueda *et al.*, 2002 Proc. 8th European Particle Accelerator Conf. (EPS) p 981 (2002).

[10] Effect of chirp on self-modulation and laser wakefield electron acceleration in the regime of quasimonoenergetic electron beam generation, B. S. Rao, A. Moorti, P. A. Naik, and P. D. Gupta, *Phys. Rev. Special Topic-Accl. And Beams*, **16**, 091301 (2013).

[11] Digital evaluation of interferograms, Measurement, M. Hipp, J. Woisetschlaeger, P. Reiterer, T. Neger, *Elsevier*, **36**, 53 (2004).

[12] Imaging plate. In: Tateno Y., Iinuma T., Takano M. (eds) Computed Radiography, J. Miyahara, Springer, Tokyo (1987).

[13] New X-ray Phosphors, L. H. Brixner, *Materials Chemistry and Physics*, **16,** 253 (1987).

[14] Durr Medical, CR 35 BIO Manual. (2009)

[15] Calibration of imaging plate for high energy electron spectrometer, A. Kazuo, A. Tanaka, T. Yabuuchi, T. Sato, R. Kodama *et al.*, *Review of Scientific Instruments* **76**, 013507 (2005).

[16] Absolute calibration of two DRZ phosphor screens using ultrashort electron bunch, Y. C. Wu, B. Zhu, K. G. Dong, Y. H. Yan, and Y. Q. Gu, Rev. Sci. Instrument, **83**, 026101 (2012).

[17] GEANT 4- a simulation toolkit, S. Agostinelli, J. Allison, K. Amako, J. Apostolakis, H. Araujo *et al.*, *Nucl. Instrum.v Methods Phys. Res. A*, **506**, 250 (2003).

[18] Diagnostic for simultaneous online recording of high-energy electron beam profile and its spectrum for laser wakefield accelerator, Shikha Mishra, M. Tech Thesis, *Homi Bhabha National Institute* (2018).

[19] An experimental and GEANT4 simulation study on design of a broad energy-range magnetic spectrograph for laser plasma accelerator, S. Mishra, D. Hazra, A. Moorti, and J. A. Chakera, *JINST*, **15**, P01034 (2020).

[20] Two-screen single-shot electron spectrometer for laser wakefield accelerated electron beams, A.A. Soloviev *et al*., *Rev. Sci. Instrum*. **82,** 043304 (2011).

[21] Novel method for characterizing relativistic electron beams in a harsh laser-plasma environment, B. Hidding, G. Pretzler, M. Clever, F. Brandl, F. Zamponi *et al*., Rev. Sci. Instum. **78**, 083301 (2007).

[22] Calibration and cross-laboratory implementation of scintillating screens for electron bunch charge determination, T. Kurz, J. P. Couperus, J. M. Krämer, H. Ding, S. Kuschel *et al.*, Rev. Sci. Instrum. **89**, 093303 (2018).

[23] Absolute calibration for a broad range single shot electron spectrometer, Y. Glinec, J. Faure, A. Guemnie-Tafo, V. Malka, H. Monard *et al*., Rev. Sci. Instrument **77**, 103301 (2006).

[24] Light angular distribution of fluorescent screens excited by x-rays, G. E. Giakoumakis and D. M. Miliotis, *Phys. Med. Biol*., **30**, 21 (1985).

[25] Broadrange single shot electron spectrometer, Y. Glinec, J. Faure, A. Guemnie-Tafo, V. Malka, H. Monard *et al*., CARE-Report 2006-036-PHIN (2006).

[26] Electron acceleration from the breaking of relativistic plasma waves, A. Modena, Z. Najmudin, A. E. Dangor, C. E. Clayton, K. A. Marsh *et al., Nature* (London) **377**, 606 (1995).

[27] Electron Trapping in Self-Modulated Laser Wakefields by Raman Backscatter, C. I. Moore, A. Ting, K. Krushelnick, E. Esarey *et al.*, *Phys. Rev. Lett.*, **79**, 3910 (1997).

[28] Spectral blue shifting of a femtosecond laser pulse propagating through a high pressure gas, S. P. Le Blanc, R. Sauerbrey, S. C. Rae and K. Brunett, *J. Opt. Soc. Am. B*, **10**, 1801 (1993).

[29] Ionization-induced frequency shifts in intense femtosecond laser pulses, B. M. Penetrante , J. N. Bardsley, W M. Wood, C. W Siders, and M. C. Downer, *J. Opt. Soc. Am. B*, **9**, 2032 (1992).

[30] High intensity scattering processes of relativistic electrons in vacuum, F. V. Hartemann, *Phys. Plasmas*, **5**, 2037 (1998).

[31] Classical theory of the scattering of intense laser radiation by free electrons, E. S. Sarachik and G. T. Schappert, *Phys. Rev. D.*, **1**, 2738 (1970).

[32] Electron Acceleration by a Laser Wakefield in a Relativistically Self-Guided Channel, R. Wagner, S.-Y. Chen, A. Maksimchuk, and D. Umstadter, *Phys. Rev. Lett.*, **78**, 3125 (1997).

[33] Plasma Wave Generation in a Self-Focused Channel of a Relativistically Intense Laser Pulse, C. E. Clayton, K.-C. Tzeng, D. Gordon, P. Muggli, W. B. Mori *et al.*, *Phys. Rev. Lett.*, **81**, 100 (1998).

[34] Polyethylene Glycol Reduces Early and Long-Term Cold Ischemia-Reperfusion and Renal Medulla Injury, J. Faure, T. Hauet, Z. Han, J. M. Goujon, I. Petit *et al.*, *Phys. Plasmas*, **9**, 756 (2002).

CHAPTER 4

Investigation of laser plasma acceleration using long laser pulse duration of 200 fs

4.1. Motivation:

Laser wakefield acceleration mechanism (LWFA) [1] in laser plasma acceleration (LPA) has been explored in detail for several years and has proved to be potential candidate, as it could demonstrate generation of sub-GeV to multi-GeV class good quality quasi-monoenergetic electron beams [2-6]. This acceleration mechanism has been identified over a wide range of laser and plasma parameters.

1. Short laser pulse regime of $L<\lambda_p$ showing quasi-monoenergetic spectra (bubble regime) [7-20].
2. Long laser pulse regime of $L>\lambda_p$ showing quasi-monoenergetic spectra (SM-LWFA) [21-27].
3. Very long laser pulse regime of $L>>\lambda_p$ showing broad continuous spectra (SM-LWFA) [28-31].

In the $L>>\lambda_p$ regime, initially (1995-1998) investigation of wakefield was performed where wakefield was driven mostly by the Raman scattering instability [28-31]. However, later in 1999, it was reported that, in such long laser pulse duration regime, another acceleration mechanism of DLA could be applicable [32] which, was also experimentally demonstrated in few reports [34-36]. However, electron beams in this $L>>\lambda_p$ regime accelerated through DLA was found to be with continuous/ quasi-thermal spectra [34-36]. Subsequent to this, there has been no further experimental investigation in this regime of $L>>\lambda_p$, confirming the dominant acceleration mechanism of DLA or showing efforts to improve the electron beam properties. Such study would be important because it has been shown that electrons accelerated from DLA is capable of generating high energy betatron radiation compared to wakefield [37-39]. Further, studies in the L>>λ_p regime would also be of importance considering developments in the fiber lasers technology suggesting it as a compact and more efficient suitable driver for future particle accelerators, although in the long laser pulse duration regime (>100 fs) [40, 41]. Hence, in the present scenario, when LPA is being considered for short wavelength radiation source [42] and various investigations are still being undertaken to push the radiation energy more towards the hard X-ray regime with high flux [37], a detailed experimental investigation addressing the above mentioned issues would be of importance.

With this motivation, in the present study we performed an experimental investigation in L>>λ_p in underdense He plasma gas-jet target interacting with long laser pulse duration of ~200 fs. In this study, we identified DLA as the dominant applicable acceleration mechanism, which was further supported by 2D PIC simulations using code EPOCH [43] and theoretical analysis. Maximum electron energy observed was ~30 MeV mostly with quasi-thermal spectra. Interestingly, generation of quasi-monoenergetic ($\Delta E/E$~10% – 20%) electron beams with a peak energy of ~17–22 MeV was also observed, even with such long laser pulses, although with a low probability of occurrence and a plausible explanation of such an important observation has been made through estimation of dephasing length of electrons in DLA.

4.2. Experimental set up and parameters:

Fig. 4.1 shows the schematic of the experimental set up. Ti:sapphire laser pulse of duration of ~200 fs was used during the experiment, in which a slight positive chirp was introduced in the pulse by stretching the pulse using compressor grating system. Laser peak power was ~15 TW. Using f/5 Off-Axis-Parabolic (OAP) mirror, the laser was focused to a focal spot size of ~25×12 μm^2 (radius at $1/e^2$ of the peak value), delivering a peak laser intensity of ~2.1×10^{18} Wcm^{-2} (normalized laser vector potential a_0~1). The Rayleigh length (Z_R) was estimated to be ~180 µm. He plasma target of length of 1.2 mm using rectangular slit nozzle of dimension 1.2 mm×10 mm was used with the plasma density varying in the range of ~3.6×10^{19} cm^{-3} to ~1.1×10^{20} cm^{-3}. For detection of electron beams DRZ phosphor screen was used and a magnetic spectrograph (diameter: 50 mm, pole gap: 9 mm, peak magnetic field: 0.45 T), with a resolution of ~10% at 10 MeV and ~20% at 20 MeV (for a beam divergence of 10 mrad), was used to record the electron beam spectra.

The side scattered images were recorded 90˚ to the laser propagation direction using lens. The spatial resolution of the imaging system was limited by the pixel size of the CCD camera, which was for the present case ~6.45 µm and also by the magnification of 5X used in recording the images. So, the overall spatial resolution of the imaging system used was ~1.3 µm.

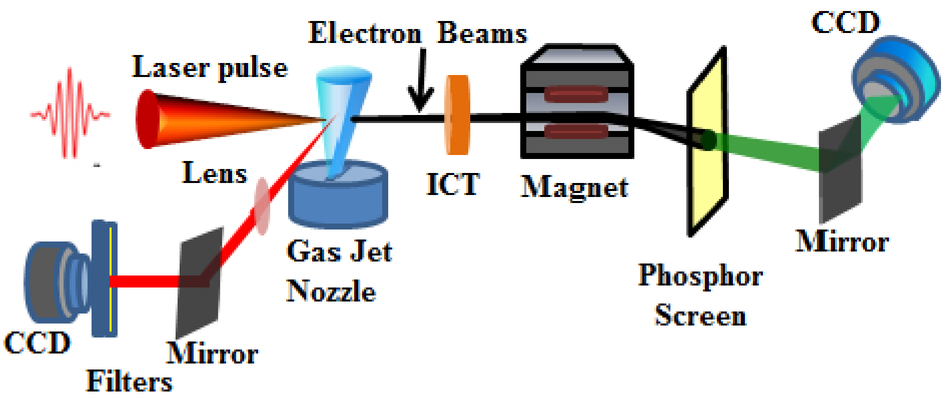

Fig. 4.1: Schematic of the experimental set up

4.3. Experimental results:

4.3.1. Recording of electron beam profiles:

Spatial profile of electrons beams for the range of plasma densities used is shown in Fig. 4.2. A 6 mm thick aluminium plate was placed in contact with the phosphor screen, which helped in recording only the intense collimated core of the electron beam cutting off the low energy diffused background component. For densities of up to ~7×10^{19} cm^{-3}, electron beams with full angle divergence of ~40 mrad (FWHM) were observed (Fig. 4.2 a–e). At higher density of ~9×10^{19} cm^{-3}, the overall beam divergence increased (~120 mrad), however, an intense central spot was still seen (Fig. 4.2 f). The total charge contained within the $1/e^2$ area of the collimated electron beam profile was estimated using the DRZ-high calibration data [44-46], and was found to be in the range of 10–50 pC for density ~4×10^{19} - 7×10^{19} cm^{-3}, which increased to >450 pC at a higher density of ~9×10^{19} cm^{-3}.

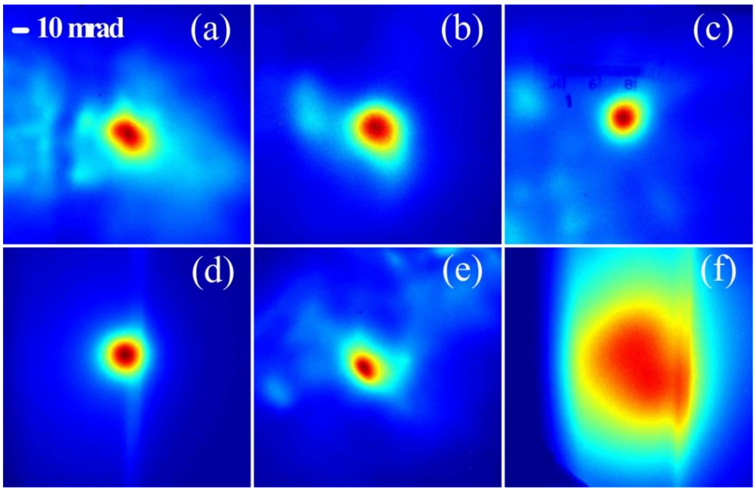

Fig. 4.2: Typical electron beam profiles recorded for various densities, with 6mm Al plate in front of phosphor screen, Energy cut off ~2.7 MeV. *(a) 3.6×10^{19} cm^{-3}, (b) 4×10^{19} cm^{-3}, (c) 5×1019 cm^{-3}, (d) 6×10^{19} cm^{-3}, (e) 7×10^{19} cm^{-3}, and (f) 9×10^{19} cm^{-3}.*

4.3.2. Recording of electron beam spectra:

The electron beam spectra were measured by dispersing the electron beams through magnetic spectrograph. Since, the plate was kept in contact with the phosphor screen, the effect of divergence introduced by the plate would have negligible effect on the spectrum recorded on the phosphor. Generation of three kinds of electron beam spectra were observed during the experiment. The different kinds of spectra observed represent the statistical fluctuation of shots recorded in the same experimental conditions for fixed laser and gas-jet target conditions.

1. Single group of electrons: Generation of electron beams with peak energies of 8-10 MeV with exponential spectra were observed as shown in Fig. 4.3 for different plasma densities. An increase of electron energy with plasma densities was observed in this case. Such electron beams were observed in ~45% of the total shots during the experiment. The total charge contained within the dispersed electron beams showing single electron spectra above 7 MeV, increases from ~0.7 pC at a density of ~4×10^{19} cm^{-3} to ~12 pC at a density of ~1×10^{20} cm^{-3}.

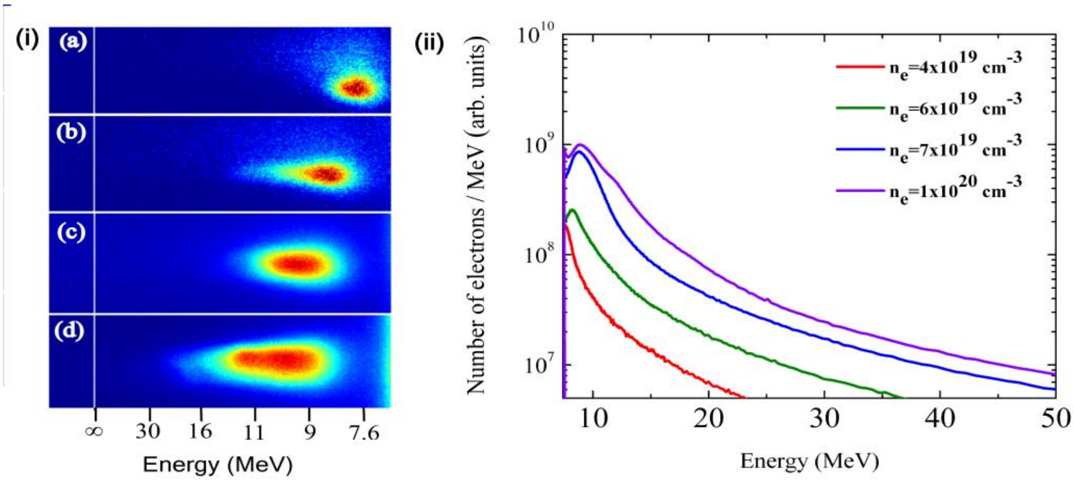

Fig. 4.3: Typical single electron beams with quasi-thermal spectra: (i) Dispersed raw images and (ii) Corresponding lineouts of electron beams, for various densities (a) 4×10^{19} cm^{-3}, (b) 6×10^{19} cm^{-3}, (c) 7×10^{19} cm^{-3}, (d) 1.1×10^{20} cm^{-3}.

2. Two groups of electrons: In addition to single group of electrons described above, sometimes two groups of electrons were also observed with a quasi-thermal spectra as shown in a series of 10 shots in Fig. 4.4. The lower energy peak correspond to ~8-10 MeV and an enhancement of electron energy was observed with the higher energy peak corresponding to ~15-25 MeV. The maximum electron energy observed was ~30 MeV (at 10% of the peak value). In this case also, increase in the maximum electron energy was observed with increase in plasma density. Such electron beams were observed in ~45% of the shots during the experiment i.e. with equal probability as that of the single electron beams. The total charge above 7 MeV varied in the range of ~2–8.5 pC.

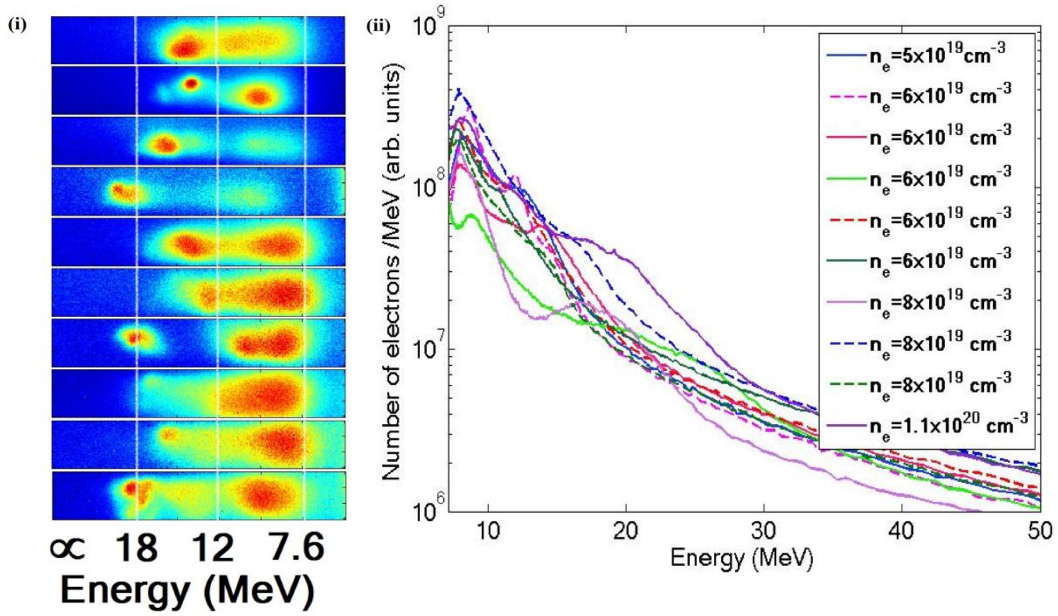

Fig. 4.4: Two groups of electrons with quasi-thermal spectra: (i) Raw image of dispersed electron and (ii) corresponding lineouts of electron beams, for densities range of the present experimental condition.

3. Quasi-monoenergetic spectra: Interestingly, in almost ~10% of the shots, quasi-monoenergetic electron beams with comparatively lower beam divergence of ~5–10 mrad, and electron peak energy of ~17–22 MeV, energy spread ~20% was observed as shown in Fig. 4.5. Generation of such quasi-monoenergetic electron beams in long laser pulse duration regime of L>>λ_p was observed for the first time.

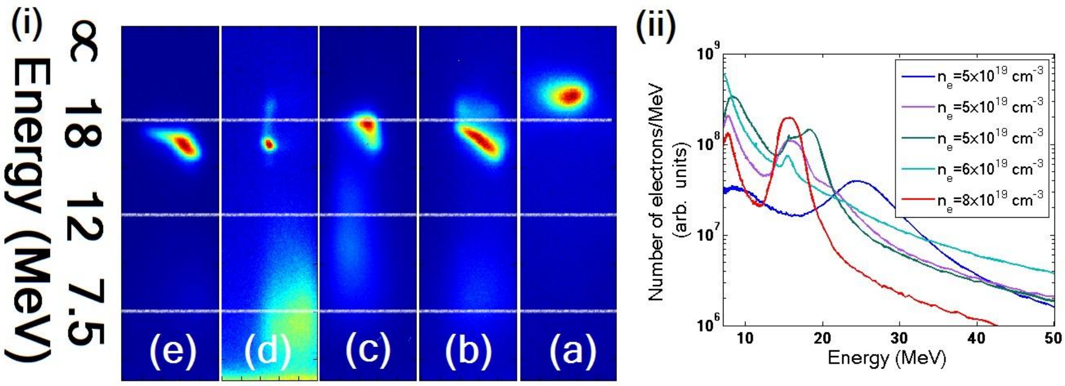

Fig. 4.5: (i) Raw images of quasi-monoenergetic electron beams at different densities. (a)–(c) 5×10^{19} cm^{-3}, (d) 6×10^{19} cm^{-3}, (e) 8×10^{19} cm^{-3}. (ii) Lineouts of the corresponding electron beams.

4.3.3. Observation of laser channeling inside plasma through 90° side scattering:

Fig. 4.6 shows the typical laser channels recorded during the experiment for the range of plasma density used at a fixed laser power of 7.5 TW showing relativistic self-focusing and guiding of the laser pulse inside plasma. In the present case, P/P_c was in the range of 9–28.

The laser propagation length increased from ~255 μm (~1.4 Z_R) for plasma density of ~3.6–4×10^{19} cm^{-3} (Fig. 4.6 a), to a maximum propagation length in the range of ~450–550 μm (~2.5–3 Z_R) (Fig. 4.6 b-e) for higher plasma density. Two stages of laser focusing and channelling were observed: initial self-focusing with a laser spot size of ~4-5 μm, followed by slight defocusing in the middle (bulging of the channel) for a small distance where laser spot size increases to ~6-10 μm, and a second stage of self-focusing at a later time where the laser pulse was found to converge to a spot size of ~4 μm.

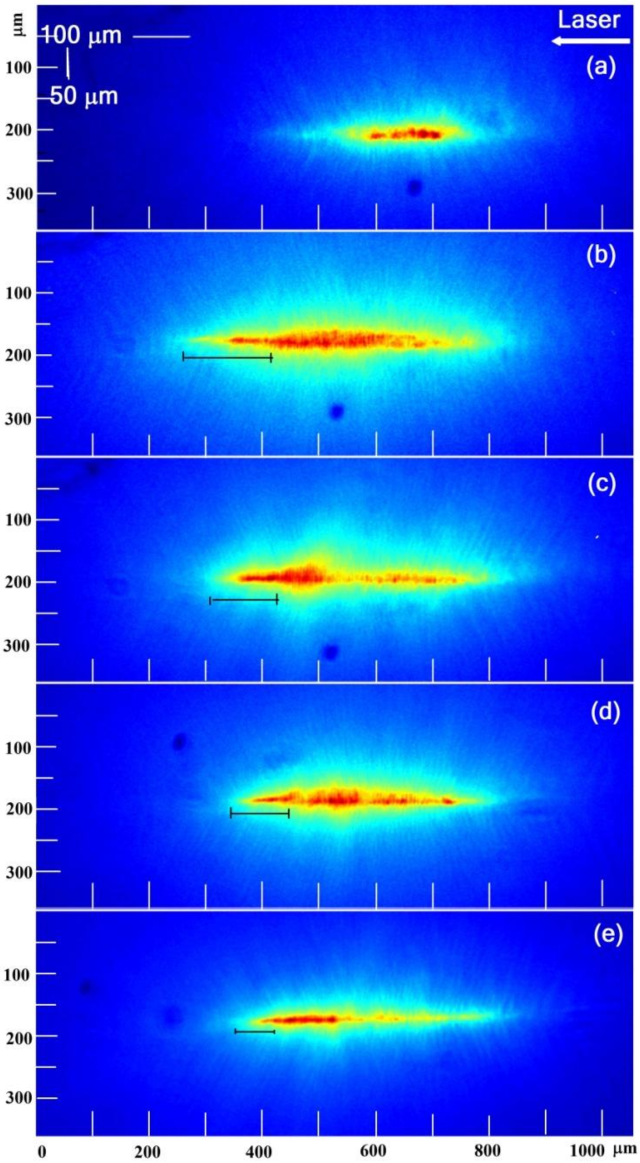

Fig. 4.6: Typical laser channels recorded for various plasma densities: (a) 4×10^{19} cm^{-3}, (b) 5×10^{19} cm^{-3}, (c) 6×10^{19} cm^{-3}, (d) 7×10^{19} cm^{-3}, and (e) 1×10^{20} cm^{-3}. Laser propagation direction is from right to left. For guidance purposes, the extent of the second stage of channelling is marked by black line segment in each frame.

The two groups of accelerated electrons could be associated with the observed two stages of laser self-focusing and channeling. The first group of lower energy electrons of 8-10 MeV is accelerated from the initial stage of laser chanelling which further accelerated to a higher energy bunch of 15-25 MeV in the second stage of laser acceleration. Since, the extents of the second stage of channelling varied from shot to shot, as have been marked in the images of Figure.4.6, the energy of the second group of electrons with higher energy also was found to be fluctuating as seen in Fig. 4.4.

Further, towards the higher density e.g. at the maximum density used (1×10^{20} cm^{-3}) the central region of the channel became comparatively narrower and intense (Fig.4.6e), and which manifested in sudden transition in the beam profile (Fig 4.2f) and beam charge (x10). This is again manifested in the electron beam spectra with increase in energy towards the higher density side (Fig. 4.3-d) and even a third bunch of electron comprising of the highest energy electrons at a density of 1.1×10^{20} cm^{-3} (Fig. 4.4).

At the same time, during the experiment, in a few percent of the shots a slight bending in the later part of the laser channel was observed and, associated with it, two electron beams were observed on the phosphor screen (without a magnet in the path) as shown in Fig. 4.7.

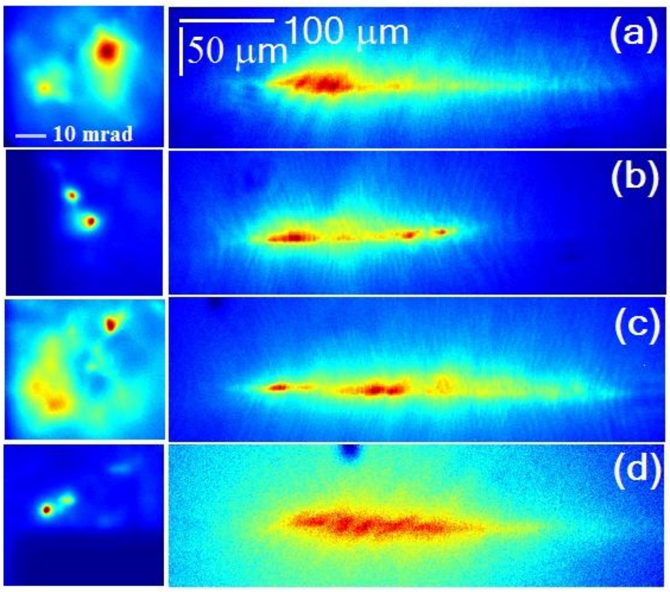

Fig. 4.7: Observation of two electron beams due to bending of the laser channel in the later part of the propagation. Plasma density: 6×10^{19} cm^{-3}.

4.4. Discussion:

4.4.1: Identification of the dominant acceleration mechanism of DLA:

In the regime of $L>>\lambda_p$, one of the applicable acceleration mechanism reported was the SM-LWFA [28-31]. However, in the following Table-4.1, we provide a comparative explanation between the electron beams properties, predicted from SM-LWFA and that we observed, which shows that in the present case, SM-LWFA could not be a dominant acceleration mechanism.

Table-4.1: Comparison of expected feature from SM-LWFA with experimental observations

Considering SM-LWFA Mechanism of Acceleration	
Expected Feature	**Experimental Observation**
Dephasing limited energy gain ~5 MeV (for highest density)	Maximum energy observed ~30 MeV
Decrease in energy with density	Increase in energy with density
Broad continuous energy spectrum	Quasi-thermal/quasi-monoenergetic spectra

Further, results of earlier PIC simulation reports in similar experimental conditions of $L>>\lambda_p$, have shown that wakefields are effective only at the foot of the laser pulse, and in the remaining unmodulated region no regular wakefield was observed [32-34]. In particular recently, Lemos *et al*. [39] found that for long laser pulses of 700 fs duration and a plasma density of $\sim 1\times 10^{19}$ cm^{-3}, nonlinear plasma waves are driven only at the front of the laser pulse, and electron acceleration was attributed to the DLA. In the present case, electron acceleration has been observed for the values of P/P_c in the range of 9 - 28, which is in agreement with earlier observation where it is demonstrated that for betatron resonance acceleration P/P_c should be greater than 6 [32], and therefore support the applicability of DLA.

In the present experiment both laser pulse duration and plasma density was varied to obtain optimum regime for relativistic electron beam generation. One regime was obtained for laser pulse duration in the range of ~200 fs, and plasma density in the range of $3.6\text{-}4\times10^{19}$ $\text{-}1.1\times10^{20}$ cm^{-3} as described above. Another regime of electron acceleration was observed at comparatively lower laser pulse duration of ~55 fs, where generation of QM electron beams of peak energy ~30 MeV with high reproducibility was observed, and this could be attributed to the SM-LWFA mechanism (discussed in the next chapter #5). The observed distinct change in the electron beam energy and spectrum at lower pulse duration of ~55 fs compared to the longer laser pulse duration of 200 fs during the same experimental campaign also suggests applicability of different electron acceleration mechanisms in the two cases.

4.4.2: Theoretical analysis on energy gain and dynamics of electrons in laser field:

Theoretical analysis has been performed for estimation of energy gain through DLA as described in Section 2.3.2 of Chapter-2 of this thesis. For the present experimental parameters, the plot of F (γ) vs γ, for η = 0.983 (corresponding to average value of the density used in the experiment i.e. n_e ~6×10^{18} cm^{-3}) and a_0=1, is shown in Fig. 4.8, following Eq. (2.44).

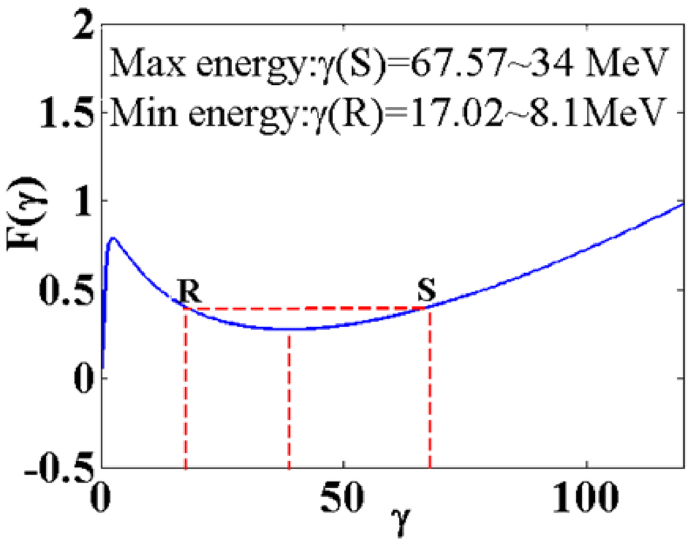

Fig. 4.8: Estimation of maximum energy of electron: Plot of F (γ) vs γ for η = 0.983 (corresponding to average value of the density used in the experiment i.e. n_e ~6×10^{18} cm^{-3}) and a_0=1.

The maximum energy estimated theoretically is γ(s) ~ 34 MeV, which very well matches with the observed maximum energy of ~30 MeV.

Further, separatrix was also plotted following Eq. (2.45) of Chapter-2, to study the trapping dynamics of electrons in the laser field for the present experimental conditions as shown in Fig. 4.9. In the present case, since estimated γ_{opt} lies in the experimental observed energy range, electrons are observed to be trapped in the laser field and complete the whole phase space rotation unlike to that observed in case of Gahn *et al.* [34] and Mangles *et al.* [36] as shown in Fig. 2.4 and Fig. 2.5 respectively. Electrons with γ > γ(S) and γ < γ(R) (blue curve) are untrapped electrons whereas electrons with γ=γ (R) to γ (S) (red curve) are trapped electrons. Hence, such trapping of electrons in the laser field with maximum energy gain which is in good agreement with the experimental observed value also supports that in the present case DLA is the dominant acceleration mechanism.

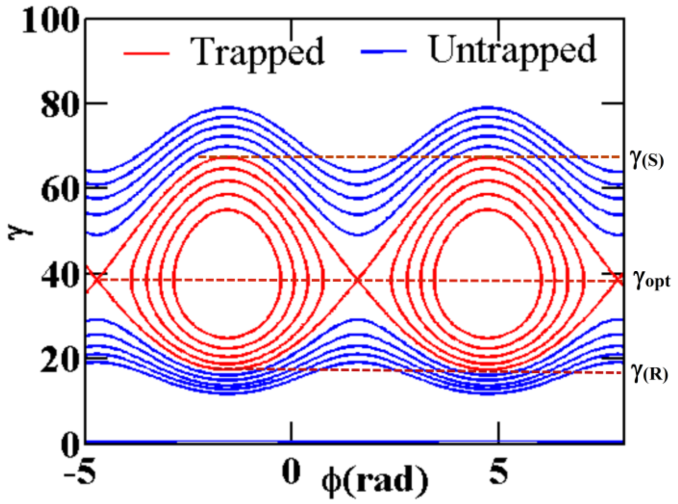

Fig. 4.9: Separatrix plot: Plot of γ vs ϕ for η = 0.983 (corresponding to average value of the density used in the experiment n_e ~6×10^{18} cm^{-3}) and a_0=1.

Further, the transverse energy gain of electrons (γ_T) vs normalized turning point radius (x_T/r_0) was also plotted following Eq. (2.46) and Eq. (2.47) of Chapter-2, for the present experimental conditions and also compared with the other reports on DLA by Gahn *et al*. [34] and Mangles *et al*. [36], and is shown in Fig. 4.10. The plot shows that, compared to other reports, in our case, significant transverse energy gain was possible from lower oscillation amplitude of electrons in the laser field, where the laser intensity remains uniform to its peak value. This explains the observation of much more collimated electron beams in our case compared to that of Gahn *et al.* (div~15° at FWHM) [34] and Mangles *et al* (div~2.8° at FWHM) [36]. Hence, present experimental conditions are found to be more favourable for DLA with respect to trapping of electrons in the laser field and also in generating comparatively more collimated electrons beams.

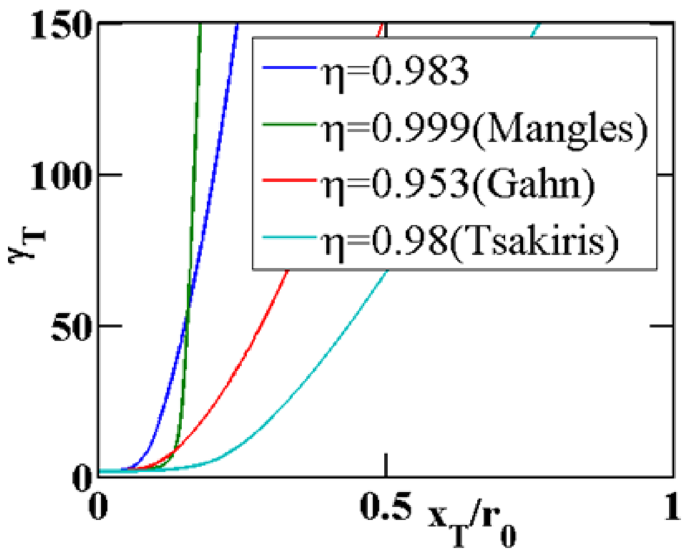

Fig. 4.10: Plot of γ_T vs x_T/r_0

4.4.3: Verification of DLA through 2D PIC simulations using code EPOCH:

To establish the dominant acceleration of DLA further in the present experimental conditions 2D PIC simulations were performed using code EPOCH [44]. The simulation was performed with laser pulses of 200 fs with a_0=1 propagating along z-axis, which interacts with underdense plasma of density 7×10^{19} cm^{-3}. The simulation was performed with box size of 450 μm × 60 μm and resolution of λ/20 in both directions. Snapshots of laser channeling inside plasma for three different time steps of 760 fs, 1040 fs and 1600 fs are shown in Fig. 4.11 (i-iii). In this case also, two stages of laser channeling was observed with length of each stage of self-focusing ~150 μm (spot radius ~4-5 μm), and slight defocusing in the middle (spot radius ~8-10 μm). This observation is consistent with the two stages laser self-focusing observed experimentally.

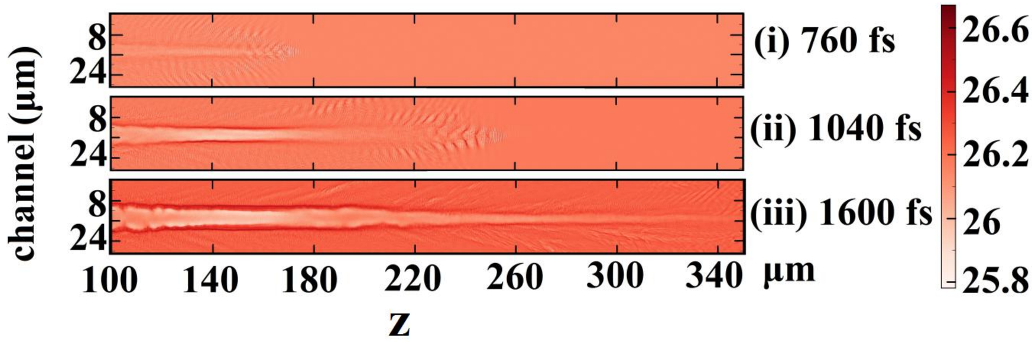

Fig. 4.11: Simulation results: Electron density profiles along z at different time steps (i) 760 fs, (ii) 1040 fs, (iii)1600 fs.

Such a effect of constriction of the laser channel at the later stage of propagation observed both in experiment (Fig. 4.6) and simulation (Fig. 4.11) could be attributed to the observed electron acceleration in the channel and its subsequent pinching due to self-generated quasi-static magnetic field [47, 48]. Such an effect was reported experimentally during propagation of a 1 ps laser pulse (intensity ~5 - 9×10^{18} W/cm^2) in near critical density plasma (produced from a foil target) with a density gradient in the laser propagation direction [36]. Mangles *et al.* [29] have also observed this effect through simulation for plasma density of ~10^{19} cm^{-3} (n_e=0.01 n_c) but at much higher laser intensity of >10^{20} W/cm^2. Generation of high energy electrons by betatron resonance acceleration was attributed to this process. In the present case, such an effect has been observed experimentally at lower plasma densities (n_e ~ 0.02 - 0.06 n_c) in a uniform gas-jet plasma at a lower laser intensity of ~2.1×10^{18} W/cm^2.

Next, P_x (momentum) versus x (propagation distance) at different time steps corresponding to channels shown in Fig. 4.12 (i–iii) has been shown. Associated with the two stages of laser self-focusing, two stages of electron acceleration was observed. In the first stage of channelling acceleration of electrons up to ~11–15 MeV is observed (Fig. 4.12-i), with further propagation, the formation of multiple bunches was observed along with a slight increase in electron energy (Fig. 4.12-ii). Finally, associated with the second stage of laser focusing and channelling of ~150 µm (Fig. 4.12-iii), enhancement of electron energy up to ~30–37 MeV occurred, along with retaining the feature of formation of multiple electron bunches. The increase in electron energy associated with the second stage of laser self-focusing whose extent fluctuates with shot-to shot gives rise to sometimes a peak or otherwise a slight bulging in the electron spectra as is observed experimentally (Fig. 4.6). Mangles *et al.* [36] have also reported through simulation two stages of electron acceleration in the case of DLA, where enhancement in the electron energy was attributed to the acceleration in the magnetically constricted part of the laser channel in the later stage of the propagation. In the present experiment, observation of two electron beams associated with the bending of the laser channel in the later part of laser propagation, as shown in Fig. 4.7, also supports the two-stage acceleration scenario.

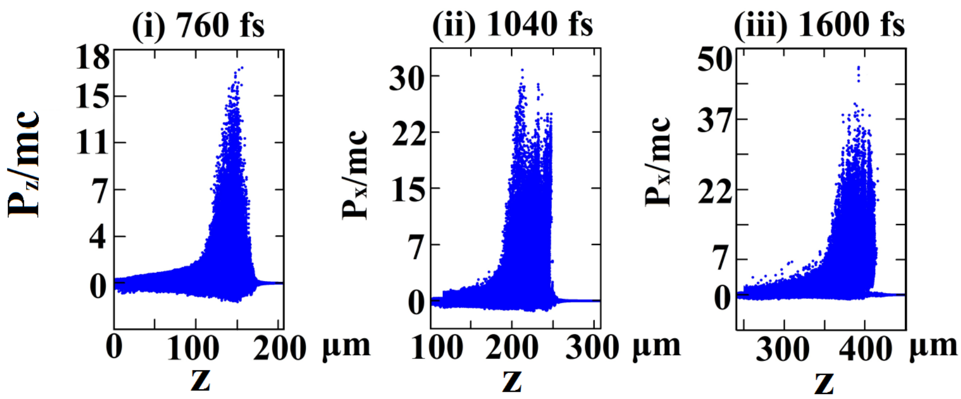

Fig. 4.12: Simulation results: Normalized Pz versus z at different time steps, (i) 760 fs, (ii) 1040 fs, (iii) 1600 fs.

Further, normalized laser amplitude and wakefield is plotted for the time step of 1040 fs and is shown in Fig. 4.13 (a & b) respectively, which also shows that wakefields were generated only at the foot of the laser pulse and did not sustain longer. This is also consistent with the earlier PIC simulation reports suggesting dominant acceleration mechanism as DLA [32-34, 39].

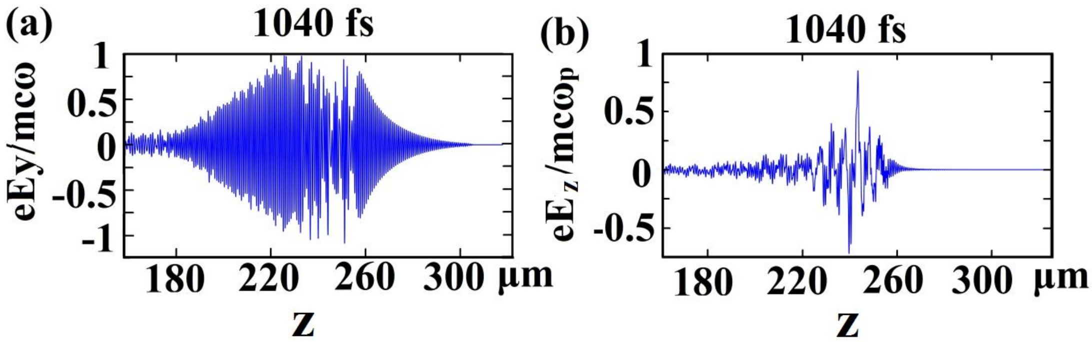

Fig. 4.13: Simulation results: (a) Normalized laser electric field along z at 1040 fs. (b) Normalized longitudinal wakefield along z at 1040 fs.

To further support the DLA mechanism, we also estimate the separate contribution of the transverse energy gain of electron in the laser to the total energy gain of electrons from simulations. Transverse and longitudinal energy gain is estimated from the relation given below [34, 36]:

$$\gamma_y = -\int_0^t \frac{2ep_y E_y}{(mc)^2} dt \tag{4.1}$$

$$\gamma_z = -\int_0^t \frac{2ep_x E_x}{(mc)^2} dt \tag{4.2}$$

The total energy gain is given by:

$$\gamma^2 = 1 + \gamma_z + \gamma_y \tag{4.3}$$

The plot of transverse energy gain ($\sqrt{\gamma_y}$) vs total energy gain (γ) is shown in Fig. 4.14, which shows that the transverse energy gain curve makes ~45° with the total energy suggesting dominant contribution of DLA in the energy gain of electrons

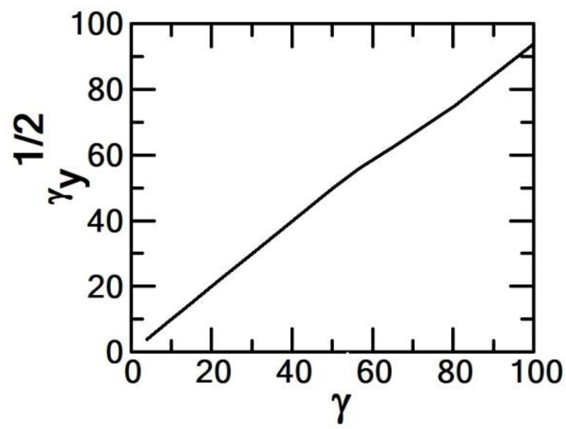

Fig. 4.14: Simulation results: Estimation of contribution of energy gain from DLA in the total energy gain

4.4.4: Plausible explanation of generation of quasi-thermal / quasi-monoenergetic electron beams:

In the present experiment, we observed mostly quasi-thermal electron beams (Fig. 4.3 & Fig. 4.4) along with observation of quasi-monoenergetic electron spectra although in a few number of shots (Fig. 4.5). To explain such observation, we estimate the dephasing length (L_d) for the betatron resonance acceleration mechanism following the coupled differential equation (Eq. (48) and Eq. (49)) derived in Chapter-2. For the range of plasma density used, L_d was in the range of ~100-150 µm as shown in Fig. 4.15 for η=0.983 (average of the present density regime) and the corresponding maximum energy gain is ~40 MeV.

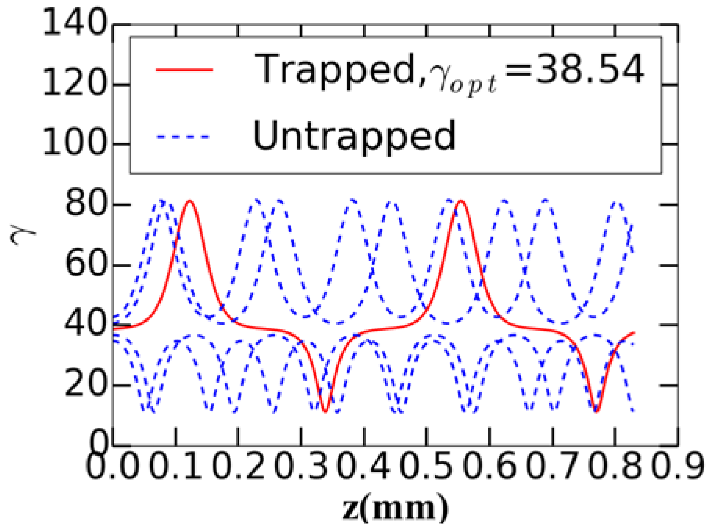

Fig. 4.15: Estimation of dephasing length of electrons in DLA: Plot of γ vs Z

In the present experiment, we observed a maximum channel length of ~500 μm with two stages of relativistic self-focusing of length ~100-150 μm which, is comparable to L_d. The electrons which are trapped, remain in phase and rotate from the accelerating to the decelerating phase and regain energy to catch up with the accelerating phase of the laser electric field. This is known as the phase space rotation of the electrons [8, 49] and more the number of cycles of rotation, more electrons participate in the phase space rotation. This could probably lead bunching of electrons in the laser field and the appearance of quasi-thermal / quasi-monoenergetic feature in the electron beam spectra. It may be pointed out here that, in a recent 2D PIC simulations [50, 51] it has been observed that even with DLA as the dominant acceleration mechanism along with wakefield acceleration, the energy spread of the electrons could be retained (even reduced), and in fact the energy distribution of the DLA electrons were found to be considerably lower than that of the non-DLA electrons.

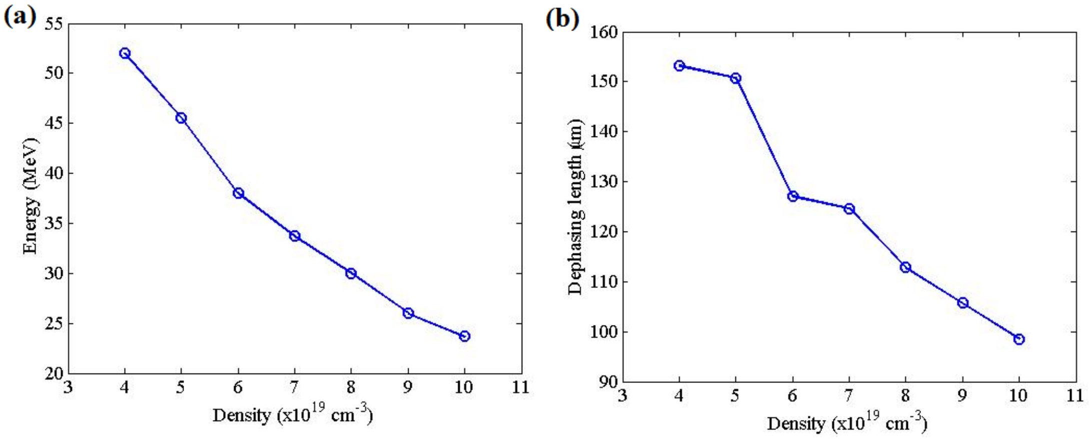

Fig. 4.16: Variation of maximum electron energy (γ(s)) and dephasing length vs density

In Fig. 4.16, we plot the variation of maximum electron energy gain γ(s) (a) and dephasing length (b) vs density estimated from the analytical model over the present density range. The model predicts decrease of electron energy with increase in density and is also consistent with the decreasing trend of dephasing length with density. However, the observed increasing energy with increase in density and also increase in the channel lengths observed in experiment could be attributed to the subsequent pinching due to self-generated quasi-static magnetic field. In this regime, additional electron energy gain could be possible even though the dephasing length decreases with density.

4.4.5: Conclusion:

An experimental demonstration of direct laser acceleration of electrons (DLA) was–presented in the L>>λ_p regime, using Ti:sapphire long laser pulses of ~200 fs duration interacting with underdense He gas-jet target with plasma density in the range of ~3.6×10^{19} cm^{-3} to ~1.1×10^{20} cm^{-3}. Two stages of laser channelling associated with acceleration of two groups of electrons were observed with lower peak energy of ~8-10 MeV and another with higher peak energy of ~15-25 MeV with maximum electron energy of ~30 MeV. Results were supported by 2D PIC simulations and detailed theoretical analysis. Interestingly, generation of quasi-monoenergetic electron beams with peak energies of ~17-22 MeV and energy spread of ~10-20 %, have been observed in such a long laser pulse duration regime for the first time.

References

[1] Laser electron accelerator, T. Tajima and J. M. Dawson, *Phys. Rev. Lett.*, **43**, 268 (1979).

[2] Physics of laser driven plasma based electron accelerators, E. Esarey, C. B. Schroeder, and W. P. Leemans, *Rev. Mod. Phys.*, **81**, 1229 (2009).

[3] Laser plasma accelerators, V. Malka, *Phys. Plasmas,* **19**, 055501 (2012).

[4] Developments in laser-driven plasma accelerators, S. M. Hooker, *Nature Photonics*, **7**, 775 (2013).

[5] Laser-driven plasma accelerators operating in the self-guided, blowout regime, C. Joshi, *IEEE Transactions on Plasma Science*, **45**, 3134 (2017).

[6] Plasma-based accelerators: then and now, C. Joshi, *Plasma Phys. Controlled Fusion*, (2019), doi.org/10.1088/1361-6587/ab396a.

[7] Laser wakefield acceleration: the highly non-linear broken-wave regime, A. Pukhov and J. Meyer-ter-Vehn, *Appl. Phys. B: Lasers Opt*.**74,** 355 (2002).

[8] Generating multi-GeV electron bunches using single stage laser wakefield acceleration, W. Lu, M. Tzoufras, C. Joshi, F. S. Tsung, W. B. Mori *et al*., *Phys. Rev. ST Accel. Beams* **10,** 061301 (2007).

[9] Monoenergetic beams of relativistic electrons from intense laser–plasma interactions, S. P. D. Mangles, C. D. Murphy, Z. Najmudin, A. G. R. Thomas, J. L. Collier *et al.*, *Nature*, **431**, 535 (2004).

[10] High-quality electron beams from a laser wakefield accelerator using plasma-channel guiding, C. G. R. Geddes, Cs. Toth, J van Tilborg, E. Esarey, C. B. Schroeder *et al.*, *Nature*, **431**, 538 (2004).

[11] A laser–plasma accelerator producing monoenergetic electron beams, J. Faure, Y. Glinec, A. Pukhov, S. Kiselev, S. Gordienko *et al.*, Nature **431**, 541 (2004).

[12] Petawatt Laser Guiding and Electron Beam Acceleration to 8 GeV in a Laser-Heated Capillary Discharge Waveguide, A. J. Gonsalves, K. Nakamura, J. Daniels, C. Benedetti, C. Pieronek *et al., Phys. Rev. Lett.*, **122**, 084801 (2019).

[13] Multi-GeV electron beams from capillary-discharge-guided subpetawatt laser pulses in the self-trapping regime, W. P. Leemans, A. J. Gonsalves, H.-S. Mao, K. Nakamura, C. Benedetti *et al., Phys. Rev. Lett.*,**113**, 245002 (2014).

[14] Quasi-monoenergetic laser-plasma acceleration of electrons to 2 GeV, X. Wang, R. Zgadzaj, N. Fazel, Z. Li, S. A. Yi *et al., Nat. Commun.*, **4**, 1988 (2013).

[15] Enhancement of electron energy to the multi-GeV regime by a dual-stage laser-wakefield accelerator pumped by petawatt laser pulses, H. T. Kim, K. H. Pae, H. J. Cha, I. J. Kim, T. J. Yu *et al., Phys. Rev. Lett.*,**111**, 165002 (2013).

[16] GeV electron beams from a centimetre-scale accelerator W. P. Leemans, B. Nagler, A. J. Gonsalves, Cs. Tóth, K. Nakamura, *et al.*, Nat. Phys. **2**, 696 (2006) .

[17] Measurements of the critical power for self-injection of electrons in a laser wakefield accelerator, D. H. Froula, C. E. Clayton, T. Döppner, K. A. Marsh, C. P. J. Barty, *et al.*, *Phys. Rev. Lett.* **103**, 215006 (2009).

[18] Near-GeV acceleration of electrons by a nonlinear plasma wave driven by a self-guided laser pulse, S. Kneip, S. R. Nagel, S. F. Martins, S. P. D. Mangles, C. Bellei *et al., Phys. Rev. Lett.*,**103**, 035002 (2009).

[19] Generation of tunable, 100–800 MeV quasi-monoenergetic electron beams from a laser-wakefield accelerator in the blowout regime, S. Banerjee, N. D. Powers, V. Ramanathan, I. Ghebregziabher, K. J. Brown *et al., Phys. Plasmas*, **19**, 056703 (2012).

[20] Self-guided laser wakefield acceleration beyond 1 GeV using ionization-induced injection, C. E. Clayton, J. E. Ralph, F. Albert, R. A. Fonseca, S. H. Glenzer *et al., Phys. Rev. Lett.*,**105**, 105003 (2010).

[21] Generation of Quasimonoenergetic Electron Bunches with 80-fs Laser Pulses, B. Hidding, K.-U. Amthor, B. Liesfeld, H. Schwoerer, S. Karsch *et al., Phys. Rev. Lett.*, **96**, 105004 (2006).

[22] Demonstration of quasi-monoenergetic electron-beam generation in laser-driven plasma acceleration, E. Miura, K. Koyama, S. Kato, N. Saito, M. Adachi *et al., Appl. Phys. Lett.*,**86**, 251501 (2005).

[23] Quasi-monoenergetic electron beam generation during laser pulse interaction with very low density plasmas, A. Yamazaki, H. Kotaki, I. Daito, M. Kando, S. V. Bulanov *et al., Phys. Plasmas*, **12**, 093101 (2005).

[24] Observation of strong correlation between quasimonoenergetic electron beam generation by laser wakefield and laser guiding inside a preplasma cavity, T. Hosokai, K. Kinoshita, T. Ohkubo, A. Maekawa, M. Uesaka *et al., Phys. Rev. E*, **73**, 036407 (2006).

[25] Tomography of Injection and Acceleration of Monoenergetic Electrons in a Laser-Wakefield Accelerator, C.-T. Hsieh, C.-M.Huang, C.-L.Chang, Y.-C. Ho, Y.-S. Chen *et al., Phys. Rev. Lett.*, **96**, 095001 (2006).

[26] Generation of quasi-monoenergetic electron beams with small normalized divergences angle from a 2 TW laser facility, B. S. Rao, A. Moorti, R. Rathore, J. A. Chakera, P. A. Naik *et al.*, *Phys. Rev.* ST Accel. Beams,**17**, 011301 (2014).

[27] Electron acceleration from the breaking of relativistic plasma waves, A. Modena, Z. Najmudin, A. E. Dangor, C. E. Clayton, K. A. Marsh *et al.*, *Nature* (London) **377**, 606 (1995).

[28] Nonlinear Optics in Relativistic Plasmas and Laser Wake Field Acceleration of Electrons, D. Umstadter,S.-Y. Chen, A. Maksimchuk, G. Mourou, R. Wagner *et al.*, *Science*, **273**, 472 (1996).

[29] Electron Acceleration by a Laser Wakefield in a Relativistically Self-Guided Channel, R. Wagner, S.-Y. Chen, A. Maksimchuk, and D. Umstadter, *Phys. Rev. Lett.*, **78,** 3125 (1997).

[30] Observation of Electron Energies Beyond the Linear Dephasing Limit from a Laser-Excited Relativistic Plasma Wave, D. Gordon, K. C. Tzeng, C. E. Clayton, A. E. Dangor, V. Malka *et al*., *Phys. Rev. Lett*., **80,** 2133 (1998).

[31] Particle acceleration in relativistic laser channels, A. Pukhov, Z.-M.Sheng, and J. Meyer-ter-Vehn, *Phys. Plasmas*, **6**, 2847 (1999).

[32] Relativistic laser-plasma interaction by multi-dimensional particle-in-cell simulations, A. Pukhov and J. Meyer-ter-Vehn, *Phys. Plasmas*, **5**, 1880 (1998).

[33] Multi-MeV Electron Beam Generation by Direct Laser Acceleration in High-Density Plasma Channels, C. Gahn, G. D. Tsakiris, A. Pukhov, J. Meyer-ter-Vehn, G. Pretzler *et al.*, *Phys. Rev. Lett.*, **83**, 4772 (1999).

[34] Generation of MeV electrons and positrons with femtosecond pulses from a table-top laser system, C. Gahn, G. D. Tsakiris, G. Pretzler, K. J. Witte, P. Thirolf *et al.*, *Phys. Plasmas*, **9**, 987 (2002).

[35] Electron Acceleration in Cavitated Channels Formed by a Petawatt Laser in Low-Density Plasma, S. P. D. Mangles, B. R. Walton, M. Tzoufras, Z. Najmudin, R. J. Clarke *et al.*, *Phys. Rev. Lett.*,**94**, 245001 (2005).

[36] Gamma-rays from harmonically resonant betatron oscillations in a plasma wake, S. Cipiccia, M. R Islam, B. Ersfeld, R. P. Shanks, E. Brunetti, *et al.*, *Nat. Phys.***7**, 867 (2011).

[37] Femtosecond x rays from laser-plasma accelerators, S. Corde, K. Ta Phuoc, G. Lambert, R. Fitour, V. Malka *et al.*, *Rev. Mod. Phys.*, **85,** 1 (2013).

[38] Self-modulated laser wakefield accelerators as x-ray sources, N. Lemos, J. Martins, L. Tsung, F. S. Shaw, J. L. Marsh *et al.*, *Plasma Phys. Control. Fusion*, **58**, 034018 (2016).

[39] Characteristics of betatron radiation from direct-laser-accelerated electrons, T. W. Huang, A. P. L. Robinson, C. T. Zhou, B. Qiao, B. Liu *et al.*, *Phys. Rev. E.*, **93** 063203 (2016).

[40] Laser-wakefield application to oncology**,** B. S. Nicks, T. Tajima, D. Roa, A. Nečas and G. Mourou, *International Journal of Modern Physics A*, **34**, 1943016 (2019).

[41] The future is fibre accelerators, G. Mourou, B. Brocklesby, T. Tajima & J. Limpert, *Nature Photonics*, **7**, 258 (2013).

[42] Applications of laser wakefield accelerator-based light sources, F. Albert and A. G. R. Thomas, *Plasma Phys. Control. Fusion*, **58**, 103001 (2016).

[43] Contemporary particle-in-cell approach to laser-plasma modelling, T. D. Arber, K. Bennett, C. S. Brady, A. Lawrence-Douglas, M. G. Ramsay *et al.*, *Plasma Physics and Controlled Fusion,* **57,** 1 (2015).

[44] Calibration and cross-laboratory implementation of scintillating screens for electron bunch charge determination, T. Kurz, J. P. Couperus, J. M. Krämer, H. Ding, S. Kuschel *et al.*, Rev. Sci. Instrum. **89**, 093303 (2018).

[45] Absolute calibration for a broad range single shot electron spectrometer, Y. Glinec, J. Faure, A. Guemnie-Tafo, V. Malka, H. Monard *et al.*, Rev. Sci. Instrument **77**, 103301 (2006).

[46] Absolute calibration of two DRZ phosphor screens using ultrashort electron bunch, Y. C. Wu, B. Zhu, K. G. Dong, Y. H. Yan, and Y. Q. Gu, Rev. Sci. Instrument, **83**, 026101 (2012).

[47] Relativistic channeling of a picosecond laser pulse in a near-critical preformed plasma, M. Borghesi, A. J. MacKinnon, L. Barringer, R. Gaillard, L. A. Gizzi *et al.*, *Phys. Rev. Lett.* **78**, 879 (1997).

[48] Relativistic magnetic self-channeling of light in near-critical plasma: three-dimensional particle-in-cell simulation, A. Pukhov and J. Meyer-ter-Vehn, *Phys. Rev. Lett.***76**, 3975 (1996).

[49] Near-GeV energy laser-wakefield accleration of self-injected electrons in a centimeter-scale plasma channel, F. S. Tsung, R. Narang, W. B. Mori , C. Joshi , R. A. Fonseca *et al*., *Phys. Rev. Lett.* **93** 185002 (2004).

[50] Synergistic Laser-Wakefield and Direct-Laser Acceleration in the Plasma-Bubble Regime, Xi Zhang, V. N. Khudik, and S. Gennady, *Phys. Rev. Lett*.,**114**, 184801 (2015).

[51] Laser wakefield and direct acceleration with ionization injection, Xi Zhang, V. N Khudik, A. Pukhov and G. Shvets, *Plasma Phys. Control. Fusion*, **58**, 034011(2016).

CHAPTER 5

Investigation of laser plasma acceleration using short laser pulse duration of 55 fs

5.1. Motivation:

Realizing the importance of Direct Laser Acceleration (DLA) mechanism of electrons in generating high energy betatron radiation due to its larger oscillation amplitude in the laser created plasma channel [1-4], recently, DLA has gained renewed interest. Contribution of DLA has been identified in a bubble acceleration regime along with wakefield acceleration driven by short laser pulse of few tens of fs such that $L>\lambda_p$ in a mixed gas-jet target of $He+N_2$ [5, 6]. Role of DLA was further verified by extensive PIC simulation studies [7-10]. It is suggested that in the case of complete overlap of the laser field with the injected electron, role of DLA cannot be ignored, and a hybrid regime of acceleration (DLA + wakefield) would take place. It was found that, the advantage of such a regime of acceleration is that electrons gain additional energy from DLA apart from wakefield and that the electron energy gain is doubled. Moreover, it was also shown that in mixed gas-targets, where ionization induced injection of electron takes place [11-13], DLA would be favored as these electrons can gain some transverse momentum from the laser field after ionization within the laser pulse [9-11]. Earlier some contribution of DLA was considered along with wakefield in a $L>\lambda_p$ regime in a He gas-jet target where injection of electrons take place by the wave breaking process [14, 15], otherwise, a pure DLA regime was identified in very long laser pulsed regime of $L>>\lambda_p$ [16, 17]. However, following the recent report by Shaw *et al.* [5, 6], no further investigations have been reported in this direction.

LPA experiments have also been performed with pure N_2 gas-jet target, apart from He and mixed gas-jet targets [18-22]. This also has the advantage of supporting ionization induced injection mechanism and can provide high charge beams. However, most of the studies were performed in the $L>\lambda_p$ regime, where wakefield was found to be the dominant acceleration mechanism [18-21]. There is only one report in N_2 gas-jet target suggesting DLA as the acceleration mechanism but that too in the $L>>\lambda_p$ regime [22]. Hence, exploring the role of DLA acceleration mechanism in N_2 gas-jet in $L>\lambda_p$ regime would be also of interest.

With this motivation, in the present study we performed an experimental investigation in $L>\lambda_p$ in three different gas-jet target of He, mixed (He+N_2) and pure N_2, using short laser pulse duration of ~55 fs in the same experimental set up. In this study, we have identified different acceleration regimes, viz. hybrid: Direct Laser Acceleration (DLA) + Wakefield, and DLA. At threshold plasma density of $\sim 2\times10^{19}$cm^{-3} in both mixed and N_2 gas-target, a pure DLA regime was identified with ionization induced injection. With increase in density, increasing role of wakefield was observed leading to hybrid regime with mixed gas-jet target. Self-injection threshold was observed at a higher density of $\sim 5.8\times10^{19}$cm^{-3} in the case of pure He gas-jet target. Results were supported by 2D PIC simulations using code EPOCH [23], interestingly, which also showed generation of surface waves, considered as a potential mechanism of pre-acceleration to DLA. Further effect of the different acceleration mechanism on electron beam properties is also discussed.

5.2. Experimental set up and parameters:

Fig. 5.1 shows the schematic of the experimental set up. The experiment was performed using a 150 TW, 25 fs Ti:sapphire laser system of RRCAT, Indore, India. Using compressor grating, the laser pulse duration was stretched to ~55 fs. Laser peak power was ~18 TW. Using f/5 Off-Axis-Parabolic (OAP) mirror, the laser was focused to a focal spot size of ~25×12 μm^2 (radius at $1/e^2$ of the peak value), delivering a peak laser intensity of ~5.1×10^{18} Wcm^{-2} (normalized laser vector potential a_0~1.5). The ASE (Amplified Spontaneous Emission) and pre-pulse contrast of the laser pulse was better than 10^{-9} (at ~1 ns) and 10^{-7} (at 11 ns) respectively. Plasma length of 1.2 mm using well characterized rectangular slit nozzle of dimension 1.2 mm×10 mm [24, 25] was used with the plasma density varying in the range of ~2-7.1×10^{19} cm^{-3}. For detection of electron beams DRZ phosphor screen was used and a magnetic spectrograph (diameter: 50 mm, pole gap: 9 mm, peak magnetic field: 0.45 T), with a resolution of ~34% at 30 MeV and ~67% at 60 MeV (for 10 mrad beam), was used to record the electron beam spectra. The spectrograph has a lower energy cut-off of ~7.8 MeV. The charge in the electron beam profile was estimated using the standard calibration data of the phosphor used [26-28].

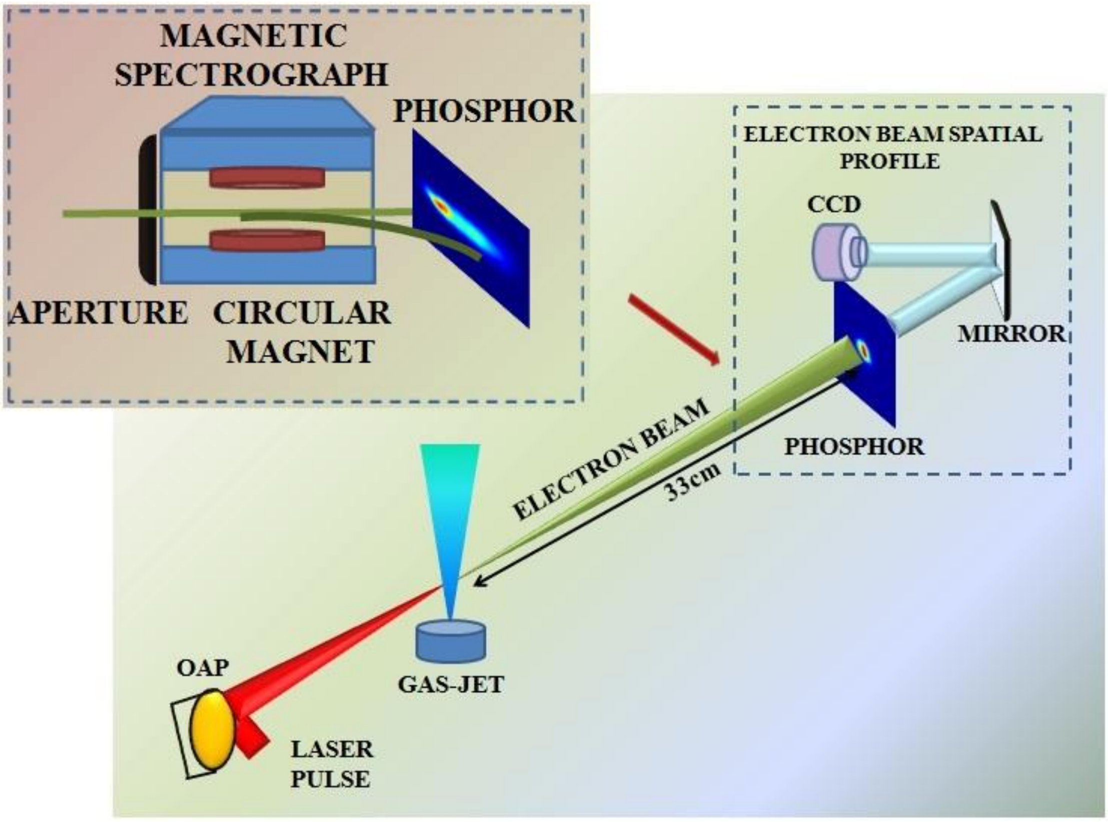

Fig. 5.1: Schematic of the experimental set up

5.3. Experimental results:

5.3.1. Recording of electron beam spectra for three different gas targets of He, mixed (He+N_2) and N_2:

Electron beam spectra were recorded after dispersing electron beam through the magnetic spectrograph. The present experimental conditions were found to be suitable for highly reproducible and stable generation of electron beams for all the three gas-jet targets used. Fig. 5.2 shows the typical raw images of the dispersed electron beams and the corresponding spectra from three different gas targets of He, mixed and N_2 at for different electron plasma densities.

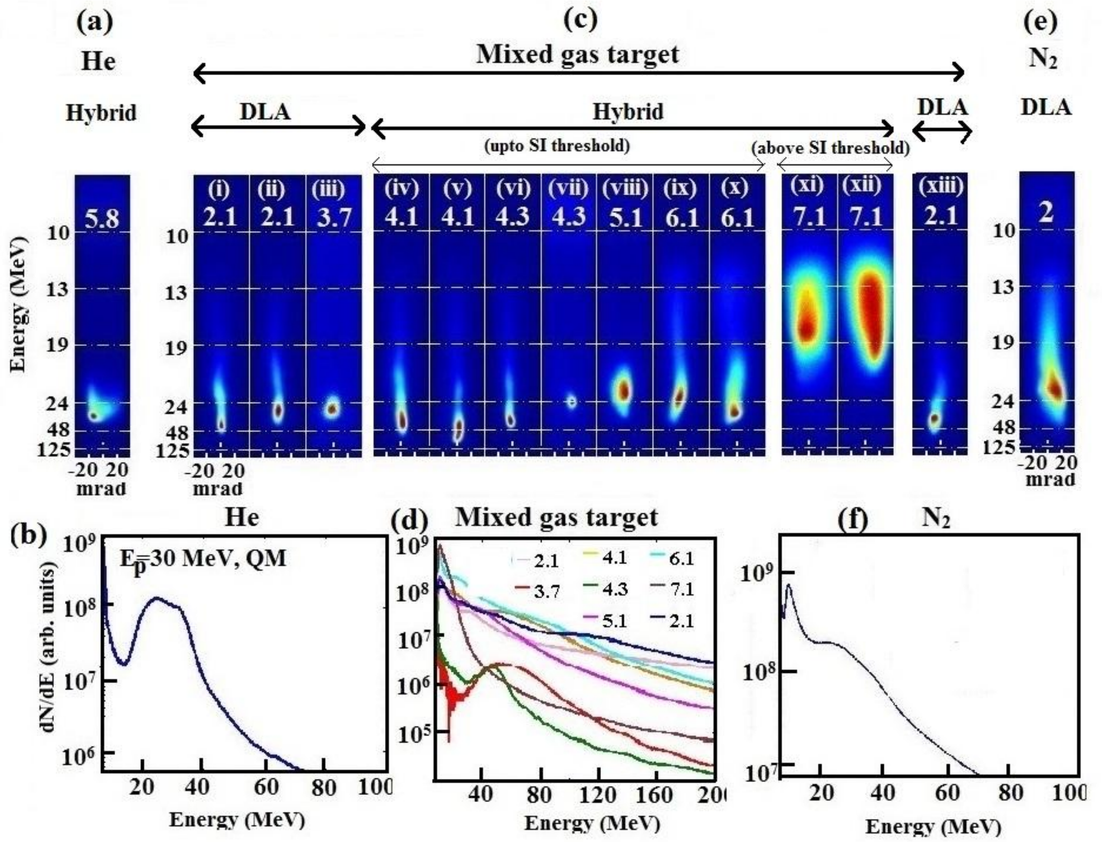

Fig. 5.2: Typical raw image of dispersed electron beam spectra obtained for various gas targets, lower energy cut-off of spectrograph is 7.5 MeV (a) for He gas-jet target at a threshold density of 5.8×10^{19} cm^{-3} (b) corresponding lineout; (c) for mixed (He+N$_2$) gas target at various densities ~2.1×10^{19} cm^{-3} (~7.5% N$_2$) to ~7.1 (~2.5% N$_2$)×10^{19} cm^{-3} (d) corresponding lineouts; (e) for N$_2$ at a density of ~2×10^{19} cm^{-3} (f) corresponding lineout. The raw images have been grouped and marked according to the regime of acceleration within the density regime in different gas-jet targets.

1. Electron beams recorded from He gas-jet target: Electron beams were generated from He gas target at a threshold density of ~5.8×10^{19} cm^{-3} (Fig. 5.2 a-b). The peak energy (E) is ~28 ± 4 MeV with maximum energy extending upto ~46 MeV (energy corresponding to 10% of the peak flux in the spectrum) with a shot to shot jitter of ± 6 MeV (i.e. ~26 %). In this case, the spectra are mostly quasi-monoenergetic with a mean energy spread (ΔE/E) of ~64% ± 26% containing ~5 pC charge above 7 MeV. Detailed statistics of electron beam spectra obtained from He gas-jet target is shown in Fig. 5.3.

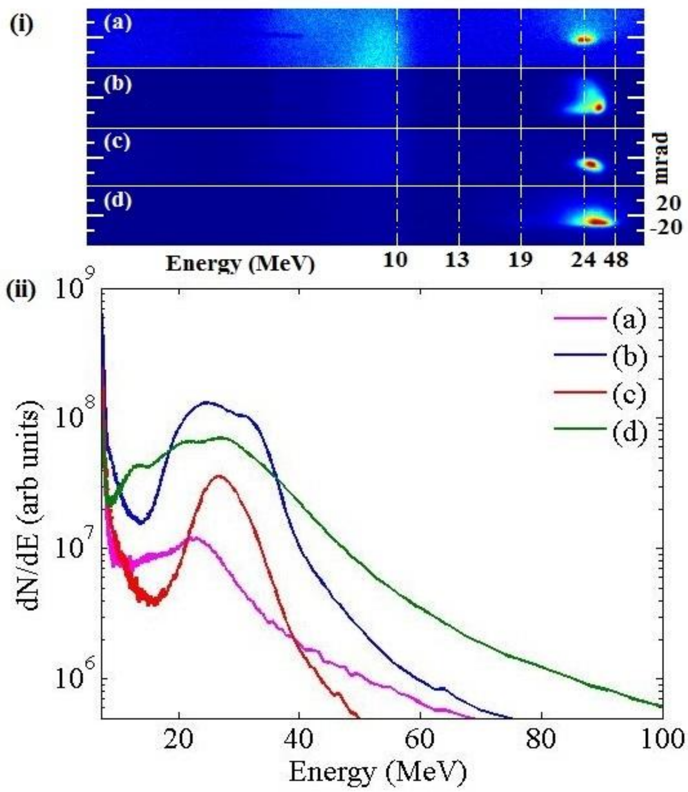

Fig. 5.3: (i) Raw images of series of dispersed electron beams from He at a density of 5.8×10^{19} cm^{-3}. (ii) Spectra of the corresponding raw images.

2. Electron beams recorded from mixed gas-jet target of He + N_2: In case of mixed gas target, effect of ionization induced injection was observed and generation of relativistic electron beams were observed at a lower threshold density of ~2.1×10^{19} cm^{-3} at gas mixture compositions of He + 7.5% N_2 compared to the self-injection threshold of ~5.8×10^{19} cm^{-3} observed with He. By gradually increasing the backing pressure of He, keeping N_2 pressure fixed, plasma density could be varied up to ~7.1×10^{19} cm^{-3} (He + 2.5% N_2), thereby achieving density both below and above the self-injection threshold. The spectra are recorded consecutively, and effect of change in plasma density is clearly visible (Fig. 5.2 c-d), and in fact at the end of the series similar feature was reproduced when density was brought back to lower density regime of ~2.1×10^{19} cm^{-3} (Fig. 5.2 c xiii), which indicates a signature of very good

stability of the accelerator. The maximum energy of the electrons varied from ~55 MeV at lower density of ~2.1×10^{19} cm^{-3} to a maximum of ~90 MeV at ~4.2×10^{19} cm^{-3} [Fig. 5.2 c (iv) - (vi)], and decreased to ~45 MeV with further increase in the density [Fig. 5.2 c (ix) - (x)]. The spectra observed were mostly quasi-thermal. Maximum energy observed was similar to that of He in similar density regime however QM feature was absent. Total charge is ~20-22 pC above 7 MeV, and with change in density, flux in the different energy regime varied.

3. Electron beams recorded from N_2 gas-jet target: At a threshold density of ~2×10^{19} cm^{-3}, generation of relativistic electron beams were observed with average maximum energy was ~40 MeV with a shot to shot jitter of ± 10 MeV and the spectra observed was quasi-thermal (Fig. 5.2 e-f). Electron beam charge above 7 MeV was ~22 pC. Detailed statistics of electron beam spectra obtained from pure N2 gas-jet target is shown in Fig. 5.4.

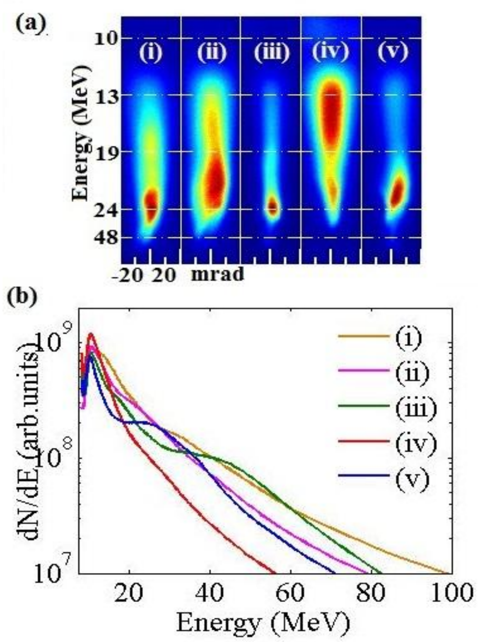

Fig. 5.4: (i) Raw images of series of dispersed electron beams from N_2 at a density of 2×10^{19} cm^{-3}. (ii) Spectra of the corresponding raw images.

5.4. Discussion:

5.4.1. Identification of different acceleration mechanisms:

The experimental study was performed using fixed laser pulse duration of ~55 fs, with plasma density in the range of ~2–7.1×10^{19} cm^{-3}. This corresponds to L/λ_p~2.2-4.1, i.e. a regime of $L>\lambda_p$ and P/P_c~12-43.

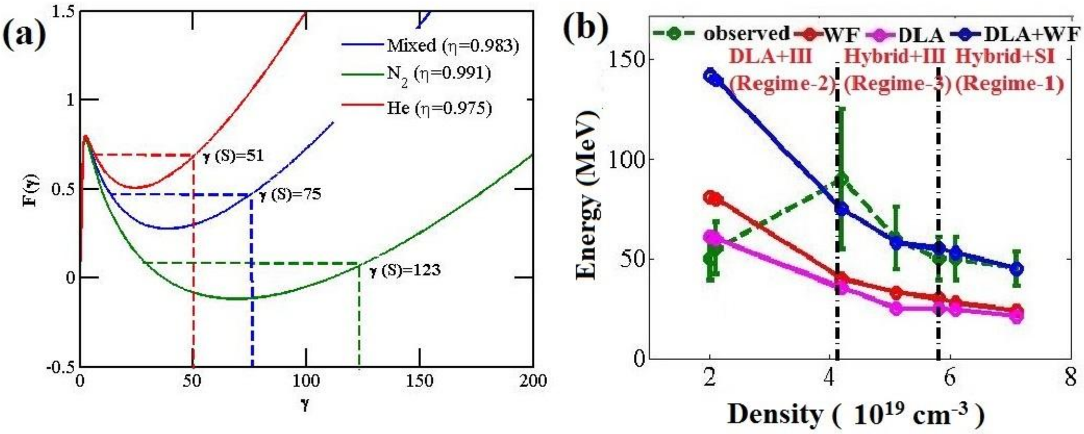

Fig. 5.5: (a) Variation of $F(\gamma)$ as a function of γ for ω_{b0}/ω=0.2, α_0=0.03 and η=0.975 (for He) for density 5.8×$10^{19}$$cm^{-3}$, η=0.983 (for mixed) for density 4×$10^{19}$$cm^{-3}$ and η=0.991 (for N_2) for density 2×$10^{19}$$cm^{-3}$. $\gamma(S)$ shows the maximum energy of the electrons. (b) Identification of different acceleration regime by theoretically estimating energy contributions from DLA (magenta) and wakefield (red) at various densities. Experimentally observed maximum electron energies are also shown (green) and compared to DLA + wakefield (blue). Error bars corresponds to spectrograph resolution/shot-to-shot jitter.

In Fig. 5.5 (a) we have shown the theoretical estimation of the maximum energy gain of electrons through DLA following using Eq. (2.44) discussed in section-2.3.2 of Chapter-2, for three different gas targets of He, mixed and N_2 at respective densities of ~5.8×10^{19} cm^{-3}, ~4.1×10^{19} cm^{-3} and ~2×10^{19} cm^{-3}. In Fig. 5.5 (b), we have shown a comparison of the observed maximum electron energies (green dashed curve) with theoretically estimated maximum electron energies from wakefield using Eq. (2.11) discussed in section-2.2.1 of Chapter-2 (red curve), from DLA (magenta curve) and the total energy gain from wakefield and DLA (blue curve) for the present range of density used in the experiment. Error bars corresponds to the spectrograph resolutions at respective electron energies, except for a data point shown for density of 2×10^{19} cm^{-3}. This corresponds to measurements with N_2 gas target where shot-to-shot jitter associated with the mean maximum energy was ~50%, and the spectrograph resolution at that energy was ~35%. Therefore, error bar here corresponds to observed shot-to-shot jitter.

1. He gas-jet target: Threshold density of ~5.8×10^{19} cm^{-3} observed for generation of relativistic electron beams in this case was considered as the self-injection threshold in the present experimental conditions. Observation of quasi-monoenergetic electron beams in this case suggests the formation of bubble and hence presence of strong wakefield. This is consistent with several other reports on quasi-monoenergetic electron beam generation via wakefield acceleration using similar parameters [29-33]. However, since $L>\lambda_p$, one would expect an overlap and interaction of laser field with the injected electrons in the bubble leading to gain in energy from DLA also [5-10]. Results of the theoretical analysis shows that maximum energy gained by electron from DLA is ~25 MeV (γ=51) and contribution from wakefield is estimated to be ~21 MeV. So the total energy from wakefield and DLA (21+25= 46 MeV) matches very well with the observed maximum energy of ~48 MeV, suggesting a hybrid regime of acceleration with almost equal contributions from both wakefield and DLA. This analysis was also applied for the conditions of Shaw *et al.* [5], and was found to explain the observed electron energy with comparable contributions from DLA (66 MeV) and wakefield (66 MeV). Resulting total energy gain of ~132 MeV is almost equal to that observed in the experiment (i.e. >120 MeV). We define this hybrid

regime of acceleration with self-injection (**Hybrid + self-injection**) observed in case of He as '**Regime-1**'.

2. Mixed gas-jet target: With the motivation to study the behavior of the accelerator below the self-injection threshold, we performed the experiment with mixed gas-jet targets where threshold density for generation of relativistic electron beams was found to reduce to ~2.1×10^{19} cm^{-3}, compared to the self-injection threshold. At lower plasma density, strength of wakefield is expected to reduce. On reduction of the plasma density, λ_p increases and this leads to deviation from the bubble matching conditions [34] when all other experimental parameters are kept constant and would not support formation of bubble and generation of strong wakefields. Hence, this suggests acceleration of electrons have taken place through DLA. Moreover theoretical energy estimations from DLA at this density of ~2.1×10^{19} cm^{-3}, also shows a good agreement with observed maximum energy. We define this DLA regime of acceleration with ionization induced injection mechanism (**DLA + ionization induced injection**) observed in case of mixed gas target as '**Regime-2**'. Pure DLA regime of acceleration in mixed gas-jet targets has been identified for the first time. Here role of ionization induced injection may be emphasized which allowed to achieve acceleration at lower density through DLA using such a short laser pulse which otherwise could not be effective. Recent simulation study has also shown favourable role of ionization induced injection for DLA [9,10].

However, on increasing the density in mixed gas-target, effect of increase in the strength of wakefield was observed as at a higher density of ~$4.1\text{-}4.3\times10^{19}$ cm^{-3} [Fig. 5.2 c (iv)-(vi)], we observed increase in the maximum energy to ~90 MeV, having almost equal contributions from DLA and wakefield. However, injection of electrons in this case takes place through ionization induced injection mechanism as this density is below self-injection threshold. We define this hybrid regime of acceleration with ionization induced injection mechanism (**hybrid + ionization induced injection**) observed in case of mixed gas target as '**Regime-3**'. This regime of acceleration is similar to that observed by Shaw *et al.* [5] in mixed gas-jet targets.

With further increase in the plasma density, maximum electron energy reduced: initially slightly lower (similar) to that observed towards threshold density end, however comparatively broad beam with longer lower energy tail were observed close to SI threshold density, as seen in Fig. 5.2 c (viii)-(x). At density higher than SI threshold density, at ~7.1×10^{19} cm^{-3}, Fig. 5.2 c (xi)-(xii), significant decrease in electron energy was observed. With increase in density, maximum energy of electrons reduced as shown in Fig. 5.2 c (viii-xii), which is in accordance with that predicted theoretically from both wakefield and DLA mechanism of acceleration.

Table. 5.1: Summary of different acceleration and injection mechanism for different gas-jet targets at different plasma densities

Gas Target	**Plasma Density**	**Maximum Energy (MeV)**	**Acceleration mechanism**	**Injection Mechanism**
He	$5.8\times10^{19}cm^{-3}$	46±10	Hybrid	Self-Injection
Mixed ($He+N_2$)	$2.1\times10^{19}cm^{-3}$	55±13	DLA	Ionization Induced Injection
Mixed ($He+N_2$)	$4.2\times10^{19}cm^{-3}$	90±35	Hybrid	Ionization Induced Injection
Mixed ($He+N_2$)	$5.1\times10^{19}cm^{-3}$	60±15	Hybrid	Ionization Induced Injection
Mixed ($He+N_2$)	$6.1\times10^{19}cm^{-3}$	50±10	Hybrid	Self-Injection assisted with Ionization Induced Injection
Mixed ($He+N_2$)	$7.1\times10^{19}cm^{-3}$	45±9	Hybrid	Self-Injection assisted with Ionization Induced Injection
N_2	$2\times10^{19}cm^{-3}$	40±10	DLA	Ionization Induced Injection

3. N_2 gas-jet target: To further confirm the role of ionization induced injection in DLA, experiment was also performed using N_2 gas target, where lower threshold density of ~2×10^{19} cm^{-3} was observed (Fig. 5.2 e-f) suggesting a pure DLA regime as observed in mixed gas targets on the same token.

A summary of the different gas-jet targets, maximum electron energy gained at different plasma densities and the applicable acceleration and injection mechanism is given in Table-5.1.

5.4.2. 2D-PIC simulation using code EPOCH to verify different regimes of acceleration:

The simulation was performed in a moving window frame with box size of 60×80 µm and resolution of λ/30 in longitudinal and transverse directions respectively. Laser pulse of 55 fs (L=16.5 µm) duration and intensity of 5×10^{18} W/cm^2, propagating along Z with polarization along Y direction, enters the simulation box from left and interacts with the plasma of 500 µm of uniform density. Fig. 5.6 shows the snapshots of the density profiles and corresponding normalized laser and wakefields obtained from He at a density of 5.8×10^{19} cm^{-3} at a time step of 1040 fs (Fig. 5.6 a), mixed gas target at a density of 4×10^{19} cm^{-3} at a time step of 1740 fs (Fig. 5.6 c), mixed gas target at a density of 2.1×10^{19} cm^{-3} at a time step of 1040 fs (Fig. 5.6 e) and N_2 gas target at a density of 2×10^{19} cm^{-3} at a time step of 1040 fs (Fig. 5.6 g).

It can be seen that, in case of He at a plasma density of 5.8×10^{19} cm^{-3} (Fig. 5.6 a & b), laser pulse modulation and pulse compression up to L~8 µm with bubble formation and strong wakefield generation with amplitude >1, has been observed. Hence, self-injection of electrons through wave breaking is observed and the injected electrons are also observed to oscillate in the bubble suggesting the contribution of

DLA. This defines a hybrid regime of acceleration. In case of mixed gas target, at a plasma density of 4×10^{19} cm^{-3} (Fig. 5.6 c & d), during initial propagation although a channel like structure tending towards bubble formation was observed with very mild laser pulse modulation, however with further propagation laser, increased pulse modulation was observed leading to initiation of bubble formation and strengthening of wakefield suggesting a hybrid regime acceleration. Since, amplitude is still <1, injection could be only due to ionization induced injection mechanism. However, at the observed threshold plasma density of 2.1×10^{19} cm^{-3} in case of mixed gas targets (Fig. 5.6 e & f), proper channel formation is observed with negligible pulse modulation and further reduction in the strength of wakefield suggesting a pure DLA regime. Simulations performed with N_2 gas target at a density of 2×10^{19} cm^{-3}, also shows clear channel formation with betatron oscillation of electrons inside it with negligible strength of wakefield. This also suggests a pure DLA regime of acceleration. The gradual decrease in wakefield amplitude with decrease in density leads to transformation from a hybrid regime to DLA dominated regime, as discussed above in the context of experimental observations. It may be noted that, hybrid regime of acceleration observed here with betatron oscillations inside bubble is similar to that also reported by Shaw *et al* (c/f from Fig. 9 in Ref. 5) and by Feng *et al*. (c/f from Fig.1a and b in Ref. 35).

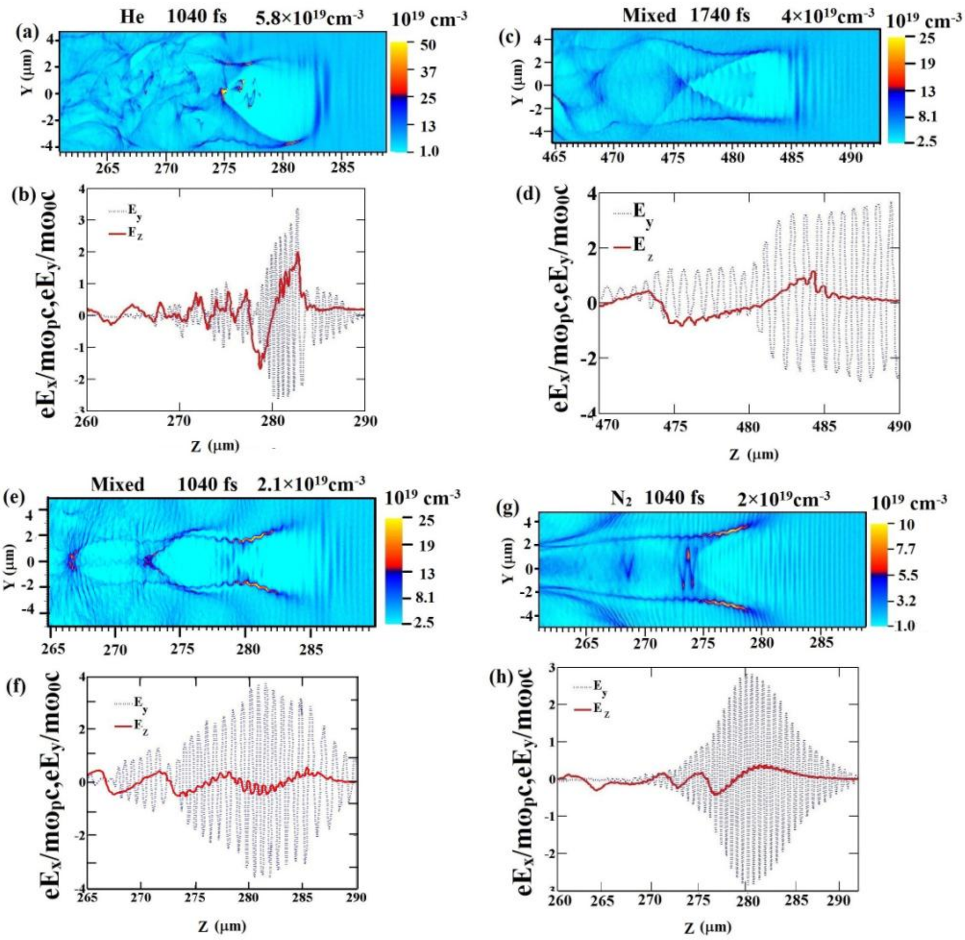

Fig. 5.6: Electron density profiles and corresponding lineouts of normalized laser field E_y (blue dot) and wakefield E_z (red solid). (a)-(b) for He at 1040fs for a density of 5.8×10^{19} cm^{-3}, (c)-(d) for mixed (He+N_2) target at 1740fs for a density of 4×10^{19} cm^{-3}, and (e)-(f) for mixed (He+N_2) target at 1040fs for a density of 2.1×10^{19} cm^{-3} and (g)-(h) for N_2 at 1040fs for a density of 2×10^{19} cm^{-3}.

Further separate contribution from wakefield and DLA has been quantified for the present cases using Eq. (4.1) and (4.2) discussed in Chapter-4 and is shown in Fig. 5.7 (i, ii & iii) respectively for He, mixed gas and N_2 gas targets.

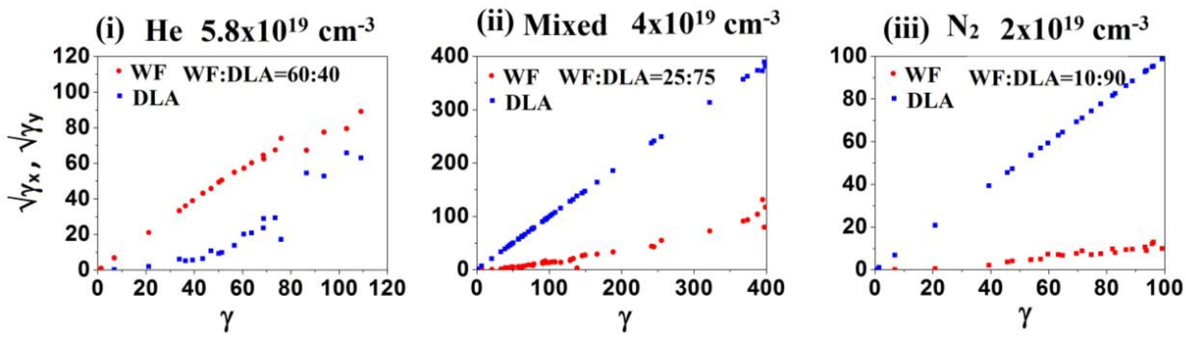

Fig. 5.7: Estimation of energy contributions from DLA and wakefield derived from simulations for (a) He at density of $5.8\times10^{19}cm^{-3}$, (b) mixed (He+N_2) at a density of $4\times10^{19}cm^{-3}$ and (c) N_2 at a density of $2\times10^{19}cm^{-3}$.

For deducing the contribution of DLA and wakefield the maximum value of E_z, E_y, P_z and P_y were taken at each time step of 20 fs, in which case all the macro electrons present in the simulation box was considered and no sampling was done to reduce the number of electrons. In case of He, both wakefield and DLA has equal contributions of ~60% and ~40% respectively suggesting a hybrid regime with self-injection (Regime-1). In case of mixed gas target, at comparatively lower density, wakefield contribution reduces to ~20-25%, but still defines a hybrid regime but with ionization induced injection (Regime-3). In case of N_2 at further lower density, wakefield contribution is very negligible, ~5-10% only, and therefore describes a pure DLA in channel with ionization induced injection (Regime-2).

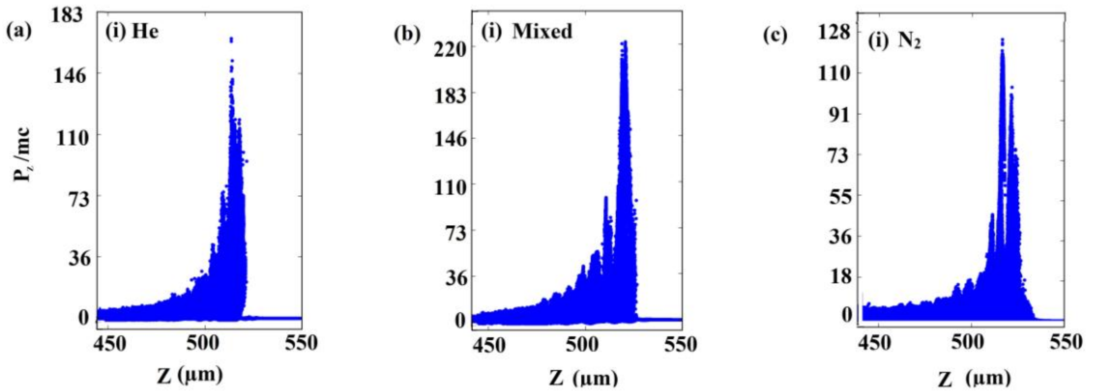

Fig. 5.8: Plot of normalized (i) P_z vs Z after the propagation of 500μm for (a) He at density of $5.8\times10^{19}cm^{-3}$, (b) mixed (He+N_2) at a density of $4\times10^{19}cm^{-3}$ and (c) N_2 at a density of $2\times10^{19}cm^{-3}$.

Further, in Fig. 5.8 (a-c) we plot normalized longitudinal momentum P_z vs Z for He, mixed gas and N_2. In the case of He at a density of 5.8×10^{19} cm^{-3}, acceleration of electrons upto ~36-73 MeV, in case of mixed gas target at a density of 4×10^{19} cm^{-3} energy gain of electron upto ~73-110 MeV and in case of N_2 at a density of 2×10^{19} cm^{-3}, acceleration of electrons upto ~36-55 MeV are observed which is found to be consistent with the experimental observed values. The maximum value of energy gain is considered not at the tail of the distribution but at an intermediate point where significant number of electrons are present. It may be noted that as the contribution of DLA increases towards lower density in case of mixed and N_2 targets, bunching of electrons is also seen to be prominent in the P_z vs Z plot which is a signature of dominant DLA mechanism [36-38].

5.4.3. Observation of surface wave generation in 2D PIC simulations:

Interestingly, electron density modulations (surface waves) at the channel boundaries with periodicity of ~1 μm was identified in case of mixed and N_2 gas targets at lower densities (Fig. 5.9 b & c). Generation of surface waves in laser created channels were reported in earlier studies using longer laser pulses of few hundred of fs

[4, 39-41]. Wavelength of density modulations for densities approaching at channels >0.1n_c is estimated to be ~2-3 μm. Generation of surface waves at the channel boundaries in case of mixed and N_2 gas-jet target, suggests dominant acceleration mechanism of DLA [4], as it has been considered as a pre-acceleration mechanism for DLA [4,39,40]. It may be noted that, in case of He (Fig. 5.9 a), where presence of strong wakefield has been identified, very faint surface wave modulations were generated only at the channel boundaries and not at the bubble boundaries. Generation of surface waves using shorter laser pulse duration of ~55 fs in a gas jet target has been shown for first time.

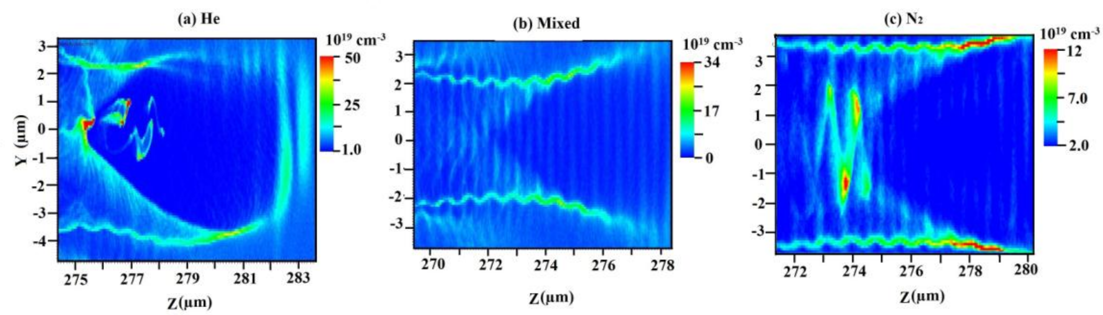

Fig. 5.9: Expanded view of electron density profiles simulated at 1040fs (a) He, (b) mixed (He+N_2) and (c) N_2 targets, showing electron density modulation (SW generation) at channel boundaries in case of mixed and N_2.

5.4.4. Effect of different regimes of acceleration on electron beam parameters:

Next, we discuss the effect of three distinct regimes (Regime: 1, 2, 3) on electron beam properties viz. spectrum, charge, beam profile and pointing stability.

1. Spectrum: In case of Regime-1, observed in He target, generation of quasi-monoenergetic electron beams is typical for bubble regime of acceleration as reported by various groups [29-32] and also observed in our earlier report [33]. Whereas, for

Regime-2 & 3, observed with mixed and N_2 gas target, the spectra are quasi-thermal with almost 100% energy spread, suggesting role of ionization induced injection.

2. Charge: Another manifestation of ionization induced injection over self-injection is the observed increase in the beam charge above 7 MeV from ~5 pC in case of He to ~22 pC in case of mixed gas and N_2 target [12, 13].

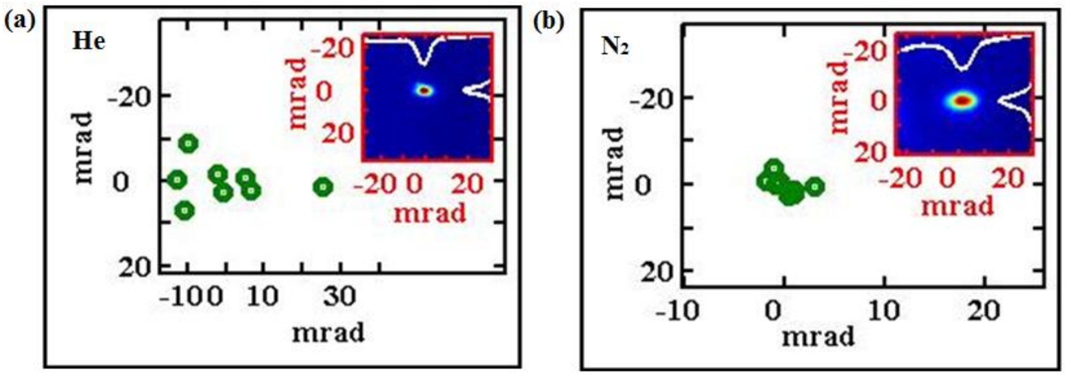

Fig. 5.10: Pointing stability and typical electron beam profiles (white curves show lineouts) for (a) He gas-jet target at a density of 5.8×10^{19}cm^{-3} and (b)N_2 gas-jet target at a density of 2×10^{19} cm^{-3}.

3. Ellipiticity: Without magnet in path, collimated electron beams were recorded on the phosphor screen for He gas-jet target having FWHM divergence in the range of ~14-21 mrad (average: ~16 mrad) and ~9-18 mrad (average: ~13 mrad) in the horizontal and vertical directions respectively. A typical electron beam profile, having a FWHM beam size of ~5 mm (~14 mrad) and ~3.3 mm (~10 mrad) respectively in the horizontal and vertical directions, is shown in the inset of Fig. 5.10 (a). As observed, electron beams generated have an elliptical profile with an average ellipticity of ~1.3 (Hybrid: Regime-1). With N_2 gas target also collimated electron beams were recorded on the phosphor screen however with a comparatively larger divergence in the horizontal direction i.e. laser polarization direction. FWHM

divergence was in the range of ~16-29 mrad (average: ~20 mrad) and 11-20 mrad (average: ~14 mrad) in the horizontal and vertical directions respectively. A typical electron beam profile is shown in the inset of Fig. 5.10 (b), having a FWHM beam size of ~6.5 mm (~19 mrad) and ~4 mm (~11 mrad) respectively in the horizontal and vertical directions. Average ellipticity of the electron beam was slightly higher to ~1.5 (DLA: Regime-2). The asymmetry of the electron beam profiles along laser polarization directions cannot be associated with the ellipticity in laser focal spot itself, as substantial modification of the laser spot size occurs due to evolution of the laser in plasma by various non-linear processes. Various earlier studies also reported observation of elliptical electron beam profile and showed that it had no correlation with the elliptical laser focal spot [43,44].

Further, while making comparative study of electron beam ellipticity generated due to two different acceleration mechanism, it would also be necessary to consider the Twiss parameters i.e. emittance and its effect on propagation and measurement. Beam emittance has been observed to increase due to interaction of electrons with the laser field [37, 43]. Hence, in the present case also, significant interaction of the electron beams with the accelerating electrons would lead to increase in emittance in the laser polarization direction compared to that in the perpendicular direction, leading to elliptical profile of the electron beams. Similar elliptical beam profile has also been observed earlier where there is significant contribution of laser electric field on electron energy gain [5, 6, 43]. This is also evident in our simulation performed (Fig.5.6 g) which shows transverse oscillation and momentum gain of electrons and the effect is more pronounced in case of N_2. However, the measurement of electron beam emittance is a complex problem and is beyond the scope of the present thesis. Also in the present case, stable propagation of laser inside plasma even for high Z gas-jet targets of N_2 was observed as any laser pulse filamentation would have led to multiple electron beam formation [46]. In many previous studies also stable focusing and propagation of laser has been observed in high-Z gases [18, 19, 47].

4. Beam pointing stability: Electron beam pointing stability was found to be better (~3×4 mrad) in case of N_2 (Regime-2: DLA + ionization induced injection), compared to that observed in case of He (~24×9 mrad) (Regime-1: Hybrid + self-injection) (Fig. 5.10). This could be attributed to the fact that uncontrolled injection in a larger bubble volume in case of self-injection (He) with further interaction with laser field will lead to larger pointing variation, compared to ionization induced injection (N_2 target) where injection primarily occurs along the laser axis.

5.5: Conclusion:

An experimental demonstration of direct laser acceleration (DLA) and hybrid (DLA + wakefield) regime of acceleration of electrons was presented in the $L>\lambda_p$ regime. Ti:sapphire short laser pulses of ~55 fs duration interacted with three different gas targets of He, mixed gas (He + few%N_2) and N_2, in the density range of 2-7.1×10^{19}cm^{-3}, in a single experimental set up. Three different regimes of acceleration are identified: hybrid + self-injection (Regime-1) in case of He, DLA + ionization induced injection (Regime-2) in case of mixed and N_2 at lower density, and transforming to hybrid + ionization induced injection (Regime-3) at comparatively higher density in case of mixed gas target. Results were supported by 2D PIC simulations. Interestingly, generation of surface waves were observed in the simulations in case of mixed and N_2 gas targets, which could be a pre-acceleration mechanism to DLA. Observation of pure DLA with ionization induced injection using short laser pulse of few tens of fs duration in mixed and N_2 gas targets have not been reported till date.

References

[1] Gamma-rays from harmonically resonant betatron oscillations in a plasma wake, S. Cipiccia, M. R Islam, B. Ersfeld, R. P. Shanks, E. Brunetti, *et al.*, *Nat. Phys.***7**, 867 (2011).

[2] Femtosecond x rays from laser-plasma accelerators, S. Corde, K. Ta Phuoc, G. Lambert, R. Fitour, V. Malka *et al.*, *Rev. Mod. Phys.*, **85** 1 (2013).

[3] Self-modulated laser wakefield accelerators as x-ray sources, N. Lemos, J. Martins, L. Tsung, F. S. Shaw, J. L. Marsh *et al*., *Plasma Phys. Control. Fusion*, **58**, 034018 (2016).

[4] Characteristics of betatron radiation from direct-laser-accelerated electrons, T. W. Huang, A. P. L. Robinson, C. T. Zhou, B. Qiao, B. Liu *et al*., *Phys. Rev. E.,* **93** 063203 (2016).

[5] Role of Direct Laser Acceleration of Electrons in a Laser Wakefield Accelerator with Ionization Injection, J. L. Shaw, N. Lemos, L. D. Amorim, N. Vafaei-Najafabadi, K. A. Marsh *et al*., *Phys. Rev. Lett.*,**118**, 064801 (2017).

[6] Experimental signatures of direct-laser-acceleration-assisted laser wakefield acceleration, J. L. Shaw, N. Lemos, K. A. Marsh, D. H. Froula and C. Joshi, *Plasma Physics and Controlled Fusion*, **60**, 044012 (2018).

[7] Role of direct laser acceleration in energy gained by electrons in a laser wakefield accelerator with ionization injection, J. L. Shaw, F. S. Tsung, N. Vafaei-Najafabadi, K. A. Marsh, N. Lemos *et al*., Plasma Phys. Control. Fusion, **56**, 084006 (2014).

[8] Estimation of direct laser acceleration in laser wakefield accelerators using particle-in-cell simulations, J. L. Shaw, N. Lemos, K. A. Marsh, F. S. Tsung, W. B. Mori *et al*., *Plasma Physics and Controlled Fusion*,**58**, 034008 (2016).

[9] Synergistic Laser-Wakefield and Direct-Laser Acceleration in the Plasma-Bubble Regime, Xi Zhang, V. N. Khudik, and S. Gennady, *Phys. Rev. Lett*.,**114**, 184801 (2015).

[10] Laser wakefield and direct acceleration with ionization injection, Xi Zhang, V. N Khudik, A. Pukhov and G. Shvets, *Plasma Phys. Control. Fusion*, **58**, 034011(2016).

[11] Theory of ionization-induced trapping in laser-plasma accelerators, M. Chen , E. Esarey , C. B. Schoeder , C. G. R. Geddes and W. P. Leemans, *Phys. Plasmas* **19** 033101 (2012).

[12] C. McGuffey, A. G. R. Thomas, W. Schumaker, T. Matsuoka, V. Chvykov, F. J. Dollar, G. Kalintchenko, V. Yanovsky, A. Maksimchuk and K. Krushelnick Phys. Rev. Lett. **104**, 025004 (2010).

[13] Injection and Trapping of Tunnel-Ionized Electrons into Laser-Produced Wakes, A. Pak, K. A. Marsh, S. F. Martins, W. Lu, W. B. Mori *et al*., *Phys. Rev. Lett*.,**104**, 025003 (2010).

[14] Generation and analysis of quasimonoenergetic electron beams by laser-plasma interaction in transitional region from the self-modulated laser wakefield to bubble acceleration regime, S. Masuda and E. Miura , *Phys. Plasmas*,**16**, 093105(2009).

[15] Characterization of electron beams produced by ultrashort (30 fs) laser pulses, V. Malka, J. Faure, J. R. Marquès, and F. Amiranoff, *Phys. Plasmas*, **8**, 2605 (2001).

[16] Multi-MeV Electron Beam Generation by Direct Laser Acceleration in High-Density Plasma Channels, C. Gahn, G. D. Tsakiris, A. Pukhov, J. Meyer-ter-Vehn, G. Pretzler *et al.*, *Phys. Rev. Lett.*, **83**, 4772 (1999).

[17] Electron Acceleration in Cavitated Channels Formed by a Petawatt Laser in Low-Density Plasma, S. P. D. Mangles, B. R. Walton, M. Tzoufras, Z. Najmudin, R. J. Clarke *et al.*, *Phys. Rev. Lett.*,**94**, 245001 (2005).

[18] Quasimonoenergetic electron beams from laser wakefield acceleration in pure nitrogen, M. Z. A. Mo, A. Ali, S. Fourmaux, P. Lassonde, J. C. Kieffer, and R. Fedosejevs, *Appl. Phys. Lett.*, **100**, 074101 (2012).

[19] Small energy spread electron beams from laser wakefield acceleration by self-evolved ionization injection, J. Wang, J. Feng, C. Zhu, Y. Li, Y. He *et al*., *Plasma Phys. Control. Fusion*, **60**, 034004 (2018).

[20] Characteristics of electron beam in laser wakefield accelerator using pure nitrogen gas, J. Kim, Y. H. Hwangbo, and K. N. Kim, *Plasma Phys. Control. Fusion*, **60**, 034008 (2018).

[21] Quasi-monoenergetic electron beams from a few-terawatt laser driven plasma acceleration using a nitrogen gas jet, B. S. Rao, A. Moorti, J. A. Chakera, P. A. Naik, and P. D. Gupta, *Plasma Phys. Control. Fusion*, **59**, 065006 (2017).

[22] Cascade Acceleration of Electrons by Laser Wakefield and Direct Laser Field, M. Adachi, E. Miura, S. Kato, K. Koyama, S. Masuda *et al*., *Japanese Journal of Applied Physics*, **45**, 4214 (2006).

[23] Contemporary particle-in-cell approach to laser-plasma modelling, T. D. Arber, K. Bennett, C. S. Brady, A. Lawrence-Douglas, M. G. Ramsay *et al.*, *Plasma Physics and Controlled Fusion*, **57,** 1 (2015).

[24] Supersonic gas jet target for generation of relativistic electrons with 12TW-50fs laser pulse, T. Hosokai, K. Kinoshita, T. Watanabe, K. Yoshii, T. Ueda *et al*., 2002 Proc. 8th European Particle Accelerator Conf. (EPS) p 981 (2002).

[25] Effect of chirp on self-modulation and laser wakefield electron acceleration in the regime of quasimonoenergetic electron beam generation, B. S. Rao, A. Moorti, P. A. Naik, and P. D. Gupta, *Phys. Rev. Special Topic-Accl. And Beams*, **16**, 091301 (2013).

[26] Calibration and cross-laboratory implementation of scintillating screens for electron bunch charge determination, T. Kurz, J. P. Couperus, J. M. Krämer, H. Ding, S. Kuschel *et al.*, Rev. Sci. Instrum. **89**, 093303 (2018).

[27] Absolute calibration for a broad range single shot electron spectrometer, Y. Glinec, J. Faure, A. Guemnie-Tafo, V. Malka, H. Monard *et al*., Rev. Sci. Instrument **77**, 103301 (2006).

[28] Absolute calibration of two DRZ phosphor screens using ultrashort electron bunch, Y. C. Wu, B. Zhu, K. G. Dong, Y. H. Yan, and Y. Q. Gu, Rev. Sci. Instrument, **83**, 026101 (2012).

[29] Generation of Quasimonoenergetic Electron Bunches with 80-fs Laser Pulses, B. Hidding, K.-U. Amthor, B. Liesfeld, H. Schwoerer, S. Karsch *et al., Phys. Rev. Lett.*, **96**, 105004 (2006).

[30] Demonstration of quasi-monoenergetic electron-beam generation in laser-driven plasma acceleration, E. Miura, K. Koyama, S. Kato, N. Saito, M. Adachi *et al.*, *Appl. Phys. Lett.*,**86**, 251501 (2005).

[31] Observation of strong correlation between quasimonoenergetic electron beam generation by laser wakefield and laser guiding inside a preplasma cavity, T. Hosokai, K. Kinoshita, T. Ohkubo, A. Maekawa, M. Uesaka *et al.*, *Phys. Rev. E*, **73**, 036407 (2006).

[32] Tomography of Injection and Acceleration of Monoenergetic Electrons in a Laser-Wakefield Accelerator, C.-T. Hsieh, C.-M.Huang, C.-L.Chang, Y.-C. Ho, Y.-S. Chen *et al., Phys. Rev. Lett.*, **96**, 095001 (2006).

[33] Generation of quasi-monoenergetic electron beams with small normalized divergences angle from a 2 TW laser facility, B. S. Rao, A. Moorti, R. Rathore, J. A. Chakera, P. A. Naik *et al.*, *Phys. Rev.* ST Accel. Beams,**17**, 011301 (2014).

[34] Generating multi-GeV electron bunches using single stage laser wakefield acceleration, W. Lu, M. Tzoufras, C. Joshi, F. S. Tsung, W. B. Mori *et al*., *Phys. Rev. ST Accel. Beams* **10,** 061301 (2007).

[35] Gamma-ray emission from wakefield-accelerated electrons wiggling in a laser field, J. Feng, Y. Li, J. Wang, D. Li, F. Li *et al.*, *Nature Scientific Reports* **9**, 2531 (2019).

[36] Particle acceleration in relativistic laser channels, A. Pukhov, Z.-M.Sheng, and J. Meyer-ter-Vehn, *Phys. Plasmas*, **6**, 2847 (1999).

[37] Laser-driven coherent betatron oscillation in a laser-wakefield cavity**,** K. Nèmeth, B. Shen, Y. Li, H. Shang, R. Crowell *et al.*, *Phys. Rev. Lett*. **100**, 095002 (2008).

[38] Observation of fine structures in laser-driven electron beams using coherent transition radiation, Y. Glinec, J. Faure, A. Norlin, A. Pukhov, and V. Malka, *Phys. Rev. Lett.* **98,** 194801 (2007).

[39] High-Power, Kilojoule Class Laser Channeling in Millimeter-Scale Underdense Plasma, L. Willingale, P. M. Nilson, A. G. R. Thomas, J. Cobble, R. S. Craxton *et al., Phys. Rev. Lett*. **106**, 105002 (2011).

[40] Surface waves and electron acceleration from high-power, kilojoule-class laser interactions with underdense plasma, L.Willingale, A. G. R. Thomas, P.M. Nilson, H. Chen, J. Cobble *et al., New J. Phys*., **15**, 025023 (2013).

[41] Channeling of Relativistic Laser Pulses, Surface Waves, and Electron Acceleration, N. Naseri, D. Pesme, W. Rozmus and K. Popov, *Phys. Rev. Lett.*, **108,** 105001 (2012).

[42] Electron acceleration in cavitated laser produced ion channels, N. Naseri, D. Pesme, and W. Rozmus, *Phys. Plasmas*, **20**, 103121 (2013).

[43] Laser-wakefield acceleration of monoenergetic electron beams in the first plasma-wave period, S. P. D. Mangles, A. G. R. Thomas, M. C. Kaluza, O. Lundh, F. Lindau *et al*., *Phys. Rev. Lett*. **96**, 215001 (2006).

[44] Study of near-GeV acceleration of electrons in a non-linear plasma wave driven by a self-guided laser pulse, S. Kneip, S. R. Nagel, C. Bellei, O. Cheklov, R. J. Clarke *et al*., *Plasma Phys. Control. Fusion* **53**, 014008 (2011).

[45] Ultralow emittance electron beams from a laser-wakefield accelerator, R. Weingartner, S. Raith, A. Popp, S. Chou, J. Wenz *et al*., *Phys. Rev. Special Topics - Accelerators and Beams* **15**, 111302 (2012).

[46] Challenges in plasma and laser wakefield accelerated beams diagnostic, A. Cianchi, M. P. Anania, M. Bellaveglia, M. Castellano, E. Chiadroni *et al.*, *Nuclear Instruments and Methods* **720**, 153 (2013).

[47] Effect of laser contrast ratio on electron beam stability in laser wakefield acceleration experiments, S. P. D. Mangles, A. G. R. Thomas, M. C. Kaluza, O. Lundh, F. Lindau *et al*., *Plasma Phys. Control. Fusion*, **48**, B83 (2006).

[48] Influence of atomic species on laser pulse propagation in underdense plasmas, N.C. Pathak, C.A.Cecchetti, A.Gamucci, A.Giulietti, D.Giulietti *et al*., *Nuclear Instruments and Methods in Physics Research A* **653**, 12

CHAPTER 6

Investigation of laser plasma acceleration in high-Z N_2 gas-jet target and optimization of threshold plasma density by mixing He and its effect on electron beam parameters

6.1. Motivation:

Direct laser acceleration (DLA) has been considered recently as an important acceleration mechanism governing laser plasma interactions, as it has shown the potential to generate high energy betatron radiation compared to wakefield [1-4] and has been identified along with wakefield in a $L>\lambda_p$ regime in a mixed gas-target of He + N_2 [5, 6]. This regime of acceleration i.e. hybrid acceleration mechanism have the advantage of doubling the energy gain of electrons in a wakefield from DLA [5-10]. We have also identified hybrid regime of acceleration of electrons in mixed and He gas target in a short laser pulse regime of $L>\lambda_p$, and observed such enhancement of electron energy as discussed in Chapter-5. Experimental investigations in mixed gas-targets have been mostly performed in the bubble regime of acceleration where wakefield was found as the dominant acceleration mechanism with broad electron spectra [11-13]. Several attempts in reducing the energy spread of electrons in mixed gas targets have been proposed and recently generation of quasi-monoenergetic electrons have been demonstrated with energy spread of few percent [14-20]. In case of N_2 also, wakefield was suggested as the dominant acceleration mechanism in studies in the regime of $L>\lambda_p$ where there is complete overlap of the laser field with the injected electrons [21-26]. There is no experimental report on pure DLA acceleration mechanism in high Z or mixed gas-jet target in such as short pulse regime of L>λ_p. However, in Chapter-5, we have also identified a pure DLA regime in such a short laser pulse duration regime of L>λ_p, in high Z N_2 and mixed gas-jet target of He + N_2. This regime of pure DLA in high Z targets is interesting as it has the potential of generating high charge electron beams oscillating in the plasma channel thereby can generate high flux betatron radiation. However, the electron beams generated was mostly quasi-thermal. In this context, further detailed experimental investigation of DLA in high Z gas-targets in a short laser pulse regime of L≥λ_p and optimizing the parameters for generating good quality electron beams would be of interest.

With this motivation, an experimental study of laser plasma acceleration in N_2 and N_2-He mixed gas-jet target in a L~λ_p regime, using laser pulses of duration ~60-70 fs with laser intensity in the range of a_0~3.5-4.2 was performed. In this study, at first experiments were performed with pure N_2 gas-jet target where generation of relativistic electron beams were observed at a threshold density of ~1.6×10^{18} cm^{-3}. Further, we have varied the threshold density by gradually varying the doping concentration of He in N_2 and studied the effect of variation of threshold density on the properties of electron beams. The doping concentration of He in N_2 was varied from N_2 + 50% He to N_2 + 98% He and correspondingly the threshold density varied from ~2-4.3× 10^{18} cm^{-3}. At an optimum fraction of 50% of He in $N_{2,}$ generation of quasi-monoenergetic electron beams with average energy spread of ~21%, were observed at threshold density of ~2×10^{18} cm^{-3}, with higher average peak energy of ~168 MeV and average total beam charge of ~220 pC. Electron acceleration could be attributed to the direct laser acceleration as well as hybrid mechanism with increase in strength of wakefield with increase in density. Observation of an optimum fraction of He in N_2 (in turn threshold plasma density) for comparatively better quality electron beam generation was further understood in terms of variation of dephasing rate of electrons in laser field with plasma density. Results are also supported by the 2D PIC simulations performed using code EPOCH [27]. It may be emphasised here that in this investigation we could observe generation of relativistic electron beams at comparatively much lower plasma densities than that presented in chapter-5, owing to the improved and smaller laser focal spot and associated higher laser intensity used. Further, the threshold densities in case of different mixed gas targets were found to be below the self-injection threshold of 5.8×10^{18} cm^{-3} observed for pure He target in similar set up (described in chapter-7), the electron injection could be attributed to ionization induced injection mostly through ionization of inner k-shell electrons of N_2. However, contribution from other background could be present as this is acceleration in a channel, and bubble formation has not taken place. In such scenario, background electron injection from the channel boundary could also take place.

In the present experimental conditions using N_2 gas-jet targets, effect of cluster formation in the laser plasma interaction was not considered as the experiments were performed as very low backing pressures of 0.5-1 bar. For the similar kind of nozzle used in the experiments cluster formation was not considered even for Ar gas-jet targets at higher gas pressures in which case probability of cluster formation is higher compared to N_2 gas-jet targets [28, 29]. In various reported investigations using N_2 gas target with similar experimental conditions also cluster formation has not been considered [21-26].

6.2. Experimental set up and parameters:

Fig.1 shows the schematic of the experimental set up. Ti:sapphire laser pulse of duration ~60 - 70 fs was focused to a spot of ~6.5×6.5 μm^2 (radius at $1/e^2$) using f/5 optics on a gas-jet target, providing a total power (P) of ~17.4 - 20.3 TW and intensity of ~3.7 - 4.3×10^{19} W/cm^2 (a_0~4.2 - 4.5). A well characterized slit nozzle of dimension 1.2 mm × 4 mm was used, and laser was propagated along 4 mm length [30]. High-Z gas target of pure N_2 and mixed gas target of N_2 + varying % of He was used and plasma density was varied in the range of ~1.6 - 4.3×10^{18} cm^{-3}. Electron beam spectrum was recorded using a magnetic spectrograph consisting of C-shaped rectangular magnet with peak magnetic field strength of ~0.9 T (dimensions 10×10×20 cm: pole gap 15 mm) covering a broad energy range of ~15 MeV to 1 GeV, with a resolution of ~8% at 100 MeV and 25% at 300 MeV (for 10 mrad divergence beam). The magnetic spectrograph was set up with provisions for simultaneous recoding of the electron beam profile and the electron beam spectra using three phosphor screens. The magnet was placed ~46 cm from the source, which provides an acceptance angle of ~36 mrad at the entrance of the magnet. Phosphor-1 (Lanex-regular) was placed before the magnet at a distance of 39 cm from the gas-jet for recording of electron beam profile. Phosphor-2 (DRZ-High) was placed at a distance of 70 cm from the source in the laser beam direction for recording electron beam profile as well as spectrum. To estimate energy of the electron beam, undeflected electron beam position on Phosphor-2 was obtained from the correlation between the electron beam positions on Phosphor-1 and Phosphor-2 recorded without magnet in between them. When magnet was inserted in between, dispersed electron could be recorded on Phosphor-2, which covered energy of >80 MeV. Further, Phosphor-3 (DRZ-high) was placed perpendicular to the laser propagation direction in the open side of C-shaped magnet to record the lower energy electrons spectrum from ~15 - 80 MeV. To study the laser plasma interaction and laser channeling inside plasma, shadowgraphy was performed by using the leakage of the main laser beam (λ= 800 nm) as the probe beam with variable delay in the few ps regime and imaged on to a 14 bit CCD camera with a magnification of 2X. The electron beam charge was estimated using standard calibration data available for various phosphor screens used [31-34].

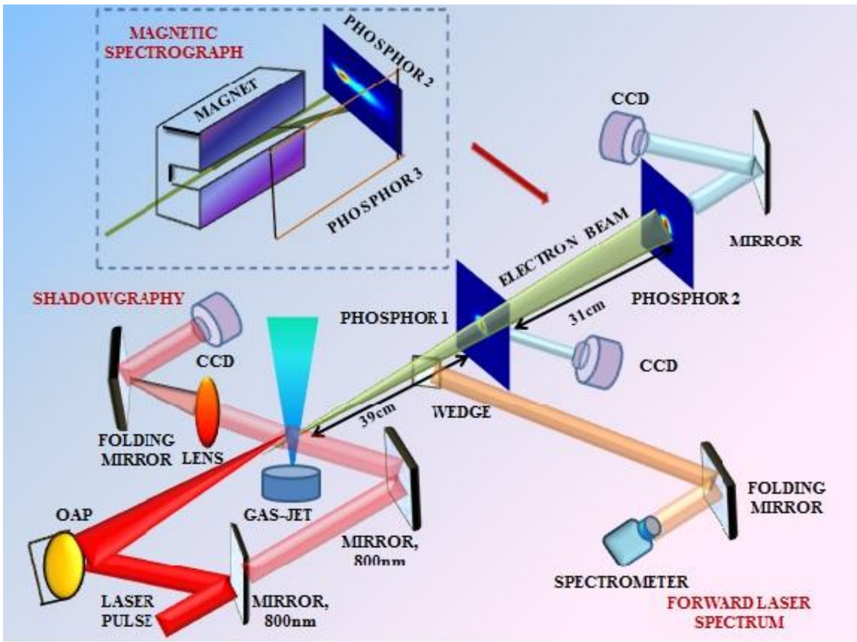

Fig.6.1: Schematic of experimental set up

6.3. Experimental results:

At first, experiments were performed with high Z gas target of pure N_2. Following this, gradually concentration of He in N_2 was increased. Threshold densities for electron beam generation were found to be different for different fraction of He in N_2 which in turn affected the electron beam properties. Various threshold densities observed were: ~1.6×10^{18} cm^{-3} (pure N_2), ~2×10^{18} cm^{-3} (N_2 + 50% He), ~2.3×10^{18} cm^{-3} (N_2 + 58% He), ~3.1×10^{18} cm^{-3} (N_2 + 75% He) and ~4.3×10^{18} cm^{-3} (N_2 + 98% He) respectively. Generation of electron beams in almost every shot was observed during the experiment.

6.3.1. Recording of electron beams generated from pure N_2 gas-jet target:

With pure N_2 gas-jet target, a threshold density was found to be ~1.6×10^{18} cm^{-3}. In Fig. 6.2 (i a-c) we show a series of electron beam profiles with divergence in the range of 5.8 - 6.7 mrad (Avg.: 6.2 mrad). In addition to the narrow directional component, the electron beam profiles were also associated with a large shot-to-shot fluctuating background. Total charge in the narrow beam varied in the range of 65 - 174 pC. Fig. 6.2 (ii a-c) and Fig. 6.2 (iii a-c) shows the corresponding raw image of the dispersed electron beam and spectra respectively. The spectra showed a lower energy cut-off with an average peak of ~100 - 125 MeV, and an exponential broad distribution towards higher energy side. Maximum energy corresponding to 10% of the peak signal was in the range of 136 - 161 MeV (Avg.: 151 MeV). With further increase in the density to ~3.5×10^{18} cm^{-3}, similar electron beam profiles with divergence of the narrow directional part is in the range of 7-10 mrad (Avg.: 8.3 mrad) were observed. (Fig. 6.3 i a-e). Fig.6.3 (ii a-e) and Fig.6.3 (iii a-e) shows the corresponding dispersed electron beams and the spectra with peak energies in the range of 138 - 173 MeV (Avg.: 148 MeV) and maximum energy in the range of 167 - 248 MeV (Avg.: 209 MeV). The spectra observed are mostly quasi-thermal. The total charge in the narrow electron beam was comparatively higher and found to be ~180 – 250 pC.

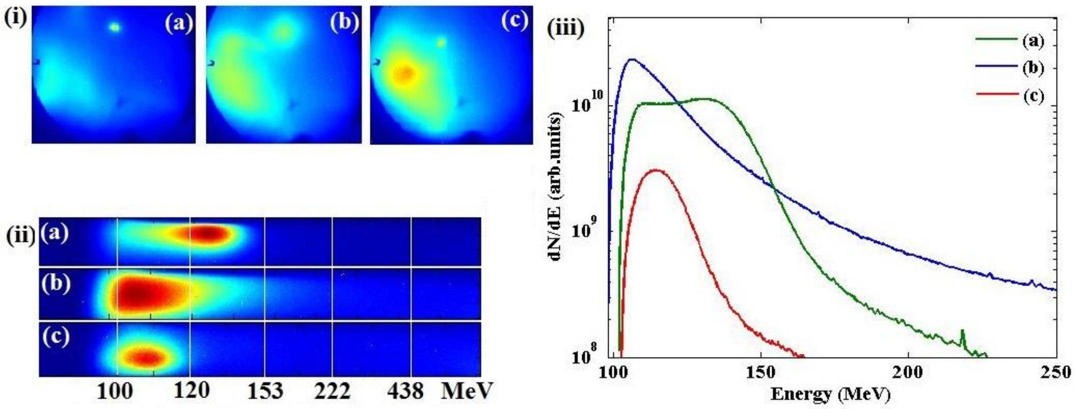

Fig.6.2: Experimental results: N_2 gas-jet target: Threshold density: ~$1.6\times10^{18}cm^{-3}$: (i) (a-c) Electron beam profiles showing narrow intense electron beam with diffused background, (ii) (a-c) Corresponding dispersed raw spectra of narrow e-beam (iii) (a-c) Lineouts of corresponding spectra.

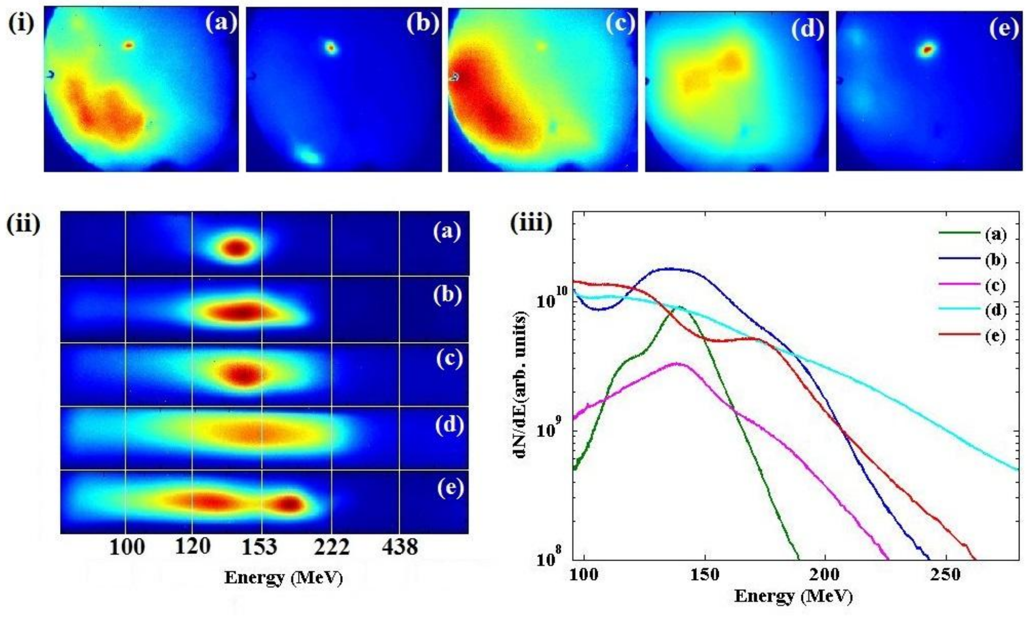

Fig.6.3: Experimental results: N_2 gas-jet target: Density: ~$3.5\times10^{18}cm^{-3}$: (i) (a-e) Electron beam profiles showing narrow intense electron beam with diffused background, (ii) (a-e) Corresponding dispersed raw spectra of narrow e-beam (iii) (a-e) Lineouts of corresponding spectra.

6.3.2. Recording of electron beams generated from mixed gas-jet target of N_2 + 50% He:

Electron beams were generated from mixed gas-jet target of N_2 + 50% He at a threshold density of ~2×10^{18} cm^{-3}. Fig.6.4 (i a-j) and Fig.6.4 (ii a-j) show the raw images of dispersed electron beam spectra and its corresponding lineout. Interestingly, generation of quasi-monoenergetic electron beams was observed with peak energies in the range of 144 - 205 MeV (Avg.: 168 MeV) and energy spread in the range of ~17% - 26% (Avg.: ~21%). Maximum energy was in the range of 171 - 265 MeV (Avg.: 206 MeV). Probability of generation of quasi-monoenergetic electron beams was found to be 65 - 70 % in a series of consecutive shots during the experiment. Fig.6.4 (iii a-d) shows typical electron beam profiles with narrow electron beam with divergence varying in the range of 7 - 9 mrad (Avg.: 7.5 mrad) and an associated diffused background, however the diffused background is comparatively less than that observed in case of pure N_2 gas-jet target. The charge contained in the narrow electron beams was 140 - 300 pC.

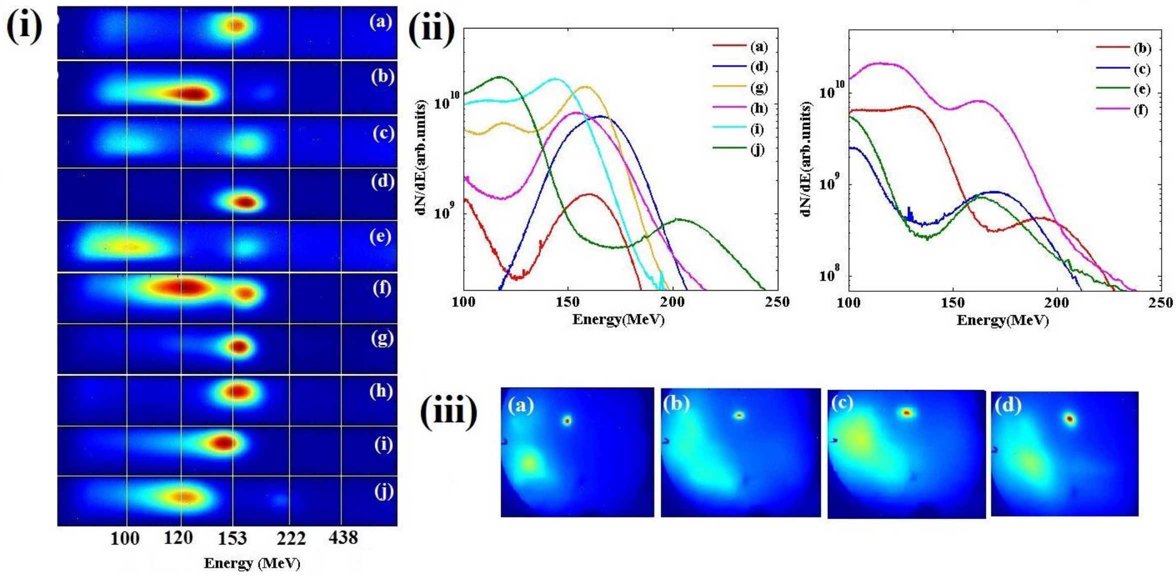

Fig.6.4: *Experimental results: N_2 + 50% He gas-jet target: Threshold density: ~$2\times10^{18}cm^{-3}$: (i) (a-j) Dispersed raw spectra of narrow e-beam generated (ii) (a, d, g, h, i, j) Lineouts of corresponding spectra shown in one frame and (ii) (b, c, e, f) Lineouts of corresponding spectra shown in separate frame for clarity. (iii) Electron beam profiles showing narrow intense electron beam with diffused background.*

6.3.3. Recording of electron beams generated from mixed gas-jet target of N_2 + 58% He, N_2 + 75% He and N_2 + 98% He:

Generation of relativistic electron beams for mixed gas-jet targets of N_2 + 58% He, N_2 + 75% He and N_2 + 98% at threshold densities of ~2.3×10^{18} cm^{-3}, ~3.1×10^{18} cm^{-3} and ~4.3×10^{18} cm^{-3} respectively. Fig.6.5, Fig. 6.6 & Fig. 6.7 show typical raw images of the dispersed electron beams and corresponding lineout of consecutive shots obtained from mixed gas-jet targets of N_2 + 58% He, N_2 + 75% He and N_2 + 98% He respectively. For N_2 + 58% He, at a threshold density of ~2.3×10^{18} cm^{-3}, electrons with peak energies in the range of 117 - 177 MeV (Avg.: 153 MeV) and maximum energy in the range of 147 - 213 MeV (Avg.: 184 MeV) were generated (Fig.6.5). Probability of generation of quasi-monoenergetic energy spectra was reduced to 30 - 40% of the total consecutive shots. The probability of quasi-monoenergetic electron beam generation was found to be almost absent for further higher percentage of He used. For N_2 + 75% He (Fig.6.6), at a higher threshold density of ~3.1×10^{18} cm^{-3}, electron beam peak energy were observed in the range of 109 - 130 MeV (Avg.: 118 MeV) with maximum energy in the range of 140 - 155 MeV (Avg.: 147 MeV). At still higher fraction of He, i.e. N_2 + 98% He (Fig.6.7), at a threshold density of ~4.3×10^{18} cm^{-3}, quasi-thermal electron spectrum with formation of multiple bunches of electrons were observed and maximum energy varied in the range of ~213 - 250 MeV (Avg.: 235 MeV).

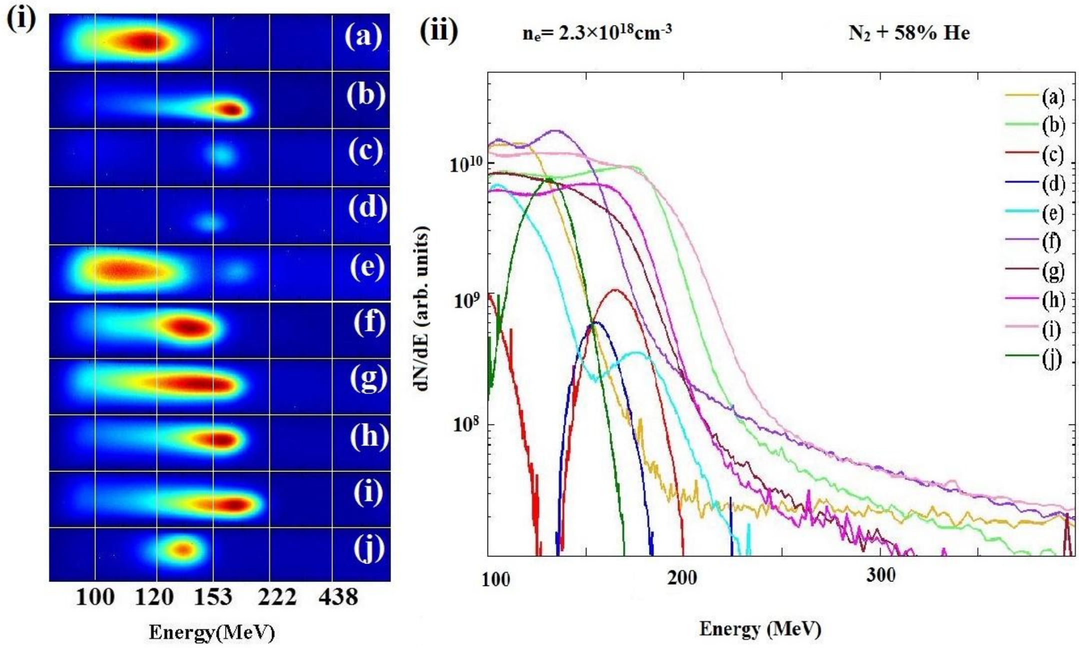

Fig.6.5: Experimental results: (i) Typical dispersed raw spectra of narrow e-beam generated and (ii) corresponding spectra for N_2 + 58% He gas-jet target: Threshold density: ~n_e= $2.3\times10^{18}$$cm^{-3}$

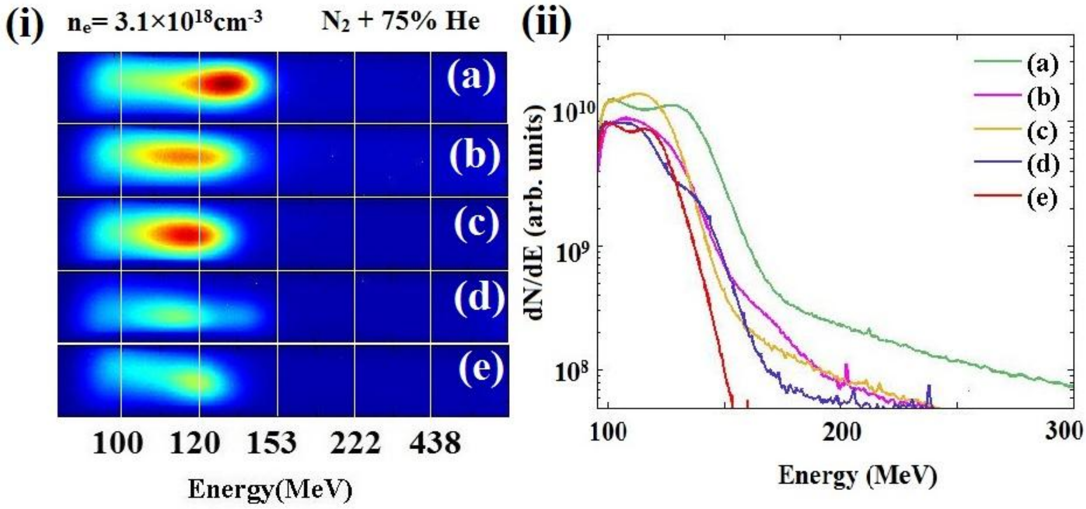

Fig.6.6: Experimental results: (i) Typical dispersed raw spectra of narrow e-beam generated and (ii) corresponding spectra for N_2 + 75% He gas-jet target: Threshold density: ~3.1×10^{18}cm^{-3}.

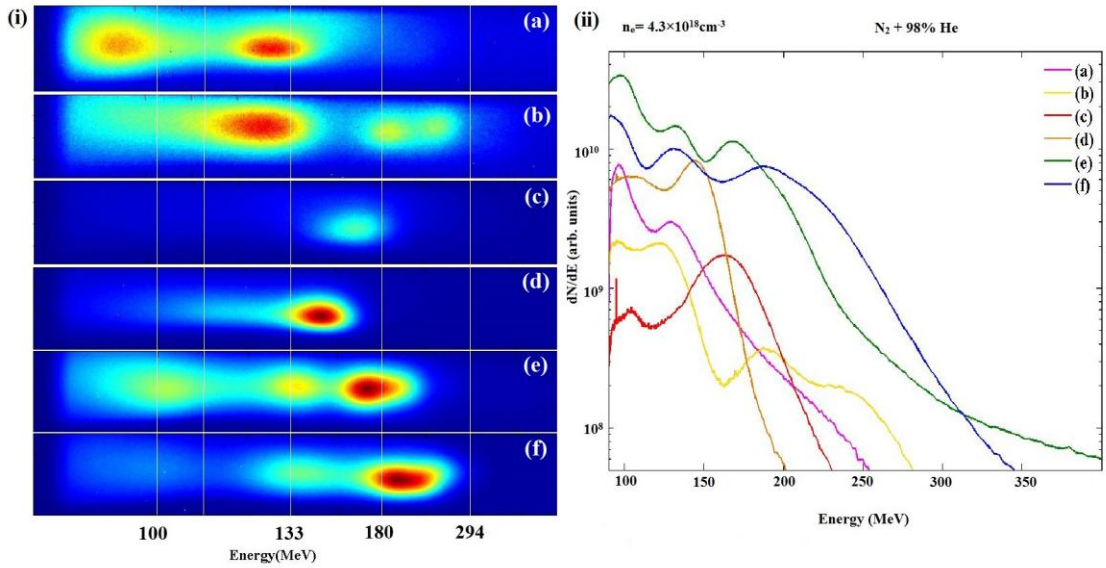

Fig.6.7: Experimental results: (i) Typical dispersed raw spectra of narrow e-beam generated and (ii) corresponding spectra for N_2 + 98% He gas-jet target: Threshold density: ~4.3×10^{18}cm^{-3}.

6.3.4. Recording of shadowgrams of laser created channels in plasma:

In Fig.6.8 (i-v) shadowgrams of laser created channels inside plasma and the corresponding electron beam profiles for various gas targets used at corresponding threshold density are shown. Laser channeling associated with relativistic self-focusing and filamentation was observed in various targets used. This is also consistent with the corresponding electron beam profiles showing generation of a narrow electron beam from the main channel and a large diffused beam from the laser filamentation part. Laser channelling in case of high-Z gas-jet targets is associated with ionization induced defocusing and unstable laser propagation, which is observed in the present case also. Stable laser propagation is expected in low Z gas- targets, as also observed in case of N_2 + 98% He (Fig.6.8-v), which is a combination also used in various other investigations on electron acceleration with ionization induced injection. However, interestingly, even for a combination of N_2 + 50% He target (Fig.6.8-ii), comparatively stable and longer channels were observed.

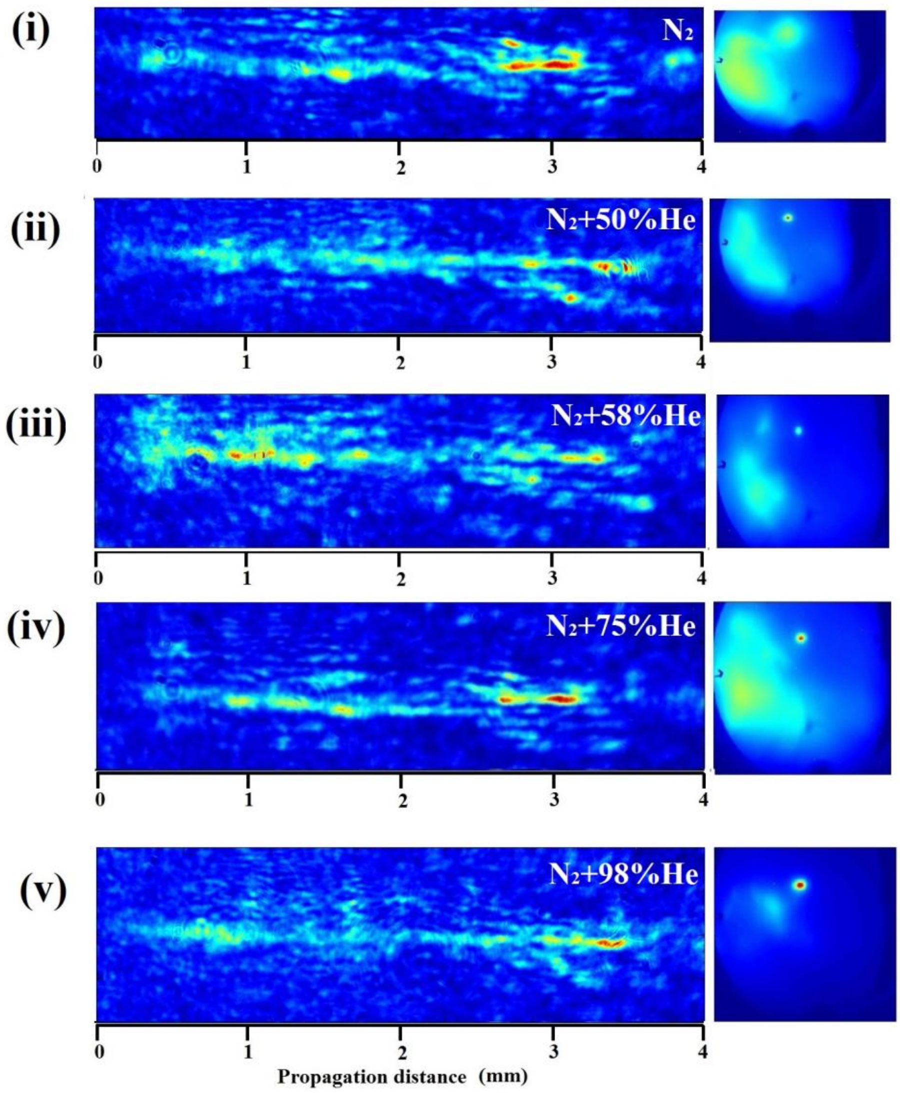

Fig.6.8: Experimental results: Shadowgrams of laser created channel and corresponding electron beam profiles for different gas targets (threshold densities) of (i) pure N_2 (~1.6×10^{18} cm^{-3}), (ii) N_2 + 50% He (~2×10^{18} cm^{-3}), (iii) N_2 + 58% He (~2.3×10^{18} cm^{-3}), (iv) N_2 + 75% He (~3.1×10^{18} cm^{-3}), and (v) N_2 + 98% He (~4.3×10^{18} cm^{-3}).

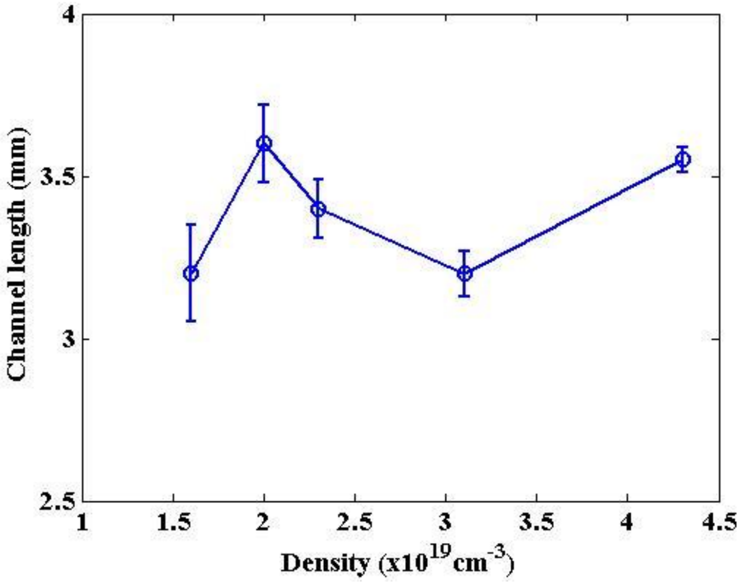

Fig. 6.9: Variation of laser channel length vs density. The length represents the average of channel lengths of 6-10 consecutive shots. Respective error bars at each density show the fluctuation in the channel lengths.

In Fig. 6.10, we plot the variation of laser channel length vs the density obtained from the typical shadowgrams shown in Fig. 6.8. The channel length of ~3.6 mm was found to be maximum at a density of ~2×10^{18} cm^{-3} (N_2+50% He), beyond which the length decreases with density and again increases to ~3.5 mm at a density of 4.3×10^{18} cm^{-3} (N_2+98%He).

6.4. Discussion:

6.4.1. Identification of acceleration mechanisms:

The present experiment was carried out with laser pulse of ~60 - 70 fs (a_0=4.2 - 4.5) at a fixed laser energy and plasma density varying in the range of ~1.6 - 4.3×10^{18} cm^{-3}. For input laser power varying from ~17.4 - 20.3 TW, P/P_c [35] varied in the range of ~1 - 2.7. For used laser and plasma parameters, L/λ_p varied from 0.8 - 1.12 i.e. $L\sim\lambda_p$, with laser pulse length (L) of ~18 - 21 μm, and λ_p of ~16 -26 μm. In such a scenario, there could be significant overlap of the laser pulse with accelerated electrons and therefore contribution of DLA mechanism of acceleration has also to be considered [5-10, 36-39]. Further, in the same experimental set up, self-injection threshold density was estimated using He gas target and was found to be of ~5.8×10^{18} cm^{-3}, for laser pulse duration of 60 fs. In this case, wakefield was found to be the dominant acceleration mechanism. The observed threshold densities for various other gas targets used in this study were below the self-injection threshold density, which also suggests applicability of acceleration mechanism other than wakefield as the strong wakefield at these densities will not be generated. This also manifested in the observed energy of the electrons.

The maximum energy gained by electrons observed in the present experiment, was compared with the theoretically estimated maximum energy gain from wakefield and DLA for the range of plasma densities used in the experiment. This is shown in Fig. 6.10. The maximum energy of electrons estimated theoretically for linear [40] /non-linear [41] wakefield mechanism are 1026 / 1593 MeV (density~1.6×10^{18} cm^{-3}), 850 / 1275 MeV (density~2×10^{18} cm^{-3}), 739 / 1108 MeV (density~2.3×10^{18} cm^{-3}), 548 / 822 MeV (density~3.1×10^{18} cm^{-3}) and 395 / 593 MeV (density~4.3×10^{18} cm^{-3}). As can be seen, these values are much higher than the observed values at corresponding densities using variety of targets. Using the formalism of maximum energy gain of electrons in case of DLA as discussed earlier in Chapter-2, for similar conditions energy estimated are 147 MeV (density ~1.6×10^{18} cm^{-3}), 151 MeV (density ~2×10^{18} cm^{-3}), 150 MeV (density ~2.3×10^{18} cm^{-3}), 138 MeV (density ~3.1×10^{18} cm^{-3}) and 130 MeV (density ~4.3×10^{18} cm^{-3}) and are found to be close to the experimentally observed values.

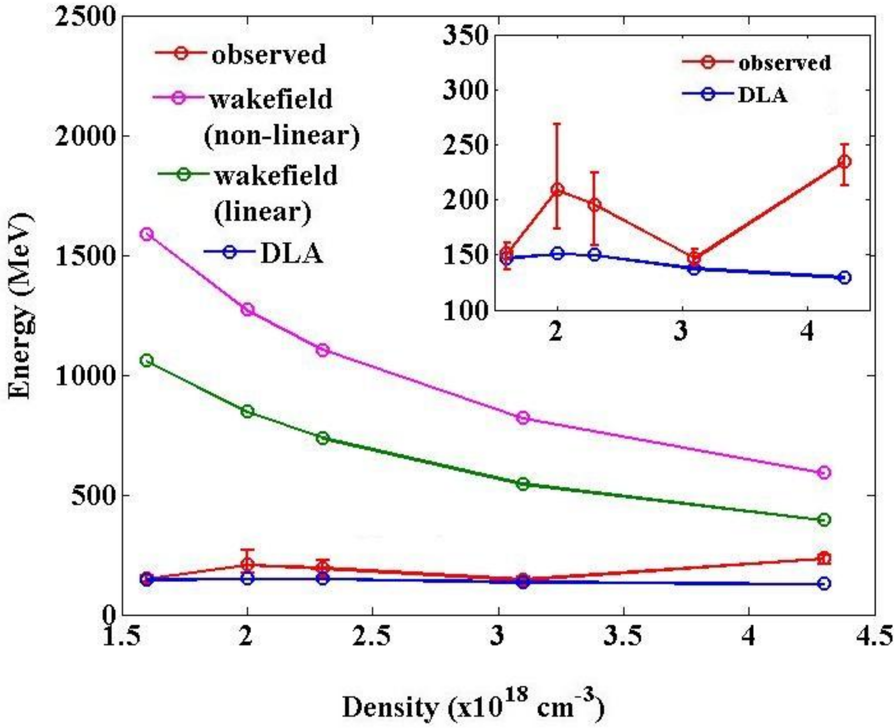

Fig.6.10: Comparison of experimentally observed maximum energy (red curve) of electrons with theoretical calculated maximum energy gain from wakefield (non-linear): magenta curve, wakefield (linear): green curve and DLA: blue curve, for the range of plasma density used. Inset shows the enlarged view of comparison of observed energy gain (red curve) with only DLA (blue curve). Error bars in maximum electron energy at a given density corresponds to observed shot-to-shot energy fluctuation.

This suggests applicability of DLA in our experimental conditions as shown in the Fig.6.10. From Fig.6.2 & 6.3, it can be observed that stable generation of relativistic electron beams in case of N_2 gas-jet target were observed at a threshold density of ~1.6×10^{18} cm^{-3} with average peak energies of ~117 MeV (Fig.6.2), having exponential spectra. However, with increase in density to ~3.5×10^{18} cm^{-3}, average peak electron energy was found to increase to ~148 MeV with quasi-thermal spectrum (Fig.6.3). The observation of exponential / quasi-thermal spectrum is a signature of

DLA acceleration mechanism [38]. For mixed gas-target also, electron acceleration was observed at density of ~2 – 4.3×10^{18} cm^{-3}, and could be attributed to pure DLA on the lower density side with increasing role of wakefield on the higher density side. Moreover, the variation in the observed electron energy gain (inset of Fig. 6.10 red curve) is in agreement with the channel length (Fig. 6.9) as we observed maximum channel length of ~3.6 mm at the optimum density of ~2×10^{18} cm^{-3} for mixed gas target of N_2+50% He. The increase in the maximum electron energy at higher threshold density of ~4.3×10^{18} cm^{-3} could also be correlated with the increase in the channel length to ~3.5 mm.

6.4.2. Verification of DLA mechanism of acceleration using 2D PIC simulations using code EPOCH:

2D PIC simulations were performed to verify the applicable acceleration mechanism of DLA for present range of plasma density used in the experiment. The simulation was performed with a simulation box size (resolution): 100 µm (λ/30) ×150 µm (λ/10) in longitudinal and transverse direction respectively. Laser pulse of duration of 60 fs, a_0=4.5 was propagated along X-direction, into a plasma length of ~2.7 mm.

Simulations were performed with three different gas targets of of pure N_2 at a density of 1.2×10^{18} cm^{-3}, mixed gas target of N_2 + 50 % He at a density of 2.6×10^{18} cm^{-3} and N_2 + 75% He at a density of 3.7×10^{18} cm^{-3}. The normalized laser and wakefield strengths have been plotted after a propagation of ~2.6 mm inside plasma for the above conditions as shown in Fig.6.11 a-d. In case of N_2 and mixed gas target of N_2 + 50% He, laser pulse modulation was almost negligible (Fig.6.11 a-b) and strength of wakefield was also low <<1 (Fig.6.11 d) suggesting dominant DLA regime of acceleration. However, for mixed gas composition of N_2 + 75% He with higher threshold density, some modulation of the laser pulse and increase in the wakefield strengths were observed (Fig.6.11 c & d). This suggests increasing role of wakefield towards higher density leading to a hybrid acceleration regime [5-10]. The above observation was also consistent with the fact that for the present experimental condition of $L \sim \lambda_p$ and $P \sim P_c$, strong self-modulation of the laser pulse hence generation of strong wakefield would not be possible.

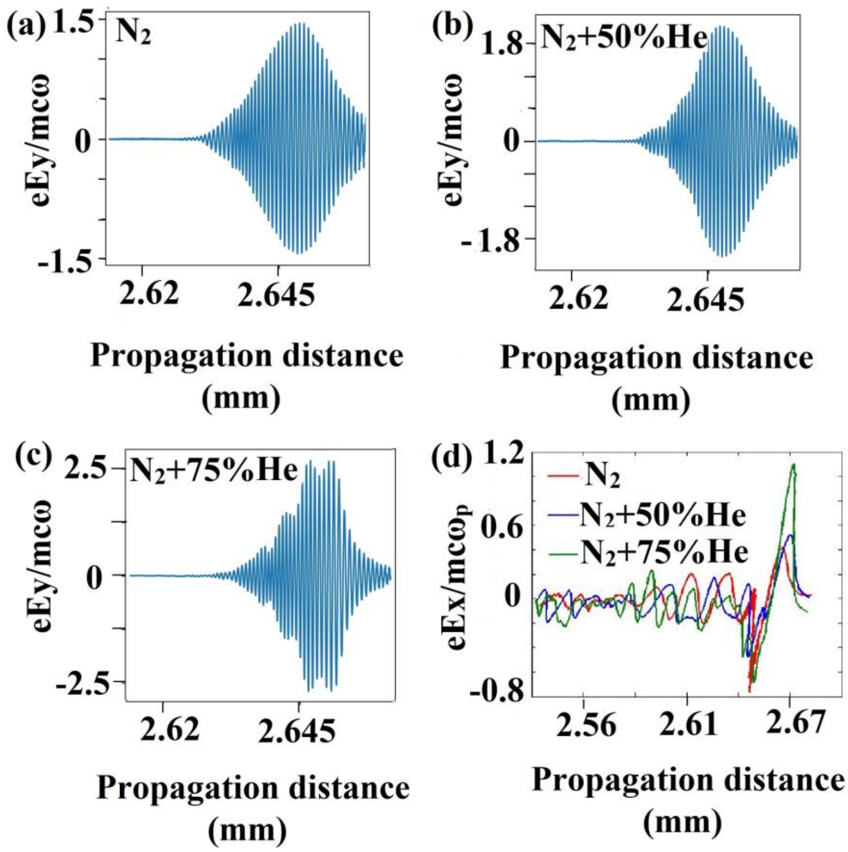

Fig.6.11: Lineouts of normalized laser field (E_y) after propagation of ~2.6 mm inside plasma for (a) N_2 gas-jet target, Threshold density: 1.2×10^{18} cm^{-3}, (b) N_2 + 50% He gas-jet target, Threshold density: 2.6×10^{18} cm^{-3} and (c) N_2 + 75% He gas-jet target, Threshold density: 3.7×10^{18} cm^{-3} (d) Comparison of normalized wakefield (E_x) for the three gas-jet targets after propagation of ~2.6 mm inside plasma.

Snapshots of the electron density profiles for three different gas targets at propagation distances of ~0.5 mm, ~1.4 mm and ~2.6 mm are shown in Fig.6.12 (i-iii) respectively. In all the three cases betatron oscillation of electrons is clearly seen in the laser created channel, also suggesting acceleration by pure DLA mechanism [7, 8, 9, 10]. Such an oscillation of electrons in laser created channel is also observed in our earlier simulation results showing hybrid acceleration discussed in Chapter-5.

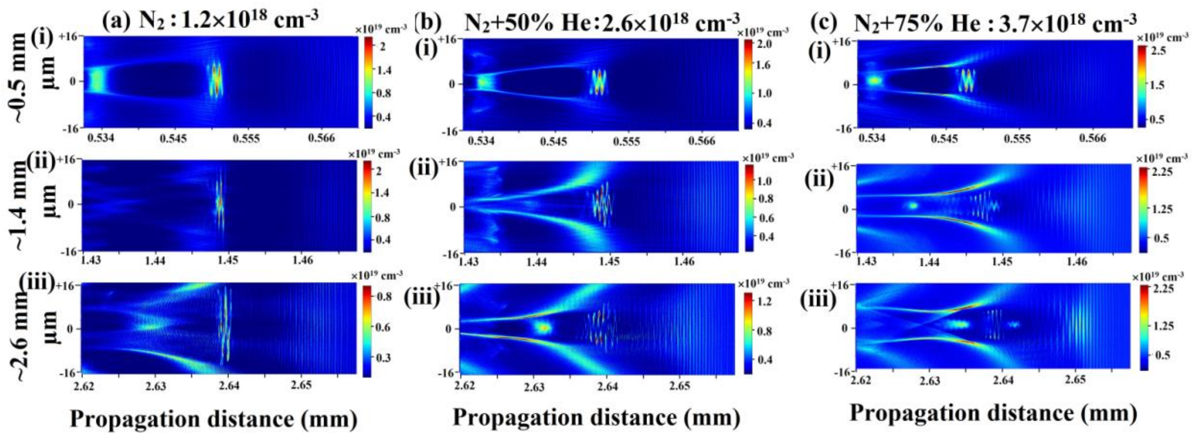

Fig.6.12: Simulation results: Electron density profiles for (a) N_2 gas-jet target, Threshold density : 1.2×10^{18} cm^{-3}, (b) N_2 + 50% He gas-jet target, Threshold density: 2.6×10^{18} cm^{-3} and N_2 + 75% He gas-jet target, Threshold density: 3.7×10^{18} cm^{-3} for propagation length of (i) ~0.5 mm, (ii) ~1.4 mm and (iii) ~2.6 mm respectively.

6.4.3. Optimization of threshold plasma density through gas target composition for DLA:

As shown in inset of Fig.6.10, for the pure DLA regime in the density range of ~1.6 – 3.1×10^{18} cm^{-3} the maximum energy gained by electrons was observed at an optimum density of ~ 2×10^{18} cm^{-3} for mixed gas target of N_2 + 50% He. Electron beams at threshold densities below and above this optimum value corresponding to different mixed gas targets were observed with comparatively lower energies. However, maximum electron energy was again found to increase at a higher threshold density of ~4.3×10^{18} cm^{-3} for mixed gas target of N_2 + 98% He, in which case the increase in energy is attributed to the enhanced contribution of wakefield leading to the hybrid acceleration mechanism. The optimization of electron beam properties for the present range of density used is summarized in Table-6.1 below.

Table-6.1: Summary of the optimization of electron beam parameters for the range of threshold density used in the experiment.

Gas-jet target (Number of shots)	**Threshold density**	**Avg. Beam divergence**	**Avg. Peak energy (MeV)**	**Avg. Max. energy (MeV)**	**Energy spread**	**Charge (pC)**
N_2	1.6×10^{18} cm^{-3}	6.2 mrad with broad diffused background	117 (5 shots)	151	Quasi-thermal	65-174
N_2 + 50% He	2×10^{18} cm^{-3}	**7.5 mrad**	**168** (30 shots)	**206**	**Quasi-monoenergetic (21%) Probability ~ 70-80%**	**140-300**
N_2 + 58% He	2.3×10^{18} cm^{-3}	7-8 mrad with diffused background	153 (10 shots)	184	Quasi-monoenergetic Probability ~ 30-40% Otherwise: broad spectrum	170-290
N_2 + 75% He	3.1×10^{18} cm^{-3}	8.3 mrad with diffused background	118 (7 shots)	147	broad	180-250
N_2 + 98% He	4.3×10^{18} cm^{-3}	8.3 mrad	183 (7 shots)	235	Multiple peaks	~400

This optimization is also observed in 2D PIC simulation (Fig.6.12). For an initial propagation of ~0.5 mm inside plasma (Fig.6.12 i a-c), in all the three cases of different gas targets, betatron oscillation of a bunch of electrons in the laser created plasma channel is observed. On further propagation of laser inside plasma up to a distance of ~1.4 mm in case of N_2 (Fig.6.12 ii-a), electrons were found to execute enhanced oscillation amplitude. Some fraction of electrons were found to move out of phase with the laser pulse with loss of synchronicity in the period of oscillation. Whereas, in case of N_2 + 50% He (Fig.6.12 ii-b), although amplitude of oscillation of electrons increased but the synchronicity of the electrons in the bunch is maintained i.e. the electrons are still in phase with the laser pulse forming a bunch. However, in case of N_2 + 75% He (Fig.6.12 ii-c), a fraction of the electrons were found to oscillate in the laser field with larger oscillation amplitude and a fraction of the electrons were found to dephase out of the laser field and oscillate with smaller oscillation amplitude. This suggests the presence of wakefield and a hybrid regime of acceleration. On still further propagation of ~2.6 mm inside plasma, electrons were found to be more dephasing out of the laser field in case of N_2 completely loosing the bunch structure (Fig.6.12 iii-a), whereas, in case of N_2 + 50% He, the electrons still maintain a bunch structure and remain in phase with the laser pulse (Fig.6.12 iii-b). This suggests a pure DLA regime as all the electrons are trapped and accelerated in the laser field only. However, in case of N_2 + 75% He, the electrons with lower oscillation amplitude interacting with wakefield now forms a distinct bunch structure and clearly separates from DLA bunch with higher oscillation amplitude. This suggests energy gain from both DLA and wakefield (Fig.6.12 iii-c). Similar kind of oscillation of electrons showing difference in the oscillation amplitude of the DLA and non-DLA accelerated electrons in a plasma channel has also been observed (c/f from Fig. 3c of ref. 9 and c/f from Fig. 4a of ref. 10), earlier in 2D PIC simulations [9, 10].

6.4.4. Theoretical explanation of optimum threshold plasma density through estimation of dephasing rate in DLA:

A theoretical analysis was also performed to support the above observed optimum value of plasma density for generation of comparatively higher energy electron beams through DLA mechanism in given experimental conditions. In earlier reports, importance of rate of dephasing of electrons in the laser field in gaining maximum energy has been discussed [42, 43]. In Chapter-2, the rate of dephasing of electrons interacting with the laser field is derived. Eq. (2.50) shows variation of rate of dephasing with plasma density.

In Fig.6.13-a, we plot the variation of R with density for $\gamma = \gamma_{opt}$ (optimum energy for electrons to be trapped and in phase with the laser field at corresponding density). It shows that R is minimum towards lower density values of 1.6 - 2×10^{18} cm^{-3} which, suggests that electrons interact maximum with the laser field and will gain maximum energy. This is consistent both with the experimental observations and simulation results showing optimum density of ~2×10^{18} cm^{-3}.

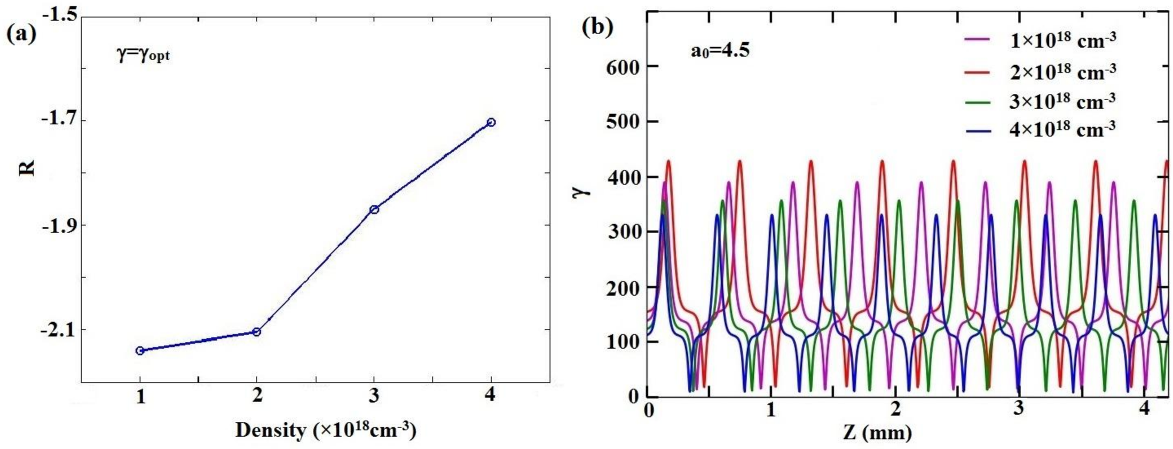

Fig.6.13: Theoretical results: (a) Plot of dephasing rate (R) vs density and (b) Plot of energy gain of electrons (γ) with propagation distance (z) for different densities of the present experimental conditions.

In Fig.6.13-b, we plot the variation of energy gain γ with propagation distance z for the range of densities used in the present experiment following Eq. (6.48) discussed in Chapter-2. It is observed that for the present density range although all electrons are trapped in the laser field, however, particularly at a density of 2×10^{18}cm^{-3} (red curve) the dephasing rate of electron is slower compared to the other densities. Within the 4 mm length of laser propagation, electrons at density of 2×10^{18} cm^{-3} covers ~7 complete phase space rotation whereas at other densities it covers ~8 complete phase space rotations. This suggests that compared to other densities, electrons remains in phase with the laser field for a longer period of time at density of 2×10^{18}cm^{-3} leading to maximum energy gain.

6.4.5. Plausible explanation of generation of quasi-monoenergetic electron beams:

It has been shown in Table-6.1 that, at the optimum composition of N_2 + 50% He (~2×10^{18}cm^{-3}) for higher energy electron beams, generation of quasi-monoenergetic electron beams were also observed (Fig.6.4) in almost 70% of the shots. Earlier it has been shown that, quasi-monoenergetic electron beams could be generated in a hybrid regime of acceleration and was also suggested that DLA accelerated electrons can have lower energy spread compared to wakefield electrons [9, 10]. The theoretical analysis above also showed that for an optimum density of 2×10^{18} cm^{-3}, electrons interact longer with the laser field which is not only favorable for higher energy gain, but also favour in bunching of electrons. This could explain the appearance of quasi-monoenergetic feature. Such bunching of electrons were also seen in the simulations, and found to be more pronounced for a density close to the case of N_2 + 50% He (Fig.6.12 b i-iii).

Further, electron spectra generated through 2D PIC simulations also showed quasi-monoenergetic feature. For the present experimental conditions, energy spectrum of electrons after a propagation distance of ~2.6 mm are shown in Fig.6.14 (a-c) for the three different gas targets respectively. At the optimum mixed gas target of N_2 + 50% He at a threshold density of ~2.6×10^{18} cm^{-3}, the spectra shows quasi-monoenergetic feature with peak energy of ~160 MeV and maximum energy of ~220 MeV (Fig.6.14-b). The increase in energy and the quasi-monoenergetic feature observed in this case suggests the effect of lower dephasing rate and hence longer interaction with the laser pulse as shown in Fig.6.12 b (i-iii). Whereas, away from the optimum, the quasi-monoenergetic feature is no longer observed in the electron energy spectrum. In case of N_2, at a lower threshold density of 1.2×10^{18} cm^{-3}, electron energy spectra is found to be quasi-thermal with maximum energy of ~180 MeV (Fig.6.14 a), which is due to early dephasing of electrons with the laser field as observed in Fig.6.12 a (i-iii). On the other hand, in case of mixed gas target of N_2 +

50% He, at a higher threshold density of 3.7×10^{18} cm^{-3}, the spectra is again quasi-thermal with multiple peak formation and maximum electron energy observed is ~310 MeV (Fig.6.14 c). Formation of multiple peaks in the energy spectrum is the manifestation of the two different electron bunch formations with different oscillation amplitude accelerated by DLA and wakefield (Fig.6.12 c i-iii).

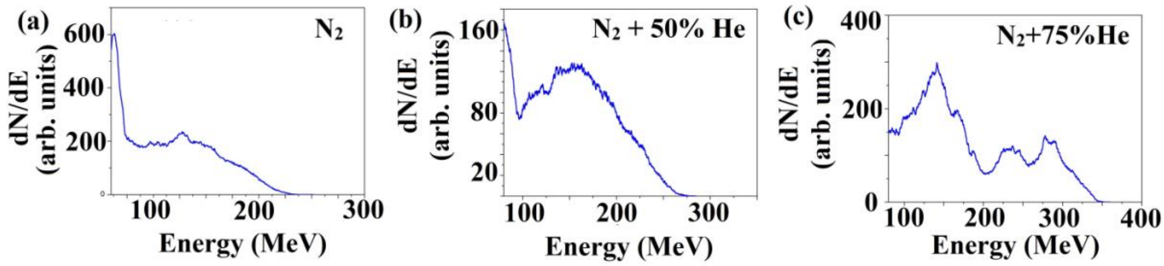

Fig.6.14. Simulation results: Electron energy spectrum (a) N_2 gas-jet target, Threshold density: 1.2×10^{18} cm^{-3}, (b) N_2 + 50% He gas-jet target, Threshold density: 2.6×10^{18} cm^{-3} and (c) N_2 + 75% He gas-jet target, Threshold density: 3.7×10^{18} cm^{-3} after propagation of ~2.6 mm inside plasma.

6.5: Conclusion:

An experimental investigation on electron acceleration in N_2 and N_2 + He mixed gas targets using Ti:sapphire short laser pulses of 60-70 fs duration such that L~λ_p was performed to study role of DLA. It was found that varying doping concentrations of He in N_2 gas target lead to change in the threshold density for generation of relativistic electron beams which further effect the electron beam properties. Threshold density was found to increase from ~1.6 (pure N_2) to 4.3×10^{18} cm^{-3} for 98% He fraction in N_2. An optimum was achieved at a composition of N_2 + 50% He (threshold density of ~2×10^{18} cm^{-3}), where generation of quasi-monoenergetic electron beams with average peak energy of ~168 MeV and average energy spread of ~21% were observed. Electron acceleration was attributed to pure

DLA mechanism towards the lower density side and with increasing role of wakefield on the higher density side leading to hybrid regime of acceleration. The optimization of electron beams was further explained through variation of rate of dephasing of electrons in the laser field with plasma density and 2D PIC simulations were also performed using code EPOCH to support the experimental observations. To our knowledge, such a study of optimization of electron beam properties by varying He gas mixture compositions in a high-Z N_2 gas target in a DLA dominated regime has not been reported earlier. Such a regime of electron acceleration with generation of high-energy, high-charge electron beams through DLA would be useful for development of high flux betatron radiation source for various practical applications.

References

[1] Gamma-rays from harmonically resonant betatron oscillations in a plasma wake, S. Cipiccia, M. R Islam, B. Ersfeld, R. P. Shanks, E. Brunetti, *et al.*, *Nat. Phys.***7**, 867 (2011).

[2] Femtosecond x rays from laser-plasma accelerators, S. Corde, K. Ta Phuoc, G. Lambert, R. Fitour, V. Malka *et al.*, *Rev. Mod. Phys.*, **85** 1 (2013).

[3] Self-modulated laser wakefield accelerators as x-ray sources, N. Lemos, J. Martins, L. Tsung, F. S. Shaw, J. L. Marsh *et al.*, *Plasma Phys. Control. Fusion*, **58**, 034018 (2016).

[4] Characteristics of betatron radiation from direct-laser-accelerated electrons, T. W. Huang, A. P. L. Robinson, C. T. Zhou, B. Qiao, B. Liu *et al.*, *Phys. Rev. E.*, **93** 063203 (2016).

[5] Role of Direct Laser Acceleration of Electrons in a Laser Wakefield Accelerator with Ionization Injection, J. L. Shaw, N. Lemos, L. D. Amorim, N. Vafaei-Najafabadi, K. A. Marsh *et al.*, *Phys. Rev. Lett.*,**118**, 064801 (2017).

[6] Experimental signatures of direct-laser-acceleration-assisted laser wakefield acceleration, J. L. Shaw, N. Lemos, K. A. Marsh, D. H. Froula and C. Joshi, *Plasma Physics and Controlled Fusion*, **60**, 044012 (2018).

[7] Role of direct laser acceleration in energy gained by electrons in a laser wakefield accelerator with ionization injection, J. L. Shaw, F. S. Tsung, N. Vafaei-Najafabadi, K. A. Marsh, N. Lemos *et al.*, Plasma Phys. Control. Fusion, **56**, 084006 (2014).

[8] Estimation of direct laser acceleration in laser wakefield accelerators using particle-in-cell simulations, J. L. Shaw, N. Lemos, K. A. Marsh, F. S. Tsung, W. B. Mori *et al*., *Plasma Physics and Controlled Fusion*,**58**, 034008 (2016).

[9] Synergistic Laser-Wakefield and Direct-Laser Acceleration in the Plasma-Bubble Regime, Xi Zhang, V. N. Khudik, and S. Gennady, *Phys. Rev. Lett*.,**114**, 184801 (2015).

[10] Laser wakefield and direct acceleration with ionization injection, Xi Zhang, V. N Khudik, A. Pukhov and G. Shvets, *Plasma Phys. Control. Fusion*, **58**, 034011(2016).

[11] Ionization Induced Trapping in a Laser Wakefield Accelerator, C. McGuffey, A. G. R. Thomas, W. Schumaker, T. Matsuoka, V. Chvykov *et al*., *Phys. Rev. Lett*., **104**, 025004 (2010).

[12] Self-Guided Laser Wakefield Acceleration beyond 1 GeV Using Ionization-Induced Injection, C. E. Clayton, J. E. Ralph, F. Albert, R. A. Fonseca, S. H. Glenzer *et al*., *Phys. Rev. Lett.*,**105**, 105003 (2010).

[13] Injection and Trapping of Tunnel-Ionized Electrons into Laser-Produced Wakes, A. Pak, K. A. Marsh, S. F. Martins, W. Lu, W. B. Mori *et al*., *Phys. Rev. Lett*.,**104**, 025003 (2010).

[14] All-Optical Cascaded Laser Wakefield Accelerator Using Ionization-Induced Injection, J. S. Liu, C. Q. Xia, W. T. Wang, H. Y. Lu, Ch. Wang *et al*., *Phys. Rev. Lett.*,**107**, 035001 (2011).

[15] Demonstration of a Narrow Energy Spread, ∼0.5GeV Electron Beam from a Two-Stage Laser Wakefield Accelerator, B. B. Pollock, C. E. Clayton, J. E. Ralph, F. Albert, A. Davidson *et al*., *Phys. Rev. Lett*.,**107**, 045001 (2011).

[16] Shock assisted ionization injection in laser-plasma accelerators, C. Thaury, E. Guillaume, A. Lifschitz, K. Ta Phuoc, M. Hansson *et al*., *Scientific Reports*, **5**, 16310 (2015).

[17] Plasma Physics and Controlled Fusion Localization of ionization-induced trapping in a laser wakefield accelerator using a density down-ramp, M. Hansson, T. L. Audet, H. Ekerfelt, B. Aurand, I. Gallardo González *et al*., *Plasma Phys. Controlled Fusion*,**58**, 055009 (2016).

[18] Demonstration of self-truncated ionization injection for GeV electron beams, M. Mirzaie, S. Li, M. Zeng, N. A. M. Hafz, M. Chen *et al*., *Scientific Reports*, **5**, 14659 (2015).

[19] Demonstration of a beam loaded nanocoulomb-class laser wakefield accelerator, J. P. Couperus, R. Pausch, A. Köhler, O. Zarini, J. M. Krämer *et al*., *Nature Communications*, **8**, 487 (2017).

[20] Improved performance of laser wakefield acceleration by tailored self-truncated ionization injection, A. Irman, J. P. Couperus, J. P. Debus, A. Köhler, A. Krämer, J. M. Pausch *et al.*, *Plasma Phys. Controlled Fusion*,**60**, 044015 (2018).

[21] Monoenergetic electron beam generation from a laser-plasma accelerator, K. Koyama, M. Adachi, E. Miura, S. Kato, S. Masuda *et al*., *Laser and Particle Beams***, 24,** 95 (2006).

[22] Quasi-monoenergetic electron beams generated from 7 TW laser pulses in N_2 and He gas targets, Z. L. Chen, C. Unick, N. Vafaei-Najafabadi, Y. Y. Tsui, R. Fedosejeves *et al*., *Laser and Particle Beams*, **26**,147 (2008).

[23] Manipulation and electron-oscillation-measurement of laser accelerated electron beams, H. Kotaki, Y. Hayashi, K. Kawase, M. Mori, M. Kando *et al*., *Plasma Phys. Controlled Fusion*, **53** 014009 (2011).

[24] Physics of fully-loaded laser-plasma accelerators, E. Guillaume, A. Döpp, C. Thaury, A. Lifschitz, J-P. Goddet *et al*., *Phys. Rev. ST Accel. Beams*, **18**, 061301 (2015).

[25] Quasi-monoenergetic electron beams from a few-terawatt laser driven plasma acceleration using a nitrogen gas jet, B. S. Rao, A. Moorti, J. A. Chakera, P. A. Naik, and P. D. Gupta, *Plasma Phys. Control. Fusion*, **59**, 065006 (2017).

[26] Characteristics of electron beam in laser wakefield accelerator using pure nitrogen gas, J. Kim, Y. H. Hwangbo, and K. N. Kim, *Plasma Phys. Control. Fusion*, **60**, 034008 (2018).

[27] Contemporary particle-in-cell approach to laser-plasma modelling, T. D. Arber, K. Bennett, C. S. Brady, A. Lawrence-Douglas, M. G. Ramsay *et al.*, *Plasma Physics and Controlled Fusion,* **57,** 1 (2015).

[28] Generation of stable and low-divergence 10-MeV quasimonoenergetic electron bunch using argon gas jet, M. Mori, K. Kondo, Y. Mizuta, M. Kando, H. Kotaki, *et al*., *Phys. Rev. Sp. Topics*, **12**, 082801 (2009).

[29] Clean source of soft X-ray radiation formed in supersonic Ar gas jets by high-contrast femtosecond laser pulses of relativistic intensity, M. Alkhimova, S. Ryazantsev, I. Skobelev, A. Boldarev, J. Feng *et al.*, *High Power Laser Science and Engineering* **8**, e26, 11 pages (2020).

[30] Supersonic gas jet target for generation of relativistic electrons with 12TW-50fs laser pulse, T. Hosokai, K. Kinoshita, T. Watanabe, K. Yoshii, T. Ueda *et al*., 2002 *Proc. 8th European Particle Accelerator Conf*. (EPS) p 981 (2002).

[31] Calibration and cross-laboratory implementation of scintillating screens for electron bunch charge determination, T. Kurz, J. P. Couperus, J. M. Krämer, H. Ding, S. Kuschel *et al*., *Rev. Sci. Instrum*. **89**, 093303 (2018).

[32] Absolute calibration for a broad range single shot electron spectrometer, Y. Glinec, J. Faure, A. Guemnie-Tafo, V. Malka, H. Monard *et al*., *Rev. Sci. Instrument* **77**, 103301 (2006).

[33] Absolute calibration of two DRZ phosphor screens using ultrashort electron bunch, Y. C. Wu, B. Zhu, K. G. Dong, Y. H. Yan, and Y. Q. Gu, *Rev. Sci. Instrument*, **83**, 026101 (2012).

[34] Self-focusing of short intense pulses in plasmas, G.-Z. Sun, E. Ott, Y. C. Lee, and P. Guzdar, *Phys. Fluids* **30**, 526, (1987).

[35] Generation and analysis of quasimonoenergetic electron beams by laser-plasma interaction in transitional region from the self-modulated laser wakefield to bubble acceleration regime, S. Masuda and E. Miura , *Phys. Plasmas*,**16**, 093105(2009).

[36] Characterization of electron beams produced by ultrashort (30 fs) laser pulses, V. Malka, J. Faure, J. R. Marquès, and F. Amiranoff, *Phys. Plasmas*, **8**, 2605 (2001).

[37] Particle acceleration in relativistic laser channels, A. Pukhov, Z.-M.Sheng, and J. Meyer-ter-Vehn, *Phys. Plasmas*, **6**, 2847 (1999).

[38] Multi-MeV Electron Beam Generation by Direct Laser Acceleration in High-Density Plasma Channels, C. Gahn, G. D. Tsakiris, A. Pukhov, J. Meyer-ter-Vehn, G. Pretzler *et al.*, *Phys. Rev. Lett.*, **83**, 4772 (1999).

[39] Electron Acceleration in Cavitated Channels Formed by a Petawatt Laser in Low-Density Plasma, S. P. D. Mangles, B. R. Walton, M. Tzoufras, Z. Najmudin, R. J. Clarke *et al.*, *Phys. Rev. Lett.*,**94**, 245001 (2005).

[40] Laser electron accelerator, T. Tajima and J. M. Dawson, *Phys. Rev. Lett.*, **43**, 268 (1979).

[41] Generating multi-GeV electron bunches using single stage laser wakefield acceleration, W. Lu, M. Tzoufras, C. Joshi, F. S. Tsung, W. B. Mori *et al*., *Phys. Rev. ST Accel. Beams* **10,** 061301 (2007).

[42] Generating "superponderomotive" electrons due to a non-wake-field interaction between a laser pulse and a longitudinal electric field, A. P. L. Robinson, A. V. Arefiev and D. Neely, *Phys. Rev. Lett.*, **111,** 065002 (2013).

[43] Beyond the ponderomotive limit: Direct laser acceleration of relativistic electrons in sub-critical plasmas, A. V. Arefiev, V. N. Khudik, A. P. L. Robinson, G. Shvets, L. Willingale *et al*., *Phys. Plasmas* **23,** 056704 (2016).

CHAPTER 7

Investigation of hybrid regime of laser plasma acceleration in He gas jet

7.1. Motivation:

Role of direct laser acceleration (DLA) and hybrid regime of acceleration of electrons with few tens of fs laser pulse in high Z (N_2) and mixed gas (He + few % N_2, and N_2 + few tens of %He) targets with ionization induced injection mechanism was identified and discussed in Chapter 5 & 6. In all these studies, the transformation from a pure DLA regime to a hybrid regime of acceleration was observed by increasing the plasma density in the same experimental set up keeping the laser pulse duration fixed. Self injection plasma density thresholds in these experiments were obtained by using He gas in same set up. Electron beam generation from He target and its comparison with other gas targets used was described in Chapter-5 itself. Here we present investigation performed with He gas-jet target for experimental conditions used in Chapter-6.

Generally, LPA experiments performed with He gas-jet target in the bubble regime of acceleration ($L<\lambda_p$) where generation of good quality sub-GeV [1-3] to multi-GeV [4-9] class quasi-monoenergetic electron beams has been observed. GeV-class electrons have also been demonstrated in mixed gas-jet targets with ionization induced injection mechanism however initially with quasi-thermal electron beam spectrum [9] and later with quasi-monoenergetic electron spectra (energy spread ~7-8%) through self-truncated ionization injection mechanism [10]. Electron acceleration in the SM-LWFA regime ($L>\lambda_p$) was also performed where wakefield was the dominant acceleration mechanism and quasi-monoenergetic electron beams up to several tens of MeV were demonstrated [11-15]. However, in few reports contribution of DLA along with wakefield was also considered in the experiments with He gas-jet target in the L>λ_p regime with electron energy of several tens of MeV [16, 17]. There are not many investigations on role of DLA with He gas-jet target particularly showing generation of sub-GeV class quasi-monoenergetic electron beams in the L>λ_p regime. Recently, role of DLA in bubble regime of acceleration i.e. hybrid regime, was investigated using mixed gas-jet target of He + few % N_2 [18].

In this context, investigation on generation of electron beams using He gas-jet target were performed with a 4 mm length of plasma in the L>λ_p regime and generation of few hundreds to sub-GeV electrons were observed. Same experimental set up described in Chapter-6 was used. The laser pulse duration was varied from shorter laser pulse duration of 60 fs to a longer laser pulse duration of 100 fs, providing a total power (P) of ~12-20 TW and intensity of ~2.6 - 4.3×10^{19} W/cm^2 (a_0~3.5 - 4.5). The plasma density was varied in the range of ~5.8 - 6.8 ×10^{18} cm^{-3}. Hybrid regime of acceleration was found to be the dominant acceleration mechanism. At shorter laser pulse duration of 60 fs contribution of wakefield was found to be higher and maximum peak electron energy of ~180 MeV has been observed. However, on increasing the laser pulse duration to 100 fs, contribution of DLA increases and peak electron energy in the range of 400-520 MeV and maximum electron energy in the range of 620-750 MeV were observed. The results were supported by 2D PIC simulations using code OSIRIS [19, 20]. Also, the electron beam charge was found to increase from 50-250 pC in the case of 60 fs, to 300-400 pC in the case of 100 fs.

7.2. Experimental results:

7.2.1. Recording of electron beam profiles:

With laser pulse duration of 60 fs, generation of relativistic electron beams were observed at a threshold density of ~5.8×10^{18} cm^{-3}. Electron acceleration was also studied at higher densities up to ~6.8×10^{18} cm^{-3}. Fig.7.1 (a-c) below shows the typical electron beam profiles obtained from interaction of shorter laser pulse duration of 60 fs for three different densities of (a) 5.8×10^{18} cm^{-3}, (b) 6×10^{18} cm^{-3} and (c) 6.8×10^{18} cm^{-3}. Fig. 7.1 (d) shows the electron beam profiles obtained with longer laser pulse duration of 100 fs at a threshold plasma density of ~6.8×10^{18} cm^{-3}. Collimated electron beams were observed with average divergence of ~6.7 mrad. On the other hand, for the longer laser pulse duration of 100 fs, collimated electron beam profile with larger average divergence of ~11.5 mrad is observed at a plasma density of ~6.8×10^{18} cm^{-3}. However, along with the main electron beam discussed above, there were also formation of some hallow and diffused electron beam similar to our previous experiment (Chapter 6 Fig.6.8-v), which is clearly separated from the main beam part, which could be associated to the laser channel filamentation observed (discussed in Section 7.2.2., Fig.7.2). The electron beam charge contained in the collimated intense part of the main electron beam was in the range of 50-250 pC for the case of 60 fs and in the range of 300-400 pC for the case of 100 fs.

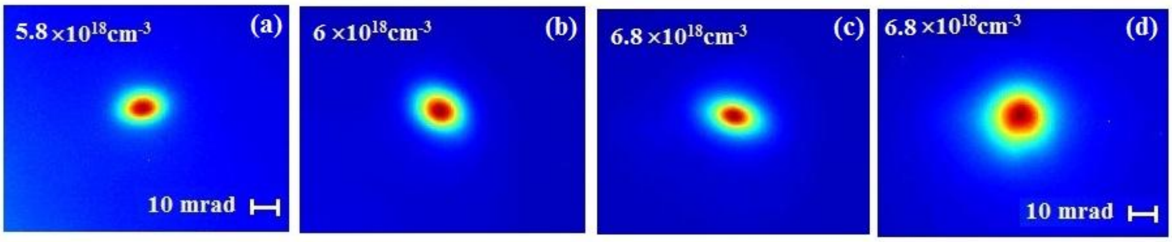

Fig. 7.1: Typical electron beam profiles in case of 60 fs at density of (a) 5.8×10^{18} cm^{-3}, (b) 6×10^{18} cm^{-3}, (c) 6.8×10^{18} cm^{-3} and (d) in case of 100 fs at density of 6.8×10^{18} cm^{-3}

7.2.2. Recording of shadowgram of laser created channel:

To study the laser interaction with the underdense plasma and laser channelling inside plasma, shadowgrams of the laser created channels were recorded as shown in Fig.7.2. In case of short laser pulse duration of 60 fs, stable and straight channel formation was observed with maximum length of ~3.5-4 mm at a threshold density of 5.8×10^{18} cm^{-3} and 6×10^{18} cm^{-3} (Fig.7.2 a & b). With further increase in density to ~6.8×10^{18} cm^{-3}, the channel was not so stable and required an initial length of 1-1.5 mm for evolution of the laser pulse (Fig.7.2 c) through relativistic self-focusing and pulse compression [21,22]. At the later stage of propagation, the channel shows slight bending. In the case of longer laser pulse duration of 100 fs, the channel becomes comparatively much more unstable with an increased bending and channel filamentation at the laser stage of propagation at the threshold density of ~6.8×10^{18} cm^{-3} (Fig.7.2 d). Also, the laser pulse requires a much longer length to evolve initially compared to the case of 60 fs case at the threshold density of ~5.8×10^{18} cm^{-3} (Fig.7.2 a).

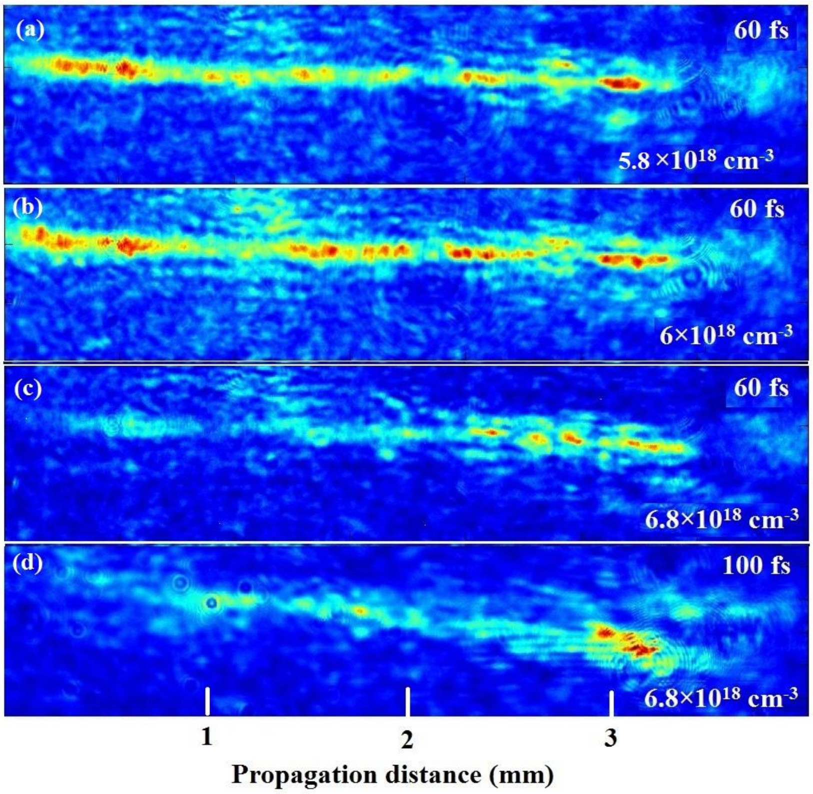

Fig. 7.2: Typical shadowgrams of the laser created channels in case of 60 fs at a density of (a) 5.8×10^{18} cm^{-3}, (b) 6×10^{18} cm^{-3}, (c) 6.8×10^{18} cm^{-3} and in case of 100 fs at a density of (d) 6.8×10^{18} cm^{-3}

7.2.3. Recording of electron beam spectra:

(i) For the case of 60 fs: Stable generation of electron beams were observed during the experiment. Fig.7.3 (i & ii) shows the typical electron beam spectra and the corresponding lineouts at density of 5.8×10^{18} cm^{-3} and 6.8×10^{18} cm^{-3} respectively. Quasi-monoenergetic electron beams with peak energy in the range of ~160-200 MeV (Avg.: 180 MeV), maximum energy in the range of ~180-250 MeV (Avg.: 215 MeV) and average energy spread of ~35% were observed at a threshold density of ~5.8×10^{18} cm^{-3} (Fig.7.3-i). On increasing the density to ~6.8×10^{18} cm^{-3}, quasi-monoenergetic electron beams were observed with average energy spread of ~32%. However, the peak electron energy decreased and is in the range of ~132-146 MeV (Avg.: 140

MeV) and the maximum energy in the rage of ~150-200 MeV (Avg. 175 MeV) (Fig.7.3-ii)

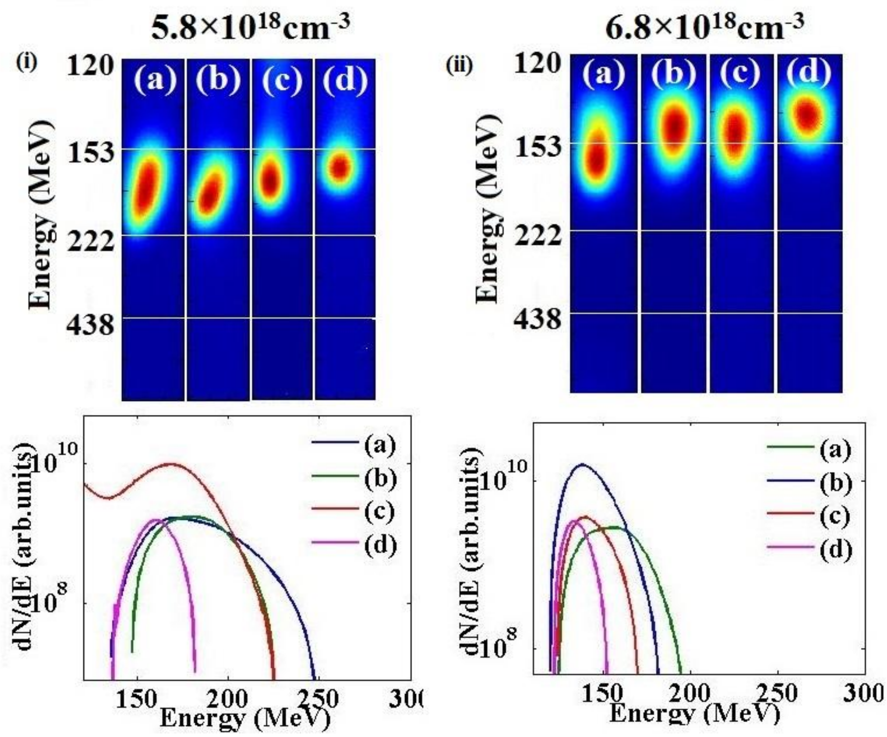

Fig. 7.3: Raw images of the dispersed electron beams and corresponding lineout in the case of laser pulse duration of 60 fs at density of (i) 5.8×10^{18} cm^{-3} and (ii) 6.8×10^{18} $cm^{-}3$.

(ii) For the case of 100 fs: In case of longer laser pulse duration of 100 fs, the threshold density for generation of relativistic electron beams observed was ~6.8×10^{18} cm^{-3}. Fig. 7.4 shows series of electron beam spectrum recorded in consecutive shots. Among these, probability of generation of quasi-monoenergetic electron beams was observed in ~15% of the shots, (Fig.7.5). Peak energy was in the range of ~133-147 MeV (Avg.: 140 MeV) with energy spread of ~18%. The maximum energy varied in the range of ~145-168 MeV (Avg.: ~158 MeV) (Fig.7.5).

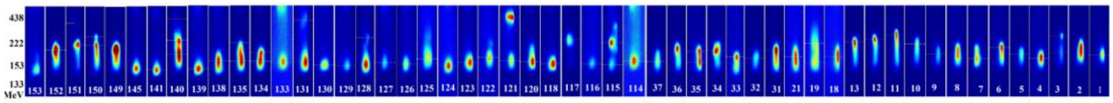

Fig. 7.4: Raw images of the dispersed electron beams in consecutive shots recorded in two separate runs first 39 shots in one frame (#114-153) and later 37 shots in second frame (Shots# 1-37) for the case of laser pulse duration of 100 fs at density of 6.8×10^18 cm^-3.

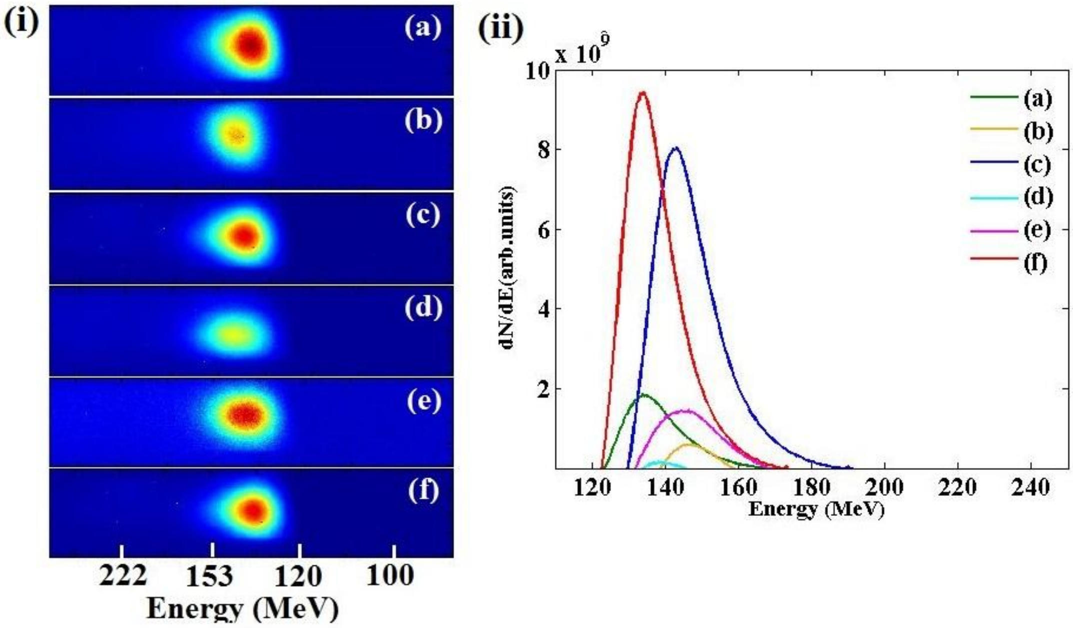

Fig. 7.5: Raw images of the dispersed electron beams and corresponding lineout for the case of laser pulse duration of 100 fs at a threshold density of 6.8×10^18 cm^-3.

However, in most of the shots (~75% of the total shots), generation of two groups of electrons were observed with quasi-thermal energy spectra (Fig.7.6i). The lower energy peak varied from ~140-160 MeV (Avg.: 150 MeV) and the higher energy peak varied from 190-335 MeV (Avg.: 233 MeV) with maximum energy varying in the range of ~210-365 (Avg.: 275 MeV). Interestingly, in few shots peak energy of the higher energy component was found to increase in the range of ~400-520 MeV with maximum energy reaching upto ~620-750 MeV (Fig. 7.6-ii).

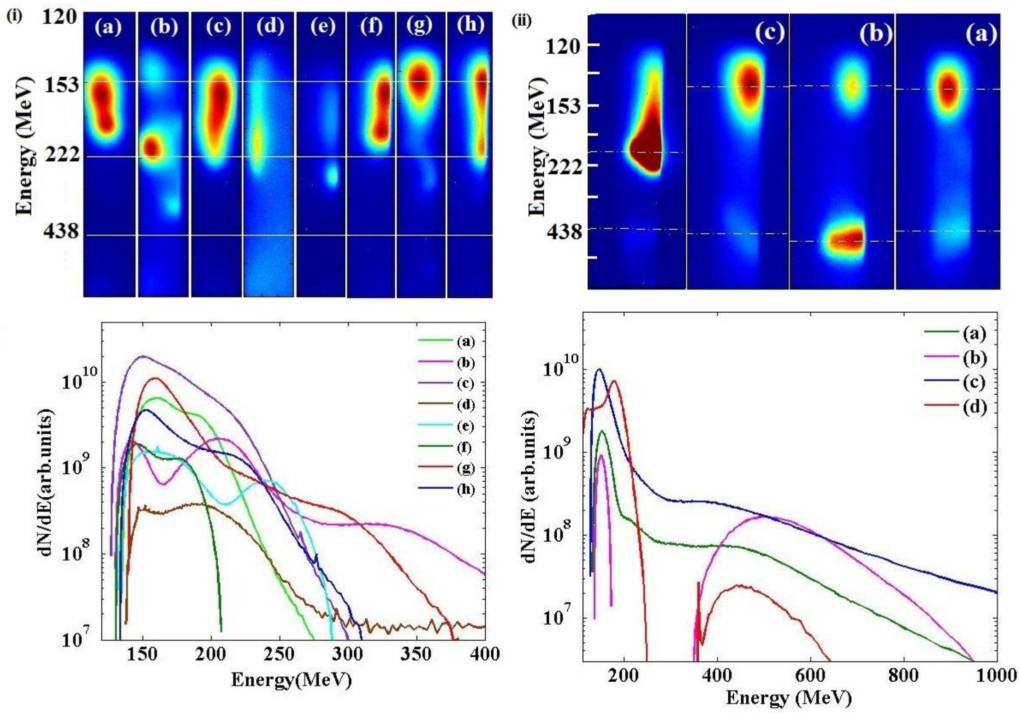

Fig. 7.6: Raw images of the dispersed electron beams and corresponding lineout for the case of laser pulse duration of 100 fs at density of 6.8×10^{18} cm^{-3}(i) showing two groups of electron beams and (ii) showing higher energy second group well separated from the first group.

7.3. Discussion:

The present experiment was performed with two different laser pulse duration of 60 fs and 100 fs with corresponding peak laser intensity of ~2.6 - 4.3×10^{19} W/cm^2 (a_0~3.5 - 4.5). The threshold plasma density for generation of relativistic electron beams was found to be ~5.8×10^{18} cm^{-3} and ~6.8×10^{18} cm^{-3} respectively. This corresponds to a regime of L/λ_p~ 2.17 and P/P_c ~3.9 for the case of 60 fs, and L/λ_p~ 2.34 and P/P_c ~2.75 for the case of 100 fs. This suggests that the regime lies in the SM-LWFA where wakefield mechanism could be a dominant acceleration mechanism [11-15]. Also, since the laser pulse completely overlaps the injected electrons contribution of DLA cannot be ignored [23-30] and hence a hybrid regime of acceleration could also be applicable.

For the case of shorter laser pulse duration of 60 fs, electron acceleration was observed at a threshold density of ~5.8×10^{18} cm^{-3} and also at a higher plasma density of ~6.8×10^{18} cm^{-3}. Generation of quasi-monoenergetic electron beams were observed as shown in Fig.7.3. However, decrease in peak energy of electron beam was observed with increase in plasma density. This suggests that contribution of wakefield is strong in this case. Generation of quasi-monoenergetic electrons in SM-LWFA regime where wakefield is the dominant acceleration mechanism has also reported earlier [11-15] where it was suggested that the long laser pulse modulates to number of short laser pulses of the order of λ_p after it interacts with plasma. Also, the theoretically estimated maximum energy gain of electrons in the linear regime [31] is 220 MeV which matches very well with the observed maximum energy of 215 MeV experimentally (Fig. 7.3). Also, for the range of plasma density 5.8-6.8×10^{18} cm^{-3} used, the dephasing length (~$\gamma_p^2\lambda_p$) is calculated to be in between ~4.1 mm and 3.2 mm, which is comparable to the length of the laser channel inside plasma, suggesting the maximum energy gain is the dephasing limited energy gain through wakefield. Further, since $P>P_c$, relativistic self-focusing and stable channelling of the laser pulse inside plasma [32] has been observed in case of 60 fs with propagation length of ~3.5-4 mm (Fig.7.2 a & b). With increase in the plasma density to ~6.8×10^{18} cm^{-3}, λ_p decreases and hence the laser pulse effectively gets longer compared to the plasma wavelength. In this case not very stable propagation of laser inside plasma in the initial stage was observed, (Fig.7.2 c), and consequently, the electron energy gain also decreases as shown in Fig. 7.3 (ii).

However, when the laser pulse duration was increased to 100 fs, the threshold density for generation of relativistic electron beams were observed to increase slightly to ~6.8×10^{18} cm^{-3}. In this case, laser pulse is longer and injected electrons interacts more with the high intense part of the laser pulse. This leads to an additional energy gain from the laser pulse also, i.e. DLA mechanism, apart from the wakefield. This justifies the observed increase in the maximum electron energy gain as shown in Fig. 7.6 (i & ii). In this case, the theoretically estimated maximum energy gain from wakefield is 280 MeV and 300 MeV respectively considering linear and nonlinear regime. Using the formulation of maximum energy gain of electrons in case of DLA (described in Chapter-2), the maximum energy gain estimated from DLA is ~104 MeV. The maximum electron energy observed in the present case, varied in a wide range from ~235 to ~650 MeV (Fig.7.6 i & ii), which is higher than the estimated maximum energy gain from DLA. Hence, energy gain of electrons have taken place both from wakefield and DLA. However, when we add the energy contributions from wakefield and DLA the maximum energy gain comes in the range of ~384 MeV (linear)-404 MeV (non-linear), which is in the range of energy observed experimentally. This suggests in the present case, with increase in the laser pulse duration, increase in contribution of DLA is observed which leads to the hybrid regime of acceleration. This is also consistent with the observation of electron beam profile with larger beam divergence compared to that observed in the case of shorter laser pulse duration of 60 fs (Fig. 7.1-d). The shot-to-shot fluctuation of generation of electron beams could be attributed to the laser channelling inside plasma. Quasi-monoenergetic electrons beams with peak energies of ~158 MeV were observed only in 15% of the shots and generation of these beams could be attributed to the wakefield mechanism. When both DLA and wakefield contributes, higher energy component could only be seen as is observed in case of two groups/multiple electron beams. These electron beams were observed for 75% of the shots.

To support the above inferences drawn transmitted laser spectrum was recorded (shown in Fig. 7.7) by collecting the scattered laser signal in the forward direction for the two different laser pulse duration of 60 fs and 100 fs. The spectrum shows significant red shift from the central laser wavelength of ~800 nm for the case of 60 fs. This also suggests strong wakefield formation and supports our claim of dominant wakefield acceleration mechanism applicable in the short laser pulse duration case of 60 fs. However, in case of 100 fs, the transmitted laser spectrum shows blue shift which suggests that in this case, strong wakefield are not generated and acceleration of electrons have taken place from both wakefield and laser electric field. This is also consistent with the hybrid regime of acceleration of electrons discussed earlier.

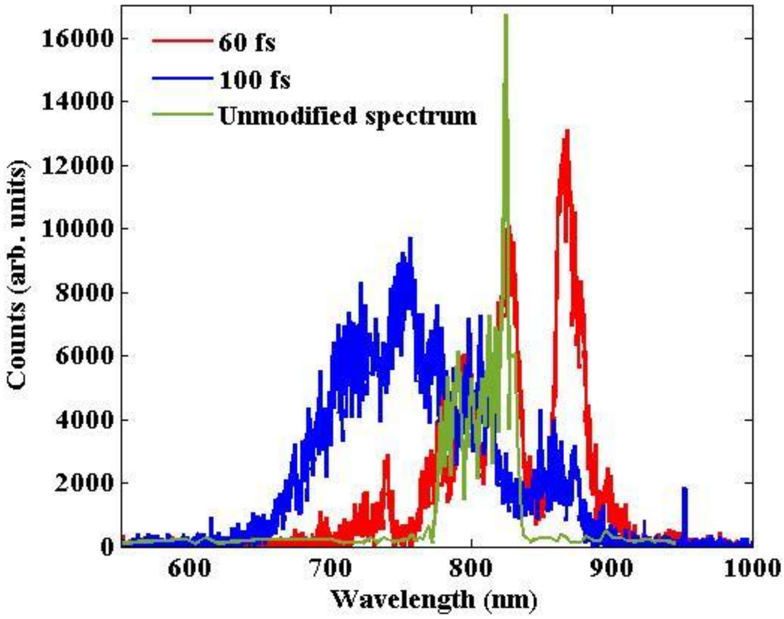

Fig. 7.7: Forward laser spectrum recorded for the case of 60 fs and 100 fs laser pulse duration.

7.4. 2D PIC simulation results using code OSIRIS:

To further understand the dynamics of effect of laser pulse duration on the acceleration of electrons 2D PIC simulations using code OSIRIS [19, 20] were performed. Simulations were performed with laser pulses of wavelength 800 nm and laser pulse duration of 60 fs, 80 fs and 100 fs. The normalized laser intensities used were a_0=4.5, 3.7 and 3.5 respectively corresponding to the three different laser pulse durations. The laser pulse propagates along x-direction and is polarized along y-direction. The plasma density profile was set such that it consists of an initial upward ramp of 100 μm and a flat top profile of 3.8 mm and a downward ramp of 100 μm. The plasma density used were 6×10^{18} cm^{-3} for laser pulse duration of 60 fs and 80 fs and a slightly higher plasma density of 6.8×10^{18} cm^{-3} for the laser pulse duration of 100 fs. Simulations were performed using a moving window frame with simulation box size of ~90 μm × 46 μm and resolution of λ/40 and λ/4 in the longitudinal and transverse direction respectively. The number of macro particle per cell was 16 with total number of 1094400 cells in the simulation box. The simulation data was dumped after every 133 fs.

Fig.7.8 (a, c, e) and Fig.7.8 (b, d, f) show the density snapshots and the normalized laser and wakefield profiles for the case of 60 fs, 80 fs and 100 fs respectively. Frames (i)-(iv) in Fig.7.8 show the evolution of the plasma density and the laser and wakefields for propagation distances of 2 mm, 2.7 mm, 3 mm and 3.5 mm respectively. The density profile shows clear formation of bubble structure with self-injection of electrons for the laser pulse duration which suggests presence of wakefield. For shorter laser pulse duration of 60 fs, after a propagation distance of 2 mm, the laser pulse was seen to undergo strong self-modulation (Fig. 7.8 b-i) and electron injected at the back of the bubble was observed to interact with the strong wakefield generated (Fig. 7.8 a-i). With further propagation of the laser pulse into the plasma up to 3 mm, further self-modulation of the laser pulse takes place (Fig. 7.8 b-ii & iii) and the bubble structure gets distorted (Fig. 7.8 a-ii & iii). At the end of propagation of 3.5 mm, the injected electrons were observed to interact with the modulated part of the laser along with strong wakefield (Fig. 7.8 b-iv) and perform small amplitude betatron oscillation within the bubble (Fig. 7.8 a-iv). This shows that although the electrons initially dominantly gain energy from wakefield, later it interacts with the laser pulse and gains energy through hybrid acceleration mechanism.

On slightly increasing the laser pulse duration to 80 fs, comparatively less laser pulse self-modulation was observed initially (Fig. 7.8 d-i) and hence no self-injection of electrons into the bubble was observed (Fig. 7.8 c-i). However, with further propagation up to 2.7 mm, self-modulation of the laser pulse was observed with increase in the wakefield strength (Fig. 7.8 d-ii), and electron injection into bubble is observed (Fig. 7.8 c-ii). With further propagation of the laser pulse into the plasma up to 3.5 mm, the trailing part of the modulated laser pulse was strong enough (Fig. 7.8 d-iv) with which the electrons interact and gain energy (Fig. 7.8 c-iv). In this case, the overlap of the injected electrons with the laser pulse occurs for a comparatively longer period of time suggesting higher contribution of the laser field in the electron energy gain.

On increasing the laser pulse further to 100 fs, as expected it takes a longer evolution time and hence at the initial time up to a propagation distance of 2 mm, only slight self-modulation of the laser pulse is observed associated with comparatively reduced strength of wakefield (Fig. 7.8 f-i). Injection of electrons into the bubble was also not observed in this case (Fig. 7.8 e-i). With further propagation of the laser pulse into the plasma, increase in self-modulation of the laser pulse was observed (Fig. 7.8 f ii-iv), and electron injection is observed at comparatively later stage of propagation of ~3 mm (Fig. 7.8 e-iii). However, since initially the laser pulse duration was longer compared to the other two cases, even after self-modulation of the laser pulse, a comparatively higher intense part of the modulated laser pulse overlaps with the injected electrons at the rear of the bubble at 3.5 mm of propagation (Fig. 7.8 e-iv). This suggests that electrons gain substantial energy from the laser field also, as consistent with the larger amplitude of oscillation of the electrons in the bubble.

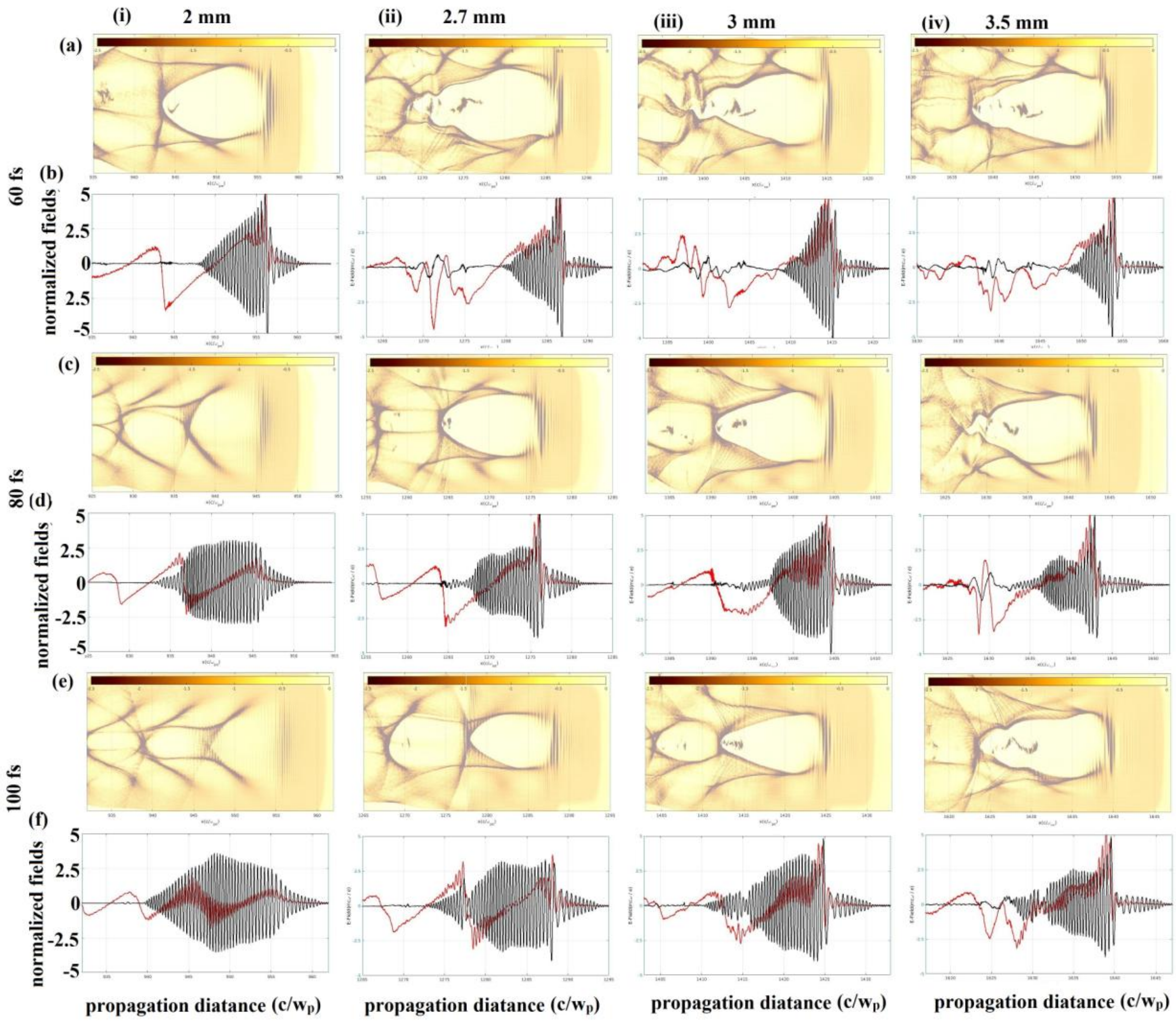

Fig. 7.8: Simulation results: Density snapshots for laser pulse duration of (a) 60 fs at a density of 5.8×10^{18} cm^{-3}, (c) 80 fs at a density of 6×10^{18} cm^{-3} and (e) 100 fs at a density of 6.8×10^{18} cm^{-3}. Normalized laser electric field by $m\omega c/e$ (black curve) and wakefield by $m\omega_p c/e$ (red curve) for laser pulse duration of (b) 60 fs, (d) 80 fs and (f) 100 fs. Frame (i-iv) shows the evolution of the laser field, wakefield and the plasma density at (i) 2mm, (ii) 2.7mm, (iii) 3 mm and (iv) 3.5 mm of propagation distance into the plasma.

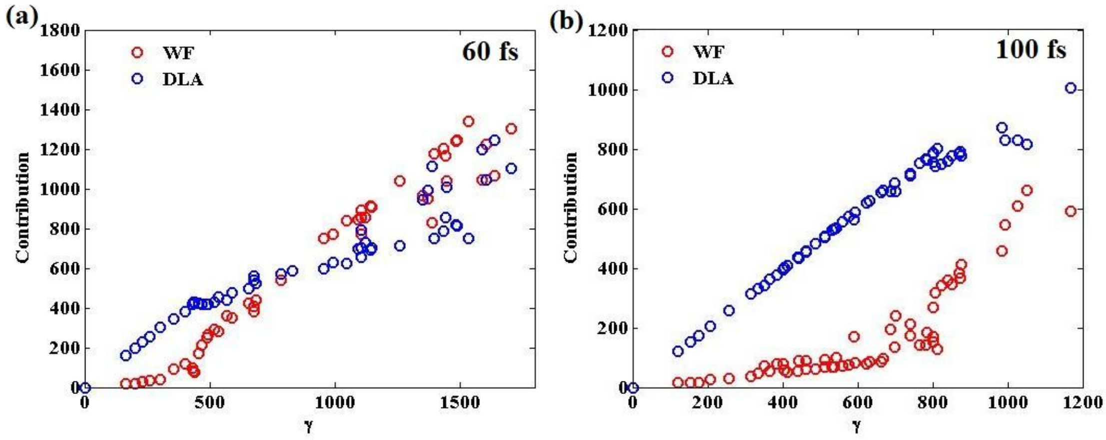

Fig. 7.9: Simulation results: Separate contribution for DLA (blue circles) and wakefield (red circles) to the total energy gain of electrons for the case of (a) 60 fs

Further, separate contributions from DLA and wakefield were calculated from the simulation results for the cases of shorter laser pulse duration of 60 fs and longer laser pulse duration of 100 fs as shown in Fig. 7.9. This clearly shows that with increase in the laser pulse duration there is increase in the contribution of DLA over wakefield.

Hence, with gradually increase of the laser pulse duration, late evolution of the laser pulse is observed which led to the increase in the overlap region of the laser pulse with the injected electrons. As a result, electrons begin to get additional energy from the laser pulse and contribution of DLA increases. This phenomenon is consistent with the experimental observations.

7.5. Conclusion:

Investigation of laser plasma acceleration using Ti:sapphire laser pulses interacting with He gas-jet plasma of 4 mm length. The study was performed with two different laser pulse duration: shorter laser pulse duration of 60 fs at a threshold plasma density of 5.8×10^{18} cm^{-3} and longer laser pulse duration of 100 fs at a higher threshold plasma density of 6.8×10^{18} cm^{-3}. In the case of shorter laser pulse duration of 60 fs the electron acceleration is attributed mainly to the wakefield mechanism with slight contribution of DLA, whereas in the longer laser pulse duration case of 100 fs, the acceleration mechanism is attributed to the hybrid regime of acceleration where the contribution of DLA was found to increase. Effect of increase of laser pulse duration was also manifested in the increase of maximum electron energy and also in the electron beam charge. Results were supported by 2D PIC simulations using code OSIRIS.

Acknowledgement:

OSIRIS simulations were performed in collaboration with Institute for Plasma Research, Gandhinagar – 382428, Gujarat, India. The authors would like to acknowledge the OSIRIS Consortium, consisting of UCLA and IST (Lisbon, Portugal) for providing access to the OSIRIS 4.0 framework. Work supported by NSFACI-1339893.

References

[1] Measurements of the critical power for self-injection of electrons in a laser wakefield accelerator, D. H. Froula, C. E. Clayton, T. Döppner, K. A. Marsh, C. P. J. Barty, *et al.*, *Phys. Rev. Lett.* **103**, 215006 (2009).

[2] Near-GeV acceleration of electrons by a nonlinear plasma wave driven by a self-guided laser pulse, S. Kneip, S. R. Nagel, S. F. Martins, S. P. D. Mangles, C. Bellei *et al., Phys. Rev. Lett.*,**103**, 035002 (2009).

[3] Generation of tunable, 100–800 MeV quasi-monoenergetic electron beams from a laser-wakefield accelerator in the blowout regime, S. Banerjee, N. D. Powers, V. Ramanathan, I. Ghebregziabher, K. J. Brown *et al., Phys. Plasmas*, **19**, 056703 (2012).

[4] Petawatt Laser Guiding and Electron Beam Acceleration to 8 GeV in a Laser-Heated Capillary Discharge Waveguide, A. J. Gonsalves, K. Nakamura, J. Daniels, C. Benedetti, C. Pieronek *et al.*, *Phys. Rev. Lett.*, **122**, 084801 (2019).

[5] Multi-GeV electron beams from capillary-discharge-guided subpetawatt laser pulses in the self-trapping regime, W. P. Leemans, A. J. Gonsalves, H.-S. Mao, K. Nakamura, C. Benedetti *et al., Phys. Rev. Lett.*,**113**, 245002 (2014).

[6] Quasi-monoenergetic laser-plasma acceleration of electrons to 2 GeV, X. Wang, R. Zgadzaj, N. Fazel, Z. Li, S. A. Yi *et al., Nat. Commun.*, **4**, 1988 (2013).

[7] Enhancement of electron energy to the multi-GeV regime by a dual-stage laser-wakefield accelerator pumped by petawatt laser pulses, H. T. Kim, K. H. Pae, H. J. Cha, I. J. Kim, T. J. Yu *et al., Phys. Rev. Lett.*,**111**, 165002 (2013).

[8] GeV electron beams from a centimetre-scale accelerator W. P. Leemans, B. Nagler, A. J. Gonsalves, Cs. Tóth, K. Nakamura, *et al.*, Nat. Phys. **2**, 696 (2006) .

[9] Self-guided laser wakefield acceleration beyond 1 GeV using ionization-induced injection, C. E. Clayton, J. E. Ralph, F. Albert, R. A. Fonseca, S. H. Glenzer *et al., Phys. Rev. Lett.*,**105**, 105003 (2010).

[10] Demonstration of self-truncated ionization injection for GeV electron beams, M. Mirzaie, S. Li, M. Zeng, N. A. M. Hafz, M. Chen *et al*., *Scientific Reports*, **5**, 14659 (2015).

[11] Generation of Quasimonoenergetic Electron Bunches with 80-fs Laser Pulses, B. Hidding, K.-U. Amthor, B. Liesfeld, H. Schwoerer, S. Karsch *et al., Phys. Rev. Lett.*, **96**, 105004 (2006).

[12] Demonstration of quasi-monoenergetic electron-beam generation in laser-driven plasma acceleration, E. Miura, K. Koyama, S. Kato, N. Saito, M. Adachi *et al., Appl. Phys. Lett.*,**86**, 251501 (2005).

[13] Observation of strong correlation between quasimonoenergetic electron beam generation by laser wakefield and laser guiding inside a preplasma cavity, T. Hosokai, K. Kinoshita, T. Ohkubo, A. Maekawa, M. Uesaka *et al*., *Phys. Rev. E*, **73**, 036407 (2006).

[14] Tomography of Injection and Acceleration of Monoenergetic Electrons in a Laser-Wakefield Accelerator, C.-T. Hsieh, C.-M. Huang, C.-L. Chang, Y.-C. Ho, Y.-S. Chen *et al., Phys. Rev. Lett.*, **96**, 095001 (2006).

[15] Generation of quasi-monoenergetic electron beams with small normalized divergences angle from a 2 TW laser facility, B. S. Rao, A. Moorti, R.

Rathore, J. A. Chakera, P. A. Naik *et al.*, *Phys. Rev.* ST Accel. Beams,**17**, 011301 (2014).

[16] Generation and analysis of quasimonoenergetic electron beams by laser-plasma interaction in transitional region from the self-modulated laser wakefield to bubble acceleration regime, S. Masuda and E. Miura , *Phys. Plasmas*,**16**, 093105(2009).

[17] Characterization of electron beams produced by ultrashort (30 fs) laser pulses, V. Malka, J. Faure, J. R. Marquès, and F. Amiranoff, *Phys. Plasmas*, **8**, 2605 (2001).

[18] Role of Direct Laser Acceleration of Electrons in a Laser Wakefield Accelerator with Ionization Injection, J. L. Shaw, N. Lemos, L. D. Amorim, N. Vafaei-Najafabadi, K. A. Marsh *et al*., *Phys. Rev. Lett.*,**118**, 064801 (2017).

[19] Lecture Notes in Computer Science: Computation Science–ICCS 2002, R. A. Fonseca *et al., edited by* P. M. A. Sloot *et al.*, Berlin: Springer **2331**, 342 (2002).

[20] Particle-in-Cell Modeling of Plasma-Based Accelerators in Two and Three Dimensions, R. G. Hemker, PhD Dissertation UCLA (1999) [arXiv:1503.00276].

[21] Self-modulation and self-focusing of electromagnetic waves in plasmas, C. E. Max, J. Arons, and A. B. Langdon, *Phys. Rev. Lett.* **33**, 209 (1974).

[22] Observation of Laser-Pulse Shortening in Nonlinear Plasma Waves, J. Faure, Y. Glinec, J. J. Santos, F. Ewald, J.-P. Rousseau *et al*., *Phys. Rev. Lett.* **95**, 205003 (2005).

[23] Multi-MeV Electron Beam Generation by Direct Laser Acceleration in High-Density Plasma Channels, C. Gahn, G. D. Tsakiris, A. Pukhov, J. Meyer-ter-Vehn, G. Pretzler *et al.*, *Phys. Rev. Lett.*, **83**, 4772 (1999).

[24] Electron Acceleration in Cavitated Channels Formed by a Petawatt Laser in Low-Density Plasma, S. P. D. Mangles, B. R. Walton, M. Tzoufras, Z. Najmudin, R. J. Clarke *et al.*, *Phys. Rev. Lett.*,**94**, 245001 (2005).

[25] Role of Direct Laser Acceleration of Electrons in a Laser Wakefield Accelerator with Ionization Injection, J. L. Shaw, N. Lemos, L. D. Amorim, N. Vafaei-Najafabadi, K. A. Marsh *et al.*, *Phys. Rev. Lett.*,**118**, 064801 (2017).

[26] Experimental signatures of direct-laser-acceleration-assisted laser wakefield acceleration, J. L. Shaw, N. Lemos, K. A. Marsh, D. H. Froula and C. Joshi, *Plasma Physics and Controlled Fusion*, **60**, 044012 (2018).

[27] Role of direct laser acceleration in energy gained by electrons in a laser wakefield accelerator with ionization injection, J. L. Shaw, F. S. Tsung, N. Vafaei-Najafabadi, K. A. Marsh, N. Lemos *et al.*, Plasma Phys. Control. Fusion, **56**, 084006 (2014).

[28] Estimation of direct laser acceleration in laser wakefield accelerators using particle-in-cell simulations, J. L. Shaw, N. Lemos, K. A. Marsh, F. S. Tsung, W. B. Mori *et al.*, *Plasma Physics and Controlled Fusion*,**58**, 034008 (2016).

[29] Synergistic Laser-Wakefield and Direct-Laser Acceleration in the Plasma-Bubble Regime, Xi Zhang, V. N. Khudik, and S. Gennady, *Phys. Rev. Lett.*,**114**, 184801 (2015).

[30] Laser wakefield and direct acceleration with ionization injection, Xi Zhang, V. N Khudik, A. Pukhov and G. Shvets, *Plasma Phys. Control. Fusion*, **58**, 034011(2016).

[31] Laser electron accelerator, T. Tajima and J. M. Dawson, *Phys. Rev. Lett.*, **43**, 268 (1979).

[32] Self-focusing of short intense pulses in plasmas, G.-Z. Sun, E. Ott, Y. C. Lee, and P. Guzdar, *Phys. Fluids* **30**, 526, (1987).

CHAPTER 8

Electron beam radiography application of LPA

8.1. Motivation:

LPA has been investigated over years and various applicable acceleration mechanisms governing the laser plasma interactions has been studied in detail [1-5]. Hence, LPA can now routinely generate stable electron beams with energy ranging from few tens to few hundreds of MeV and have become matured enough to be considered for various potential applications such as injector for conventional accelerator, generation of synchrotron radiation, and bremsstrahlung radiation (x-rays/g-rays) etc. which can be further used for nuclear and medical studies [6-8].

Another potential applications of relativistic electrons is for radiography [9]. Particle radiography started early in 1896 by Roentgen through the discovery of x-rays where he showed that high energy photons could penetrate opaque objects and reveal their internal structures [10]. Following this, a number of studies were also performed showing potential of proton radiography for biological and other non-destructive applications [11-14]. However, although proton radiography could show remarkable achievements yet these systems are very much costly.

In this context, as a potential alternative, electrons were suggested as a probe for radiography studies [9, 15, 16]. Electrons have the advantage that they do not undergo strong interactions with nucleus and hence nuclear cross-sections are small compared to protons. Electron radiography was first demonstrated by Merrill *et al.* [15, 16] using the 30MeV electron beams of linac Los Alamos National laboratory

(LANL), USA by which they have generated radiographs of thin static objects with a spatial resolution of ~100µm. The first picosecond dynamic electron radiography experiment was performed recently by Zhao *et al* [17], using the 50MeV electron beam of LINAC of Tsinghua University (THU) showing a spatial resolution of 100µm and further simulations studies were performed to build a dedicated electron beam line for radiography [18]. Recently, Merrill *et al* have demonstrated electron radiography of thick samples with 14 GeV electrons of Linac Coherent Light Source (LCLS) of Stanford Linear Accelerator Centre (SLAC), with better than 10 µm resolution, and also have shown theoretically that even 1 µm resolution could be achievable [19].

Application of relativistic electron beams generated from laser driven plasma accelerators to radiography studies have also been demonstrated [20-25]. Initially Mangles *et al*. showed the suitability of 20 MeV electron beams with broad energy spectrum for radiography of metal object, although with a poor resolution and therefore use of quasi-monoenergetic electron beam was recommended [20]. In another study, by Ramanathan *et al.*, QM electron beams with energy >100 MeV was used for radiographic study of flaws embedded in the thick solid objects placed at a distance of 2 m from the source, and submillimeter resolution was demonstrated [22]. Recently, radiography of the thin inorganic dense objects and biological samples with a spatial resolution of ~ 60 µm and placed at a distance of ~ 10 cm from the source has been reported by Bussolino *et al*. using electron beam of energy ~ 2 MeV with a broad spectrum [23, 24]. Further, ultrafast electron radiography study of temporal evolution of the magnetic fields in high intensity laser solid interaction has also been reported recently [25]. The advantage of laser driven electron beams over conventional accelerators is the generation of very short duration electron bunches of the order of femtosecond (fs), which in addition to deliver high dose, also enable the possibility of performing time-resolved studies from compact table top systems. It may be pointed out here that in addition to the thin as well as thick metallic samples, radiographies of biological samples have also been performed [16,21,23], and through which sensitivity of electron imaging for thin areal density objects and to different chemical and structural differences of the samples, similar to the x-rays, have been demonstrated [16,23]. Availability of compact and low cost laser plasma electron accelerators compared to the advanced x-ray sources like Synchrotron Radiotion sources and Free Eletron Lasers, could be found encouraging for further exploration of such applications also of electron beam radiography.

Another important potential application of relativistic electron beams is for radiotherapy purpose [26]. Mostly linacs providing lower energy (~ 4 - 25 MeV) electron beams are currently being used for treatment of superficial cancer cells in numerous sites such as head, neck, breast, skin [27]. It has been suggested that for tumors at larger depths inside the body such as lungs, prostrate, very high energy electron beams (VHEE) of ~ 150 - 250 MeV would be appropriate [28-31]. Studies using Monte Carlo simulations [28] showed that the penumbra and depth dose rates was comparable to even proton beams at depths less than 10 cm with penetration depth of ~40 cm in human tissue. Recently, treatment planning of VHEE in radiotherapy was studied [31].

Radiotherapy applications using electron beams generated from LPA has also been explored through simulations [32-35]. Various studies of radiotherapy using LWFA electron beams have been performed through Monte Carlo simulations [34-39]. In contrast to linac, it has the advantage of generating pulsed electron bunches of the order of fs duration and small divergence, which could deliver higher instantaneous dose rate [33, 35]. Simulation studies were performed using the electron beam parameters of UCLA laser plasma wakefield accelerator for treatment of prostrate cancer and found that VHEE beams in the range of 150-250 MeV have potential advantages compared to protons and photons [37, 38]. Further, they reported that the main advantage of LPA lie in the ease of delivery and manipulation of dose i.e. the tunability of electron beam energy.

With this motivation, we performed an experimental investigation on radiography of different metallic and biological plant samples using relativistic electron beams generated from LPA. Electron beams with two different properties were generated with underdense plasma of Ar and He gas targets. Radiographs were recorded at a distance of 70 cm from the source, and a minimum resolution of ~ 75 μm was achieved. Further, GEANT4 Monte Carlo simulations [40] were performed for reconstruction of the radiographs and were found to be good agreement with the experiments. Effect of different electron beam parameters on the quality of radiographs is discussed. Suitability of LPA in radiotherapy was also discussed through study of penetration depths of electrons in adipose tissue. Our study demonstrates use of a compact, table top, and stable LPA, with variable electron beam parameters for both industrial and medical applications. Such a detailed comparative study on electron radiography using LPA has not been reported earlier.

8.2. Experimental set up and parameters:

Fig. 8.1 shows the schematic of the experimental set up. Ti: Sapphire laser pulse of ~ 120 fs duration was focused to a spot of ~ 6.5×6.5 μm^2 (radius at $1/e^2$)

using f/5 off axis parabolic (OAP) mirror along 4 mm length of a well-characterized slit nozzle (1.2 mm×4 mm) [41]. Laser power (P) of ~10 TW and intensity (I) of ~ 2.2×10^{19} W/cm^2 was achieved in the laser focus which corresponds to laser strength parameter a_0=3.2. Experiments were performed with two different gas targets of He and Ar with plasma density in the range of ~ 2- 30×10^{18} cm^{-3}. Electron beam generated was transported out of the vacuum chamber through a 54 μm thick Ti foil.

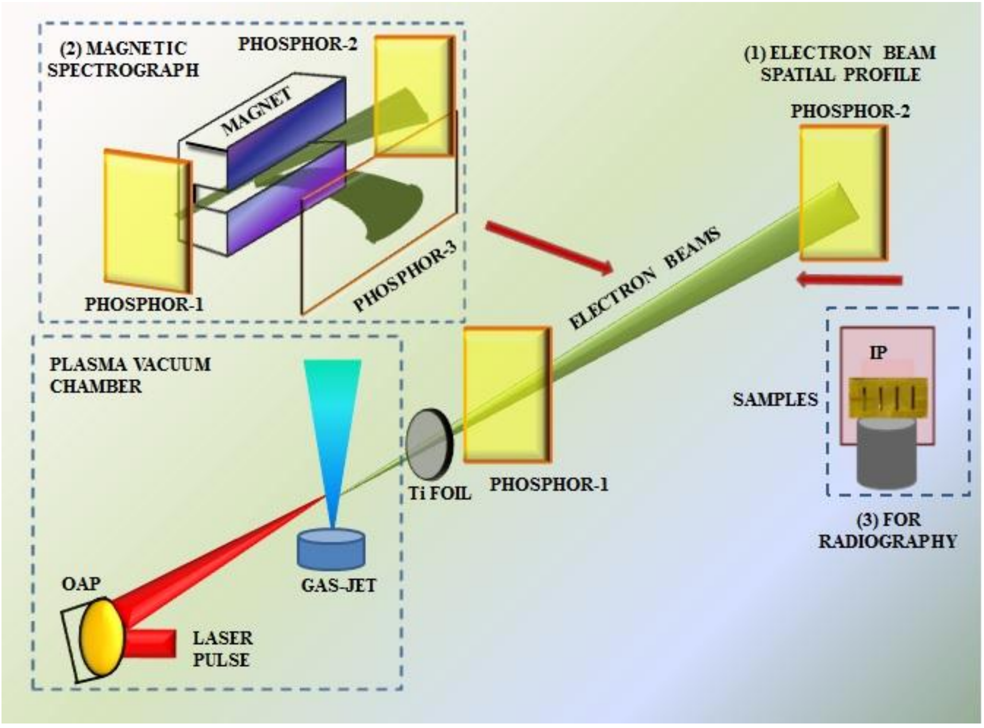

Fig. 8.1: Schematic of the experimental set up.

(i) Recording of electron beam profile: Two phosphor screens viz. Phosphor-1 (Lanex-regular) and Phoshhor-2 (DRZ-High), were placed at a distance of 39 cm and 70 cm respectively to record electron beam profile and its size at different locations.

(ii) Recording of electron beam spectra: Electron energy was estimated by dispersing the electron beams through a C-shaped rectangular magnetic spectrograph of dimensions: $20\times10\times10$ cm^3, pole gap 15 mm with peak magnetic field strength of ~ 0.9 T. The magnet was inserted in between the two phosphor screens and simultaneously electron beam profile were recorded on Phosphor-1 and its corresponding spectra on Phosphor-2, which covered energy range beyond ~80 MeV. To record electrons with lower energy values in the range of ~15-80 MeV, another Phosphor-3 (DRZ-high) was also placed in the side direction of the magnet. Resolution of the spectrograph was ~ 8% at 100 MeV and ~ 25% at 300 MeV (for 10 mrad divergence). For the side phosphor resolution was ~ 4.5% at energy of 25 MeV. The electron beam charge was estimated using standard calibration data available for various phosphor screens used [42-44].

(iii) Set up for electron radiography: Samples were kept at a distance of ~70 cm (i.e. at the location of Phosphor-2) from the source, and radiographs were recorded on another detector i.e. imaging plate (IP). Samples were kept in contact with the IP to record one to one image. The IP was scanned using a scanner (Make: Dürr Medical, Germany, Model-CR-35 bio 2136-00064), having a 635 nm He-Ne laser. The system provides a true optical resolution of 840 dpi, corresponding to ~ 30 µm. The optical density range for the scanner and IP used was estimated to be 3.05.

8.3. Experimental results and discussion:

8.3.1: Generation of relativistic electron beams:

Electron beams with two different properties were generated from two different gas target of He and Ar at threshold densities of ~ 6×10^{18} cm^{-3} and ~ 2.4×10^{19} cm^{-3} respectively. The corresponding plasma density was estimated from the neutral gas densities produced by the nozzle and considering ionization state of 2^+ and

16^+ achieved for the present laser intensities for He and Ar respectively. In the case of Ar, contribution of cluster formation on the acceleration of electrons would have very negligible effect as we have performed the experiments at very low gas pressures of ~4 bar and also at very high laser intensities of a_0=3.2. Cluster formation has also not been considered in earlier reports where experiments were performed at low gas pressures [45], however, even with comparatively higher pressures of 40-60 bar cluster formation has not been considered where very high laser intensities were used [23, 46]. Ionization states upto 16 were considered and also achieved in Ar gas-jet targets with similar laser intensities in earlier reports [24,47]. Hence, inner shell ionization taking place in case of Ar gas-jet target would facilitate ionization induced injection mechanism [48, 49]. The generation of electron beams, both from He and Ar, in the present experiment was found to be stable and highly reproducible and electron beam characterization has been made from 10-12 consecutive shots during the experiment.

In case of Ar, broad electron beams with divergence of ~ 60 - 70 mrad were observed with beam size on Phosphor-1 and Phosphor-2 is ~ 50 - 60 mm and ~ 80 - 90 mm (FWHM) respectively (shown in Fig. 8.2 insets i and ii). The typical laser created channel is shown in Fig. 8.2 (iii) showing unstable laser propagation with filamentation. Electron beam spectrum is broad with maximum energy of ~50 MeV (Fig. 8.2 iii & iv) recorded on Phosphor-3. The contained in the beam was in the range of 400 - 550 pC. Pointing variation of electron beams on phosphor-2 in this case was 10×20 mrad.

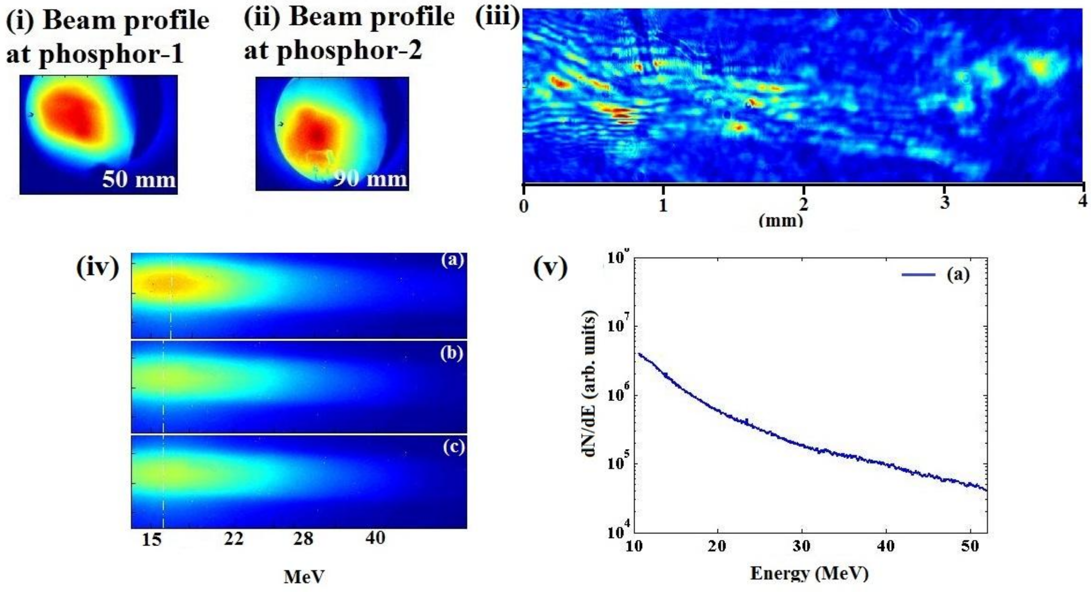

Fig. 8.2: Results with Ar gas-jet target: (i) Electron beam profile on phosphor-1, (ii) electron beam profile at phosphor-2, (iii) Typical shadowgram of the laser created channel, (iv) Raw images of typical dispersed electron beams, (v) Typical lineout of the electron spectra.

From He gas-jet target, comparatively more collimated electron beams with divergence of ~ 5 - 7 mrad were observed showing electron beam size of ~4 - 5 mm on Phosphor-1 and ~10 - 15 mm (FWHM) on Phosphor-2 (shown in Fig. 8.3 insets i and ii). The electron beam spectrum shows a peak energy of ~ 150-170 MeV and comparatively narrow energy spread (QM feature) were observed, however some fraction of higher energy component was also present (Fig. 8.3 and inset-iii shows the raw image of the dispersed electron beam). Electron beam total charge and pointing variation on phosphor-2 in case of He was comparatively lower in the range of 100 - 200 pC and ~8×4 mrad respectively. In Chapter-7, electron beam generation from He gas-jet target was described in detail.

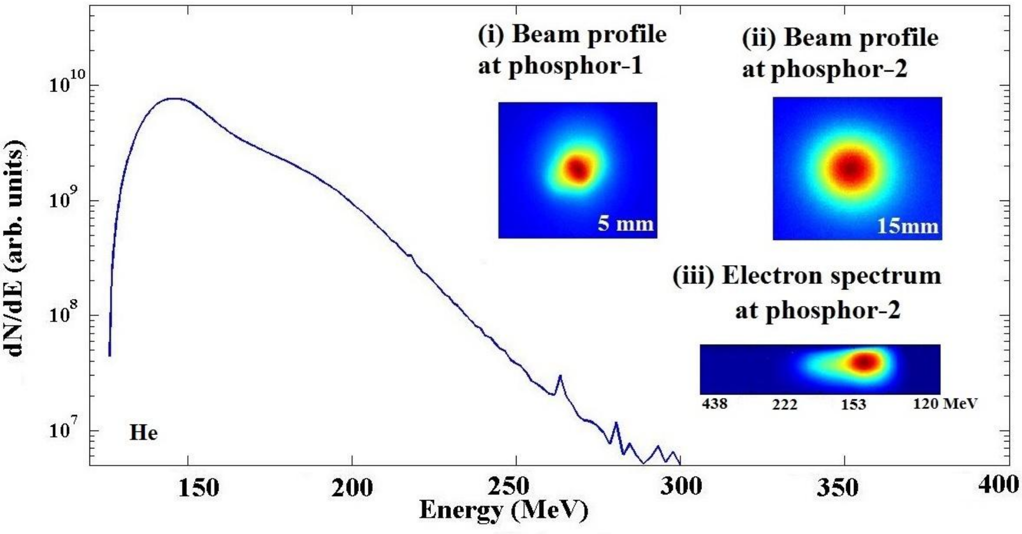

Fig. 8.3: Results with He gas-jet target: Generation of quasi-monoenergetic electron spectra (i) Electron beam profile on phosphor-1, (ii) electron beam profile at phosphor-2, (iii) Raw images of typical dispersed electron beams.

Hence, acceleration of electrons through wakefield excitation is a probable case [50-55] where generally generation of high energy quasi-monoenergetic electron is observed [54, 55]. This is similar to that we have observed in the case of He in the present experiment, suggesting the dominant mechanism of wakefield. However, in case complete overlap of the laser pulse, contribution from DLA cannot be ignored [56, 57], where generally electron beams with large divergence and broad spectrum are generated [56, 57], similar to that observed in case of Ar in the present case. Theoretical energy estimations made for the respective cases of He and Ar also suggests the dominant contribution of wakefield and DLA respectively. In earlier reports using Ar gas-jet targets electron acceleration has also been attributed to DLA [23, 58]. In case of Ar gas-jet target, ionization induced injection mechanism also helps to support DLA [59, 60]. The electron beam parameters and the corresponding acceleration mechanism in case of Ar and He gas-jet targets are summarized in below in Table-8.1.

Table 8.1: Summary of the electron beam properties generated from Ar and He gas-jet target.

Gas	Beam Size (mm)		Energy (MeV)	Spectrum	Acceleration mechanism
	Phosphor-1 (39 cm)	Phosphor-2 (70 cm)			
Ar	50-60	80-90	Max: 50	broad	DLA
He	4-5	10-15	Peak:150-170	Quasi-monoenergetic	Hybrid: Wakefield + DLA

8.3.2: Radiography using LPA electron beams:

Various thin metallic and biological plant samples were kept at a distance of 70 cm from the gas-jet target and were radiographed on IP using two different electron beams generated from He and Ar gas-jet targets. Fig. 8.4 shows the various samples used for radiography. i) Cu mesh with wire thickness 200 µm and separation of 500 µm, ii) Ti strip of gap: 2.5 mm, strip width: 2 mm and 1 mm thickness, iii) IC chip with leg material of Cu alloy with tin plating and thickness 300 µm, iv) Cu wire of ~ 250 µm thickness, v) cross section of Aloe-vera of 1.1 cm thickness, vi) Al disc of 3 mm thickness with holes of diameter 1.3 cm at center and of diameter 4 mm at the outer periphery, vii) a cross-section of a thick leaf sample, viii) & ix) different cross sections of Aloe-vera of thickness 0.5 cm and 1.75 cm respectively.

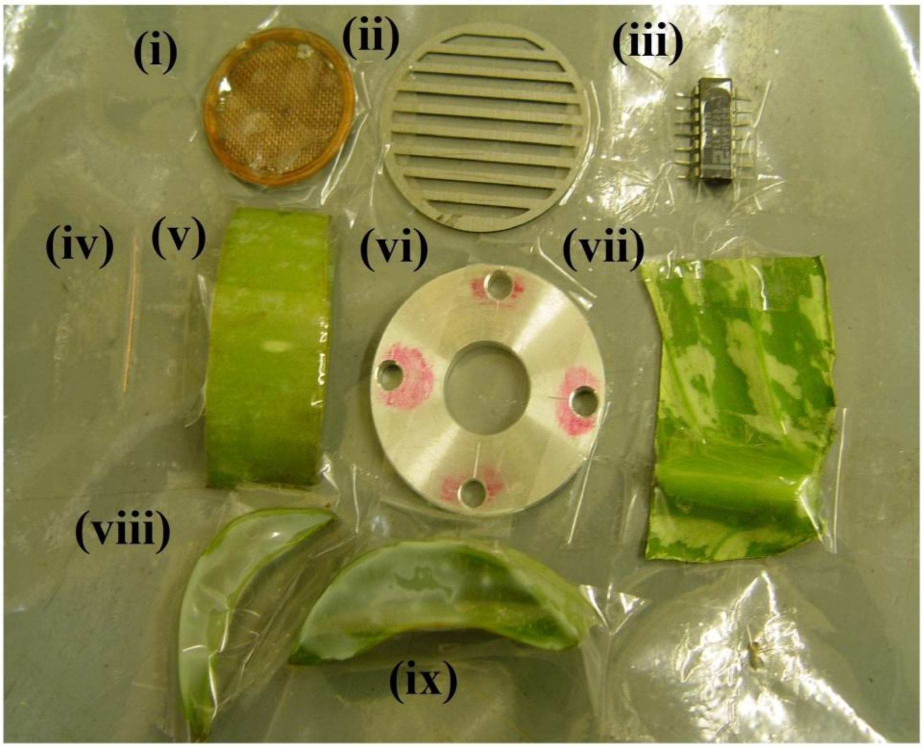

Fig. 8.4: Image of different samples (i) Cu mesh, (ii) Ti circular strip, (iii) IC chip, (iv) Cu wire, (v) Aloe-vera cross-section, (vi) Al disc, (vii) thick leaf, (viii) Aloe-vera cross-section and (ix) Aloe-vera cross-section.

Fig. 8.5 (a & b) shows the radiograph of the above samples recorded using electron beams generated from Ar and He respectively. It is observed that, compared to the radiographs using He electron beams, radiographs using Ar electron beams are comparatively clear and covers a laser sample area. This is due to the large beam size and uniformity of the beam profile of the Ar electron beams.

(a) 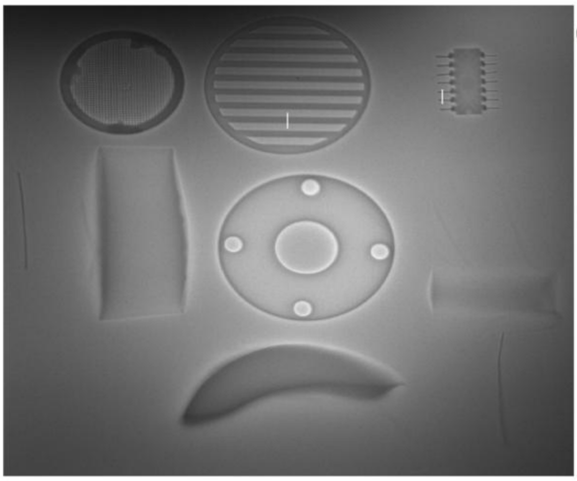 (b) 

Fig. 8.5: (a) Radiograph of samples recorded using Ar electron beam. (b) Radiograph of samples recorded using He electron beam.

Further, resolution of the radiograph recorded using Ar electron beam was determined by taking lineouts across the edges of the chip legs (Fig.8.6-a) and the Ti strip (Fig.8.6-b) shown by white lines in Fig.8.5-a. The lineouts have been fitted by a higher order Gaussian function and the resolutions have been determined from the FWHM width of the derivative of the Gaussian (inset of Fig. 8.6-a and 8.6-b) and are estimated to be ~360 µm and 150 µm respectively. The composition of the IC chip legs is Cu alloy with tin plating having density of 8.2 g/cc, whereas density of Ti is 4.5 g/cc. In this case, although, Ti has lower density, resolution with Ti sample is observed comparatively better than that with chip legs. This could be attributed to the difference in the thicknesses of the two samples (Ti strip of 1 mm thickness vs chip legs of 0.3 mm thickness), and also slight difference in the energy of electrons incident on them because of their different positions with respect to the beam centre. This is because, in general, in case of laser wakefield accelerator, the higher energy part of the electron beam has lower divergence compared to the low energy component as the high energy component experiences lower space charge effect after exiting the plasma [61, 62].

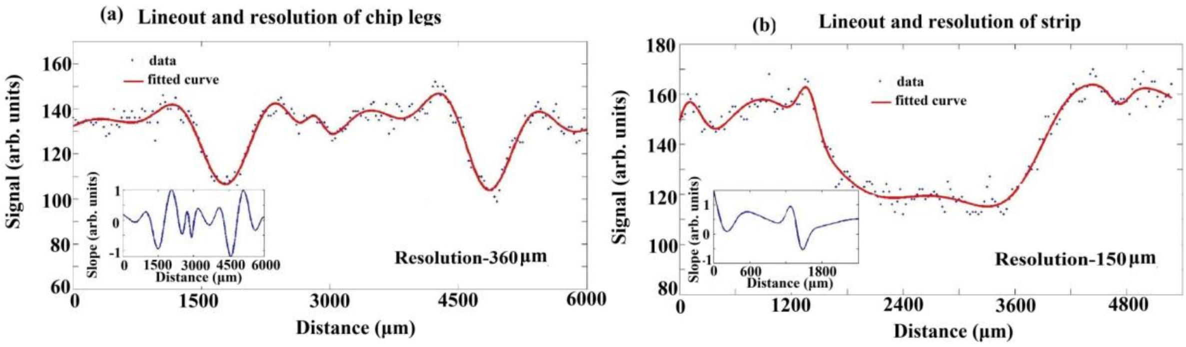

Fig. 8.6: Lineout of radiograph using Ar electron beams taken across the white line of (a) chip legs (iv) (b) Ti circular strip (iii). Corresponding derivatives are shown in the insets.

Further, enlarged radiographs of IC chip and Cu mesh recorded using Ar and He electron beams are shown in Fig. 8.7 (a-i & ii) & (b-i & ii) respectively. Inner electronic circuit structure and legs of the IC chip are clearly visible and Cu mesh structure of wire thickness 200 µm and separation of 500 µm is resolved.

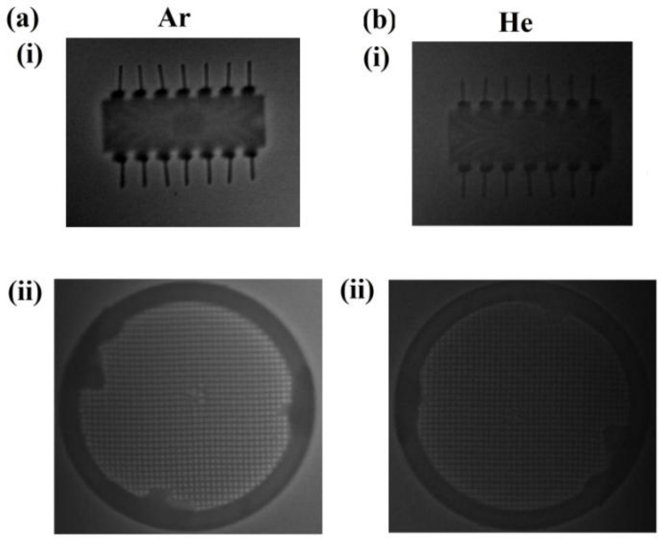

Fig. 8.7: Enlarged image of (i) IC chip of length 18 mm, and (ii) Cu mesh disc of diameter 30 mm, radiographed with electron beams generated from (a) Ar and (b) He gas-jet targets.

Next, a much thicker sample made of brass i.e. a 5 cm thick block dimension (60 mm × 20 mm) with 4 grooves (2 mm × 12 mm) (Fig. 8.8 a-i) and another block of dimension (50 mm × 20 mm) with 5 grooves (2 mm × 12 mm) (Fig. 8.8 a-ii) were used. Fig. 8.8 b-(i) and (ii) show the radiographs recorded correspondingly using electron beams generated from Ar and He respectively. Radiograph of grooves is observed to be much sharper in the case of He compared to the case of Ar. Electron beams generated from Ar having comparatively lower energy with broader spectrum (~ 20-50 MeV) compared to He, leads to significant scattering of electrons that causes blurring of the sample edges. However, enhanced blurring effect of the radiographs, due to the larger beam divergence in case of Ar compared to He can be discarded as the detector was placed in contact with the samples [63, 64]. The resolution of the radiograph of grooves recorded using Ar electron beams (as shown in Fig.8.8-c) was estimated and was found to be ~ 75 µm. In case of He, the signal was found to be saturated in the region where the most intense part of the beam passed through the central groove (Fig. 8.8-d). However, resolution was estimated from the lineout of the neighboring groove and was estimated to be ~60 µm which is comparatively better than the above estimated value for Ar. This is due to comparatively higher energy electron beams with lower energy spread in case of electron beams obtained from He gas target. As described above it may be noted that the detector limited resolution is ~ 30 µm.

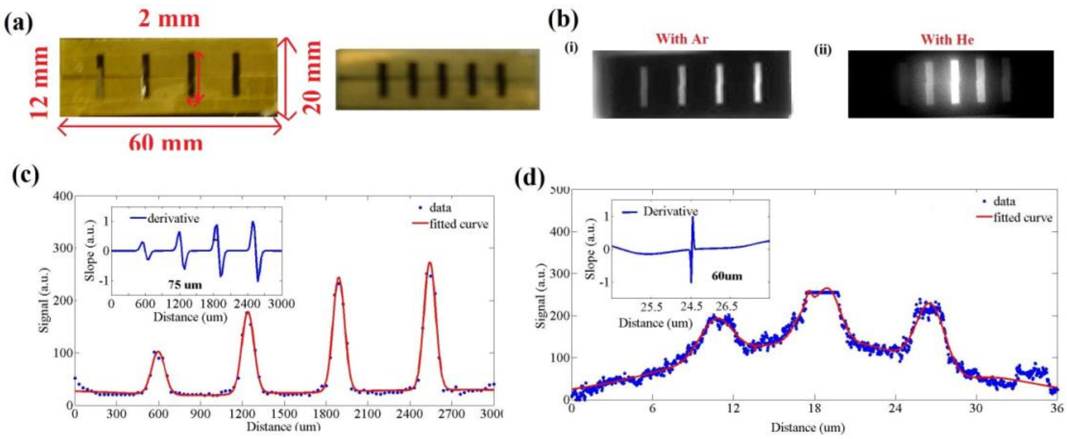

Fig. 8.8: (a) Image of brass blocks (60mm×20mm) with grooves (2mm×12mm) with (i) 4 and (ii) 5 slits. (b) Experimental radiographs of the blocks using (i) Ar electron beam (ii) He electron beam. Lineout of radiograph of groove taken horizontally and Gaussian fitting of the data points for radiograph (c) using Ar electron beams, (d) using He electron beams. Inset shows the derivative of the Gaussian fitting.

Further thick samples were also radiographed using He electron beam. Radiography of a 3 mm thick stainless steel key kept behind a 6 cm thick Al block (Fig. 8.9-a) was recorded. In the radiograph (Fig. 8.9-b), the radiograph of the key is clearly visible. Also the intense part of the electron beam is also visible as energy of ~ 150 MeV is sufficient to transmit through the 6 cm thick Al block. Generation of Bremsstrahlung radiation in the sample has created a background and hence reduces the contrast of the image. Earlier also, radiography of a key sample was demonstrated using lower energy electrons of 20 MeV by Mangles *et al.* [20]. Radiography study of voids and cracks embedded in thick dense steel block using >100 MeV QM electron beam with sub-millimeter resolution has also been demonstrated [22]. This shows that high energy electron beams can be used for the interrogation of interior of thick metallic structures used in various industrial applications and also for security purposes.

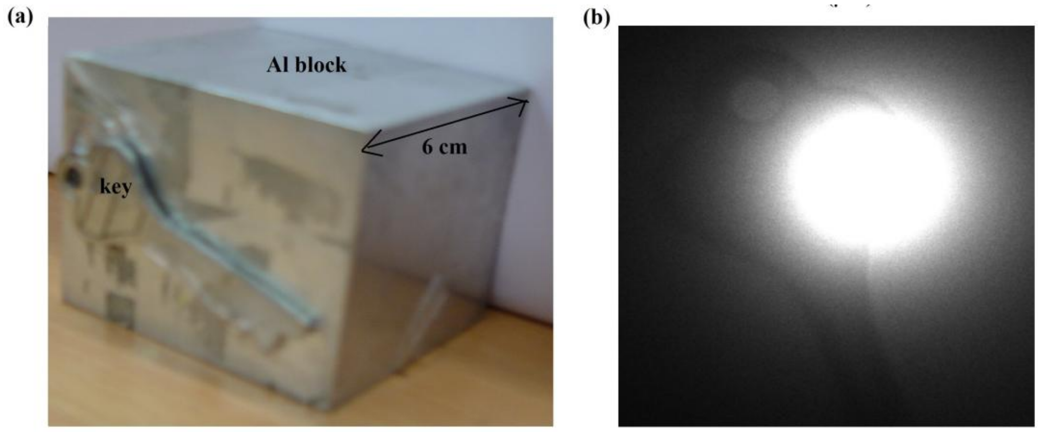

Fig. 8.9: (a) Image of Al block+key. (b) Radiograph of key using He electron beam.

Next, we have also performed electron radiography of biological samples e.g., plant tissue of thick leaf (central vein thickness of 0.5 cm) and various cross sections of aloe-vera (thickness of 1.75 cm) (see Fig. 3) with electron beams from Ar and He gas-jet target. In Fig. 8.10 (a, b & c), enlarged view of the radiographic image of a thick leaf and cross-section of aloe vera is shown. The radiograph of the thick leak using low energy Ar electron beams shows clear finer veins (Fig. 8.10-a). Fig. 8.10 (b) and Fig. 8.10 (c) show enlarged images of the radiographs of cross section of the aloe-vera leaf recorded using lower energy (Ar) and higher energy (He) electron beams respectively. For lower energy electron beams outer thick chlorophyll rich cover layer of the cross section of aloe-vera appears darker compared to the inner jelly component (Fig.8.10-b). However, contrast of radiograph generated by higher energy electrons using He gas target is comparatively poor (Fig.8.10-c).

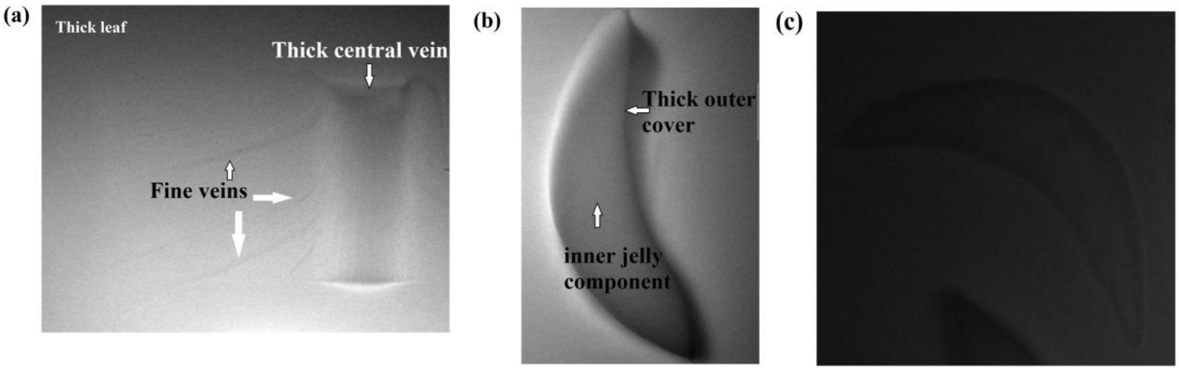

Fig. 8.10: Magnified radiograph recorded using lower energy Ar electron beam of (a) thick leaf showing inner veins. (b) Aloe vera cross-section of 1.75 cm thickness showing contrast in outer thick and inner jelly layer. (c) Radiograph of Aloe-vera cross section using higher energy He electron beam.

8.3.3: Reconstruction of images of radiographs using GEANT4 simulations:

(i) Simulation set up: GEANT4 [40] Monte Carlo simulations were performed to reconstruct the images of the radiographs of various samples. GEANT4 is a toolkit where interaction of charged particles such as electrons, protons, photons etc. with various objects can be studied and is able to facilitate handling of experimental conditions and tracking of various particles inside matter. Fig. 8.11 shows the set up used for simulating the experimental set up (Fig. 8.1) of laser plasma interaction for electron beam generation and transport through 54 μm thick Ti foil, phosphor-1 (thickness: 500 μm) and 36 μm Al foil placed in the electron beam path. In the simulation set up a plasma chamber of dimension 60×15×15 cm^3 was considered where vacuum was set as the environment. The electron beam source i.e. gas-jet was positioned at the center of the plasma chamber and electrons were allowed to propagate 30 cm along z-axis before exiting the vacuum chamber through a 54 μm Ti foil. Following this, the electron beam was allowed to propagate approximately 40 cm in air and was interacted with the target samples. In between, Phosphor-1 was placed at a distance of 9 cm from the Ti foil with 36 µm of Al foil kept in touch with it. A virtual screen (detector) was placed just behind the samples at a distance of 31 cm from Phosphor-1 and 70 cm from the source. Divergences and energy losses by the all above components introduced in the electron beam of given parameters for both He and Ar cases were estimated and was found to be negligible. To reconstruct various samples, standard modules adopted in GEANT4 for variety of materials were used and the final exit co-ordinate positions (at the detector) of transmitted primary electrons only were considered, neglecting all other secondary particles.

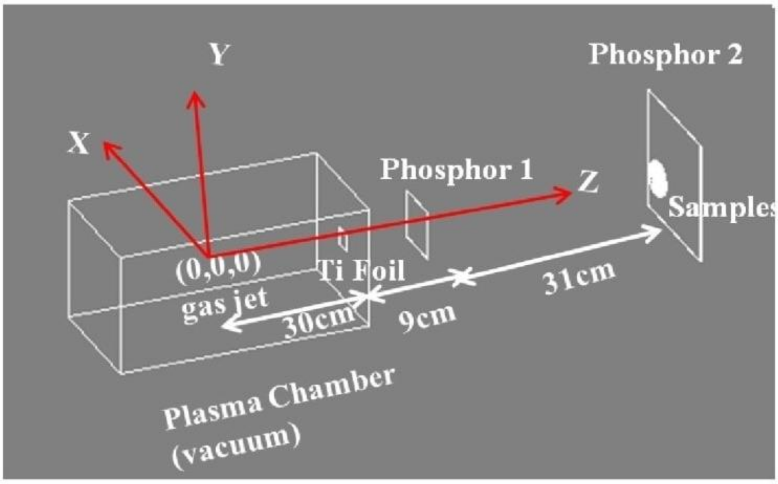

Fig. 8.11: Set up used for GEANT4 simulations

(ii) Reconstruction of spectra of electron beam of Ar and He gas-jet targets: Electron beams were constructed considering 10^6 number of particles and was defined in a cone shape (with flat profile) having divergences equal to that observed in experiments. For the case of Ar gas-jet electron beam, the cone angle was defined such that it makes a beam size of ~ 10 cm at the samples kept at 70 cm from the source similar to that observed in the experiment. Input electron beam spectra generated in this case was exponential with maximum energy of ~ 50 MeV and minimum energy of ~1 MeV and the ratio of the number of electrons at maximum to minimum energy was kept of the order of 10^2 (Fig. 8.12 (i)). It may be noticed that, towards the lower energy side, there is slight difference in the energy than that observed in the experiment. This is because in the experiment due to the limitation of our magnetic spectrometer we could not detect electrons below ~12 MeV but direct electron beams from Ar, contained energy below 12 MeV. For reconstruction of images recorded using He gas-jet beams, the divergence of the beam was kept such that electron beam size of ~ 1.5 cm is achieved at the samples. For the case of He, the electron spectra was generated (Fig. 8.12 (ii)) similar to that observed in the experiment. It has peak energy of ~ 150 MeV, beyond which the spectrum decreases exponentially to a maximum energy of ~ 250 MeV and towards the minimum energy side it drastically decreases to ~120 MeV.

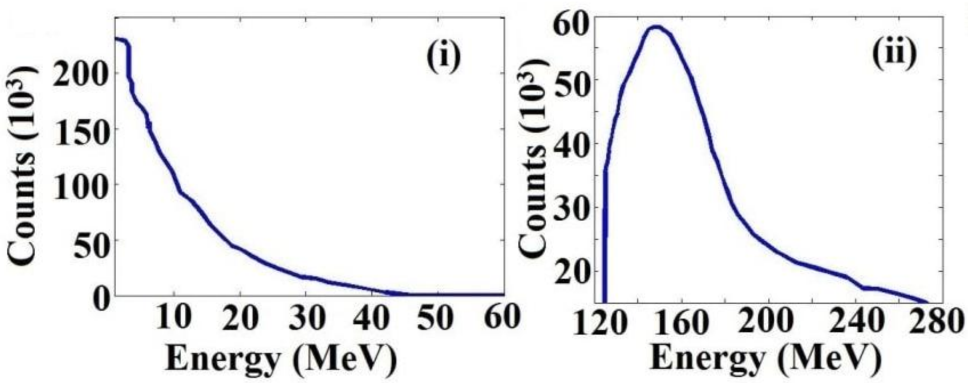

Fig. 8.12: Electron energy input spectra considered for GEANT4 simulations corresponding to electron beam generated from (i) Ar and (ii) He gas-jet targets

(iii) Reconstruction of images: The images were reconstructed by plotting the final exit point of the electrons just after the sample; hence one electron count represents one count. This process is independent of the energy of the electrons exiting the sample. Fig.8.13 (a) shows the reconstructed Al disc image using Ar electron beam which is in good agreement that with observed experimentally (Fig.8.5-vi). However, reconstruction of images using He electron beams, was not possible due to the larger penetration depth of high energy electrons compared to the sample thickness. Fig. 8.13 b-i & ii show the reconstructed image of the brass block with 4 grooves for Ar and He electron beams respectively. The reconstructed images using He electron beams with higher energy quasi-monoenergetic electron beams also shows sharper image compared to the lower energy electrons with broad spectrum (Ar) similar to that observed in experiments. This is due to the fact that, the lower the energy of incident electron beams, the more will be the diffraction at the sample edges [63], leading to erroneous measurement of the object dimensions. The reconstruction of radiograph of key (Fig. 8.13 c), using He electron beams was done with a 1 cm thick Al block only as larger thickness introduced very large scattering.

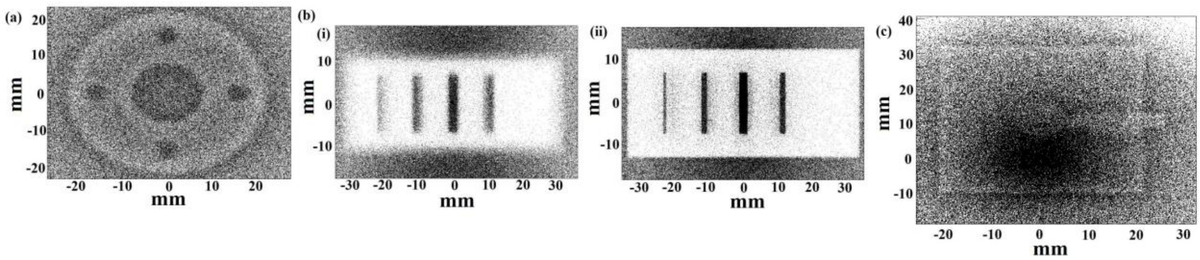

Fig. 8.13: (a) Reconstruction of image of Al disc for electron beam parameters of Ar. (b) Reconstruction of image of brass groove for parameters of (i) Ar electron beams and (ii) He electron beams (c) Reconstruction of image of key with 1 cm thick Al block for electron beam parameters of He electron beams.

Further, to compare the reconstructed image using GEANT4 with the experimental radiographs recorded quantitatively, lineout of the reconstructed image of brass block with 4 grooves using both Ar and He electron beams both along horizontal and vertical directions respectively is shown in Fig. 8.14 (i & ii) respectively. The lineouts are then fitted with higher order Gaussian function and length and breadth of the brass sample has been estimated from the FWHM width of the Gaussian. It is found that, the groove dimensions could closely match the original dimensions considering He compared to that of Ar electron beams. Thus lower energy electron radiography not only produces poor contrast images but also loses the original identity of the sample compared to higher energy. Further resolutions of the reconstructed image were also calculated from the FWHM width of the derivative of fitted Gaussian function. The resolution obtained using 20 MeV and 150 MeV monoenergetic electrons is ~150 µm and ~90 µm respectively as shown in the inset of Fig.8.14 (i & ii). The observed difference in the resolution values for experiment and simulation could be attributed to the different detection techniques used in both cases, however, for 150MeV both values are comparatively comparable.

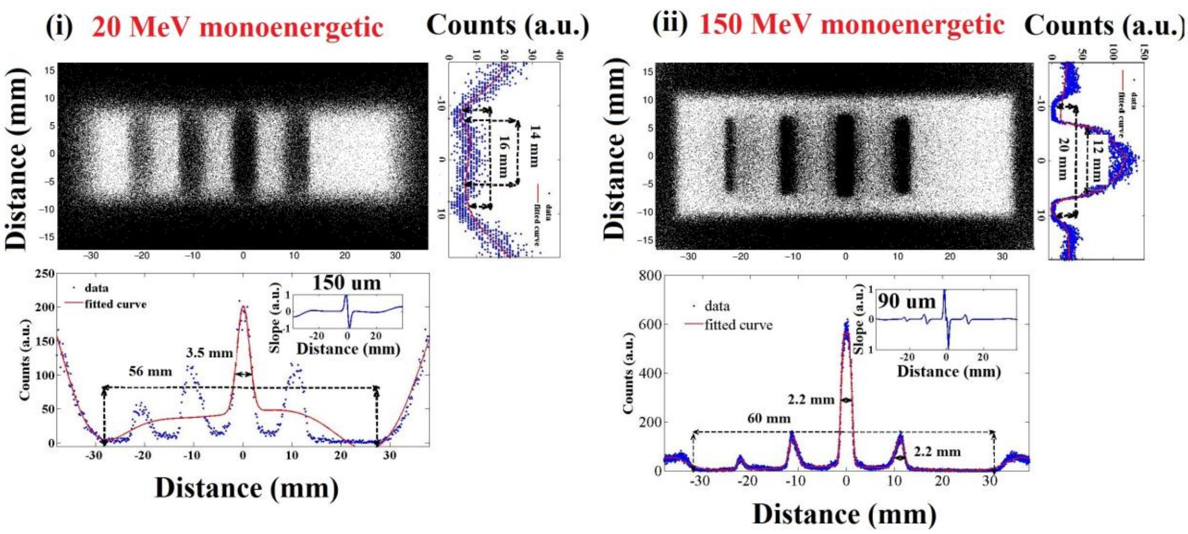

Fig. 8.14: (i) Reconstruction of brass groove using 20 MeV monoenergetic electron beams and corresponding longitudinal and transverse lineouts. Inset shows the resolution. (ii) Reconstruction of brass groove using 150 MeV monoenergetic electron beams and corresponding longitudinal and transverse lineouts. Inset shows the resolution.

Finally, we analyse the contribution of x-rays in the radiography. First of all, laser plasma accelerators are also a good source of betatron x-rays. In present experimental conditions, corresponding to the maximum electron energy of ~250 MeV observed in case of He at a density of ~6×10^{18}cm^{-3}, the calculated critical energy of x-rays generated would be of ~15 keV [66]. Generation of betatron x-rays of similar energy range have been observed in the earlier experiments from similar experimental conditions [67, 68]. In case of Ar, x-rays generated would be of even much lower energy as the generated electron beam has much lower energy. As discussed in our experimental set up, we have used a 54 μm thick Ti foil, followed by a Lanex regular (Phosphor-1) i.e. 180 μm of phosphor layer of Gadox (having Gd high Z material) in the electron beam path after which the samples were placed in contact with the IP. Betatron x-rays of above energy would be almost completely blocked by above elements in the path. Therefore, flux of x-rays on the IP will be almost nil. No traces of betatron x-rays in the laser direction was recorded on the detector when spectrum of the electron beam generated was recorded using magnet in the path which dispersed all the electrons from the laser beam path. Samples used were also quite thick considering the expected energy of the betatron x-rays.

Another source of x-rays is the bremsstrahlung generated from interaction of relativistic electrons with Ti foil and the dense samples materials. Since the radiographs were recorded keeping the samples kept in contact with the IP, magnet could not be placed in between them to deflect the electrons. It was found from GEANT4 simulations that, for electron beam of 150 MeV, bremsstrahlung generated from 54 μm thick Ti foil which reaches the detector varies in the range of 5-30 MeV, with a few present conversion. However, the imaging plates used in the experiment have x-ray sensitivity less than 10^{-5} PSL/photon for energy greater than 1.25MeV, whereas electron sensitivity is 0.01 PSL/electron. So flux of electrons relative to x-rays detected on IP would be 10^{5} times higher. Moreso, Bremsstrahlung generated in case of radiography of key kept behind 6mm thick Al plate would be high in energy and very penetrating to produce good contrast radiograph of the 5 mm thick key. Bremsstrahlung radiation in the sample shall created a background and hence reduce the contrast of the image only. Image reconstruction with secondary x-ray produced by the interaction with Ti foil and from the samples itself was also simulated in the GEANT4, in which case, the images generated were not sharp and generate only uniform background. Merrill *et al*. [19] has also reported observation of bremsstrahlung background even in case of radiography of thick samples with high-energy electron beams. Further, earlier reported experimental studies on radiography using electron beams generated from LPA with similar experimental technique also did not consider role of betatron or bremsstrahlung x-rays [22,23]. The above discussion supports that the radiographs recorded are from electrons only.

8.3.4. GEANT4 simulation on energy deposition in adipose tissue:

Further, we have also extended our studies by simulating the dose deposition rate in adipose tissue using GEANT4 simulations. The simulations were performed for the experimentally used electron beams parameters i.e. one with lower energy (~20 MeV) and the other with higher energy (~150 MeV) both with monoenergetic spectrum. Fig. 8.15 shows the dose deposition vs depth of the electrons in adipose tissue. For the case of 20 MeV electrons, the depth of maximum dose deposition was found to be ~ 5 - 6 cm, beyond which the dose deposition decreases rapidly within 10 cm of length. Similar dose distribution curve for 20 MeV electrons have also been reported earlier [23]. But for the 150 MeV electron beams, the depth of maximum dose deposition increases to about 20 -30 cm, beyond which the dose decreases to ~ 50% within 40 cm. Similar observation has also been reported earlier [27]. It is to be noted that compared to photons of similar energy, in case of electrons, beyond the maximum dose deposition, the dose deposition rate decreases rapidly. Whereas, the dose deposition rate curve was found at first to increase to a maximum and falls slowly with further depths in case of photons [69]. This suggests that photons would deposit substantial dose to the inner healthier tissues compared to electrons and hence, in this regard, electron beam radiotherapy becomes a better alternative for treatment of tissues at a particular depth.

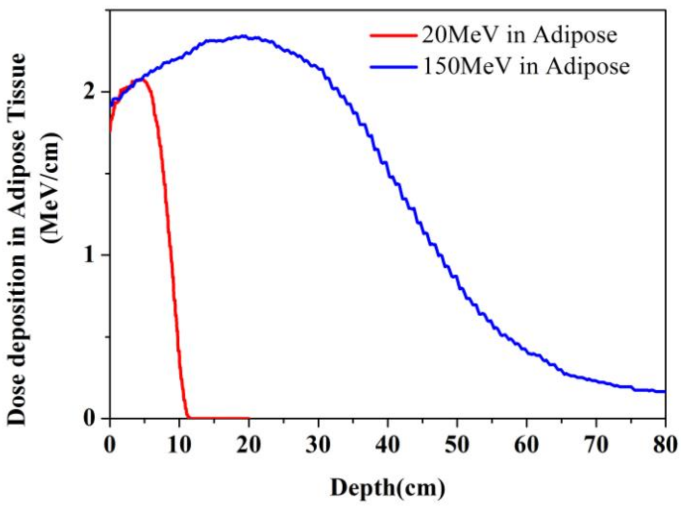

Fig. 8.15: GEANT4 simulation generated penetration depth of monoenergetic electron beams in adipose tissue. Red Curve: 20 MeV energy, and Blue Curve: 150 MeV energy.

Hence, it is clear that lower energy electron beams of few tens of MeV can be applicable for treatment of superficial tissues such as skin, brain etc., as it can penetrate up to certain length within biological samples of thickness of few cm. On the other hand, higher energy electron beams (~ 150 - 200 MeV) can penetrate deeper into the tissues and would be of use for inner deep seated tissues such as prostrate, lungs etc.

8.4: Conclusion:

An experimental investigation on electron radiography of various metallic and biological plant samples using LPA was performed. Ti:sapphire laser of 120 fs duration was allowed to interact with underdense gas-jet plasma targets of He and Ar. Electron beams were generated with two different parameters viz. maximum energy ~ 50 MeV with broad continuous spectrum, divergence of ~ 60 - 70 mrad (in case of Ar), and of peak energy ~ 150 MeV with QM spectra, divergence of ~ 5 - 7 mrad (in case of He). Radiographs were recorded at a distance of 70 cm from the source, and a minimum resolution of ~ 75 µm in case of Ar was demonstrated. Further, to support the experimental reults, GEANT4 Monte Carlo simulations were performed to reconstruct the radiographs. Role of electron beam parameters for radiography application was discussed through a comparative study of the quality of radiographs. Further, penetration depths of electron beams in human adipose tissue were studied, and its suitability for radiotherapy applications was discussed. Thus our study suggests a stable, tunable electron source based on LPA, generating electron beams in the range of ~ 50 MeV to ~ 200 MeV, suitable for both industrial applications and medical radiography.

References

[1] Physics of laser driven plasma based electron accelerators, E. Esarey, C. B. Schroeder, and W. P. Leemans, *Rev. Mod. Phys.*, **81**, 1229 (2009).

[2] Laser plasma accelerators, V. Malka, *Phys. Plasmas*, **19**, 055501 (2012).

[3] Developments in laser-driven plasma accelerators, S. M. Hooker, *Nature Photonics*, **7**, 775 (2013).

[4] Laser-driven plasma accelerators operating in the self-guided, blowout regime, C. Joshi, *IEEE Transactions on Plasma Science*, **45**, 3134 (2017).

[5] Plasma-based accelerators: then and now, C. Joshi, *Plasma Phys. Controlled Fusion*, (2019), doi.org/10.1088/1361-6587/ab396a.

[6] Femtosecond x rays from laser-plasma accelerators, S. Corde, K. Ta Phuoc, G. Lambert, R. Fitour, V. Malka *et al.*, *Rev. Mod. Phys.*, **85** 1 (2013).

[7] Applications of laser wakefield accelerator-based light sources, F. Albert and A. G. R. Thomas, *Plasma Phys. Control. Fusion*, **58**, 103001 (2016).

[8] Principles and applications of compact laser–plasma accelerators, V. Malka, J. Faure, Y. A. Gauduel, E. Lefebvre, A. Rousse *et al*., *Nature Physics*,**4**, 447 (2008).

[9] Charged particle radiography, C. L. Morris, N. S. P. King, K. Kwiatkowski, F. G. Mariam, F. E. Merrill *et al*, *Rep. Prog. Phys*. **76**, 046301 (2013).

[10] Crystallography: past and present, W. C. Roentgen, *Nature*, **53**, 274 (1986).

[11] Proton Radiography, A. M. Koehler, *Science*, **160**, 3825 (1968).

[12] Proton Radiography in the Diagnosis of Breast Carcinoma, V. W. Steward and A. M. Koehler, *Radiology*, **110**, 217 (1974).

[13] Flaw detection with medium-energy protons, V. I. Gorbunov, V. P. Ivakin, B. A. Kononov, and A. L. Lukin, *Sov. J. Nondestr. Test.*,**12**, 338 (1976).

[14] Application of charged particle beams of TWAC-ITEP accelerator for diagnostics of high dynamic pressure processes, S. A. Kolesnikov , A. A. Golubev, V. S. Demidov, S. V. Dudin, A. V. Kantsyrev *et al*., *High Pressure Res.*,**30**, 83 (2010).

[15] Charged particle radiography, F. E. Merrill, C. L. Morris, K. Folkman, F Harmon ,A Hunt *et al*., *IEEE Particle Accelerator Conf. (PAC)*, 1–4, 1704–6,4387, (2005).

[16] Electron radiography, F. E. Merrill, F. Harmon, A. Hunt, F. Mariam, K. Morley, *et al*, *Nuclear Instrum. Methods Phys. Res. B*, **261**, 382 (2007).

[17] High Energy Electron Radiography Experiment Research Based on Picosecond Pulse-width Bunch, Q. Zhao, S. Cao, R. Cheng, X. Shen, Z Zhang *et al., Proceedings of LINAC Geneva, Switzerland*, (2014).

[18] High energy electron radiography system design and simulation study of beam angle-position correlation and aperture effect on the images, Q. Zhao, S. C. Cao, M. Liu, X. K. Sheng, Y. R. Wang *et al*., *Nuclear Instrum. Methods Phys. Res. B*, **832**, 144 (2016).

[19] Demonstration of transmission high energy electron microscopy, F. E. Merrill, J. Goett, J. W. Gibbs, S. D. Imhoff, F. G. Mariam *et al*., *Appl. Phys. Lett.*,**112**, 144103 (2018).

[20] Table-top laser-plasma acceleration as an electron radiography source, S. P. D. Mangles, B. R. Walton, Z. Najmudin, A. E. Dangor, K. Krushelnick *et al*., *Laser and Particle beams,* **24**, 185, (2006).

[21] Electron radiography using hot electron jets from sub-millijoule femtosecond laser pulses, C. G. Serbanescu, and R. Fedosejevs, *Appl. Phys B*, **83**, 521 (2006).

[22] Submillimeter-resolution radiography of shielded structures with laser-accelerated electron beams, V. Ramanathan, S. Banerjee, N. Powers, N. Cunningham, A. Nathan. C. Smith *et al.*, *Physical Review Special Topics - Accelerators and Beams*, **13**, 104701 (2010).

[23] Electron radiography using a table-top laser-cluster plasma accelerator, Bussolino G, C Faenov, A Giulietti, A Giulietti, D Koester *et al.*, *J. Phys. D: Appl. Phys.*, **46**, 245501 (2013).

[24] High-charge divergent electron beam generation from high-intensity laser interaction with a gas-cluster target, P. Koester, G. C. Bussolino, G. Cristoforetti, A. Faenov, A. Giulietti *et al.*, *Laser and Particle Beams*, **33**, 331 (2015).

[25] Ultrafast electron radiography of magnetic fields in high-intensity laser-solid interactions, W. Schumaker, N. Nakanii, A. Maksimchuk, C. McGuffey, K. A. Tanaka *et al.*, *Phys. Rev. Lett.*, **110**, 015003 (2013).

[26] The Physics of Radiation Therapy, F. M. Khan, Williams & Wilkins, (1994).

[27] Review of electron beam therapy physics, K. Hogstrom and P. R. Almond, *Phys. Med. Biol.*, **51**, R455 (2006).

[28] 150-250 MeV electron beams in radiation therapy, C. DesRosiers, V. Moskvin, A. F. Bielajew and L. Papiez, *Phys. Med. Biol.*, **45**, 1781 (2000).

[29] Treatment planning for radiotherapy with very high-energy electron beams and comparison of VHEE and VMAT plans, M. B.-Carter, B. Qu, B. Palma, B. Hårdemark, E. Hynning *et al*., *Medical Physics*,**42**, 2615 (2015).

[30] Very high-energy electron (VHEE) beams in radiation therapy; Treatment plan comparison between VHEE, VMAT, and PPBS, E. Schüler, K. Eriksson, E. Hynning, S. L. Hancock, S. M. Hiniker, *Med. Phys.*, **44**, 2544 (2017).

[31] Treatment planning for radiotherapy with very high-energy electron beams and comparison of VHEE and VMAT plans, M. B. Carter, B. Qu, B. Palma, B Hardemark, E. Hynning *et al.*, *Medical Physics*, **42**, 2615 (2015).

[32] Ultra-short electron beams based spatio-temporal radiation biology and radiotherapy, V. Malka, J. Faure and Y. A. Gauduel, *Mutation Research*,**704**, 142 (2010).

[33] Laser-Driven Particle Acceleration Towards Radiobiology and Medicine, Antonio Giulietti, *Springer International Publishing, Switzerland*, (2016).

[34] Principles and applications of compact laser–plasma accelerators, V. Malka, J. Faure, Y. A. Gauduel, E. Lefebvre, A. Rousse *et al*., *Nature Physics*,**4**, 447 (2008).

[35] Radiotherapy with laser-plasma accelerators: Monte Carlo simulation of dose deposited by an experimental quasimonoenergetic electron beam, Y. Glinec, J. Faure, V. Malka, T. Fuchs, H. Szymanowski *et al*., *Med. Phys.*, **33** (1), 155 (2006).

[36] Dosimetry of laser-accelerated electron beams used for in vitro cell irradiation experiments, C. Richter, M. Kaluza, L. Karsch, H.-P.Schlenvoigt, M. Schürer *et al*., *Radiation Measurements*, **46**, 2006 (2011).

[37] Laser-plasma generated very high energy electrons in radiation therapy of the prostate, C. DesRosiers, V. Moskvin, M. Cao, C. Joshi, M. Langer, *SPIE Proceedings*, **6881**, 688109 (2008).

[38] Treatment planning for laser-accelerated very-high energy electrons, T. Fuchs, H. Szymanowski, U. Oelfke, Y. Glinec, C. Rechatin *et al*., *Phys in medicine and biology*, **54**, 11 (2009).

[39] Characteristics of High Electron Beam Generation and Dose Distribution in Laser Wakefield Accelerator for Cancer Treatment, K. N. Kim, Y. Hwangbo, S.-GyJeon, and J. Kim, 2018 IEEE Advanced Accelerator Concepts Workshop (AAC) (2018). https://doi.org/10.1109/AAC.2018.8659415.

[40] GEANT 4-a simulation toolkit, S. Agostinelli, J. Allison, K. Amako, J. Apostolakis, H. Araujo *et al*., *Nucl. Instrum.vMethods Phys. Res. A*, **506**, 250 (2003).

[41] Supersonic gas jet target for generation of relativistic electrons with 12TW-50fs laser pulse, T. Hosokai, K. Kinoshita, T. Watanabe, K. Yoshii, T. Ueda *et al*., 2002 Proc. 8th European Particle Accelerator Conf. (EPS) p 981 (2002).

[42] Calibration and cross-laboratory implementation of scintillating screens for electron bunch charge determination, T. Kurz, J. P. Couperus, J. M. Krämer, H. Ding, S. Kuschel *et al.*, Rev. Sci. Instrum. **89**, 093303 (2018).

[43] Absolute calibration for a broad range single shot electron spectrometer, Y. Glinec, J. Faure, A. Guemnie-Tafo, V. Malka, H. Monard *et al*., Rev. Sci. Instrument **77**, 103301 (2006).

[44] Absolute calibration of two DRZ phosphor screens using ultrashort electron bunch, Y. C. Wu, B. Zhu, K. G. Dong, Y. H. Yan, and Y. Q. Gu, Rev. Sci. Instrument, **83**, 026101 (2012).

[45] Generation of stable and low-divergence 10-MeV quasimonoenergetic electron bunch using argon gas jet, M. Mori, K. Kondo, Y. Mizuta, M. Kando, H. Kotaki, *et al.*, *Phys. Rev. Sp. Topics*, **12**, 082801 (2009).

[46] Clean source of soft X-ray radiation formed in supersonic Ar gas jets by high-contrast femtosecond laser pulses of relativistic intensity, M. Alkhimova, S. Ryazantsev, I. Skobelev, A. Boldarev, J. Feng *et al.*, *High Power Laser Science and Engineering* **8**, e26, 11 pages (2020).

[47] Hot-electron influence on the x-ray emission spectra of Ar clusters heated by a high-intensity 60-fs laser pulse, J. Abdallah, Jr., A. Ya. Faenov, I. Yu. Skobelev, A. I. Magunov, T. A. Pikuz *et al.*, *Phys. Rev. A*, **63**, 032706 (2001).

[48] Ionization Induced Trapping in a Laser Wakefield Accelerator, C. McGuffey, A. G. R. Thomas, W. Schumaker, T. Matsuoka, V. Chvykov *et al.*, *Phys. Rev. Lett.*, **104**, 025004 (2010).

[49] Injection and Trapping of Tunnel-Ionized Electrons into Laser-Produced Wakes, A. Pak, K. A. Marsh, S. F. Martins, W. Lu, W. B. Mori *et al.*, *Phys. Rev. Lett.*,**104**, 025003 (2010).

[50] Self-Focusing and Raman Scattering of Laser Pulses in Tenuous Plasmas, T. M. Antonsen and P. Mora, *Phys. Rev. Lett.*, **69**, 2204 (1992).

[51] Propagation and Guiding of Intense Laser Pulses in Plasmas, P. Sprangle, E. Esarey, J. Krall, and G. Joyce, *Phys. Rev. Lett.*, **69**, 2200 (1992).

[52] Resonant excitation of wakefields by a laser pulse in a plasma, N. E. Andreev, L. M. Gorbunov, V. I. Kirsanov, A. A. Pogosova, and R. R. Ramazashvili, *JETP Lett*. **55**, 571 (1992).

[53] Electron acceleration from the breaking of relativistic plasma waves, A. Modena, Z. Najmudin, A. E. Dangor, C. E. Clayton, K. A. Marsh *et al., Nature* (London) **377**, 606 (1995).

[54] Generation of Quasimonoenergetic Electron Bunches with 80-fs Laser Pulses, B. Hidding, K.-U. Amthor, B. Liesfeld, H. Schwoerer, S. Karsch *et al., Phys. Rev. Lett.*, **96**, 105004 (2006).

[55] Generation of quasi-monoenergetic electron beams with small normalized divergences angle from a 2 TW laser facility, B. S. Rao, A. Moorti, R. Rathore, J. A. Chakera, P. A. Naik *et al., Phys. Rev*. ST Accel. Beams,**17**, 011301 (2014).

[56] Multi-MeV Electron Beam Generation by Direct Laser Acceleration in High-Density Plasma Channels, C. Gahn, G. D. Tsakiris, A. Pukhov, J. Meyer-ter-Vehn, G. Pretzler *et al*., *Phys. Rev. Lett.*, **83**, 4772 (1999).

[57] Electron Acceleration in Cavitated Channels Formed by a Petawatt Laser in Low-Density Plasma, S. P. D. Mangles, B. R. Walton, M. Tzoufras, Z. Najmudin, R. J. Clarke *et al., Phys. Rev. Lett.*,**94**, 245001 (2005).

[58] Ultrarelativistic electron generation during the intense, ultrashort laser pulse interaction with clusters, Y. Fukuda, Y.Akahane, M. Aoyama, Y. Hayasi, T. Homma *et al*., *Physics Letters A*, **363,** 130 (2007).

[59] Synergistic Laser-Wakefield and Direct-Laser Acceleration in the Plasma-Bubble Regime, Xi Zhang, V. N. Khudik, and S. Gennady, *Phys. Rev. Lett.*,**114**, 184801 (2015).

[60] Laser wakefield and direct acceleration with ionization injection, Xi Zhang, V. N Khudik, A. Pukhov and G. Shvets, *Plasma Phys. Control. Fusion*, **58**, 034011(2016).

[61] Laser plasma acceleration of electrons: Towards the production of monoenergetic beams, K. Krushelnick, Z. Najmudin, S. P. D. Mangles, A. G. R. Thomas, M. S. Wei *et al*., *Phys. Plasmas* **12**, 056711 (2005)

[62] Monoenergetic electron beam optimization in the bubble regime, V. Malka, J. Faure, Y. Glinec, A. Pukhov, and J.-P. Rousseau, *Phys. Plasmas* **12**, 056702 (2005).

[63] A numerical study on charged-particle scattering and radiography of a steep density gradient, G. Shao and X. Wang, *Phys. Plasmas*, **23**, 092703 (2016).

[64] Small angle scattering in neutron imaging—a review, M. Strobl, R. Harti, C. Grünzweig, R. Woracek and J. Plomp, *J. Imaging***,** **3**, 64 (2017).

[65] Laser wakefield acceleration with high-power, few-cycle mid-IR lasers, Z.-H. He, A. G. R. Thomas, B. Beaurepaire, J. A. Nees, B. Hou *et al*., *Appl. Phys. Lett*. **102**, 064104 (2013).

[66] Production of a keV X-Ray Beam from Synchrotron Radiation in Relativistic Laser-Plasma Interaction, A. Rousse, K.T. Phuoc, R. Shah, A. Pukhov *et al*., *Phys. Rev. Lett*. **93**, 135005 (2004).

[67] Demonstration of the synchrotron-type spectrum of laser-produced Betatron radiation, S. Fourmaux, S. Corde, K.T. Phuoc, P. M. Laguay, S. Payeur *et al*., *New Journal of Physics* **13,** 033017 (2011).

[68] Femtosecond x rays from laser-plasma accelerators, S. Corde, K. T. Phuoc, G. Lambert, R. Fitour, V. Malka *et al*., *Rev. Mod. Phys*., **85**, 1 (2013)

[69] Secondary prompt gamma rays to improve proton range verification, J. Saunders, Ph.D. Thesis, Georgia Institute of Technology, 2016.

CHAPTER 9

Conclusion and future perspective

This chapter summarizes the present thesis work and discusses prospects of future investigations in light of it.

9.1. Conclusions:

Laser wakefield acceleration mechanism (LWFA) has been investigated in detail over years in various experimental conditions and has shown its potential for generation of high-quality GeV-class electron beams [1-5]. Developments during last two decades or so has led LPA to be recognized as a potential candidate for future generation compact table top accelerators suitable for various possible applications [6-9]. Today when LPA is considered as a source of high energy short wavelength radiation, the other dominant acceleration mechanism governing laser plasma interaction i.e. DLA is being considered again along with wakefield in a hybrid regime acceleration [10-15]. This regime of acceleration has two fold advantages: one is the enhancement of electron energy gain in LWFA as the electrons ~~now~~ gains additional energy from the DLA over wakefield [10-15], and the other very important advantage is the potential to generate high-energy betatron radiation compared to only wakefield mechanism as in this case oscillation amplitude of electrons could be comparatively larger [16-20]. Thus, DLA shows a promising path to enhance the betatron radiation generated from LWFAs. Realizing the importance of DLA, Shaw *et al*. [21] have proposed for optimization of the DLA in LWFA either by optimizing the laser pulse duration or by experimentally verifying the two laser pulse scheme of Zhang *et al*. [10,11].

The present thesis work focuses on the experimental investigation of LPA and identification of the role of direct laser acceleration (DLA) of electrons in a wide range of laser and plasma parameters. All the experiments were performed with the CPA based 150 TW, 25 fs, Ti:sapphire laser system of RRCAT, Indore, India. The laser and plasma parameters were varied such that it covers a long laser pulse duration regime of $L>>\lambda_p$ to shorter laser pulse duration regime of $L\geq\lambda_p$, and the laser pulse completely overlaps the injected electrons. Various gas-jet targets were used such He, N_2, Ar and mixed gas targets of He doped with few % of N_2 and N_2 doped with few tens of % of He with varying concentrations of dopant.

9.1.1: Identification of role of DLA in different experimental regime:

In $L>>\lambda_p$ regime, where laser plasma interaction of long laser pulse duration of 200 fs with underdense He plasma was studied, a pure DLA regime was identified as discussed in Chapter-4, as is also observed in earlier reports by Gahn *et al*. [22] and Mangles *et al*. [23].

On reducing the laser pulse duration to ~55-60 fs such that $L>\lambda_p$, contribution of DLA along with wakefield in the total energy of electrons was observed and thereby a hybrid regime of acceleration (DLA + wakefield) was identified in He gas-jet plasma with equal contribution from both wakefield and DLA. The identification of a hybrid regime of acceleration in $L>\lambda_p$ regime at the self-injection threshold density of He gas target has been discussed in Chapter-5 and was also verified later in another experiment using He gas-jet target and is discussed in Chapter-7.

The acceleration regime of short laser pulse duration of $L>\lambda_p$ was further explored in detail in similar conditions using ~55-60 fs duration laser pulses and mixed gas-jet targets of He + N_2 and high Z target of pure N_2. Due to the effect of ionization induced injection mechanism associated with mixed gas and high Z targets, the threshold density for generation of relativistic electron beams was reduced compared to the self-injection threshold density observed for He gas-jet target. However, the laser and plasma parameters still lies in the $L \geq \lambda_p$ regime and complete overlap of the laser pulse with the injected electrons takes place. On decrease of density, strength of wakefield was observed to reduce, and interestingly a pure DLA regime of acceleration was identified. To the best of our knowledge, such an observation of pure DLA mechanism with short laser pulse duration of few tens of fs regime using mixed and high Z gas targets has not been investigated earlier. The investigations have been discussed in Chapter-5 and Chapter-6.

Further, in the similar conditions, threshold density for generation of relativistic electron beams was varied in mixed gas-jet target by varying the doping concentration of He and N_2 in the gas mixture and its effect on acceleration mechanism was studied. With increase in density, role of wakefield was observed to increase and hybrid mechanism was identified as the dominant applicable acceleration mechanism. In this case, a regime of onset of wakefield was observed where strength of wakefield slowly increases and hence the contribution of energy gain from wakefield gradually increases. Thus the hybrid acceleration mechanism observed in case of mixed gas-jet target is associated with ionization injection mechanism and is different from that observed in case of He gas-jet target at the self-injection threshold density where equal contribution of wakefield and DLA was observed. The observations have been discussed in Chapter-5 and Chapter-6. Further, for comparison experiments were also performed with Ar gas-jet targets in the $L > \lambda_p$ regime using longer laser pulse duration of 120 fs. In this case also, a pure DLA regime was identified and the results are discussed in Chapter-6 and Chapter-8.

Hence, the present thesis focuses on the identification of DLA mechanism and the suitable laser and plasma conditions were identified in different gas-jet targets of He, N_2, Ar and mixed gas of He + N_2 either by varying the laser pulse duration or by varying the plasma density. The identification of the acceleration mechanism of DLA has been based on the theoretical analysis on DLA performed in the different laser and plasma conditions supported by various experimental observations and 2D PIC simulations performed using code EPOCH [24] and OSIRIS [25,26].

9.1.2: Generation of relativistic electron beams and its characteristics:

Stable and reproducible generation of electron beams were observed during the experiment for the wide range of laser and plasma parameters. However, the electron beam properties were observed to vary depending on the acceleration mechanism i.e. either a pure DLA or hybrid regime. Electron beam properties were also observed to be affected by the injection mechanism i.e. either self-injection in case of He gas-jet target or ionization induced injection mechanism in case of pure N_2, mixed (He + N_2) and Ar gas-jet target.

For 1.2 mm length of plasma, in pure He gas-jet target where a pure DLA regime of acceleration was identified with 200fs duration laser pulse, collimated electron beams with typical divergence of ~30-40 mrad were observed with mostly quasi-thermal electron spectra with maximum energy of ~30 MeV (Chapter-4). In few shots, quasi-monoenergetic electron beams with peak energy of ~17-22 MeV and energy spread of ~10-20% were also observed from the similar experimental conditions. With 55fs laser pulse and N_2 gas-jet target, collimated electron beams with divergence of ~15-30 mrad and quasi-thermal electron beams with maximum energy of ~ 60 MeV were observed in a pure DLA regime (Chapter-5). Electron beams with similar energy and with quasi-thermal spectra were also observed from mixed gas-jet target of He + N_2 in a pure DLA dominated regime (Chapter-5). However, enhancement of electron energy was observed up to ~90 MeV in mixed gas-jet target when electrons were accelerated from a hybrid regime of acceleration (Chapter-5). The electron beam spectra were quasi-thermal. With He gas-jet target, quasi-monoenergetic electron beams with peak energy of ~28 MeV and energy spread of ~64% were observed accelerated through hybrid mechanism (Chapter-5).

For 4 mm length of plasma, in mixed gas-jet target of N_2 + He, where a pure DLA regime was identified, collimated electron beams with divergence of ~7-8 mrad were observed. Electron beam spectra were quasi-monoenergetic with energy spread of ~21 % and peak energy of ~168 MeV (maximum energy ~206 MeV) were observed (Chapter-6). On increasing density, hybrid regime of acceleration was identified and enhancement of electron energy upto ~235 MeV was observed with quasi-thermal electron spectra (Chapter-6). Hybrid regime of acceleration was also identified in He gas-jet target where quasi-monoenergetic electron beam with peak energy of ~140 MeV and energy spread of ~18% were observed (Chapter-7). In few shots, the peak electron energy was observed to increase up to ~400-520 MeV with maximum energy in the range of ~620-750 MeV.

9.1.3: Radiography applications:

The present thesis also focuses on the study of radiography applications of various metallic and biological plant samples using the relativistic electron beams generated from LPA using He and Ar gas-jet targets (Chapter-8). The radiographs were generated with a minimum resolution of ~75 μm. Further, reconstruction of the radiographs of various samples was performed using GEANT4 simulations [27]. Penetration depth of electrons generated through LPA was studied through simulations and in this regard suitability of LPA in radiotherapy was also discussed.

9.2. Future outlook:

In the present thesis, experimental investigations in different parametric conditions were performed and role of DLA was identified. The complexity associated with this aspect of laser plasma accelerators suggests further investigations (experimental and simulations) which is not possible to address through a single thesis work. The thesis work thus brings out vast scope for possible future investigations, and several points could be considered as dedicated research problems for further investigations in this field.

Through experimental observations, various regimes of acceleration were identified viz. pure DLA, and hybrid (WF+DLA). DLA signatures were established through its manifestation in observed maximum electron energy, spectrum characteristics (quasi-monoenergetic, broad continuous spectrum and appearance of multiple groups of electrons), and also through electron beam profile (ellipticity and larger divergence) and transmitted laser spectrum wherever available and applicable. Dedicated experiments towards establishing the signature of DLA could be useful in establishing and improving the understanding, e.g. appearance of fork structures in energy spectrum when dispersed perpendicular to the laser polarization as observed by Shaw *et al.*, [12], and also other parameters as stated above. Simultaneous use of many diagnostics such as recording of laser forward spectrum, laser channeling and propagation inside plasma through Thomason scattering, Shadowgraphy, interferrogram would lead to more detailed information about the interaction of the high intense laser pulse with plasma. Although positive chirp was found favorable for present experimental conditions, further detailed study in this direction on effect of laser chirp on DLA would be of interest. Effect of other laser parameters e.g. focal spot size, pulse front tilt etc. could also be considered. Finally, as high-power laser systems are mostly operated in single shot mode, and therefore in general there has been limitation on statistics of data on LPA, investigations with detailed statistics could be targeted.

Another signature of DLA mechanism would be manifested from the simultaneous recording of betatron radiation experimentally which would be another aspect of our future investigation. Optimum regimes could be identified for generation of betatron radiation from the accelerating electrons particularly in the laser created channel in high Z gas-targets. Studies devoted to fundamental understandings e.g. injection mechanism of electrons in DLA, particularly injection through surface wave generation so that better control of the accelerator can be achieved, would also be necessary and interesting.

2D PIC simulation studies were performed primarily to support the experimental observations and distinguish the underlying acceleration mechanism for which bubble formation, channel creation, separate contributions in energy gain has been studied. However, more detailed investigation could be useful such as retrieving electron beam profile, charge, betatron radiation etc. would strengthen the claim. A much more rigorous study of 2D PIC simulations on DLA and hybrid acceleration mechanism is required particularly tracking of individual electrons and understanding the electron energy gain separately from wakefield and DLA.

Further, a more detailed theoretical model on the understanding of electron dynamics in the laser channel accelerated by DLA would be of much interest. It is understood that the applicability of theoretical estimation of the maximum energy gain in the hybrid regime is not straight forward. Study of dynamics of the electron in the presence of laser and wakefield and the trapping conditions of electrons in such complex field structure would be of interest. Subsequently, detailed theoretical analysis of the hybrid regime of acceleration of electrons needs to be performed and this leaves a huge scope for future investigation from the theoretical point of view. Another important study in this direction could be study of effect of chirp on generation relativistic electron beams through DLA.

Further experimental investigation on the radiography application using electrons generated from LPA should be performed for special target samples and optimization of parameters is required for achieving higher resolution. Also, study with biological samples should also be performed and experimental estimation of dose deposition on adipose tissue could also be carried out.

References

[1] Physics of laser driven plasma based electron accelerators, E. Esarey, C. B. Schroeder, and W. P. Leemans, *Rev. Mod. Phys.*, **81**, 1229 (2009).

[2] Laser plasma accelerators, V. Malka, *Phys. Plasmas,* **19**, 055501 (2012).

[3] Developments in laser-driven plasma accelerators, S. M. Hooker, *Nature Photonics*, **7**, 775 (2013).

[4] Laser-driven plasma accelerators operating in the self-guided, blowout regime, C. Joshi, *IEEE Transactions on Plasma Science*, **45**, 3134 (2017).

[5] Plasma-based accelerators: then and now, C. Joshi, *Plasma Phys. Controlled Fusion*, (2019), doi.org/10.1088/1361-6587/ab396a.

[6] Applications of laser wakefield accelerator-based light sources, F. Albert and A. G. R. Thomas, *Plasma Phys. Control. Fusion*, **58**, 103001 (2016).

[7] Principles and applications of compact laser–plasma accelerators, V. Malka, J. Faure, Y. A. Gauduel, E. Lefebvre, A. Rousse *et al*., *Nature Physics,***4**, 447 (2008).

[8] Applications of laser driven particle acceleration, P. R. Bolton, K. Parodi and J. Schreiber, *CRC Press*, Taylor & Francis Group (2018).

[9] Laser-Driven Particle Acceleration Towards Radiobiology and Medicine, Antonio Giulietti, *Springer International Publishing, Switzerland*, (2016).

[10] Synergistic Laser-Wakefield and Direct-Laser Acceleration in the Plasma-Bubble Regime, Xi Zhang, V. N. Khudik, and S. Gennady, *Phys. Rev. Lett.*,**114**, 184801 (2015).

[11] Laser wakefield and direct acceleration with ionization injection, Xi Zhang, V. N Khudik, A. Pukhov and G. Shvets, *Plasma Phys. Control. Fusion*, **58**, 034011(2016).

[12] Role of Direct Laser Acceleration of Electrons in a Laser Wakefield Accelerator with Ionization Injection, J. L. Shaw, N. Lemos, L. D. Amorim, N. Vafaei-Najafabadi, K. A. Marsh *et al*., *Phys. Rev. Lett.*,**118**, 064801 (2017).

[13] Experimental signatures of direct-laser-acceleration-assisted laser wakefield acceleration, J. L. Shaw, N. Lemos, K. A. Marsh, D. H. Froula and C. Joshi, *Plasma Physics and Controlled Fusion*, **60**, 044012 (2018).

[14] Role of direct laser acceleration in energy gained by electrons in a laser wakefield accelerator with ionization injection, J. L. Shaw, F. S. Tsung, N. Vafaei-Najafabadi, K. A. Marsh, N. Lemos *et al*., Plasma Phys. Control. Fusion, **56**, 084006 (2014).

[15] Estimation of direct laser acceleration in laser wakefield accelerators using particle-in-cell simulations, J. L. Shaw, N. Lemos, K. A. Marsh, F. S. Tsung, W. B. Mori *et al*., *Plasma Physics and Controlled Fusion*,**58**, 034008 (2016).

[16] Bright betatron X-ray radiation from a laser-driven-clustering gas target, L. M. Chen, W. C. Yan, D. Z. Li, Z. D. Hu, L. Zhang *et al., Scientific Reports*, **3**, 1912 (2013).

[17] Observation of Synchrotron Radiation from Electrons Accelerated in a Petawatt-Laser-Generated Plasma Cavity, S. Kneip, S. R. Nagel, C. Bellei, N. Bourgeois, A. E. Dangor *et al., Phys. Rev. Lett.*,**100**, 105006 (2008).

[18] Gamma-rays from harmonically resonant betatron oscillations in a plasma wake, S. Cipiccia, M. R Islam, B. Ersfeld, R. P. Shanks, E. Brunetti, *et al.*, *Nat. Phys.***7**, 867 (2011).

[19] Femtosecond x rays from laser-plasma accelerators, S. Corde, K. Ta Phuoc, G. Lambert, R. Fitour, V. Malka *et al.*, *Rev. Mod. Phys.*, **85** 1 (2013).

[20] Characteristics of betatron radiation from direct-laser-accelerated electrons, T. W. Huang, A. P. L. Robinson, C. T. Zhou, B. Qiao, B. Liu *et al.*, *Phys. Rev. E.*, **93** 063203 (2016).

[21] Direct laser acceleration in laser wakefield accelerators, PhD Thesis, J. L. Shaw, University of California (2016).

[22] Multi-MeV Electron Beam Generation by Direct Laser Acceleration in High-Density Plasma Channels, C. Gahn, G. D. Tsakiris, A. Pukhov, J. Meyer-ter-Vehn, G. Pretzler *et al.*, *Phys. Rev. Lett.*, **83**, 4772 (1999).

[23] Electron Acceleration in Cavitated Channels Formed by a Petawatt Laser in Low-Density Plasma, S. P. D. Mangles, B. R. Walton, M. Tzoufras, Z. Najmudin, R. J. Clarke *et al.*, *Phys. Rev. Lett.*,**94**, 245001 (2005).

[24] Contemporary particle-in-cell approach to laser-plasma modelling, T. D. Arber, K. Bennett, C. S. Brady, A. Lawrence-Douglas, M. G. Ramsay *et al.*, *Plasma Physics and Controlled Fusion,* **57,** 1 (2015).

[25] Lecture Notes in Computer Science: Computation Science–ICCS 2002, R. A. Fonseca *et al.*, *edited by* P. M. A. Sloot *et al.*, Berlin: Springer **2331**, 342 (2002).

[26] Particle-in-Cell Modeling of Plasma-Based Accelerators in Two and Three Dimensions, R. G. Hemker, PhD Dissertation UCLA (1999) [arXiv:1503.00276].

[27] GEANT 4-a simulation toolkit, S. Agostinelli, J. Allison, K. Amako, J. Apostolakis, H. Araujo *et al*., *Nucl. Instrum.vMethods Phys. Res. A*, **506**, 250 (2003).

<u>List of keywords</u>

Name of the Student: DIPANJANA HAZRA

Name of the CI/OCC: RRCAT, INDORE **Enrolment No.: PHYS03201304009**

Thesis Title: Laser driven plasma based electron acceleration, applicable mechanisms and its applications

1. Laser plasma electron acceleration
2. Advanced laser plasma acceleration
3. Laser wakefield electron acceleration
4. Direct laser acceleration
5. Hybrid laser plasma acceleration
6. Ionization induced injection
7. Energy gain and dephasing in direct laser acceleration
8. PIC simulations on plasma acceleration
9. Ultrashort ultrahigh-intensity laser plasma interaction
10. Laser guiding and channelling
11. Laser filamentation
12. Electron radiography

<u>**Thesis Highlights**</u>

Name of the Student: DIPANJANA HAZRA

Name of the CI/OCC: RRCAT, INDORE **Enrolment No.: PHYS03201304009**

Thesis Title: Laser driven plasma based electron acceleration, applicable mechanisms and its applications

Discipline: Physical Sciences **Sub-Area of Discipline: Plasma Physics**

Date of viva voce: 6-11-2020

The thesis work presents investigations on Laser Plasma Acceleration (LPA) for generation of relativistic electron beams through ultra-short, ultra-high intensity laser interaction with gas-jet plasma targets. Particular emphasis has been on determination of different acceleration mechanisms applicable in varying laser and plasma conditions, along with application in electron radiography. LPA process is also understood through theoretical model for estimation of energy gain and dephasing effects and 2D PIC simulations.

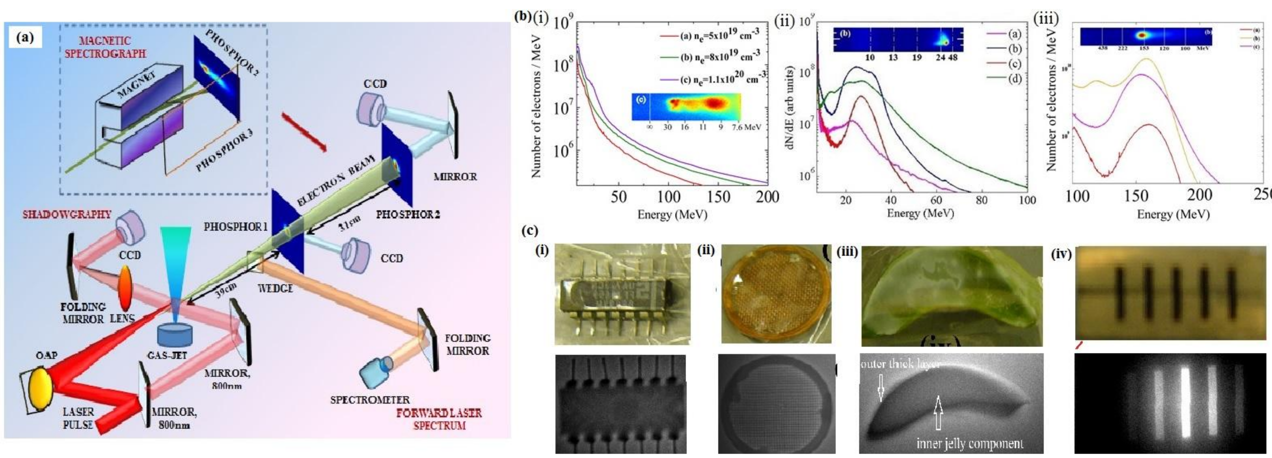

(A) Schematic of experimental set up. (B) Electron beam spectra in He gas-jet target with laser pulse duration of (i) ~200 fs through DLA (ii) ~55 fs through hybrid, (iii) in mixed gas-jet target of N_2+50%He with laser pulse duration of ~60 fs through DLA and (C) Radiographs of various samples recorded using relativistic electron beams generated from LPA.

Experiments were performed using Chirped Pulse Amplification (CPA) based 25 fs, 150 TW Ti:sapphire laser system at RRCAT, Indore, India. Direct laser acceleration (DLA) and hybrid regime of acceleration (DLA + wakefield) of electrons in different gas-jet targets of He, N_2, Ar and mixed gas targets of He + N_2 were identified. A pure DLA regime was identified as the applicable acceleration mechanism with long laser pulse duration of 200 fs in He gas-jet target. Interestingly, a pure DLA regime of acceleration was also identified with short laser pulse duration of 55-60 fs in high-Z N_2 and mixed gas targets. Electron beams with few tens of MeV energy with quasi-thermal distribution, and also quasi-monoenergetic (energy spread ~21%) electron beams with peak energy of ~168 MeV were observed. Hybrid regime of acceleration in He has demonstrated acceleration of electrons to few hundreds of MeV and maximum up to ~750 MeV. Further, radiography application of relativistic electron beams was explored along with suitability for radiotherapy application. Many interesting results have been brought out through these investigations which to the best of our knowledge are not reported earlier. The studies would be of significance for developing stable laser plasma accelerator through understanding of acceleration mechanisms involved and high flux short wavelength betatron radiation source based on that.